DISSERTATION

ROLE OF RIGHT VENTRICULAR ANISOTROPIC VISCOELASTICITY IN PATHOPHYSIOLOGY OF RV FAILURE

Submitted by

Kristen LeBar

Department of Mechanical Engineering

In partial fulfillment of the requirements

For the Degree of Doctor of Philosophy

Colorado State University

Fort Collins, Colorado

Fall 2024

Doctoral Committee:

Advisor: Susan James
Co-advisor: Zhijie Wang

Kirk McGilvray
Adam J. Chicco
Ketul Popat

ABSTRACT

ROLE OF RIGHT VENTRICULAR ANISOTROPIC VISCOELASTICITY IN PATHOPHYSIOLOGY OF RV FAILURE

Right ventricular (RV) failure is a key contributor to the mortality and morbidity of multiple cardiovascular diseases, such as congenital heart disease, heart failure with preserved ejection fraction, and pulmonary hypertension (PH). There has still, though, been a lack of treatment for such patients, due largely to a lack of understanding of the pathology and physiology of RV failure. Right ventricular passive stiffness is significantly increased in disease progression, and this change in mechanical behavior have been shown to markedly contribute to RV diastolic and systolic function. However, the myocardium is viscoelastic, and there is both energy storage (elasticity) and dissipation (viscosity) involved in the dynamic deformation within each cardiac cycle. Therefore, the long-ignored viscous component and its impact on organ performance must be investigated. Understanding of the impact of RV viscoelasticity in RV performance will fill a key knowledge gap in RV pathophysiology.

Furthermore, the microtubule (MT), a cytoskeletal component of the cardiomyocyte (CM), is known to significantly contribute to the pathophysiology of multiple cardiovascular diseases. In the pressure-overloaded RV, MT density increases, leading to a stiffening of the CM and thus potentially the entire ventricular wall. Moreover, recent cell studies have shown that the pharmaceutical removal of the MT network reduces CM viscoelasticity and increases the extent of shortening, indicating a key role of the MT network myocardial viscoelasticity and contractile

function. These findings suggest a regulation of myocardial viscoelasticity and organ contractility via the MT network.

Therefore, the overall goal of my study is to determine the contribution of right ventricular anisotropic viscoelasticity to organ function during PH progression. The three specific aims of my dissertation research are: determine the alterations of RV anisotropic viscoelasticity in PH; delineate the contribution of the microtubules network to RV anisotropic viscoelasticity; explore the impact of the RV viscoelasticity on organ function using experimental and computational approaches.

TABLE OF CONTENTS

LIST OF TABLES

LIST OF FIGURES

CHAPTER 1 - Determine the alterations of RV anisotropic viscoelasticity in pulmonary hypertension

Aim 1a: Investigate changes in RV viscoelasticity with pulmonary hypertension using experimental approaches.[1]

1. Background

Right ventricle (RV) failure is a lethal condition that contributes significantly to the mortality and morbidity in a variety of cardiovascular diseases including pulmonary hypertension (PH), congenital heart disease, and left heart failure with preserved ejection fraction (HFpEF) [1], [2], [3], [4], [5]. Unfortunately, there has been a lack of effective treatment for these patients, which is due in part to an inadequate understanding of the structure-function relationship of the right ventricle (RV) in physiological and pathological conditions [3], [5]. The biomechanical properties of the RV free wall (RVFW) are considered to impact its organ function [6], [7], [8], and a recent rodent study has reported a correlation between the passive elastic modulus of the RV and the end-diastolic volume [6], which is often used as an indicator of heart failure [9], [10], [11], [12], [13]. Furthermore, our own ovine study showed that the RV elasticity is correlated with RV geometry and hemodynamic properties [7]. These studies directly relate the RV tissue biomechanics to clinically relevant parameters, leading to a unique perspective to link the tissue biomechanics with organ function to advance the understanding of biomechanical mechanism of RV failure.

It is well known that the ventricular wall is an anisotropic and viscoelastic material [14], [15], [16], [17]. Such behavior indicates that the tissue's mechanical behavior is strain and strain-rate dependent, and there are energies stored and dissipated during the deformation due to the material's elasticity and viscosity, respectively. These energy expenditure events closely affect the use of metabolic energy from

[1] (Sections adapted from "Alterations of biaxial viscoelastic properties of the right ventricle in pulmonary hypertension development in rest and acute stress conditions": https://doi.org/10.3389/fbioe.2023.1182703; "Role of Microtubules in the Passive Anisotropic Viscoelasticity of the Right Ventricle in Pulmonary Hypertension Progression": https://doi.org/10.1016/j.actbio.2024.01.023; "Changes in right ventricle free wall hysteresis and viscoelastic anisotropy with pulmonary hypertension development": in submission)

cardiomyocytes during ventricular dilation and contraction in physiological conditions (e.g., at rest or under acute stress). However, most previous studies on RV biomechanics have focused on the elasticity of the tissue [18], [19], [20], [21], [22], [23], [24], [25]. A few studies that reported the viscoelastic behavior of the RV have used an indentation test of the RVFW [26], the tensile mechanical test of neonatal RVFW [16] or the length-tension test of RV papillary muscles [27]. Thus, the biaxial viscoelastic behavior of adult RVFW remains little investigated. Our group originally examined the biaxial viscoelasticity of RVFW in healthy adult sheep [17], [28], but the changes in the viscoelastic behavior in pathological conditions are unclear. Furthermore, at the cell level or in papillary muscles, it has been shown that the myocardial viscoelasticity is increased in hypertrophy/diseased hearts and significantly weakens the muscle's contractile function [29], [30]. Thus, the viscoelastic behavior of myocardium is critical to cardiac function. But how exactly the tissue-level viscoelasticity is altered in pathological remodeling and affects the myocardial function remains a knowledge gap.

The strain-rate dependent character of viscoelasticity determines that the ventricle wall's mechanical behavior is different at different heart rates (HR), such as those at rest (normal HR) and under acute stress or exercise conditions (increased HR) [31]. Unlike chronic stress that reduces the HR, acute stress caused by a psychological or physical stressor typically results in an elevated HR. The adaptation to acute stress involves changes in multiple cardiovascular parameters (e.g., cardiac output, blood pressure), which is often known as cardiovascular reactivity [32]. But little is studied on the acute mechanical changes of the ventricle wall. The investigation of the RVFW viscoelastic changes under increased strain-rate (HR) will provide novel biomechanical insights for the RV adaptation to acute stress. Additionally, healthy myocardium adapts to the increased workload during exercise by increasing stroke volume and heart rate, thus increasing the cardiac output—the blood supply to downstream organs. However, an impaired cardiac reserve has been noted in pulmonary arterial hypertension (PAH) and HFpEF patients, and the inability of the RV to increase cardiac output during exercise is one of key contributors [33], [34]. Whether the diseased (failing) RV has a distinct response to increased HR in its viscoelastic properties than the healthy RV is

completely unknown, and the investigation of the viscoelastic changes will bring additional information to the capacity of failing RVs to adapt to the increased myocardial demand.

2. Goal and hypothesis of my research

Therefore, the goal of this study was to investigate the alterations of RVFW biaxial viscoelastic behavior with PH development and at normal and increased heart rates simulating resting and acute stress conditions. We hypothesize that the remodeling in pulmonary hypertensive RVs leads to increased viscoelastic properties and tissue anisotropy and decreased damping capacity, and the increased HR causes a stronger reduction in damping capacity in the diseased RV than the healthy RV. This is the first study to investigate and compare the biaxial dynamic mechanical properties of the RVFW in various physiological and pathological states. The novel findings will improve our understanding of RV tissue biomechanics in response to PH progression and increased heart rates and offer new insights into the adaptation of RV to chronic pressure overload and acute stress.

3. Materials and Methods

3.1 Animal model and in vivo measurement

All procedures were approved by Institutional Animal Care and Use Committee (IACUC #1438) at Colorado State University. All animal experiments were performed in accordance with the guidelines and regulations of the Colorado State University Institutional Animal Care and Use Committee. All procedures were performed in accordance with the ARRIVE guidelines. Briefly, the monocrotaline (MCT) (60 mg/kg, Sigma) was injected once subcutaneously into 6-week-old male Sprague Dawley rats (Charles River) and the animals were housed in normal conditions for 3 weeks to develop PH. Similar healthy rats were used as controls (CTL). One or 2 days before euthanasia, the RV function was obtained by 2D echocardiography. Briefly, rats were anesthetized using inhaled isoflurane (0.5%–2%) and then subjected to transthoracic echocardiography using a Phillips HD11 ultrasound with a 15 mHz sector array probe. Right ventricular dimensions and contractile function including RV end-diastolic area (EDA), end-systolic area (ESA), and

fractional shortening (FS) were measured in the apical four-chamber view in 2D B-mode. On the day of euthanasia, animals were anesthetized via i.p. injection of urethan (1.2mg/kg) and intubated. The chest was opened to expose the RV, and the chamber was catheterized using a 1.9F admittance catheter (Transonic/Scisense). The stable pressure-volume (PV) relation were obtained and functional measurements such as RV end-systolic pressure (ESP), cardiac output (CO), and the end-systolic PV relation (ESPVR) were derived. Rats were then euthanized by exsanguination and the entire heart was harvested.

3.2 Ex vivo equibiaxial mechanical testing

After harvest, the entire RVFW was dissected in cardioplegic solution (CPS) and placed in 30mM 2,3-butanedione monoxime (BDM) solution at body temperature for 30 minutes to remove the contractility of the myocardium. The outflow tract direction was defined as the longitudinal (L) direction. The tissue was then preloaded to approximately 0.05 N to specify the zero-stress configuration, and calipers were used to measure the dimensions of the square sample. Four markers were placed on the center region of the surface in a square formation for strain analysis. 15 cycles of equibiaxial preconditioning were then conducted (at 1 Hz and 20% maximal strain).

RV tissue then underwent equibiaxial stress relaxation to obtain the passive, biaxial viscoelastic behavior using an in-house biaxial tester. The RV was stretched to maximal strains of 6% and 15%, which correspond to the early and late diastolic strain, respectively. For each strain level, the tissue was tested at three stretch rates: 1Hz and 5Hz, which relate to a sub-physiological and physiological heart rate of the adult rat, respectively. We also tested the tissue to a maximum strain level of 20% and under rest (5Hz) and acute stress (8Hz) mechanical conditions. Between each test, a recovery time of ten times that of the previous testing period was included to ensure full recovery of the tissue after deformation.

After stress-relaxation testing, we conducted cyclic sinusoidal mechanical tests. The tissue underwent equibiaxial sinusoidal stretches with 20% of strain at 0.1, 1, 5, and 8 Hz were performed, with the resting

period equivalent to 10 times of the prior testing period between tests [35], [36]. Biaxial stretch forces were obtained by 5-lb load cells (Honeywell) at a sampling frequency of 200 Hz.

3.3 Stress relaxation data analysis

After data collection, the engineering (σ) and the second Piola-Kirchhoff (P-K) (S) stresses, and Green strain (E) were calculated for each direction ($\sigma = F/A_0$, $S = \sigma/\lambda_i$, and $E = \frac{1}{2}(\lambda_i^2 - 1)$, where F is the measured force, A_0 is the initial cross-sectional area, and λ_i is the stretch in the i = L, C direction with L and C denoting the longitudinal and circumferential directions, respectively.

Relaxation modulus (relax modulus) from each direction was used as a measure of RVFW elasticity and was calculated as described previously [37]. We further quantified RV elasticity and viscosity from the stress relaxation raw data by the stored energy (W_S) and dissipated energy (W_d), respectively, using the 2nd P-K stress formulation. At any input strain level (ε_{input}), we derived W_S as a function of time (t) using the total area (A_S) under the curve from peak stress to the relaxed stress at any time (t) (Eq. 1), and derived W_d using the area (A_d) between the stress relaxation curve and the curve describing the response of a purely elastic material from peak stress to the relaxed stress at time t (Eq. 2) (**Fig. 1.1**).

$$Relaxation\ modulus\ = \sigma(t)/\varepsilon_{input} \qquad \text{Eq. 1.1}$$

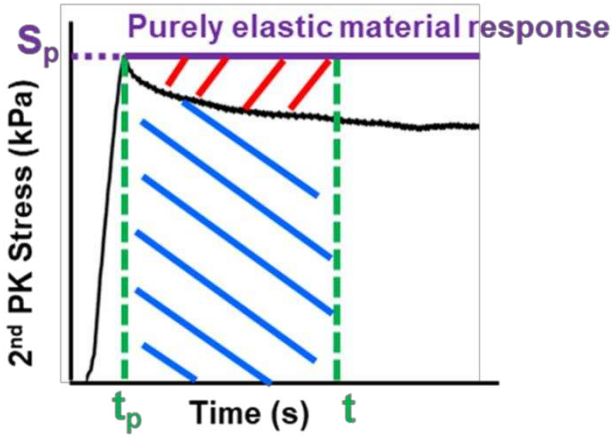

Figure 1.1 The stored energy (W_S) and dissipated energy (W_d) are derived from the blue (A_S) and red (A_d) shaded area, respectively. These integrated areas (A_S and A_d) are calculated between the time (t_p) of peak stress (S_p) and any time point (t) during relaxation

$$W_S(t) = \int_{t_p}^{t} S(t)\, \varepsilon_{input} dt = \varepsilon_{input} \int_{t_p}^{t} S(t)\, dt = \varepsilon_{input} \times A_S \quad \text{Eq. 1.2}$$

$$W_d(t) = \int_{t_p}^{t} S_p \varepsilon_{input} dt - \int_{t_p}^{t} S(t)\, \varepsilon_{input} dt = \varepsilon_{input} \left(\int_{t_p}^{t} S_p dt - \int_{t_p}^{t} S(t) dt\right) = \varepsilon_{input} \times A_d \quad \text{Eq. 1.3}$$

we then derived the relative change of viscosity (W_d) and elasticity (W_S) as damping.

$$Damping = \frac{W_d}{W_d + W_S} \quad \text{Eq. 1.4}$$

3.4 Hysteresis data analysis

After data collection, the engineering (σ) and the 2nd Piola-Kirchhoff (PK) (*S*) stresses, and Green strain (E) were calculated in each direction ($\sigma = F/A_o$, $S = \sigma/\lambda_i$, and $E = \frac{1}{2}(\lambda_i^2 - 1)$), where F is the measured force, A_o is the initial cross-sectional area, and λ_i is the stretch in the i = L, C direction with L and C denoting the longitudinal and circumferential directions, respectively[28], [38], [39], [40]. In each direction, an average hysteresis stress-strain loop was derived from the last three cycles of data. Additionally, the stored energy (W_S) and the dissipated energy (W_d) were calculated from the hysteresis loop as indices of the elasticity and viscosity of the tissue, respectively, as described previously [36]. Next, we quantified the ratio of W_d and W_S (V/E) and the damping (W_d / (W_S + W_S)) to evaluate the relative strength of viscosity and elasticity in the tissue [36], [41]. Elastic modulus (*M*) was derived as the slope of loading curve of the loop, and the loop height in the middle strain (50% of maximal strain) was derived as additional elastic and viscous indices [42], [43].

3.5 Microstructural measurements

The tested RV tissue samples were fixed in 10% formalin and embedded in paraffin wax. Samples were then stained with Picrosirius red (PSR) for collagen area fraction quantification, and hemotoxylin eosin for myofiber hypertrophy analysis.

3.5.1 Collagen area fraction

Three regions of interest were selected in each sample and imaged at 20X under brightfield using AmScope. A color thresholding method was applied to separate the collagen content, and the area fraction (%) was calculated as the ratio of the collagen area to the total tissue area.

3.5.2 Myofiber hypertrophy

Three regions of interest were selected in each sample and imaged at 20X under brightfield using AmScope. The width of five myofibers was then measured and the average width for each sample was compared between CTL and MCT samples. A higher myofiber width indicated RV hypertrophy.

3.6 Statistical analysis

Unpaired and paired student t-test was used to compare data between stretch rates, strain levels, directions, between healthy and diseased mechanical behavior, and between healthy and diseased tissue microstructure. All data are presented as mean ± SEM. $p<0.05$ was considered statistically significant.

4. Results

4.1 Pulmonary hypertension impairs RV function

Transthoracic echocardiography revealed significant enlargement of RV chamber size (increased EDA and ESA) and reduced RV FS characteristic of RV dilation and systolic dysfunction (**Table 1.1**). From the PV loop measurement, we observed an elevated end-systolic pressure, and an impaired SV and CO. Although the reduction in SV was non-significant. We also observed a trend of weakened E_{es}. These results

demonstrate the expected establishment of pathological RV remodeling in MCT rats.

Table 1.1 RV echocardiography and pressure-volume measurements in healthy (CTL) and diseased (MCT) rats. *p<0.05 compared to MCT.

Echocardiography	CTL	MCT
RV end diastolic area (cm^2)	0.18±0.01	0.30±0.03*
RV end systolic area (cm^2)	0.09±0.01	0.22±0.03*
RV fraction shortening (%)	40±1	28±3*
PV Loop	**CTL**	**MCT**
RV systolic pressure (mmHg)	46.2 ± 6.0	74.1 ± 9.1*
Cardiac output (mL/min)	80.0 ± 5.9	48.1 ± 10.4*
End systolic elastance (mmHg/μL)	1.08 ± 0.5	0.65 ± 0.1

4.2 Stretch-rate (frequency) dependent viscoelastic behavior of RVFW altered by PH – stress-relaxation

We first investigated the frequency-dependent viscoelastic behavior obtained from the Set 1 tests. **Fig. 1.2** shows significant frequency-dependent changes in the relaxation modulus measured at 0.01 s after the peak force in both groups. Firstly, the relaxation modulus curves from the MCT group were above those from the CTL group, indicating increased RV viscoelasticity in the MCT group. We further present detailed changes in the physiologically relevant conditions in the next section. Second, the MCT group presented monotonically decreased relaxation modulus with the increasing frequency in both directions, whereas the CTL group presented weaker frequency-dependent behavior than the MCT group. Therefore, PH altered the frequency-dependent viscoelastic behavior of the RV. Similar frequency-dependent behavior was observed at other time points.

4.3 Stretch-rate (frequency) dependent viscoelastic behavior of RVFW altered by PH – hysteresis

We next examined the effect of testing frequency (i.e., strain rate) on healthy and diseased RVs' viscosity and elasticity. In the healthy RVs, we observed no significant effect of strain rate on stored or dissipated energy (**Fig. 1.3A&B**). Interestingly, despite non-significant frequency-dependent changes in W_S and W_d, the V/E ratio and damping capacity were both elevated at 8Hz compared to 0.1Hz and 1Hz (**Fig. 1.3C&D**), suggesting a greater increase of W_d than W_S only at the strain rate under acute stress. These frequency-dependent changes, though, were only observed in the longitudinal direction. Finally, if we only compare

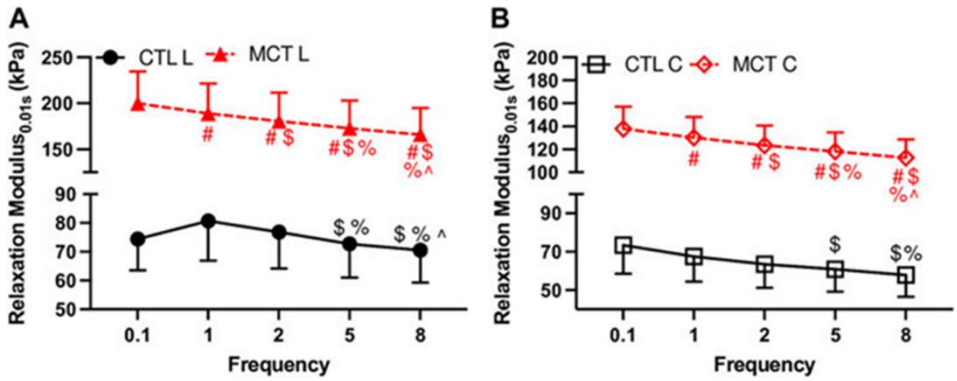

Figure 1.2. Frequency-dependent changes in the relaxation modulus at 0.01 s after peak force with an input strain of 20%. (A): relaxation modulus in the longitudinal (L) direction for both groups; (B): relaxation modulus in the circumferential direction for both groups. # <.05 vs. 0.1 Hz, $ <.05 vs. 1 Hz, % <.05 vs. 2 Hz, ^ <.05 vs. 5 Hz, respectively.

the behavior between 5Hz and 8Hz (using a paired t test), we found that the V/E ratio tended to increase from the strain rate at resting heart rate (5Hz) to that at acute stress (8Hz) ($p=0.06$ in the C direction).

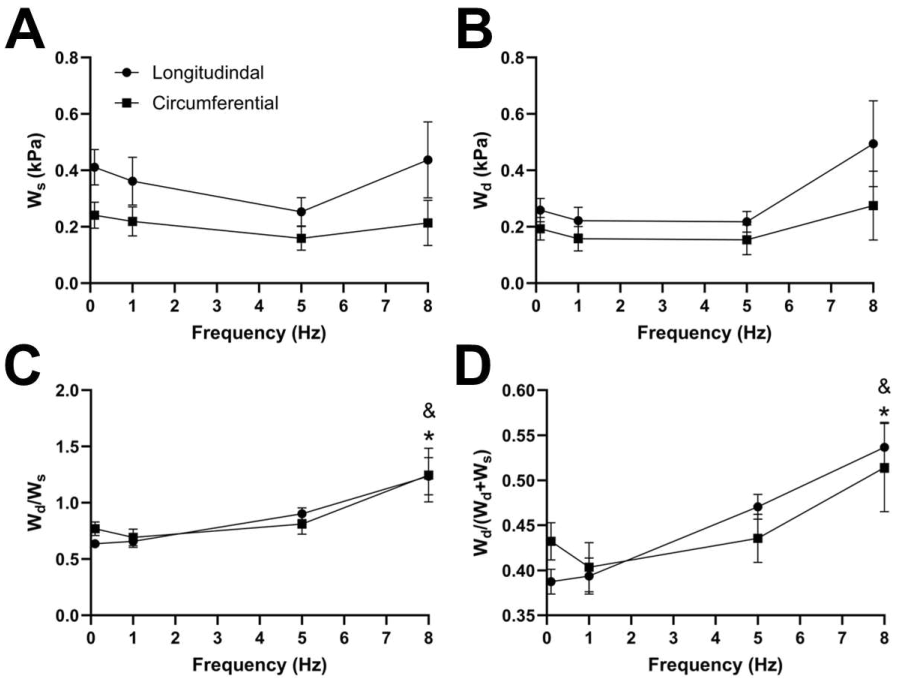

Figure 1.3. Frequency-dependent behavior of healthy RV elasticity (A), viscosity B), ratio of viscosity to elasticity (C), and damping (D). & $p<0.05$ compared to 0.1Hz in same direction; *$p<0.05$ compared to 1Hz in same direction.

In the diseased RVs, we observed a general trend of increase in stored and dissipated energies with elevated testing frequency (**Fig. 1.4A&B**), although these changes were non-significant. Finally, the V/E ratio and damping capacity displayed a monotonic increase with increasing testing frequency (**Fig. 1.4C&D**), and they were both significantly elevated at 5Hz and 8Hz. Like in the healthy RVs, these increases suggest a stronger contribution of viscosity (W_d) than elasticity (W_S) to the total energy use at physiological strain rates. Interestingly, in both the CTL and MCT RVs, the V/E ratio at the 8Hz testing frequency was greater than 1.0, indicating a higher viscous response than elastic response under dynamic loadings (**Fig. 1.3C&D, 1.4C&D**).

4.4 Pulmonary hypertension increases RVFW viscosity and elasticity at sub- and physiological mechanical conditions, with weak effects on the ratio of viscosity to elasticity – stress-relaxation

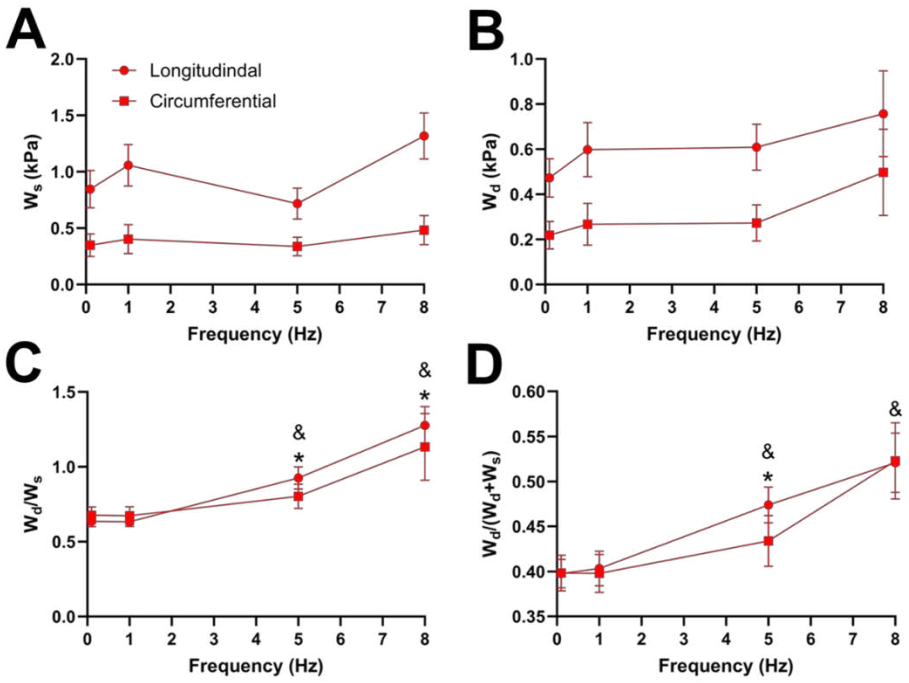

Figure 1.4. Frequency-dependent behavior of diseased RV elasticity (A), viscosity (B), ratio of viscosity to elasticity (C), and damping (D). & $p<0.05$ compared to 0.1Hz in same direction; *$p<0.05$ compared to 1Hz in same direction.

Next, we examined the effect of pulmonary hypertension on RVFW viscoelasticity at the early and end diastolic strain level, and at the sub- and physiological stretch rates. At the early diastolic strain level and sub-physiological stretch rate, RVFW elasticity was elevated during PH progression (**Fig. 1.5A**). Similarly, RVFW viscosity was also significantly increased with disease progression (**Fig. 1.5B**). The degree of increase in W_d in the C direction was greater than W_S, which resulted in an elevated V/E ratio in this direction with PH (**Fig. 1.5C**). Additionally, both groups displayed anisotropic behavior in elasticity and viscosity (**Fig. 1.5A&B**). At the early diastolic strain and physiological stretch rate, we observed strengthened RVFW elasticity and viscosity in both directions with the development of PH, and the increases (in percentage) were larger in the circumferential than longitudinal direction (**Fig. 1.5D&E**). A decrease of the V/E ratio with PH progression was observed, but the change reached significance in the longitudinal direction only (**Fig. 1.3F**). Next, we examined RVFW viscoelasticity at end diastolic strain and physiological stretch rate. Similarly, tissue elasticity and viscosity were enhanced with PH progression, and the increases were stronger in the circumferential than longitudinal direction (**Fig. 1.5G&H**). However, the

V/E ratio was not significantly changed by PH progression in either direction (**Fig. 1.5I**). Finally, all parameters (W_S, W_d, and W_d/W_S) from these testing conditions showed significant anisotropy in healthy and failing RVs.

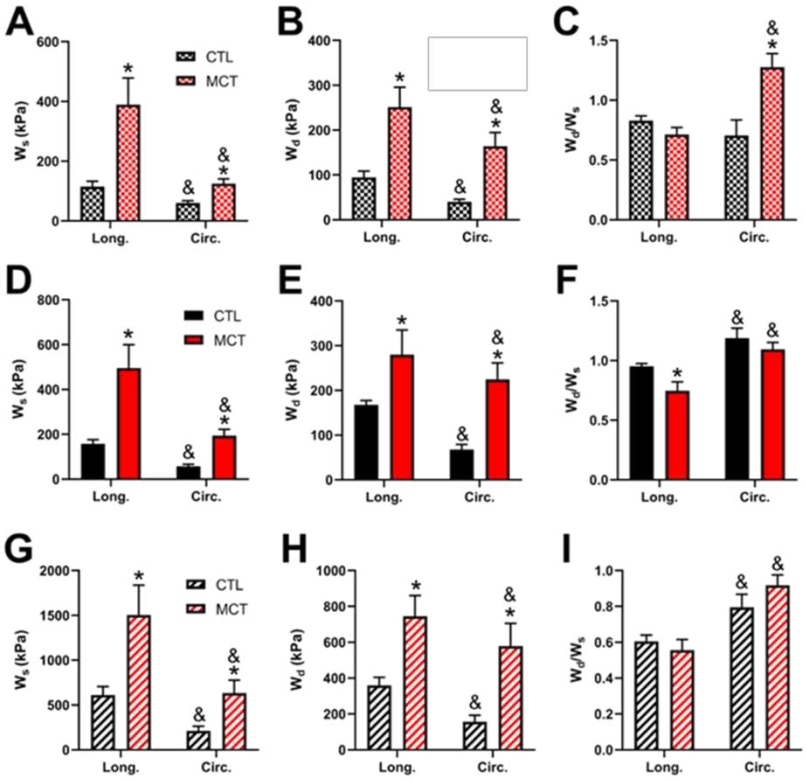

Figure 1.5. The elasticity (WS) (A, D, G), viscosity (Wd) (B, E, H), and the V/E ratio (C, F, I) of the healthy and diseased RVFW that are obtained at sub-physiological stretch rate and early diastole strain level (A-C), physiological stretch rate and early diastole strain level (D-F), and physiological stretch rate and end diastole strain level (G-I). *p<0.05 compared to CTL in same direction; &p<0.05 compared to L direction in same group.

4.5 Pulmonary hypertension increases RVFW viscosity and elasticity at sub- and physiological mechanical conditions, with weak effects on the ratio of viscosity to elasticity – hysteresis

We first compared RV viscoelastic properties between the healthy (CTL) and diseased (MCT) groups in each direction. In the longitudinal direction, the stored energy (elasticity) was elevated in the failing RV group at all testing frequencies (**Fig. 1.6A**). The elastic modulus was increased with PH progression in a similar manner (**Fig. 1.6B**). These results indicate the stiffening of the tissue. These behaviors were similarly observed in the circumferential direction ($p<0.05$, data not shown). Additionally, in the longitudinal direction, the dissipated energy and loop height, which are both metrics of viscosity, were

significantly elevated at multiple frequencies in the failing RV group (**Fig. 1.6C&D**), indicating more viscous behavior of the tissue. However, we did not observe significant changes in these parameters in the circumferential direction with disease progression. Therefore, the stiffening of the RV tissue occurred in both directions, whereas the tissue viscosity increased only in the longitudinal direction.

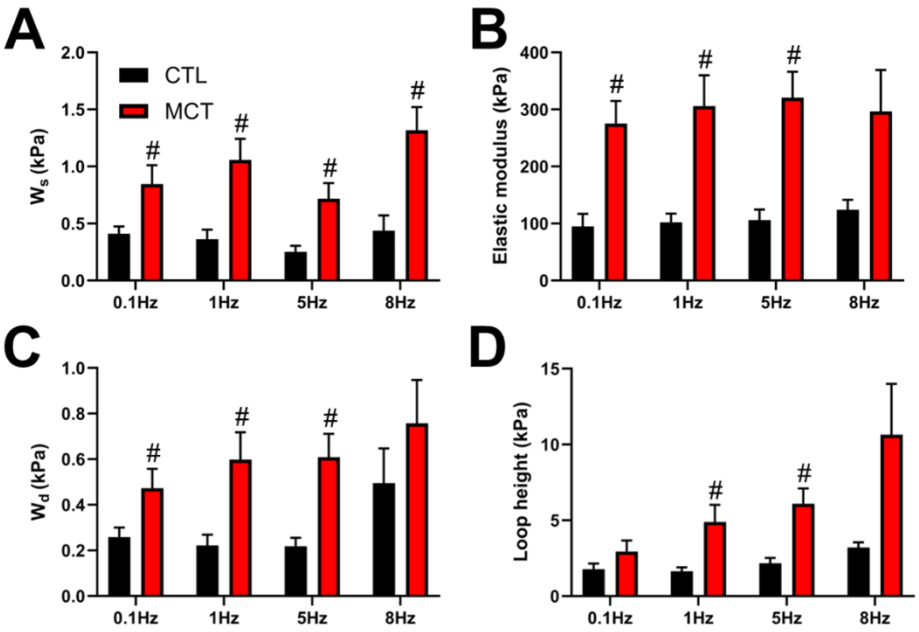

Figure 1.6. Comparison of the elasticity (A&B) and viscosity (C&D) between healthy (CTL) and diseased (MCT) RVs in the longitudinal direction. # $p<0.05$ compared to CTL.

Next, we examined the ratio of viscosity and elasticity (V/E) in the CTL and MCT RVs using measurements of dissipated energy and stored energy (**Fig. 1.7**). In both directions, there was no significant difference in the V/E ratio or damping between the healthy and diseased RVs at any testing frequency. These results indicate that despite the individual changes in elasticity and viscosity with PH development, the relative strength of elasticity and viscosity remains constant in cyclic deformation of the tissue.

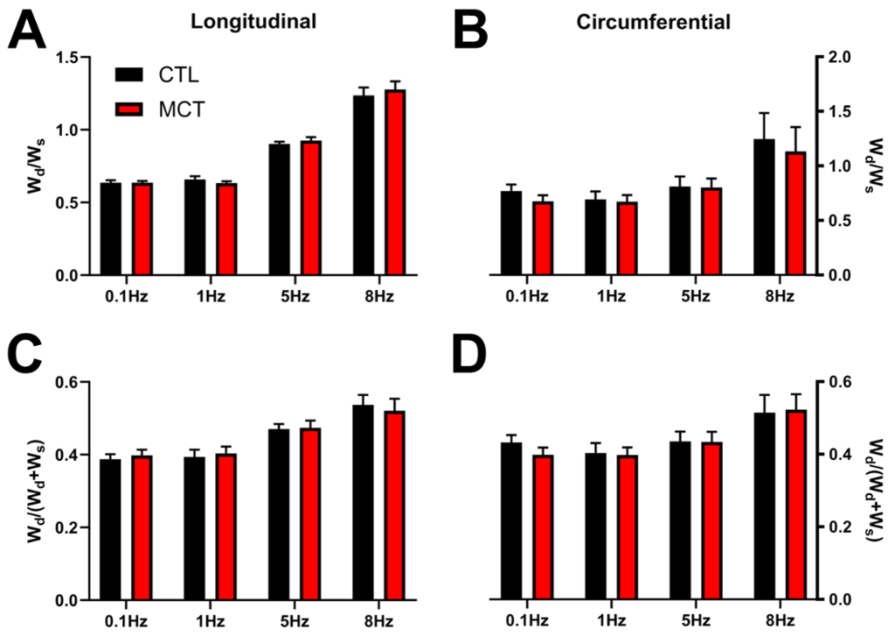

Figure 1.7. Comparison of the V/E ratio (A&B) and damping (C&D) between healthy (CTL) and diseased (MCT) RVs.

We then examined the anisotropic behavior of the RV in the healthy and diseased groups. In the healthy RVs, we observed significant anisotropy in elasticity and viscosity at physiological frequencies (5Hz and 8Hz), but not at the sub-physiological testing frequencies (0.1Hz and 1Hz) (**Fig. 1.8A&B**). In contrast, in the diseased RVs, we observed significant anisotropy in both parameters across all testing frequencies (**Fig. 1.8C&D**). This data indicates that both healthy and diseased RV exhibit anisotropic elasticity and viscosity, and there was a stronger degree of anisotropy with diseased progression.

4.6 PH increases RVFW biaxial viscoelasticity and enhanced the tissue anisotropy at rest and acute stress mechanical conditions

Next, we focused on the RV biaxial viscoelasticity obtained from 5 and 8 Hz with an input strain of 20%. As shown in **Fig. 1.9A**, we observed that the MCT RV had increased relaxation modulus than the CTL RV in both directions, and the MCT RV became anisotropic with a larger stiffness in the longitudinal than circumferential direction during PH development. Similar observation was found in the stored energy W_S, another index of tissue elasticity (**Fig. 1.9B**), and the dissipated energy W_d, an index of tissue viscosity (**Fig. 1.9C**). The same changes in these viscoelastic parameters were also observed under acute stress.

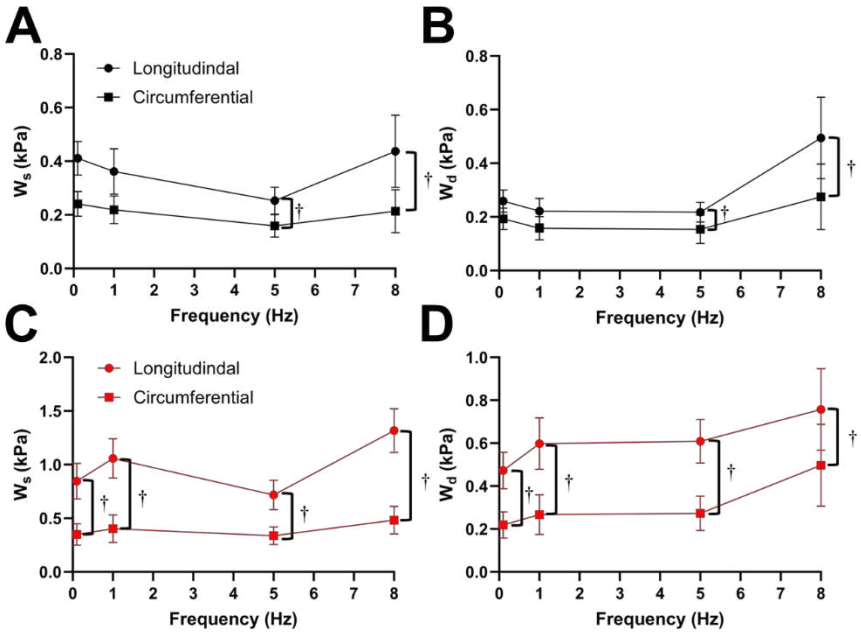

Figure 1.8. Anisotropic behavior of healthy (A&B) and diseased (C&D) RV elasticity (A&C) and viscosity (B&D). † $p<0.05$ compared to the longitudinal direction.

Moreover, like the elastic property, the viscous property was similar between directions in the CTL RV, suggesting an isotropic type of tissue. In the MCT RV, the viscous anisotropy was pronounced in the acute stress condition ($p < 0.05$ at 0.01, 10, and 100 s, $p = 0.058$ at 1 s) and was absent in the resting condition across all relaxation stages ($p = 0.052$ at 100 s, **Fig. 1.9C**). We further derived various anisotropic indices (AI) as the ratio of elastic (or viscous) parameters between longitudinal and circumferential directions (**Table 1.2**). We observed that most of the AI values were larger than 1 (except for those derived from W_d in CTL group), indicating a stronger elastic or viscous behavior in the longitudinal direction, and that the AI values were also larger in the elastic than viscous parameters. Moreover, the increases in AI from healthy to diseased RVs was evident only in the viscous behavior. These data indicate that PH increases RVFW elasticity and viscosity and enhances tissue anisotropy. In the diseased RV, while the elastic anisotropy was significant at both resting and acute stress conditions, the viscous anisotropy was only evident under acute stress.

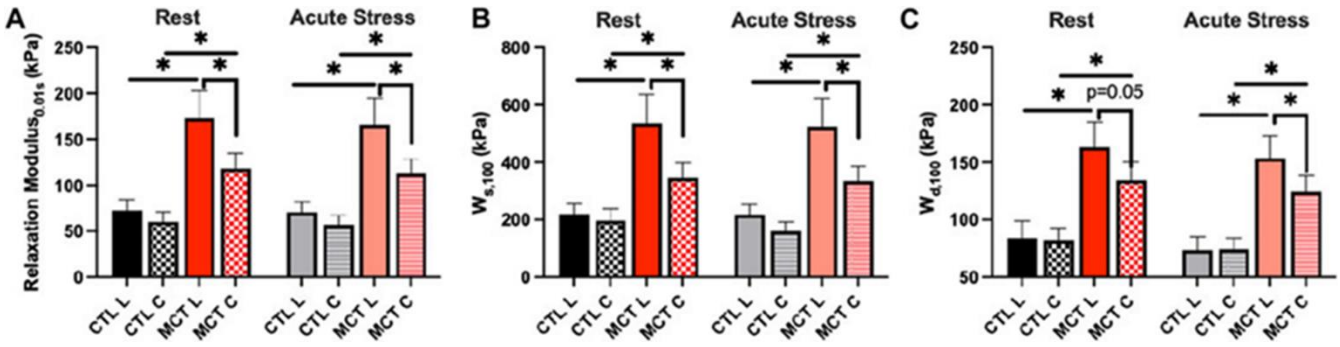

Figure 1.9. RVFW viscoelasticity before and after PH development and at resting and acute stress states. (A): RV elasticity measured by relaxation modulus at 0.01 s after peak force; (B): RV elasticity measured by WS at 100 s after peak force; (C) RV viscosity measured by Wd at 100 s after peak force. *p <.05.

Table 1.2. Summary of various RVFW anisotropic indices (AI) obtained from different elastic or viscous parameters in both groups and testing conditions. Data are present as mean ± SEM.

Group	AI (from relaxation modulus$_{0.01s}$)	AI (from $W_{s,100}$)	AI (from $W_{d,100}$)
At Rest			
CTL	1.40 ± 0.27	1.54 ± 0.30	0.87 ± 0.11
MCT	1.45 ± 0.13	1.54 ± 0.16	1.23 ± 0.08[a]
Under Acute Stress			
CTL	1.20 ± 0.18	1.61 ± 0.30	0.88 ± 0.11
MCT	1.46 ± 0.14	1.55 ± 0.16[b]	1.25 ± 0.08[a]

[a]< 0.05 vs. CTL in the same condition;
[b]< 0.05 vs. resting condition of the same group.

4.5 PH increased RVFW damping capacity in both directions

We have shown previously that both elasticity and viscosity of the RV were increased with PH development, but it is unclear if these increases were equal or not. To evaluate the relative change of viscosity to elasticity, we examined the damping capacity as the percentage of dissipated (wasted) energy to the total energy during the relaxation. We found that in the longitudinal direction, the MCT RV had decreased damping capacity than the CTL RV in early relaxation (up to 1 s), and in the circumferential direction the MCT RV had reduced damping capacity in almost all stages of the relaxation ($p < 0.05$ for all time points except for $p = 0.09$ for 0.01 s) (**Table 1.3**). We presented the results at 0.01 s and 100 s (equilibrium) of the relaxation obtained in normal heart rate condition in **Fig. 1.10**. Similar changes were found in and the acute stress condition as well (**Table 1.3**). Therefore, this is the first report that the PH-induced RV remodeling led to reduced damping capacity of the RVFW. Lastly, we found that except for the early stage of the relaxation

(at 0.01 s and 0.1 s), the RVFW damping capacity exhibited an anisotropic behavior in both rest and acute stress conditions (**Fig. 1.10B; Table 1.3**).

Table 1.3. Summary of the RVFW damping capacity obtained from different groups, directions, and testing conditions. Data are present as mean ± SEM.

	Relaxation time (sec)	0.01	0.1	1	10	100
At Rest ($\times 10^{-3}$)						
CTL	Longitudinal	2.86 ± 0.52	36.50 ± 5.02	118.52 ± 10.87	201.63 ± 14.64	282.01 ± 20.97
	Circumferential	2.68 ± 1.05	48.82 ± 9.51	152.18 ± 12.14[a]	258.25 ± 13.79[a]	358.81 ± 15.66[a]
MCT	Longitudinal	0.43 ± 0.10[b]	15.95 ± 2.36[b]	90.35 ± 10.15[b]	174.86 ± 13.90	254.09 ± 17.23
	Circumferential	0.73 ± 0.20	23.72 ± 3.84[a, b]	106.20 ± 8.44[a, b]	203.99 ± 12.11[a, b]	292.07 ± 15.72[a, b]
Under Acute Stress ($\times 10^{-3}$)						
CTL	Longitudinal	3.54 ± 1.18	34.78 ± 7.11	118.33 ± 16.57	197.41 ± 19.13	266.88 ± 21.11
	Circumferential	3.25 ± 1.05	45.28 ± 7.33	139.27 ± 11.15	246.65 ± 13.24[a, c]	333.04 ± 14.72[a, c]
MCT	Longitudinal	0.99 ± 0.27	16.61 ± 2.76[b]	87.69 ± 8.72	170.99 ± 12.66	247.59 ± 16.11[a]
	Circumferential	0.85 ± 0.20[b]	24.13 ± 4.04[a, b]	103.43 ± 7.99[a, b]	198.46 ± 11.24[a, b, c]	283.99 ± 14.69[a, b, c]

[a]< 0.05 vs. longitudinal;
[b]<0.05 vs. CTL;
[c]< 0.05 vs. resting condition.

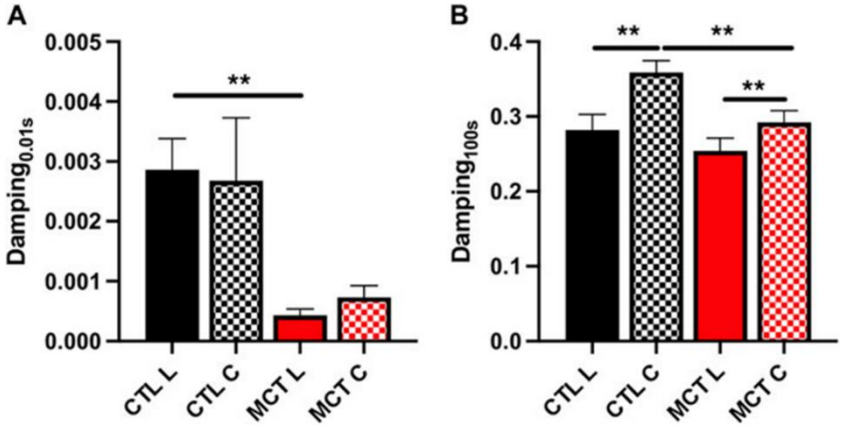

Figure 1.10. The damping capacity of the RVFW before and after PH development quantified (A) at 0.01 s and (B) 100 s after peak force. **p <.01.

4.6 Acute stress reduced damping capacity differently between healthy and diseased groups

We further investigated the changes in the damping capacity from normal to high heart rates to reveal the viscoelastic alteration from resting to acute stress conditions. We observed that in the early stage of the relaxation (up to 1 s) there was no significant change in damping capacity in either group. At later stage of the relaxation (at 10 s or 100 s), however, the damping capacity was reduced in the tissue for both groups (**Fig. 1.11; Table 1.3**). Moreover, the alteration was different between the CTL and MCT groups. The damping capacity was decreased only in the circumferential direction in the CTL group, whereas in the MCT group the decrease was observed in both directions and with small p values (**Fig. 1.9B**). These data suggest that PH-induced remodeling causes a stronger reduction in damping capacity under acute stress condition than the healthy tissues.

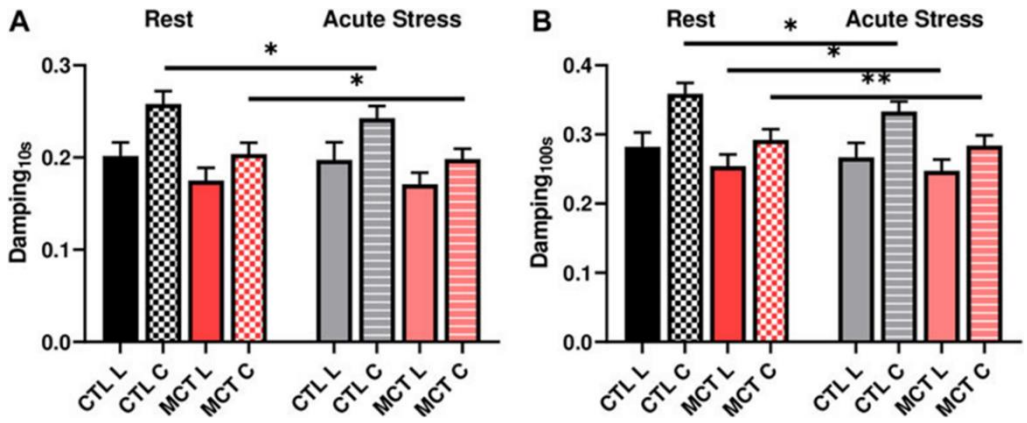

Figure 1.11. Changes in RVFW damping capacity from the resting to acute stress states at (A) 0.01 s after peak force and (B) 100 s after peak force. * <.05, ** <.01, respectively.

4.7 Correlations between the RVFW viscoelastic properties and in vivo *measurements*

We further investigated the relationships between the RVFW viscoelastic parameters and the echocardiography measurements to explore potential implications of RVFW viscoelasticity. In both directions, we observed that the RVFW damping capacity tended to be strongly or was significantly correlated with the RV EDA, AT and AT/ET (**Fig. 1.12**). It is worthy of note that neither the elastic nor

viscous parameter was correlated with any of these functional parameters. Our findings suggest that the damping capacity is a better indicator of RV function than the tissue elasticity or viscosity alone.

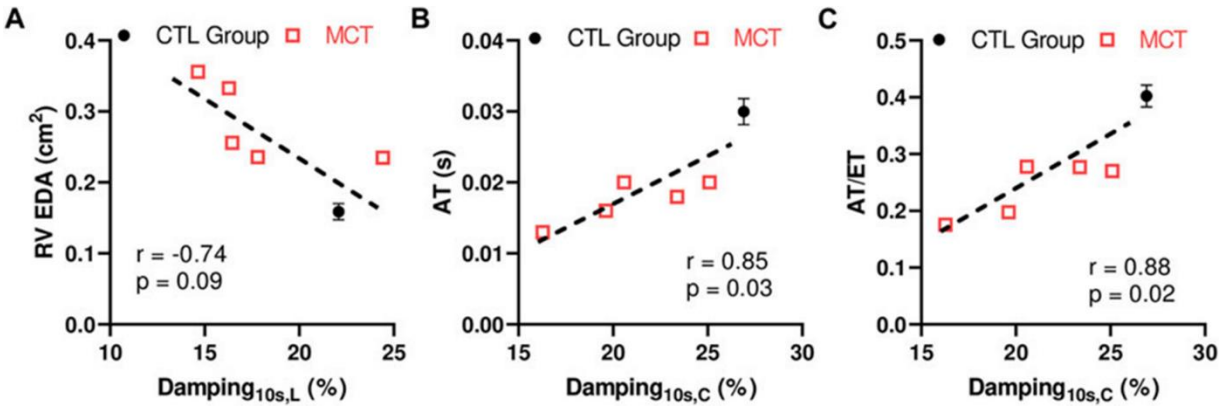

Figure 1.12. Correlations between the RVFW damping capacity at 10 s after peak force and (A) RV EDA, or (B) AT, or (C) ratio of AT and ET. The CTL data were included as the group average measurement (n = 8) and the error bar shows the standard error. The MCT data were included as individual data points (n = 5). L: longitudinal direction; (C) circumferential direction.

4.8 Collagen and Cardiomyocyte Correlates with Dynamic Mechanical Properties at physiological condition

To investigate the structural changes of the tissues, we quantified the total collagen area fraction in the free wall in healthy and diseased RVs by histology image analysis. Collagen area percentage was significantly increased from CTL (1.9±0.1%) to MCT (2.3±0.2%) RVs ($p<0.05$). We also found interesting correlations between collagen area fraction and various viscoelastic parameters at physiological states (i.e., 5Hz, 20% of strain) (**Fig. 1.13**). First, we observed significant correlations between collagen content and dissipated energy in both directions (**Fig. 1.13A&B**), and the correlation was stronger (i.e., with a larger R-value) in the longitudinal than circumferential direction. Additionally, the stored energy was significantly correlated with the collagen content in both directions as well (**Fig. 1.13C&D**), and the strength of the correlation was similar between directions. These data suggest a marked contribution of collagen content to RV biaxial elasticity and viscosity. At the sub-physiological (1Hz) stretch rate, collagen was significantly correlated with both stored and dissipated energy in both the longitudinal and circumferential directions (data not shown). Additionally, at the acute stress (8Hz) frequency, collagen correlated with stored energy in both

directions, but only circumferential dissipated energy. These results suggest a dominant role of collagen in RV mechanics under both sub- and physiological stretch rates.

We then quantified the degree of RV hypertrophy using the width of the cardiomyocytes. There was an approximate 30% increase in myofiber width from the healthy (15.6±0.2m) to the diseased (20.2±1.1μm) groups ($p<0.05$), indicating significant hypertrophy of the muscles. Moreover, the dissipated energy was significantly correlated with myofiber width in both directions (**Fig. 1.14A&B**), and the correlation was stronger in the longitudinal than circumferential direction. Similarly, the stored energy was significantly correlated with myofiber width in both directions (**Fig. 1.14C&D**), and the correlation was stronger in the longitudinal than circumferential direction. These data suggest that cardiomyocyte is a significant contributor to RV elasticity and viscosity as well. Moreover, under sub-physiological conditions (1Hz), myofiber width was correlated with only circumferential stored and dissipated energy, while, under acute stress (8Hz), myofiber width was only correlated with circumferential dissipated energy (data not shown). These findings indicate that myofibers predominantly contribute to RV mechanics under physiological (5Hz) conditions.

As collagen content and myofiber size were both correlated with biaxial elasticity and viscosity, we further examined their relative contribution to the dynamic mechanical properties using multiple linear regression analysis. We found that the myofiber width, not collagen content, was significantly and positively related to the viscosity (W_d) in both directions ($p<0.05$). The relation was more significant in the longitudinal ($p=0.0005$) than circumferential ($p=0.01$) directions. However, both myofiber width and collagen content were significantly and positively correlated to the elasticity (W_S) in the longitudinal direction (**Fig. 1.14**). Moreover, the coefficient (β) estimation showed that collagen had a much greater contribution ($\beta=0.34$) than the myofiber ($\beta=0.05$) to the elasticity in this direction. In the circumferential direction, there was only a positive and significant relation between myofiber width and elasticity ($\beta=0.02$).

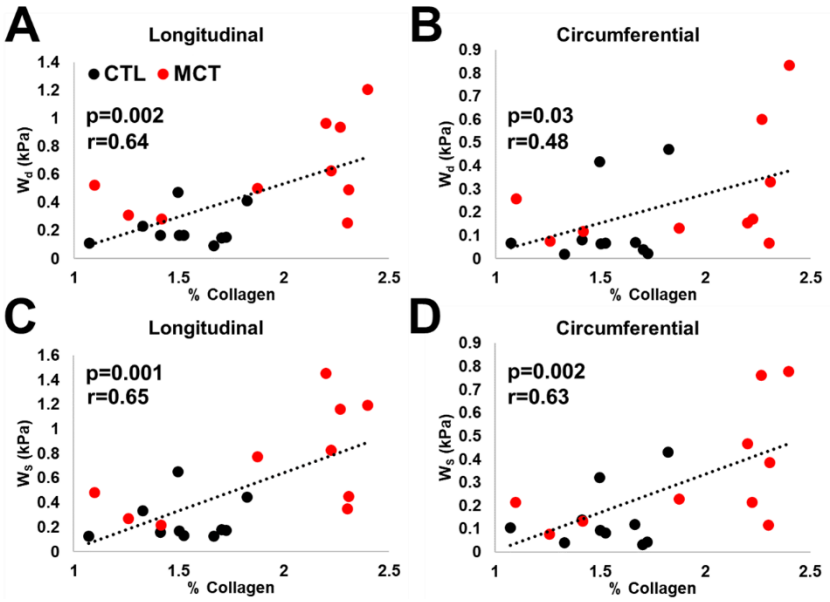

Figure 1.1.13. Correlations between RV viscosity and collagen content (A&B), and RV elasticity and collagen content (C&D), in the longitudinal (A&C) and circumferential (B&D) direction. Mechanical data was measured at physiological conditions (5Hz and 20% strain).

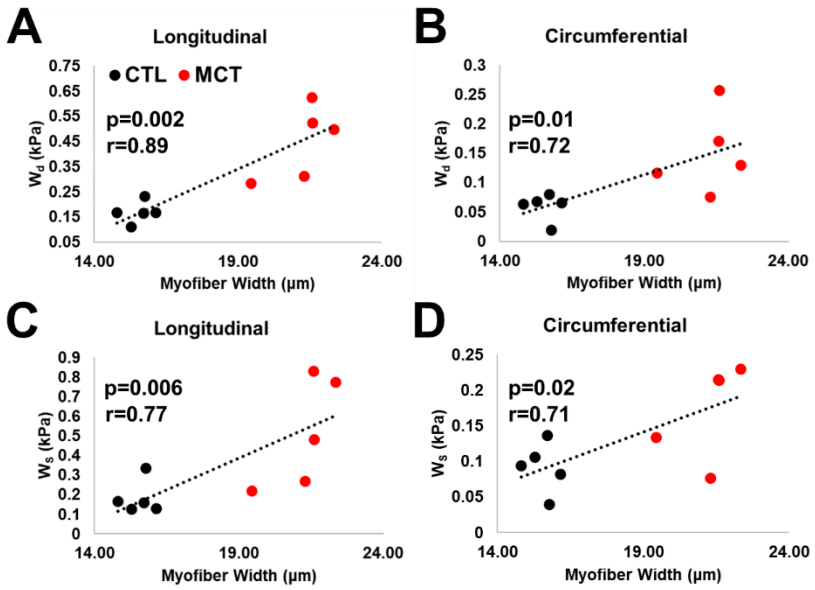

Figure 1.1.14. Correlations between RV viscosity and myofiber width (A&B), and RV elasticity and myofiber width (C&D), in the longitudinal (A&C) and circumferential (B&D) direction. Mechanical data used was measured at physiological conditions (5Hz and 20% strain).

5. Discussion

To the best of our knowledge, this is the first study to investigate the changes in RVFW biaxial viscoelasticity during PH progression. We originally found: 1) PH increased RVFW viscosity and elasticity at the sub- and physiological stretch rates and the early and end diastolic strain; 2) PH decreased RVFW damping capacity (ratio of dissipated energy to total energy) in both directions; 3) The RVFW viscoelasticity was differently altered from resting to acute stress conditions between these groups—the damping capacity was decreased only in the circumferential direction for the healthy RV, but it was reduced in both directions for the diseased RV. 4) Some correlations were observed between the damping capacity and RV function indices. These findings will improve the understanding of RV tissue dynamic mechanical behavior with PH development and under acute stress and shed light onto the biomechanical mechanism of RV failure and the reduced exercise capacity of failing RVs.

5.1 PH increased RVFW elasticity and viscosity

The hemodynamic measurements clearly show that RV failure was established [38], with severe dilation and hypertrophy of the RV with PH progression (**Table 1.1**). From our mechanical data, the development of PH significantly enhanced RVFW elasticity and viscosity (**Fig. 1.5&1.6**) and this effect was present at the sub- and physiological stretch rate and at both the early and end diastolic strain levels. Such findings of enhanced viscoelasticity with disease progression have been reported previously at the tissue and cellular level [14], [27], [29], [30], [38], [44]. At the cellular level, cardiomyocyte viscosity (hysteresis loop area) and elasticity (slope of the loop) were enhanced from the normal to the failing group [44]. Interestingly, though, this effect was more notable at the diastolic stretch rate compared to the sub-physiological stretch rate.

In the present study, RVFW displayed anisotropic behavior in the healthy and diseased state, with the C direction demonstrating lower elasticity and viscosity than the L direction (**Fig. 1.6&1.8**). We observed similar trends in our previous study [38]. Interestingly, though, the effect of disease progression on the ratio of viscosity to elasticity was direction and stretch rate dependent. At the sub-physiological stretch rate and early diastolic strain level, the V/E ratio was *strengthened* in the C direction only (**Fig. 1.5C**), which is a

result of a weaker increase in elasticity than viscosity in this direction. Alternatively, the V/E ratio at the physiological stretch rate and early diastolic strain level was *weakened* in the L direction only (**Fig. 1.3F**), indicating a greater increase of elasticity with disease progression than viscosity in this direction. Moreover, the V/E ratio was not significantly changed with disease progression at the physiological and end diastolic strain level (**Fig. 1.3I**). However, there was a trend of decrease in the L direction, and a trend of increase in the C direction. We hypothesize that these differing effects are a result of the microstructural remodeling in the hypertrophied tissue. During PH progression, the myo- and collagen fibers realign with a preferred direction in the longitudinal direction [6], [8], [23], where the change in W_S was higher than W_d. Furthermore, due to the higher collagen content in the failing RV, we expect a greater change in elasticity along this direction. This structural remodeling may result in a weaker elastic response (stronger viscous response) in the C direction at the physiological stretch rates. However, under the sub-physiological stretch rate and the early diastolic strain level, collagen is not fully recruited and may be playing a weaker role in the myocardial mechanics than the myofibers, resulting in conflicting results compared to the other two testing conditions.

Lastly, since both elasticity and viscosity were increased in diseased RV, we examined the relative change of viscosity to elasticity by quantifying the damping capacity ($W_d/(W_d + W_S)$). We observed the reduction of damping capacity in both directions (**Fig. 1.10**). But the reduction was significant only in the early relaxation (up to 0.1 s) in the longitudinal direction and was significant in the most stages of relaxation in the circumferential direction (**Table 1.3**). This is observed both in resting and acute stress conditions. These data suggest that the changes of viscosity and elasticity are not “matched” and the increase in elasticity is more pronounced than that in viscosity in PH development. It is accepted that the stiffer myocardium results in elevated wall stress and it is detrimental to the cardiomyocytes. But the role of viscosity in myocardium physiology is less clear. On one hand, the higher viscosity of the diseased tissue could result in more energy waste; but on the other hand, it may protect the cells by damping the stress. Moreover, it has been shown from cell mechanotransduction studies that the viscous substrate reduces the cell’s focal adhesion area due

to a dissipation (loss) of tractional force and cytoskeletal tension, thus producing enhanced cell spreading (morphology) and the associated mechanosensing pathway [45], [46]. Therefore, the concomitant changes in myocardial elasticity and viscosity may be driven to maintain a mechanical homeostasis for the cardiomyocytes. However, in the failing RVs, the homeostasis (unmatched elasticity and viscosity) cannot be preserved, and such disturbance may be responsible for the cellular dysfunction and organ failure.

4.2 Stronger rate response of the V/E ratio and damping in diseased RVs – hysteresis

The RV is known to exhibit nonlinear viscoelastic behavior, which means the mechanical properties of the tissue are altered with various strains and strain-rates [28]. The understanding of the frequency response is important to fully describe the viscoelastic behavior of a material. In this work, we found that both healthy and diseased RVs had non-significant changes in stored and dissipated energies with elevated frequency (**Fig. 1.3A&B, Fig. 1.4A&B**). Sommer et al. measured increased human myocardium tissue viscoelasticity in a strain-rate range of 3 - 30 mm/min [47]. These strain rates, though, were not associated with physiological loading conditions and, therefore, the *in vivo* viscoelastic behavior remains unknown. At the cell level, Caporizzo et al. observed enhanced elasticity (slope of hysteresis loop) and viscosity (hysteresis loop area) with increased strain-rate [48]. However, this study was done in isolated cardiomyocytes and the tissue-level frequency (rate) dependent viscoelastic behavior remains unclear.

Under physiological loading conditions, our study showed an absence of rate-dependent response in stored and dissipated energies, which are representative of elastic and viscous properties. The lack of response was especially noticeable in the sub-physiological frequencies (0.1-5Hz), and a trend of increased stored and dissipated energies from 5Hz to 8Hz (physiological frequencies) was shown. The plateau region in the low frequency range has been similarly reported in a viscoelastic study of mouse proximal pulmonary artery [35]. The dynamic elastic modulus (measure of elasticity) and damping (measure of viscosity) remained unchanged from 0.01Hz to 1Hz and were then rapidly increased just above the natural heart rate of the mouse (~10Hz). In large animal vascular tissues, the frequency-dependent behavior was different: in canine and human large arteries in which the normal heart rate is ~1 Hz, the elastic parameter increases rapidly at

2- to 3-times the natural heart rate and then plateaus at higher frequencies (10- to 20-times higher than the natural heart rate) [49], [50], [51], [52]. Due to the fast heart rates of rodent species and the limitation of the biaxial tester, we were unable to capture the frequency-response up to 100-200Hz. But these data suggests that the viscoelastic behavior of cardiovascular tissues was highly dependent on the species' natural heart rate. In other words, the tissue may be designed to function differently in the physiological, sub-physiological and supra-physiological heart rate ranges. Different molecular mechanisms may be involved to recruit extracellular and intracellular components and contribute to the rate-dependent response between various strain rates.

Interestingly, despite a lack of change in viscosity or elasticity individually, we observed that the V/E ratio and damping increased at physiological frequencies (at 8Hz for healthy RVs and at 5 & 8Hz for diseased RVs) in both healthy and diseased groups (**Fig. 1.3C&D, 1.4C&D**). The increase was more marked in the diseased tissue as both resting (5Hz) and acute stress (8Hz) loadings led to significantly higher values compared to sub-physiological loadings (**Fig. 1.4C&D**). Our results indicate that as the oscillation frequency increases, the relative strength of tissue viscosity is enhanced. Since this "mechanism" is preserved in failing RV tissues, we speculate that certain molecular element that exists in both healthy and diseased RVs, rather than quantification of individual cellular or extracellular components or crosslinking, contribute to this rate-dependent behavior. The pathological remodeling may trigger an earlier activation of this "mechanism" so that a stronger dissipation is evident at resting conditions as well.

5.2 Altered response of the diseased RV to acute stress

In the present study, we exposed the RVFW to acute stress condition by increasing the stretch rate and examined the viscoelastic response of the tissue. Our results showed that when changed from the resting to acute stress conditions, the healthy RVFW had decreased damping capacity only in the circumferential direction, whereas the failing RVFW had decreased damping capacity in both directions (**Fig.1.11**). Therefore, a healthy RV may be better in handling acute stress in terms of maintaining mechanical homeostasis. Moreover, the unchanged damping capacity in the longitudinal direction in the healthy RV

suggests that the mechanical energy waste in the main blood flow direction is preserved. In contrast, the diseased RV had a more significant reduction in damping capacity in both directions, suggesting the tissue has poor response to manage the acute stress. It has been noted recently that heart failure patients, including RV failure patients, have reduced exercise tolerance [33]. That is, the exercise challenge imposes a negative impact on the RV function and the dysfunctional RV has poor cardiac reserve for exercise [33]. In response to acute stress such as exercise, the ventricle typically contracts faster and stronger, thus leading to higher heart rate and stroke volume to increase the blood supply and meet the elevated metabolic demand. However, a clinical study showed that in the RV dysfunction patients with reduced exercise capacity, despite an increased heart rate, the increase in cardiac output was limited due to a weaker contractility [34]. Therefore, our finding offers a mechanical explanation of the impaired exercise capacity in failing RVs: the healthy RVs adapt to the acutely increased heart rate by preserving the mechanical homeostasis along the main blood flow direction, whereas the diseased RVs failed to do so. Our data suggest that the damping capacity may be a critical viscoelastic parameter of the RV biomechanics, and we should include this viscoelastic property of the myocardium into consideration to fully understand the role of RV biomechanics in maladaptive remodeling.

5.3 Microstructural changes and correlations between RV viscoelasticity and tissue microstructure

Finally, we observed marked changes in RV microstructure during pressure-overload induced remodeling. Both collagen content and myofiber width were increased, indicating collagen deposition and myocardial hypertrophy. These findings are consistent with prior studies reporting collagen accumulation and elevated myofiber density in pulmonary hypertension [53], [54]. Furthermore, for the first time, we showed in this study that there were significant correlations between the structural changes (collagen deposition or degree of hypertrophy) and the tissue's viscoelastic behavior (elasticity or viscosity) (**Fig. 7&8**) in both directions, indicating the contribution of collagen and myofibers to the mechanical behavior of RVFW. Among these individual correlations, we first observed a stronger relationship between the microstructure and the

mechanical properties in the longitudinal than the circumferential direction. This suggests a greater role of collagen RV viscosity in the longitudinal rather than circumferential direction. Moreover, collagen content was more strongly correlated with elasticity than viscosity in both directions. Fibrosis – accumulation of collagen and other extracellular matrix proteins – is a common response in disease progression and a mark of disease severity [55]. It is well established that enhanced fibrosis and collagen deposition results in a stiffening of the tissue and progresses disease development [53]. Moreover, Liu et al. observed that total collagen content was significantly correlated with RV high-strain elastic modulus (stiffness) [56], which may be contributed by type I collagen. Moreover, as suggested from the multiple linear regression analysis, collagen is playing a more significant role in RV elasticity than viscosity. The contribution of collagen was also more dominant in the longitudinal rather circumferential direction. This behavior may be a result of the more fibrillar rather than mesh structure of collagen, which can be investigated in future work. In PH progression, collagen fiber orientation changes to a preferred alignment in the longitudinal (outflow tract) direction [23], [57], [58], which may explain the stronger contribution of this structural component to RV elasticity in this direction.

Interestingly, we observed a stronger correlation between RV viscosity and myofiber width than collagen, indicated by the results of the multiple linear regression analysis. Myofiber width was significantly correlated with RV viscosity in both directions, while collagen was not. This discrepant contribution of collagen and myofibers could be due to the structure of the muscle fibers. For example, our group recently found a significant effect of microtubules, a cytoskeletal structure of the cardiomyocyte, on healthy and pressure-overloaded viscoelasticity [40], [59]. The contribution of this intracellular fibrous structure was found to be greater in the diseased RV than the healthy RV, and it played a more dominant role in RV viscosity rather than elasticity. The contribution of microtubules to viscosity was not direction-dependent in prior work [40], [59], as we observed from the multiple linear regression in this study. It is known that the microtubule cytoskeleton forms a mesh-like network within the cardiomyocyte instead of a fibrillar structure, and we speculate that the similar mechanical response in each direction implies an even distribution of cross-linking in the network.

Moreover, recent work investigating the role of the microtubule network in ventricular function has revealed a significant effect of microtubule on ventricular stroke volume [60], [61]. Specifically, Hancock et al. found that the depolymerization of the microtubule network via colchicine enhanced the area of myocardial work loops of healthy rat LV samples [60]. Additionally, in a mouse model of hypertrophic cardiomyopathy, Pietsch et al. observed improved stroke volume and LV performance after the detyrosination of the microtubule network [61]. As our own group has observed reduced elastic and viscous resistance after the breakdown of the microtubule network, it can be inferred that the reduced mechanical resistance *in vivo* resulted in an improved stroke volume (length-dependent activation). These findings suggest a critical role of this cytoskeletal structure and, therefore, the myofibers, in organ function. However, these studies have only investigated microtubules in the LV, and their role in RV function has yet to be investigated.

6. Conclusions

To the best of our knowledge, this is the first study on the changes of RV biaxial viscoelastic behavior during PH development. Our results from the ex vivo stress relaxation tests showed that PH increased RV viscoelasticity in both directions. These changes resulted in an anisotropic viscoelastic behavior of the diseased RV with marked elastic anisotropy in both resting and acute stress conditions and the viscous anisotropy only in acute stress condition. PH development also reduced the damping capacity (ratio of dissipated energy to total energy) of the tissue in both directions. In addition, the RV viscoelasticity was acutely altered from resting to acute stress conditions—the damping capacity was decreased only in the circumferential direction for healthy RVs, but it was decreased in both directions for diseased RVs, indicating an impaired response to acute stress. Lastly, the RVFW exhibited a fully NLV behavior and this behavior was altered by disease progression (PH) or heart rate. These novel findings improve our understanding of RV biomechanics in response to chronically elevated pulsatile mechanical loadings or acutely increased heart rates, and they will shed light on the mechanical mechanism of RV failure and the reduced exercise capacity.

Aim 1b: Characterize RV mechanics using constitutive models.[2]

1. Background

1.1 Viscoelastic modeling

Moreover, the myocardium is a viscoelastic material presenting elastic and viscous mechanical behaviors. That is, both energy storage (related to tissue elasticity) and energy dissipation (related to tissue viscosity) occur during the tissue deformation [8]. However, compared to the elastic behavior, the viscoelastic behavior of right ventricle (RV) myocardium is less studied. As lately reviewed [8], [62], [63], the experimental evidence of myocardium passive viscoelasticity was debatable originally, but recent studies demonstrated the presence of significant hysteresis of passive myocardium from animal to human specimens [14], [16], [24]. This is in contrast to the long known viscoelastic behavior of individual cardiomyocytes or papillary muscles from either side of the heart [27], [44], [64], [65], [66], [67], [68]]. As a result, the knowledge about RV myocardium passive viscoelasticity remains a gap in cardiac biomechanics.

Constitutive modeling of myocardial tissues has received growing interest in recent years with evolving experimental findings. Multiscale and multiphysics computational models have been developed to address the complex microstructure of myocardium and its function associated with various physical properties (mechanical behavior, electrical conduction, and electromechanical coupling). Detailed reviews of constitutive and computational modeling of the myocardium can be found in [62], [63], [69], [70], [71], [72]. The most common models to capture the macroscopic viscoelastic behavior of the myocardium are various formats of Maxwell models, composed of springs and dashpots that represent the elastic and viscous behaviors, respectively. A spring connected to two or more Maxwell elements in parallel (a.k.a. generalized

[2] (Sections adapted from "Multiscale Contrasts Between the Right and Left Ventricle Biomechanics in Healthy Adult Sheep and Translational Implications": https://doi.org/10.3389/fbioe.2022.857638; "Strain-Dependent Stress Relaxation Behavior of Healthy Right Ventricular Free Wall": https://doi.org/10.1016/j.actbio.2022.08.043)

Maxwell model) have been used to describe the stress relaxation or cyclic loading mechanical data in papillary muscles [27], [73] or the ventricular wall [62], [63], [64], [71], [74], [75]. These models are considered as phenomenological models. Another type of viscoelastic model is the biphasic model which attributes the overall viscoelastic behavior to the fluid and solid components in the tissue [76], [77], [78]. In this model, the muscle can be modeled as an incompressible, poroelastic solid saturated by an incompressible, isotropic viscous fluid. Viscoelasticity mainly arises from interstitial fluid flow through pores, and thus viscoelasticity origins from other components (e.g., extracellular matrix proteins) is neglected. Furthermore, Gultekin et al. [62] introduced a new viscoelastic model by decomposing the free energy function into volumetric-isochoric elastic and isochoric-viscoelastic parts (or equilibrium and non-equilibrium parts), assuming incompressible deformation of the myocardium. An important feature of this model is that it combines the mechanical continuum and thermodynamic principles and describes the energy dissipation directly, but more work is needed to further improve the model to reduce the discrepancy between the experimental data and model fits. Finally, the latest viscoelastic model for myocardium was developed by Nordsletten et al. [63]. In this model, a 'fractional viscoelasticity' strategy was adopted to reveal a spectrum of relaxation response of the myocardium presumably caused by different scales of collagen structure (from fibrils to large sheets and bundles). However, this model is unable to capture the nonlinear viscous behavior nor strain-dependent viscoelastic behavior. As a result, the model belongs to the quasi-linear viscoelastic (QLV) model family. To date, Fung's QLV formulation [79] remains a prominent model to describe viscoelasticity in soft tissues and has been used to capture the experimental data of myocardium. The QLV formulation can be found in previous works [63], [77], [78], [80], [81], [82] covering applications from papillary muscles to ventricle free walls (left ventricle only), including both embryonic and adult heart tissues. This model is popular for other types of soft tissues due to its simplicity with a convenient assumption that the elastic and viscous (time-dependent) mechanical behaviors of the tissue are separable. However, one must note that many biological tissues such as tendon, ligaments and spinal cord exhibit fully nonlinear viscoelastic (NLV) behavior [83], [84], [85], [86].

Our recent empirical study found that the ovine left ventricular (LV) and RV myocardium exhibit different types of viscoelastic behaviors [17]. That is, the RV free wall (RVFW) has different relaxation rates at different strain levels in both longitudinal (outflow track) and circumferential directions, suggesting a fully NLV behavior of the tissue. In contrast, the LVFW presents a QLV behavior in the longitudinal direction and a NLV behavior in the circumferential direction. This is the first report of distinct viscoelastic properties of LV and RV in healthy adults. Our experimental findings call for a need to characterize the stress relaxation behavior of RVFW by viscoelastic constitutive modeling, which lends into a deeper understanding of the passive elastic and viscous resistances of the tissue during diastole. Such research is clinically relevant due to the increasing awareness of the prevalence of RV failure in the advanced stage of diseases such as pulmonary hypertension, congenital heart diseases, and left heart failure with preserved ejection fraction [3]. The clinical challenge becomes significant as it is evident that the LV and RV are different in their embryologic origin, anatomy and function [87]. Therapies that work for LV failure patients do not achieve similar effectiveness in the RV failure patients [88], [89], [90]. To the best of our knowledge, studies on the viscoelastic constitutive modeling of the RVFW remain limited. The only modeling study specific to the RVFW viscoelasticity was reported in rats using indentation tests [26]. However, the focus of that study was on the regenerative therapy for hypertensive hearts failure patients, and only a simple linear viscoelastic model (Maxwell model) was used. As a result, comprehensive viscoelastic constitutive modeling is needed to describe the anisotropic viscoelastic behavior of the RVFW.

2. Goals and hypothesis of my research

Therefore, the goal of this study was to characterize the passive, anisotropic and strain-dependent viscoelastic behavior of healthy RVFW using constitutive modeling. We applied the QLV theory to the biaxial stress relaxation data obtained from healthy adult ovine RVFW. Furthermore, we referred to the low strain state as early diastole whereas the high strain state as late diastole, with the unloaded configuration being our ‘reference state’. Our results showed that the RVFW exhibited significantly anisotropic and strain-dependent viscoelastic behavior, individual relaxation function coefficients G_n, shear modulus and

nonlinearity were all strain-dependent, the relaxation term associated with the largest time constant played the dominant role in the overall relaxation behavior at most strains from early to late diastole, and the term associated with the smallest time constant was prominent only at small strains in early diastole. These findings characterize the anisotropic, viscoelastic deformation of the RVFW to fully capture the elastic and viscous resistances and energy expenditure of the tissue during diastole. Such knowledge will deepen the understanding of the mechanical mechanisms of diastolic function of the RV.

3. Materials and Methods

3.1 Tissue sample preparation

Fresh hearts (n = 11) were obtained from 4+ year-old female sheep with no known cardiovascular disease or defects after the animals were euthanized for unrelated studies. Within 4 h of sacrifice, the tissues were immersed in physiological saline solution (PBS) at room temperature until mechanical testing [91]. The outflow tract (OT) direction was used as the longitudinal direction as in previous studies [6], [17], [23], [25]. A cruciform section (total dimensions: 30 mm × 30 mm; center square dimensions: 20 mm × 20 mm) was cut from each ventricle in a similar anatomic region (anterior free wall, with similar distance to the apex and base) and free of fibrotic deposition. For both ventricles, we used the middle layer for mechanical tests after cleaning of the endocardial and epicardial surfaces, including the removal of papillary muscles and trabeculae. The tissue thickness was ∼3–4 mm in all testing samples to achieve negligible shear deformation requirement for the biaxial test [92].

3.2 Equibiaxial ex vivo mechanical testing

The sample was then mounted onto an in-house biaxial tester and then ex vivo mechanical tests were performed at room temperature, with a regular spray of PBS solution to keep the tissue moist. Prior to testing, graphite powder (AGS, MI) was dusted onto the sample for strain characterization. Before testing, approximately 0.1 N of force was applied to pre-load the tissue in both directions. Next, biaxial testing was performed at two different displacement ratios (longitudinal:circumferential) in random order (2:1 and 1:2)

and then at an equibiaxial test (2:2). The first ratio test was completed with 15 cycles including preconditioning cycles. The following ratios' tests were completed with eight cycles per ratio. Finally, the first ratio test was repeated to confirm that no tissue damage occurred. Data acquisition was performed with an in-house LabVIEW program [92].

Each sample underwent a maximum of 25% strain following the reported physiological strains (Rappaport et al., 2006) and the maximum strain rate was 1% s−1. Sample images were taken with a CCD camera (Nikon) at one fps and tissue deformations were obtained by digital image correlation [92]. The digital image correlation was applied to the region of interest (ROI), which was the central, square-shaped region far enough from the boundaries, and we have verified that the deformation in the ROI was nearly homogeneous. The Cauchy (**σ**) and the second Piola-Kirchhoff (P-K) (**S**) stresses, and Green strain (**E**) were calculated for each direction ($\sigma=\lambda_i P$, $S=P/\lambda_i$, and $P=F/A_0$, $E=\frac{1}{2}(\lambda_i^2-1)$), where F is the measured force, P is the engineering stress, A_0 is the initial cross-section area, and λ_i is the stretch in the i=L, C direction with L and C subscripts denoting the longitudinal and circumferential directions, respectively), where the width and thickness were the original dimensions at no load. The elastic moduli (M) were derived as the slopes of the stress-strain curves at the low and high strain ranges (i.e., the first and last 20% of the loading stress-strain curve)[6]. Then, the ratio M/ε in the low or high strain range was used to assess the modulus (M) normalized by the maximal Green strain (ε) in the corresponding strain range and the respective direction [17].

3.3 Microstructural Measurements

3.3.1 Fiber orientation measurement

The tested RV tissue samples were fixed in 10% formalin and embedded in paraffin wax. The longitudinal (outflow tract) direction was marked. The tissue blocks were sectioned into 8 serial slides from the epi- to endocardial side and stained with Picrosirius Red for fiber orientation measurement using in-house MATLAB codes [28]. Briefly, the transmural fiber change was quantified from the serial histology sections

as described previously [69]. Each serial section was imaged using bright field light microscopy and the main collagen fiber direction in the plane was calculated using an orientation distribution function. The transmural fiber orientation was then represented by a Beta distribution function to fit a surface to the 3D data. The mean transmural fiber orientations were calculated using a 1D Hermit shape function and used as the main fiber orientation in the model fitting.

3.3.2 Collagen and myofiber content quantification

The collagen and myofiber area fraction (%) were measured as described in section 2.4.1 in Aim 1a.

3.4 Constitutive model of tissue viscoelasticity

An established QLV model was used to fit the experimental data as previously described [28]. Equibiaxial stress relaxation data was obtained as described in Aim 1a, with input strain levels of 3%, 6%, 9%, 12%, and 15%, and a ramp speed corresponding to 5Hz stretch rate. Assuming incompressibility and negligible shear deformation, the QLV construction for the 2nd Piola-Kirchhoff (PK) stress tensor (**S**) can be presented as [83]:

$$\boldsymbol{S}(\boldsymbol{E},t) = \boldsymbol{S}_0 + \int_0^t \boldsymbol{G}(t-\tau)\frac{\partial \boldsymbol{S}^e}{\partial \boldsymbol{E}} : \frac{\partial \boldsymbol{E}(\tau)}{\partial \tau} d\tau \qquad \text{Eq. 1.5}$$

where **E** is the Green strain tensor, t is time, $\mathbf{S_0}$ is the initial stress pretension obtained from the force in the zero stress configuration, which was set to zero [83], [93], [94]. **G**(t) is the reduced relaxation function, $\mathbf{S^e}$ is the instantaneous elastic stress, and τ is a time variable of integration. The strain tensor (**E**) was prescribed by the global position of the actuators, with linear increments during the ramp period and held fixed during the relaxation period. Only normal (longitudinal and circumferential) strains were applied, and shear strains were negligible at the boundaries at all times. The anisotropic Ogden strain energy density function (ψ) was used to derive the instantaneous elastic stress $\mathbf{S^e}$ [94],[95]:

$$\psi = \frac{2\mu}{\alpha^2}(\lambda_1^\alpha + \lambda_2^\alpha + \lambda_3^\alpha - 3) + \frac{2k\mu}{\alpha^2}(I_4^{\frac{\alpha}{2}} + I_4^{-\frac{\alpha}{4}} - 3) \qquad \text{Eq. 1.6}$$

using

$$\boldsymbol{S^e} = 2\frac{d\psi}{dC} - p\boldsymbol{C^{-1}} \quad \text{Eq. 1.7}$$

where the parameters α, μ and *k* represent the nonlinearity, infinitesimal shear modulus and anisotropy of the tissue, respectively. The principal stretch λ_i are the diagonal elements of the deformation gradient tensor when no shearing is present. **C** is the right Cauchy-Green deformation tensor and **C=2E+I**. With the L and C directions aligned to the λ_L and λ_C, respectively, the anisotropic invariant I_4 was equal to:

$$I_4 = \boldsymbol{a}_0 \cdot \boldsymbol{C}\boldsymbol{a}_0 = \lambda_L^2 \cos\theta^2 + \lambda_C^2 \sin\theta^2 \quad \text{Eq. 1.8}$$

where $\mathbf{a_0}$ is a vector describing the fiber orientation defined by the θ, and $\theta = 0$ represents the fiber aligned along the longitudinal (outflow tract) direction.

In this study, the reduced relaxation function *G(t)* in each direction was defined by the Prony series as:

$$G(t) = G_\infty + \sum_{n=1}^{3} G_n e^{-t/\tau_n} \quad \text{Eq. 1.9}$$

such that:

$$G_1 + G_2 + G_3 + G_\infty = 1 \quad \text{Eq. 1.10}$$

where G_∞ is the long-term relaxation coefficient, which quantifies the proportion of instantaneous elastic stress $\mathbf{S^e}$ remaining in the RVFW over a long (infinite) period. G_n are relaxation coefficients corresponding to the following time constants in the relaxation: $\tau_1 = 0.3\ s, \tau_2 = 3\ s,\ and\ \tau_3 = 30\ s$. These time constants were selected because they have been shown to successfully fit ovine RVFW viscoelastic behavior. Each G_n represents the relaxation strength at the corresponding time constant.

4. Results

4.1 QLV model successfully fit the stress relaxation data at a fixed strain level

The QLV model offered a good fit to the experimental data for all fixed-strain tests (i.e., tests at 3, 6, 9, 12, and 15% equibiaxial strain levels). **Fig. 1.15** shows the representative fitting results. Although the RMSE values increased with the increase of the strain level (from 0.13±0.02 kPa at 3% strain to 2.56±0.22kPa at 15%), the RMSE values were still relatively small at their corresponding strain level, confirming the goodness-of-fit for the QLV model. Next, we tested the ability of the QLV model, fit to a single strain level, to predict the experimental data at other strain levels.

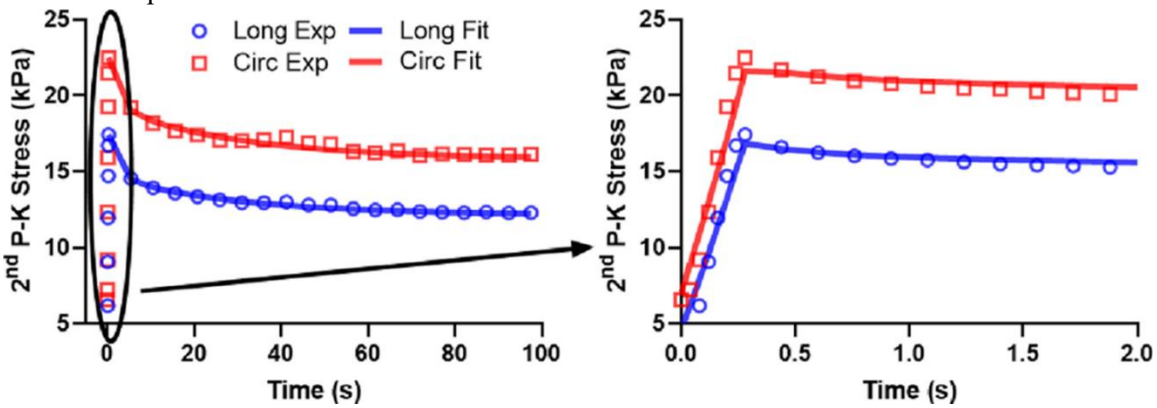

Figure 1.15. Representative fitting results of the QLV model for a RVFW sample at 12% strain level. Long: longitudinal direction; Circ: circumferential direction; Exp: experimental data; Fit: model fitting data.

When the fitting was performed for the 3% strain data, we observed that the fitting parameters did not predict the experimental data at 15% strain level well in either direction (**Fig. 1.16**). We also used the fitting parameters derived from 15% strain data to predict the experimental data at 3% and observed poor fitting

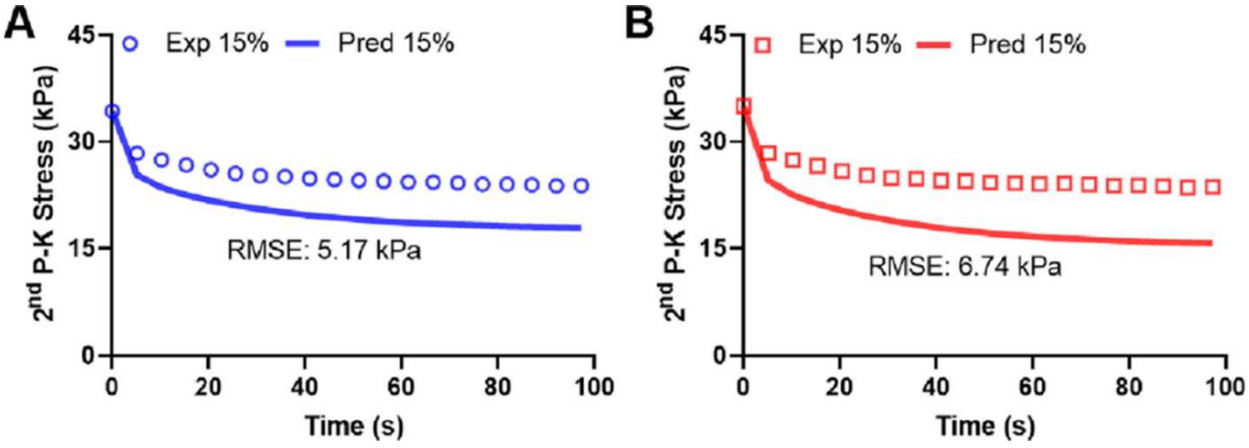

Figure 1.16. Representative results of the QLV model's capability to predict the average relaxation behavior at the fixed 15% strain level using the fitting parameters obtained from fits to the 3% strain test in (A) longitudinal direction and (B) circumferential direction. Exp: experimental data, Pred: predication data. RMSE: root mean square error.

outcomes as well (data not shown). Therefore, in the QLV formulation, the fitting results from one strain level could not predict experimental data obtained at other strain levels.

4.2 Relaxation function, shear modulus, nonlinearity, and anisotropy change with strain

Next, we examined the effect of strain level on the reduced relaxation function G(t). We observed that the relaxation function G(t) was strongly dependent on the strain levels in both directions, and the curve was shifted upward with an increase in strain level (**Fig. 1.17**). Furthermore, we examined the dependence of the shear modulus, nonlinearity and anisotropy on strain levels. We found that the RVFW shear modulus monotonically increased with increasing strains (**Fig. 1.18A**), whereas the RVFW nonlinearity (**Fig. 1.18B**) and anisotropy (**Fig. 1.18C**) exhibited a 'fluctuating' change over strain levels. Lastly, the RVFW anisotropy values were positive (**Fig. 1.18C**), which indicates that the tissue is stiffer along the measured myofiber orientation.

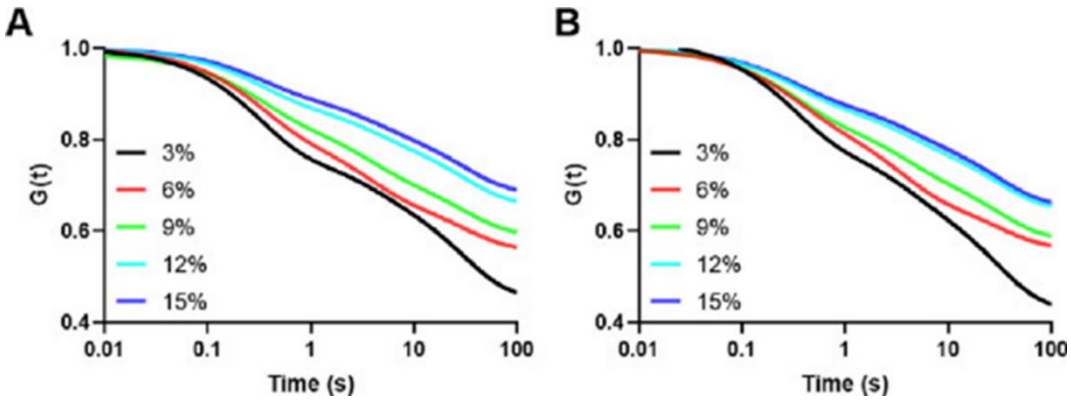

Figure 1.17. The reduced relaxation function G(t) obtained from the average fitting values of coefficients at each strain level in (A) longitudinal direction and (B) circumferential directions.

4.3 Relaxation coefficients G_n were strain-dependent

Next, we compared the individual relaxation coefficients at different strain levels and in different directions. In both directions, G_∞ and G_n changed significantly with strain levels (**Fig. 1.19**). Interestingly, G_∞ was monotonically increased with increasing strains, whereas the opposite behavior was observed for the G_1 (**Fig. 1.19A&B**). While G_2 increased first and then gradually decreased, the opposite behavior was observed

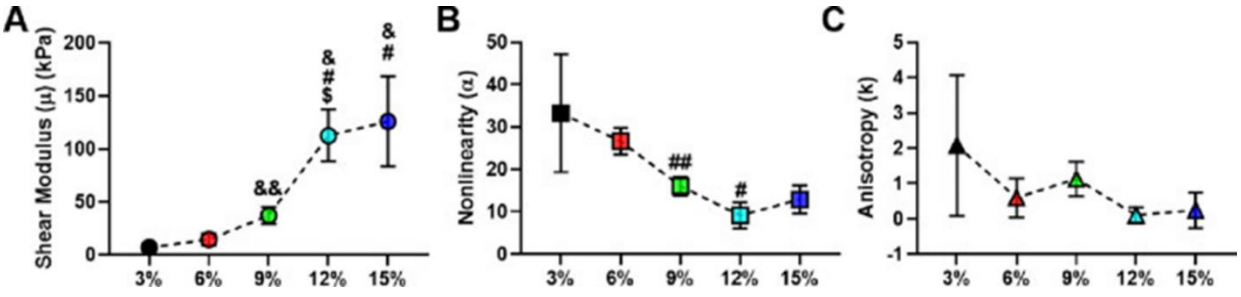

Figure 1.18. Fitted parameters of the Ogden strain energy density function. (A) Infinitesimal shear modulus (kPa), (B) nonlinearity and (C) anisotropy. &<.05 and &&<.01 vs. 3% strain, #<.05 and ##<.01 vs. 6% strain, and $<.05 and $$<.01 vs. 9% strain.

for G_3 (**Fig. 1.19C&D**). Lastly, at most strain levels, the relaxation coefficients did not differ between directions, except that at 15% of strain there was a larger G_∞ in the longitudinal direction compared to the circumferential direction (**Fig. 1.19A**). The coefficient quantifies G_∞ the proportion of instantaneous elastic stress S_i^e remaining in the RVFW over a long (infinite) period of time. A larger G_∞ in the longitudinal direction indicates the anisotropic behavior of the RVFW, and RVFW has more remaining elastic stress in the longitudinal direction than the circumferential direction.

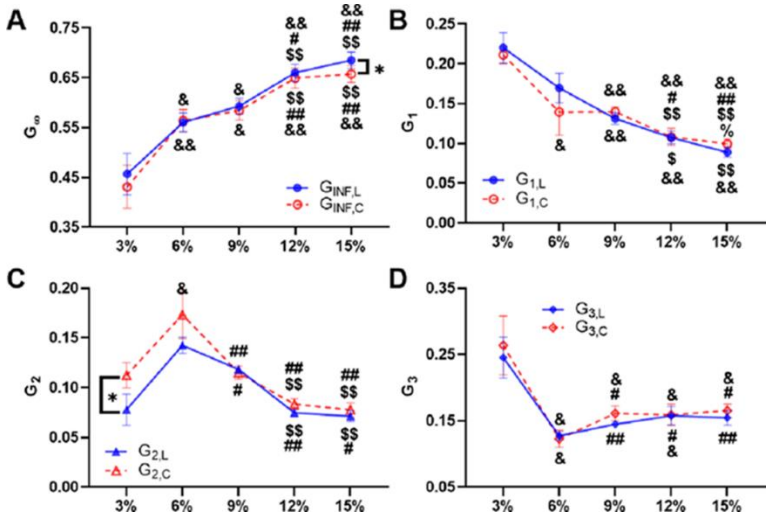

Figure 1.19. Relaxation coefficients Gn at five different strain levels and in longitudinal (L) and circumferential (C) directions. (A) G∞, (B) G1, (C) G2 and (D) G3. &<.05, &&<.01, #<.05, ##<.01, $<.05, $$<.01, %<.05 vs 3, 6, 9 and 12% strain, respectively and *<.05.

4.4 Contribution of relaxation coefficients G_n to relaxation response changes with strain

Next, we compared the relaxation coefficients G_2 at each individual strain level to reveal the individual coefficient's contribution to the entire relaxation response (**Fig. 1.20**). First, we observed similar values of individual G_n in both directions at all strain levels. This indicates that the relaxation coefficients contribute to the RVFW relaxation behavior equally in each direction. Second, except for the 6% strain, G_1 and G_3 played more significant roles than G_2 for all other strain levels. We also noticed that G_1 and G_3 were both prominent at low strains (3% and 9%) (Fig. 6A&C), whereas at high strains (12 and 15%) G_3 was more prominent (**Fig. 1.20D&E**). This indicates that the dominant G_n varied at different strain levels.

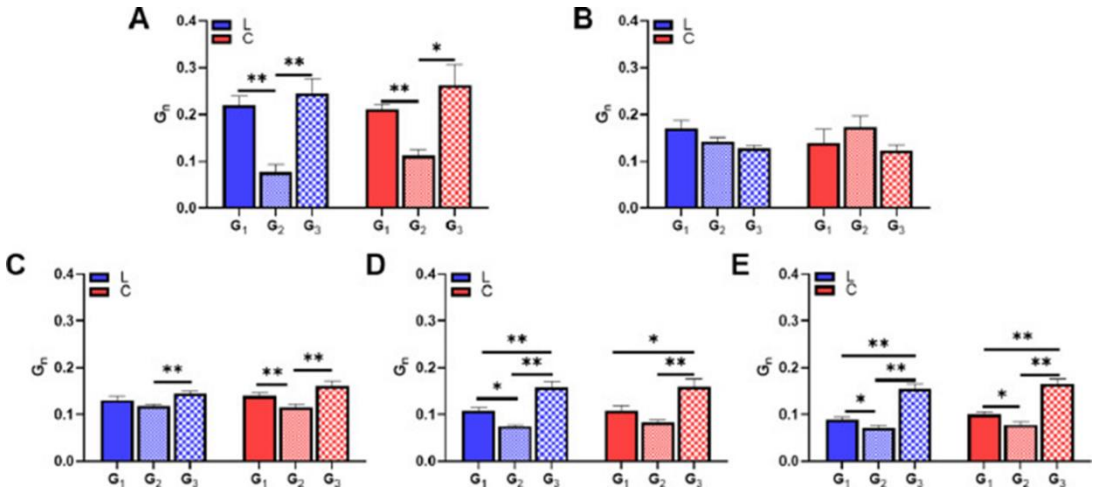

Figure 1.20. Relaxation coefficients Gn at different strain levels in longitudinal (L) and circumferential (C) directions. (A) 3%, (B) 6%, (C) 9%, (D) 12% and (E) 15%. *<.05 and **<.01.

5. Discussion

To the best of our knowledge, these are the first constitutive modeling studies of the contrasts of healthy adult LV and RV free wall in large animal species and the passive, anisotropic viscoelastic behavior of healthy ovine RV. We observed that for RVFW tissues: 1) individual relaxation function coefficients G_n, shear modulus and nonlinearity were all strain-dependent; 2) The relaxation coefficient G_3 was larger than other coefficients at most strains, indicating a dominant role in the overall relaxation behavior from early (low strain) to late (high strain) diastole. In contrast, the relaxation coefficient G_1 was large only at small strains, suggesting a pronounced effect only at early diastole; These findings provide fundamental

information on the biomechanics of the RV as well as the viscoelastic characterization of the RV free wall, which is valuable for the design of tissue and regenerative engineering studies.

5.1 The relaxation function is strain-dependent

The reduced relaxation function G(t) contains the core characteristics of the time-dependent, relaxation response (i.e., viscosity) of the RVFW. Previous modeling studies for other soft tissues have used different numbers of terms in G_n (from 2 to 4 [78], [83], [94], [96]) and different decadal values of τ_n (0.1, 1, 10…. or 0.3, 3, 30… [83], [94], [96]). In our data, we explored two to four terms associated with different sets of time constants τ_n, either using assigned decadal values or those determined from the relaxation time distribution spectrum [94]. The fitting results showed that a three-term function associated with decadal values of 0.3, 3 and 30 as the time constants offered the best fitting results.

Using a three-term relaxation function and the time constants described above, strain-dependent behavior of the reduced relaxation function G(t) was evident: the relaxation function curve shifted upward in both directions with an increase in strain level (**Fig. 1.17**). The observed up-shift of the curves indicates more viscoelastic behavior of the RV at higher strain levels. This phenomenon may be due to the strain-dependent viscoelasticity of collagen or myofiber (like strain-stiffening typically seen in hydrogels or biological tissues [97]). It can also be partly a result of the straightening and increased recruitment of collagen fibers as the stretch increases. The straightening and de-slacking of collagen fibers by load increase contribution of collagen (versus myofibers) [69] to the overall mechanical behavior of the myocardium (evidenced by a nonlinear stiffening of the myocardium by strain) that is expected to change viscoelastic behavior of the myocardium. Similarly, we anticipate that inter-fibrillar interactions (including the cross-linking) will increase at larger strains, perhaps due to both increased number of loaded fibers and increased interactions per fiber, and thus contributes to more friction (viscosity) at the tissue level. But how exactly the microscopic changes lead to macroscopic viscoelastic behavior alteration remains a knowledge gap.

5.2 Different roles of G_∞ and G_n in the relaxation response and implications

We also observed strain-dependent behavior for the relaxation coefficients G_n in both directions, which suggests that they have different weights on relaxation response at low and high strain levels. The long-term parameter G_∞ was monotonically increased with increasing strain, suggesting more stress remaining at equilibrium state under larger deformations. In other words, more energy was stored at equilibrium with a larger G_∞. In contrast, the opposite trend was observed for the G_1, G_2, and G_3. As the strain increased, the strength of the relaxation in relatively short terms (e.g., at time constant of 0.3s) became less pronounced. This suggests that the underlying mechanisms of short-term relaxation response have a strong influence on the overall relaxation behavior at small deformations and a weak influence on the relaxation behavior at large deformations. Furthermore, we observed that at small deformation (3% of strain), G_1 and G_3 had similar strength of relaxation, whereas at large deformation (15% of strain), G_3 had the most significant strength of the relaxation than other coefficients (**Fig. 1.20**). This implies that different G_n dominates the relaxation response at different strain levels. Different trends of increase or decrease in relaxation coefficients G_n with the increasing strain have been reported in other soft tissues, and the trends seem to be tissue dependent. For example, the anterior and posterior longitudinal ligament (ALL, PLL) and ligamentum flavum (LF) are collagen rich connective tissues, and they all had decreasing behavior with the increasing strain for the G_∞ [83]. But in terms of G_1, increasing (LF), decreasing (PLL) and no significant changes (ALL) have been observed for these tissues with the increasing strain.

The underlying mechanisms of short- versus long-term relaxation coefficients G_n can be related to various relaxation processes, including the atomic and molecular motion processes, coupled effects of multiple fields (electrical, magnetic, thermal or fluidic) and heterogenous relaxation [98]. For composite biological tissues, tissue composition (cellular and extracellular components) and the specific microstructure associated with anatomical location and function may all play a role to determine these relaxation coefficients. Unlike the ligament, the RVFW is mainly composed of cardiac muscle cells (myofibers) that have preferred and transmural changes of orientations from epicardial to endocardial layers. We speculate that as the myofibers are more stretched, less energy will be dissipated due to reduced intermolecular

frictions (e.g., less overlapping of actin-myosin), which results in elevated equilibrium stress. But the role of collagen fibers should not be excluded as we recently observed a correlation of type III collagen and low-strain elastic modulus in ovine LV and RV (unpublished data), and a correlation of the type III collagen and RV function [99]. Furthermore, with the increasing strain, the role of collagen will be more significant in determining the entire tissue's mechanical behavior. Therefore, different microstructure components (myofibers, type III collagen, type I collagen, etc.) may be associated with different relaxation time scales (G_n). Nordsletten et al. [63] proposed recently that multiscale mechanisms of molecular friction is likely occurring at different microstructures of collagen, from collagen fibrils to collagen fibers, to bundles and meshes.

5.3 Strain-dependent and anisotropic viscoelastic behavior

As the strain increased, the shear modulus increased monotonically. But this trend was absent from the tissue nonlinearity or anisotropy parameter (**Fig. 1.18**). The monotonically increasing behavior of the shear modulus is consistent with the observation that the myocardium elasticity (e.g., measured by tensile modulus) increases nonlinearly with strain. This behavior can be understood by the continuous recruitment of collagen fibers at larger deformations. An increase in collagen fiber recruitment increases its contribution to load bearing and the tissue elasticity becomes more dominated by collagen rather than myofibers.

The nonlinearity parameter α also presented strain-dependent behavior and it may be attributed to different roles of myo- and collagen fibers at different strain levels. It is known that myo- and collagen fibers play key roles in the tissue elasticity at low and high strain levels, respectively [6], [69]. We speculate that the reduced nonlinearity of RVFW at high strains is due to the fully recruited and stretched collagen fibers, whereas the nonlinearity at small strains is contributed by the nonlinear muscle fibers. The anisotropic parameter κ barely changed with the strain level. As tissue anisotropy has been mostly to the ‘fiber’ orientation, the results indicate negligible change in the orientation of myo- and collagen fibers within the testing strain range. This is not surprising as we performed equibiaxial stretch and the increase of loading in each direction was identical, therefore the load bearing distribution in different directions does not need

to be altered. Furthermore, the anisotropic parameter κ has positive values across all strain levels, indicating an anisotropic elastic behavior. Consistently, we also observed the anisotropic RV relaxation response at end-diastole (15% of strain), which is evidenced by a larger G_∞ (**Fig. 1.19A**).

6. Conclusions

To the best of our knowledge, these are the first constitutive modeling studies of the passive, anisotropic viscoelastic behavior of healthy ovine RV, and the contrasts of healthy adult ovine LV and RV free wall. We observed that for RVFW tissues: 1) the RVFW exhibited significantly anisotropic and strain-dependent viscoelastic behavior; 2) individual relaxation function coefficients G_n, shear modulus and nonlinearity were all strain-dependent; 3) The relaxation coefficient G_3 was larger than other coefficients at most strains, indicating a dominant role in the overall relaxation behavior from early (low strain) to late (high strain) diastole. In contrast, the relaxation coefficient G_1 was large only at small strains, suggesting a pronounced effect only at early diastole. Such knowledge will deepen the understanding of the mechanical mechanisms of diastolic function of the RV.

CHAPTER 2 - Delineate the contribution of the microtubule network to RV anisotropic viscoelasticity

Aim 2a: Investigate the role of the microtubule network in healthy RV anisotropic viscoelasticity.[3]

1. Background

It is widely accepted that the stiffening of the myocardium occurs during heart failure progression and leads to diastolic dysfunction of the ventricle [8]. Recently, correlations between the *ex vivo* elasticity of right ventricle (RV) free wall and *in vivo* indices of diastolic function have been reported in small and large animal models [6], [100]. Additionally, one study has reported the correlation of the passive elastic properties with systolic function [101]. Thus, the significance of myocardium mechanical behavior in its physiological performance is evident. However, the myocardium is viscoelastic, which means there exists both elastic and viscous resistance during the cyclic deformation *in vivo*. Viscous resistance originates from the sliding and friction of molecular bonds, and it works as a 'damper' to cause a delay between the force and deformation as well as a time-dependent mechanical behavior. The current literature of myocardium biomechanics mainly investigates the tissue as a hyperelastic material and ignores the viscous property. Thus, the understanding of the dynamic mechanical behavior of myocardium remains incomplete.

Increasing evidence of myocardial tissue viscoelasticity in both left and right ventricles (LV, RV) has been reported recently, including those from our group [16], [24], [64], [102], [103]. The myocardium is a complex tissue comprised of myofibers, collagen, vasculature, and other extracellular matrix (ECM) components, which all exhibit viscoelastic behavior and contribute to the anisotropic mechanical properties of the tissue. It has long been established that cardiomyocytes (CM) or papillary muscles exhibit viscoelastic properties [27], [30], [65], [68], [104], [105]. CM (myofibers) are responsible for the contractile function of the organ and the contractility is dependent on the viscoelastic behavior of the cell [30],[44],

[3] (Sections adapted from "Role of Microtubule Network in the Passive Anisotropic Viscoelasticity of Healthy Right Ventricle": https://doi.org/10.1115/1.4064685)

[106]. In a study of adult CM from healthy feline RV, it was revealed that the depolymerization of microtubules (MT) via colchicine treatment reduced CM viscoelasticity and enhanced the extent and velocity of shortening [107], demonstrating a critical role of the MT network in CM mechanics and contractile function. Additionally, Caporizzo et al. found that the treatment of colchicine on isolated CM from healthy and failing LVs leads to a reduction of the cell viscoelasticity (viscosity and elasticity) [30], [44], [65], [104]. They obtained both stress relaxation and hysteresis mechanical data of the CM, but the mechanical characterization was for 1D mechanics of the isolated muscle cells. Thus, the role of the MT network in tissue-level biaxial mechanics of the myocardium remains largely unknown.

2. Goal and hypothesis of my research

Therefore, the aim of this study is to investigate the contributions of MT network to the passive anisotropic viscoelasticity of healthy RVs. I hypothesize that the removal of the MT network will reduce RVFW elasticity and viscosity, with stronger effects at the early diastolic strain level. We conducted equibiaxial stress relaxation in healthy rat RVFW with and without colchicine treatment to remove MT polymerization. We then applied the quasilinear viscoelastic (QLV) model established previously to the experimental data to further characterize the relaxation behavior of the RVFW. Our study revealed that 1) RVFW viscosity, not elasticity, was increased from sub-physiological to physiological stretch rate in both directions; 2) the RVFW elasticity and viscosity was enhanced from early to late diastolic strain levels in both directions; 3) the removal of MT network reduces RVFW elasticity and viscosity at both early and late diastolic strains, with a stronger degree of reduction at the early diastolic strain and a larger decrease in elasticity in the longitudinal direction; 4) from the QLV modeling, the contribution of the MT network to the relaxation strength is the strongest in the late (G_3) rather than early (G_1 and G_2) relaxation time constants. To our knowledge, this is the first tissue-level examination of the MT's role in the RVFW anisotropic viscoelasticity. These findings will deepen the understanding of the microstructural contributions to RV mechanics.

3. Materials and Methods

3.1 Ex vivo equibiaxial mechanical testing

All animal procedures were approved by and performed in accordance with the Institutional Animal Care and Use Committees (IACUC, protocol #1438) at Colorado State University. 9-week-old healthy adult male Sprague-Dawley rats (body weight ~360g) (n=8) were euthanized by CO_2 inhalation, and the heart was excised and placed in phosphate buffer solution (PBS) on ice. The RVFW was dissected in cardioplegic solution (CPS) and placed in 30 mM 2,3-butanedione monoxime (BDM) solution at body temperature (37^{o}C) for 30 minutes to remove the active contractility of the myocardium. The outflow tract direction was defined as the longitudinal (L) direction. The tissue was then preloaded to approximately 0.05 N to specify the zero-stress configuration, and calipers were used to measure the thickness of the square sample. 15 cycles of equibiaxial preconditioning were then conducted (at 1 Hz and 20% maximal strain).

RV tissue then underwent equibiaxial stress relaxation to obtain the passive, biaxial viscoelastic behavior, using an in-house biaxial tester [38]. It is known that the myofibers are dominant in myocardial mechanics at low (early diastole) strain levels, while collagen fibers dominate the mechanical behavior at high (late diastole) strain levels [6], [57]. Thus, the RV was stretched to a strain of 6% and 15%, which corresponds to early and late diastolic strain, respectively. For each strain level, the tissue was tested at two stretch rates (ramp speeds) that correspond to a sub-physiological (1 Hz) and physiological (5 Hz) heart rate of the adult rat, respectively. Between each test, a resting time of ten times that of the previous testing period was included to ensure the full recovery of the tissue. After the tissue was tested at the baseline condition (base), 0.3 mM colchicine (COL) (Sigma-Aldrich) was added to the perfusate for 30 minutes to de-polymerize the MT in the RVFW, and the same mechanical testing was performed. The removal of the MT network was confirmed by a notable (30%) reduction in the peak force during stress relaxation test.

3.2 Data analysis

We performed the same viscoelastic parameter analysis as presented in Aim 1a.

3.3 Constitutive model of tissue viscoelasticity: Quasilinear viscoelastic fitting

We performed the same quasilinear fitting procedure as presented in Aim 1b.

3.4 Statistical analysis

Paired student t-test was used to compare data between stretch rates, strain levels, directions, and before and after MT de-polymerization. All data are presented as mean ± SEM. $p<0.05$ was considered statistically significant.

4. Results

4.1 RVFW viscosity, not elasticity, is elevated from sub-physiological to physiological ramp speed in both directions

We first examined the effect of ramp speed on RV viscoelasticity in the baseline condition. RV relaxation modulus was reduced from sub-physiological to physiological ramp speeds in the C direction only (**Fig. 2.1A**), and RV stored energy was not affected significantly by ramp speed (**Fig. 2.1B**). These results showed that a higher ramp speed does not enhance RV elasticity. However, RV viscosity was markedly elevated with increasing ramp speed in both directions, as evidenced by the dissipated energy (**Fig. 2.1C**). Therefore, RVFW viscosity, not elasticity, was elevated from sub-physiological to physiological ramp speeds.

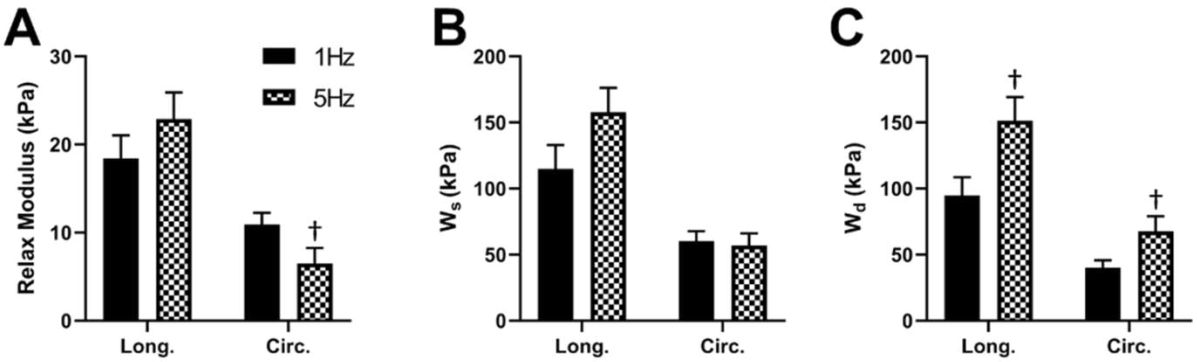

Figure 2.1 RV elasticity (A&B) and viscosity (C) at sub-physiological (1Hz) and physiological stretch rates (5Hz). †$p<0.05$ compared to 1Hz in same direction.

4.2 Enhanced RVFW elasticity and viscosity in both directions from early to late diastole strain

We also investigated the strain dependency of RV viscoelasticity in the baseline condition. We observed significant elevation in relaxation modulus with the increased strain in both directions (**Fig. 2.2A**). Additionally, the stored energy was higher at 15% strain compared to 6% in both directions, too (**Fig. 2.2B**). Therefore, a strain-stiffening behavior was observed in the RV in both directions. We then observed an elevated RV viscosity with the increased strain, revealed by increased dissipated energy from the early to late diastole strain (**Fig. 2.2C**).

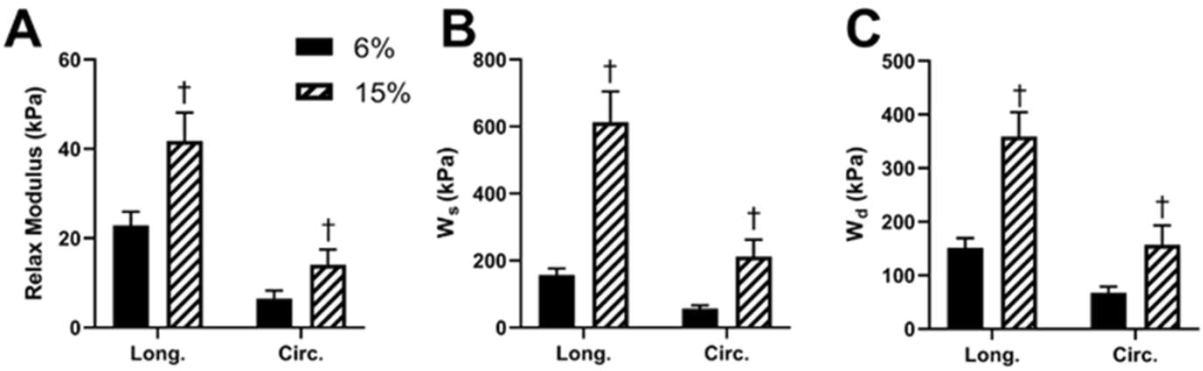

Figure 2.2 RV elasticity (A&B) and viscosity (C) at early (6%) and late (15%) diastolic strain levels. †p<0.05 compared to 6% in same direction.

4.3 Removal of MT network weakens RVFW elasticity and viscosity at early and late diastole strains

Next, we examined the role of the MT network at the physiological ramp speed and firstly at 6% strain to represent early diastolic mechanical behavior. We observed that the removal of the MT network tended to decrease RV relaxation modulus in the L direction (**Fig. 2.3A**, p=0.05). Additionally, the tissue's stored energy was reduced in both directions, with a larger percentage of decrease in the L direction (**Fig. 2.3B**). These results indicate that the MT contributes to RV elasticity in both directions and with a stronger effect in the L direction. The responses of RV dissipated energy to MT removal displayed similar behavior as observed in the stored energy (**Fig. 2.3C**), but the percentage of reduction in dissipated energy was similar

between directions. These results suggest an equivalent contribution of the MT to tissue viscosity at both directions.

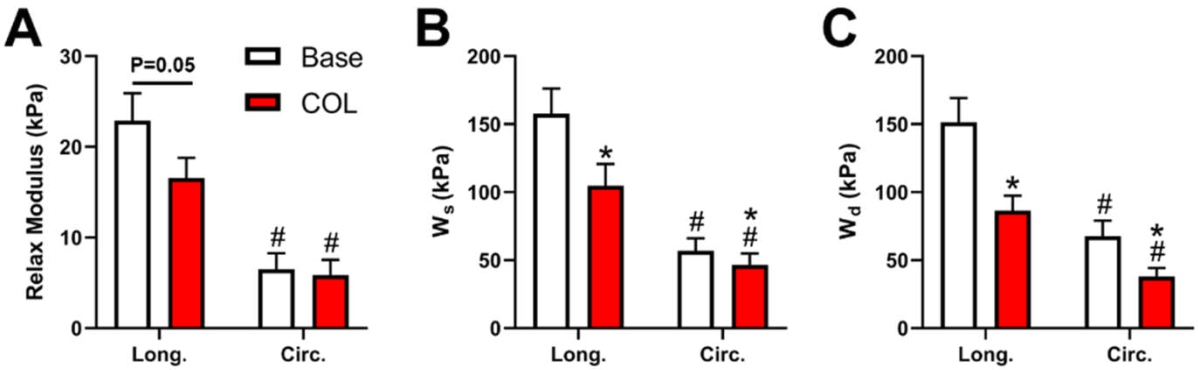

Figure 2.3 RV elasticity (A&B) and viscosity (C) after the removal of the MT network (COL) under 6% strain and ramp speed corresponding to 5Hz. *p<0.05 compared to baseline in same direction; #p<0.05 compared to L direction in same condition.

Next, we examined the contribution of the MT network at a higher strain (15%), to capture the late diastolic mechanical behavior. We observed similar effects of colchicine at 15% as found at 6%. First, the relaxation modulus tended to decrease in the L direction (**Fig. 2.4A**, p=0.05), and the stored energy was reduced in both directions (**Fig. 2.4B**) after MT removal. Moreover, the dissipated energy was also decreased in both directions after the removal of MT (**Fig. 2.4C**). Similar to the observation at 6%, the degree of reduction in

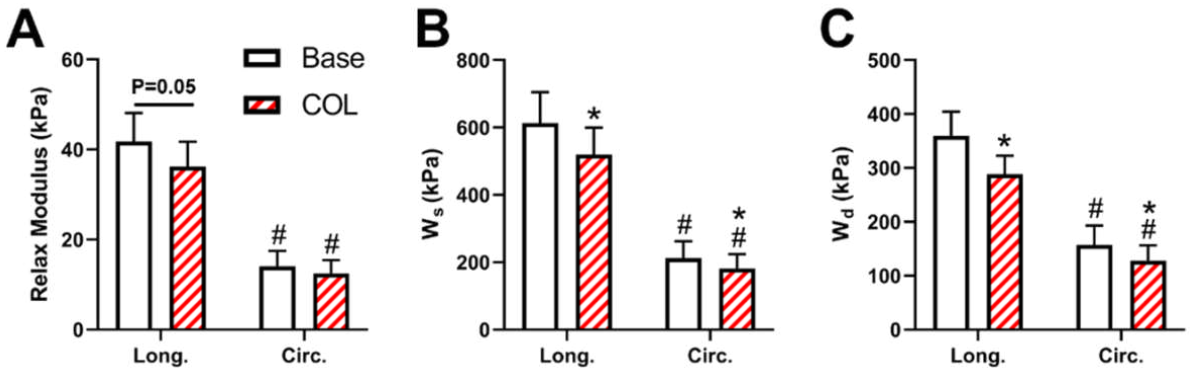

Figure 2.4 RV elasticity (A&B) and viscosity (C) after the removal of the MT network (COL) under 15% strain and ramp speed corresponding to 5Hz. *p<0.05 compared to baseline in same direction; # p<0.05 compared to L direction in same condition.

elasticity was stronger in L direction, whereas the degree of reduction in viscosity was equivalent in both

directions. However, the degree of reduction in RV elasticity and viscosity was less at 15% strain than that at 6% strain, indicating a smaller contribution of MT to RV viscoelasticity at higher strains.

4.4 QLV modeling shows stretch-rate dependent changes in RVFW viscoelasticity

We next applied a QLV formulation to the experimental data at 6% of strain since a stronger effect of MT was noted at early diastolic strains. We found that the shear modulus was elevated from sub-physiological to physiological ramp speed, indicating a greater resistance to shear deformation at elevated stretch rates (**Fig. 2.5A**). We did not observe significant difference in anisotropy index (κ) between the stretch rates (**Fig. 2.5B**). The elastic anisotropy value was negative at both stretch rates, indicating a stiffer mechanical behavior in the cross-fiber (C) direction. Finally, we examined the average relaxation function (G(t)) of the RV tissue. At the sub-physiological ramp speed, the G(t) curve in L direction was above that in the C direction; but at the physiological ramp speed, the G(t) curve in the C direction was above that in the L direction (**Fig. 2.5C**). This data indicates a change in the viscous anisotropy with increasing stretch rate. Moreover, the 5-Hz curves are higher than the 1-Hz curves, suggesting a stronger viscous relaxation at a physiological stretch rate.

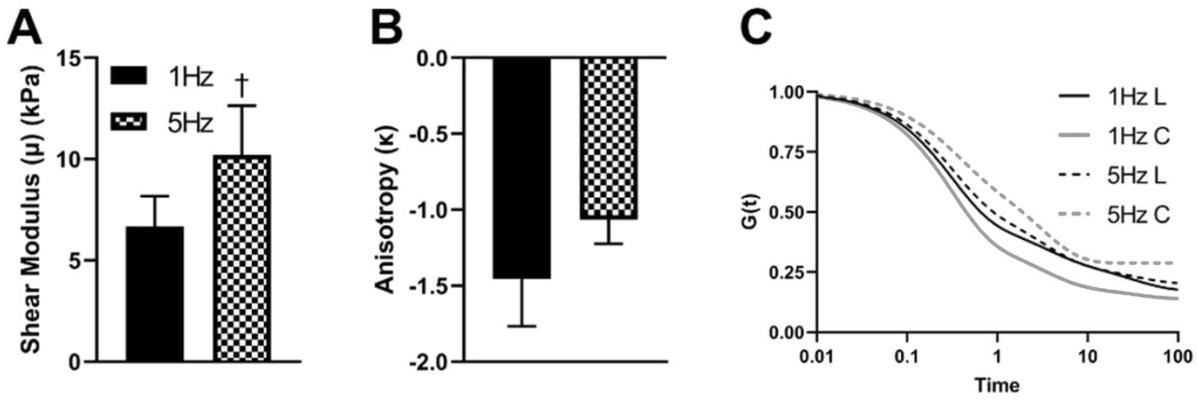

Figure 2.5 RV elasticity (A), elastic anisotropy (B), and average relaxation function G(t) (C) at sub-physiological (1Hz) and physiological (5Hz) stretch rates derived from the QLV modeling. † $p<0.05$ compared to 1Hz.

4.5 QLV modeling shows strain dependent changes in RVFW viscoelasticity

We then compared the modeling parameters between 6% and 15% strain levels obtained at the physiological stretch rate. First, there was a significant increase in shear modulus from 6% to 15% of strain (**Fig. 2.6A**). The elastic anisotropy was not significantly impacted by strain levels (**Fig. 2.6B**). Interestingly, though, from the average relaxation function, G(t), we observed that the curves at 15% strain were lower than the curves at 6% strain in both directions (**Fig. 2.6C**).

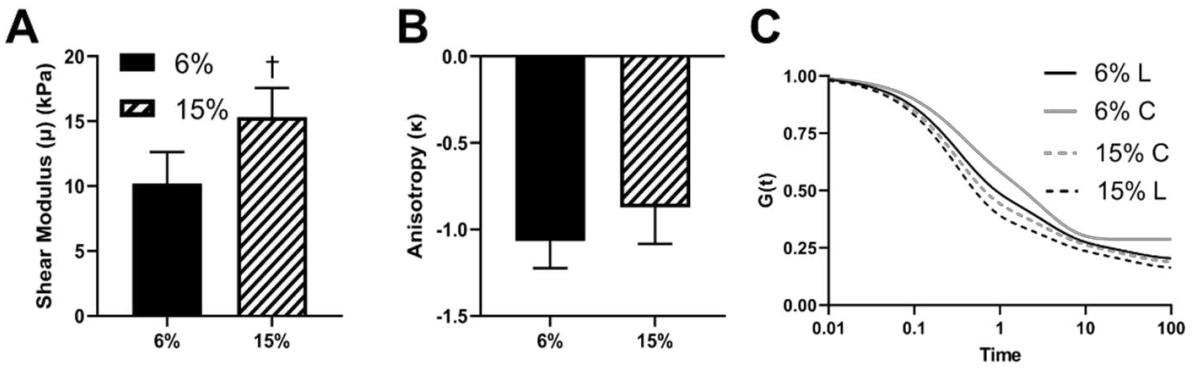

Figure 2.6. RV elasticity (A), anisotropy (B), and average relaxation function G(t) (C) at early diastolic (6%) and late diastolic (15%) strain levels from the QLV modeling. † $p<0.05$ compared to 6%.

4.6 MT network contributes to RVFW relaxation strength predominantly at a later time scale (G_3) and in the longitudinal direction

Finally, RV relaxation strength (G_n) and the overall relaxation behavior (G(t)) were compared before and after the removal of MT under physiological stretch rates. At the early diastolic strain (6%), we observed a reduced relaxation strength at a later time constant (G_3) and in the L direction only after MT removal (**Fig. 2.7A&B**). Additionally, the average reduced relaxation function curves were lower after MT removal, and the reduction was more pronounced in the C direction (**Fig. 2.7C**). At the late diastolic strain (15%), we observed a similar effect of MT removal on the relaxation strength (**Fig. 2.7D-F**). However, the reduction in G_3 at the 15% strain level (8%) was less than that at the 6% strain level (23%), indicating a stronger effect of the MT network at the early diastolic strain level compared to the late diastolic strain level.

Similarly, after the removal of the MT network, the average reduced relaxation function (G(t)) curve was shifted down from the baseline curve, and the shift was more pronounced at the 6% strain level than at the 15% strain level (**Fig. 2.7C&F**).

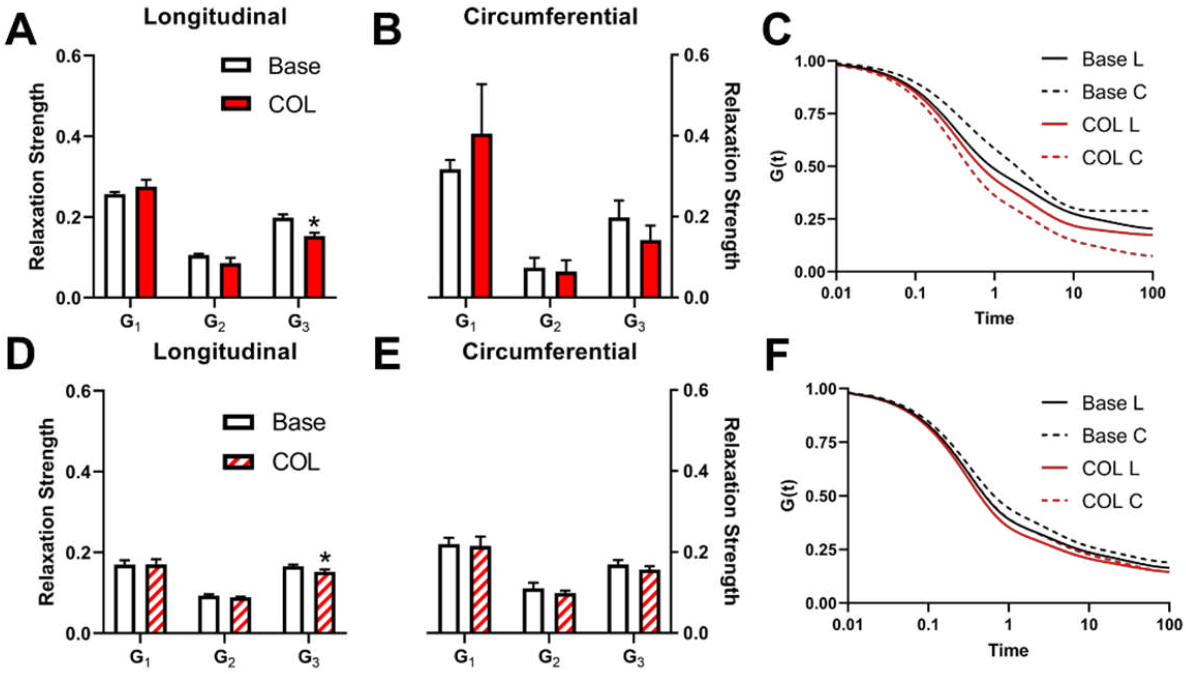

Figure 2.7. RV relaxation strength (Gn) (A&B, D&E) and reduced relaxation function, G(t) (C&F), before and after the removal of the MT network (COL) measured under early (A-C) and late (D-F) diastolic strains at physiological stretch rate in each direction. *p<0.05 compared to baseline in same direction.

5. Discussion

To our knowledge, this is the first investigation of the effect of MT network on healthy RVFW anisotropic viscoelasticity. We originally found that (1) higher (physiological) stretch rate elevates RV viscosity in both directions as well as the shear modulus; (2) higher (end diastolic) strain enhances RV elasticity and viscosity in both directions; (3) the removal of MT network reduces RV elasticity and viscosity in both directions and at both strain levels, with a larger degree of reduction at early than late diastole and a larger decrease in elasticity in the longitudinal direction; (4) QLV modeling revealed that the MT network plays a dominant role in a later relaxation time constant (G_3) and its effect on tissue viscoelasticity is stronger at early than

late diastolic strain. The understanding of contributions of MT network to RV tissue-level mechanics further deepens the knowledge of RV dynamic mechanical behavior regulated by cytoskeleton components.

5.1 Stretch-rate dependent changes in RVFW viscosity and elasticity

The mechanical behavior of tissues, including their viscoelasticity, can be strain or stretch rate dependent [15]. For instance, the conduit arteries (systemic or pulmonary) exhibit frequency-dependent viscoelastic behavior when tested under cyclic deformations [35], [108], [109]. Interestingly, while healthy pulmonary artery had increased elasticity (dynamic elastic modulus) as frequency increases, the hypertensive pulmonary artery had decreased elasticity [35]. Recently, stretch-rate dependent change in elasticity was also reported in heart valves. Anssari-Benam et. al reported elevated elastic modulus in semilunar valves from quasi-static to dynamic loadings [110], [111]. Stretch-rate dependent viscoelasticity of myocardium has been reported as well [14], [16], [24]. At the cellular level, Caporizzo et. al found that the isolated cardiomyocytes display greater dissipation of energy and elastic modulus under diastolic stretch speed (10% over 5 ms) compared to sub-physiological stretch speed (10% over 200 ms) [44]. But at the tissue level measurements, discrepant results are observed. Sommer et. al. investigated the mechanical behavior of human LV and RV free walls and showed that the hysteresis loop area (i.e., viscosity) enlarges from quasi-static (3mm/min) to dynamic (30mm/min) stretch rates [24], but the slope of the loop (i.e., elasticity) was not affected significantly. We observed similar responses in rat RVs here: with elevated strain rate (from sub-physiological to physiological), the RV viscosity was strengthened in both directions (**Fig. 2.1C, Fig. 4.1.5C**). However, the increase in relaxation modulus or stored energy (W_S) was lacking (**Fig. 2.1A&B**). These findings suggest that different molecular mechanisms may be responsible for myocardium tissue viscosity and elasticity, and these two mechanical properties may be independent.

Furthermore, our results from model fitting showed that RV shear modulus was increased from low to high ramp speeds (**Fig. 2.5A**) [7][16]. For isotropic linear elastic materials, the shear modulus and elastic modulus are inter-dependent, and the changes in these parameters are in parallel. But in anisotropic materials, elastic modulus is direction-dependent, while shear modulus is direction-independent; thus, the

two moduli will not necessarily have similar alterations under different loads. Moreover, the shear modulus measures the intrinsic resistance to *shear* deformation and the elastic modulus measures the intrinsic resistance to *tensile* deformation. In our experiment protocol, the shear deformation of the tissue was negligible. But the modeling result suggests that the shear elastic resistance is elevated at higher heart rates during the *in vivo* 3D deformation of the heart wall. The physiological significance awaits further investigations. Finally, we used an Ogden strain energy function to characterize the elastic response in the QLV modeling because the same model has been shown to successfully describe the viscoelastic behavior of RVFW [28]. Future studies can explore other commonly used hyperelastic models to predict the elastic/Young's modulus of the tissue. Overall, our results clearly show the importance of using a physiological stretch rate in capturing the viscous and elastic behavior of myocardium tissue.

5.2 Strain-dependent changes in RVFW viscosity and elasticity

Strain-stiffening phenomena has been found in a variety of biological tissues, and a typical experimental measurement of it is through the J-shaped stress-strain curve. For myocardium tissues, numerous studies have reported this nonlinear behavior of the tissue [24], [68], [102], [112], with a low elastic modulus at small strains and high elastic modulus at high strains. Similar behavior can be found at the cellular level of myocardium as well [104]. Strain-stiffening phenomena has been explained by the increased alignment or recruitment of stiffer (collagen) fibers or by the increased crosslinks between the polymers as the strain increases. As expected, we observed a larger relaxation modulus and stored energy (W_S) of the RV at late diastolic strains (**Fig. 2.2A&B**). Results from the QLV modeling showed a similar trend in shear modulus (**Fig. 2.6A**). Thus, our results are consistent with findings from prior work. Moreover, our study has found novel strain-dependent viscous behavior in the RV: the measurement of W_d showed significant elevation in RV viscosity from early to end diastole strains. However, the average reduced relaxation function (G(t)) curves were reduced at larger strains in both directions (**Fig. 2.6C**), indicating a weakened viscous behavior. In most of our data, the measurements of W_d and G(t) give consistent findings as we treat those parameters as indicators of viscosity. However, the discrepancy here calls for a deeper reflection of the measurements

of viscosity through these parameters. In the present study, W_d is essentially a measure of the total dissipated energy during the relaxation phase, and it is affected by both the intrinsic viscous property as well as the peak stress, which involves the elastic property of the material. However, the G(t) is a modeling result that is derived after the separation of the elastic and viscous stresses, so it is not affected by the elastic property of the material. It can be viewed as a representation of the intrinsic viscous property. Thus, although both parameters can capture the viscous behavior of the material, the W_d is more of a measure of the extrinsic viscosity, where the relaxation strength (G_n) is a modeling metric of the intrinsic viscosity.

5.3 Removal of the MT network reduces RVFW viscosity and elasticity in a strain-dependent and direction-dependent manner

As the first investigation on the role of MT in RVFW tissue viscoelasticity, we found that RV elasticity and viscosity were significantly reduced after the removal of MT network in both directions and at both early and late diastolic strain levels (**Fig. 2.3&2.4**). The responses of isolated cardiomyocytes to MT removal display similar behavior, with both cell elasticity and viscosity reduced [30], [44], [105], [107], [113]. Therefore, our and prior findings have confirmed a critical contribution of MT network to the myocardium viscoelasticity at tissue and cell level, respectively. However, there are some new findings from this current work.

First, we found that the reduction in RV viscoelasticity after the removal of MT network was much stronger at the early diastolic strain (6%) compared to the late diastolic strain (15%). The strain-dependent effect of MT network shows a larger effect of MT at small strains, and this could be explained with the increasing recruitment of collagen at large strains. It is known that at early diastole, myofibers play a more dominant role in myocardial mechanics; while at late diastole, collagen has been fully recruited and is contributing more to the mechanical behavior of the tissue [6], resulting in higher elasticity at elevated strains [102]. Second, the effect of MT network on elasticity and viscosity is different and can be direction dependent. At early diastolic strain, we observed a stronger reduction in RV elasticity in the L direction compared to the C direction (~37% vs 18%). However, the reduction in viscosity between the two directions was nearly

identical (~44%). The different changes of reduction in elasticity and viscosity suggest that MT network contributes to these mechanical behaviors distinctly. The MT cytoskeletons are predominantly aligned in the main direction of contraction in the muscle cells [104]. Thus, our results indicate that the MT contributes to RV viscosity regardless of preferred direction, whereas its contribution to RV elasticity is more dependent on the alignment. Various molecular mechanisms may be responsible for the elasticity and viscosity of MT network. Titin, a sarcomeric protein, is interconnected with the MT network and provides structural support to the network. Disruption of the MT network, as in after depolymerization, may affect the mechanical behavior of titin, and we acknowledge its potential role in myocardial mechanics.

5.4 MT network contributes to the relaxation behavior of RVFW at a later time scale, with a stronger effect at the early diastolic strain level

Despite the novel findings from the experimental work, the computational work done in this study provides further insights on the relaxation behavior of the tissue that experimental data cannot provide. In this study, we used three terms of G_n to capture the relaxation strength of the RV at the beginning of relaxation and the G_{inf} to capture the relaxation strength at the end (equilibrium) of the relaxation.

The removal of the MT network at both strain levels resulted in a reduction of relaxation strength at 30 sec. after peak stress (i.e., τ_{30}) (**Fig. 2.7**). This change was only present in the L direction. Interestingly, there were no significant effects of the MT network on G_n at early relaxation times. Our results suggest that the MT is playing a dominant role in the relaxation response at a later time scale. In this traditional Fung's QLV model, G_n mainly describes the relaxation strength at different time constants of the relaxation. Whether it is related to different biological components (e.g., myofiber or collagen) or different molecular structures (e.g., tiny fibrils or large fibers) remains unknown. Nordsletten et. al has proposed that the hierarchical structure of the extracellular matrix is responsible for the molecular mechanism of relaxation at different time scales– from fibrils, to fibers, to bundles, to sheets – in human myocardium [63]. If this is the case, our results suggest that the MT network serves as an intermediate fibrous component, and other smaller components (e.g., actin, collagen fibril) may be responsible for more earlier relaxation responses. MT

network not only contains cytoskeletons with the diameter of ~ 25 nm but also has crosslinks between the coiled polymers. How the microstructure of crosslinks (in L and C directions) is involved in the relaxation strength distribution is unknown. Moreover, there are influences from other intra-cellular and extra-cellular components as well as the interactions between these components. Therefore, future work should investigate how the relaxation constants are affected by various biological elements and the architectures in a complex tissue like myocardium.

6. Conclusions

This is the first study to investigate the contribution of microtubules to the RVFW anisotropic viscoelasticity. Our results showed that the RV exhibits stretch-rate dependent and strain dependent viscoelastic behavior. The removal of MT network reduces RV viscosity and elasticity in both directions, with a greater reduction at early than late diastolic strain and a larger decrease in elasticity in the longitudinal direction. From the QLV modeling, it is shown that the MT network plays a dominant role in a later relaxation time constant and the effect of MT on tissue relaxation is stronger at early than late diastolic strain. These new findings characterize the distinct role of the MT network in healthy RVFW passive anisotropic viscoelasticity. Such knowledge will deepen the understanding of the microstructural contributions to myocardial mechanics.

Aim 2b: Investigate the role of microtubule network in RV biaxial viscoelasticity with pulmonary hypertension progression.[4]

1. Background

Heart failure (HF) is the leading cause of death in the US and worldwide [114], and ventricular dysfunction is a main contributor to HF. Specifically, right ventricular (RV) failure contributes significantly to the mortality and morbidity of various cardiovascular diseases, such as congenital heart disease, left ventricular failure with preserved ejection fraction (HFpEF), and pulmonary hypertension (PH). There has still, though, been a lack of treatment for such patients, due largely to a lack of understanding of the pathology and physiology of RV failure. It is accepted that the mechanical behavior of the organ largely impacts its function [6], [7], [8]. A prior rodent study found a correlation between the passive stiffness of the RV and end diastolic volume [6], and our own ovine study showed that RV elasticity is positively correlated with geometry and hemodynamic properties [7]. While such studies suggest a key role of the organ elastic behavior in clinical parameters, the RV is viscoelastic. This indicates that the tissue exhibits both elastic and viscous resistance in response to deformation.

There has been increasing evidence of myocardial tissue viscoelasticity in both the left and right ventricle (LV, RV), including those from our group [16], [17], [24], [28], [64]. The RV free wall (RVFW) is comprised of myofibers, collagen, vasculature, and other extracellular matrix (ECM) components that form a complex mesh. These components all exhibit viscoelastic properties and contribute to the anisotropic mechanical behavior of the tissue. Cardiomyocytes (CM) or papillary muscles are known to demonstrate viscoelastic behavior [27], [30], [65], [68], [104], [105], and CM are key determinants of the contractile function of the myocardium, which is directly related to the viscoelasticity of the cell [30], [44], [106]. A recent study of isolated healthy CM showed that the depolymerization via colchicine of the microtubule (MT), a

[4] (Sections adapted from "Role of Microtubule Network in the Passive Anisotropic Viscoelasticity of Right Ventricle in Pulmonary Hypertension Progression": https://doi.org/10.1016/j.actbio.2024.01.023)

cytoskeletal structure of the cell, reduces the cell's viscoelasticity and strengthens the degree and velocity of shortening [107], suggesting a key role of the MT network in the mechanical behavior of the CM and its contractile function. Additionally, Caporizzo et. al treated isolated adult healthy CM from the LV with colchicine and observed a weakened cell viscosity and elasticity [30]. These studies, though, only obtained healthy cell behavior. In the hypertrophied myocardium, both MT density and myofiber viscoelasticity are increased [44], [115]. Moreover, the treatment of colchicine on isolated adult CM from a failing LV still reduced the cell elasticity and viscosity [44]. While both stress relaxation and cyclic mechanical tests were conducted, the distinct role of the MT network on the failing RV mechanical behavior remains unknown.

2. Goal and hypothesis of my research

Therefore, the aim of this study is to characterize the role of the MT network in RV passive anisotropic viscoelasticity during PH progression. I hypothesize that the role of the MT network in RVFW viscosity and elasticity is different between the early and end diastolic strains due to collagen recruitment and between healthy and diseased RVFW due to denser and disorganized MT in the diseased tissue. We induced PH in adult male Sprague-Dawley rats and performed equibiaxial stress relaxation testing on the entire RVFW with and without the treatment of colchicine to depolymerize the MT network. Our study revealed that 1) PH enhances RVFW viscoelasticity at sub- and physiological stretch rates, and at early and end diastolic strain levels; 2) the diseased RVFW elasticity and viscosity were enhanced from a sub- to physiological stretch rate, but only healthy RVFW viscosity was strengthened; 3) both healthy and diseased RVFW elasticity and viscosity were increased from the early to the end diastolic strain level; 4) at the early diastolic strain level, the removal of the MT network reduced tissue elasticity, viscosity, and the ratio of viscosity to elasticity in both the healthy and diseased RVFW; 5) at the end diastolic strain level, the removal of the MT network reduced healthy RVFW longitudinal viscoelasticity, but only effects circumferential viscosity in the diseased RVFW. To our knowledge, this is the first study to investigate the role of the MT network in the viscoelastic behavior of hypertrophied myocardium. These findings will deepen the

understanding of microstructural determinants of RV mechanics, as well as their contribution to the pathophysiological of RV failure.

3. Materials and Methods

3.1 Specimen preparation and disease model

All animal procedures were approved by the Institutional Animal Care and Use Committees (IACUC, protocol #1438). 6-week-old male Sprague-Dawley rats (n=6) were administered a subcutaneous injection (60mg/kg) of monocrotaline (MCT) to induce PH and housed in normal conditions for three weeks. We followed the identical disease model protocol as described previously, in which we observed overt PH [38]. Healthy age matched animals served as control (CTL) (n=6). At 3 weeks post injection, the animals were euthanized, and the heart was excised and placed in phosphate buffer solution (PBS) on ice.

3.2 Ex vivo equibiaxial mechanical testing

After harvest, the entire RVFW was dissected in cardioplegic solution (CPS) and placed in 30mM 2,3-butanedione monoxime (BDM) solution at body temperature for 30 minutes to remove the contractility of the myocardium. The outflow tract direction was defined as the longitudinal (L) direction. The tissue was then preloaded to approximately 0.05 N to specify the zero-stress configuration, and calipers were used to measure the dimensions of the square sample. Four markers were placed on the region of interest of the surface in a square formation for strain analysis. 15 cycles of cyclic equibiaxial preconditioning were then conducted (at 1Hz and 20% maximal strain).

RV tissue then underwent equibiaxial stress relaxation to obtain the passive, biaxial viscoelastic behavior using an in-house biaxial tester. The RV was stretched to maximal strains of 6% and 15%, which correspond to the early and late diastolic strains, respectively, to examine the behavior before and after collagen recruitment [6], [69]. For each strain level, the tissue was tested at two stretch rates: 1Hz and 5Hz, which relate to a sub-physiological and physiological heart rate of the adult rat, respectively. Between each test, a recovery time of ten times that of the previous testing period was included to ensure full recovery of the

tissue after deformation. Biaxial stretch forces were obtained by 5-lb load cells (Honeywell) at a sampling frequency of 200 Hz. After the intact tissue was tested at the baseline condition (base), the RV was exposed to 0.3mM colchicine [44] (COL) for 30 minutes to de-polymerize the MT, and the same mechanical testing was performed.

3.3 Data analysis

We performed the same viscoelastic parameter analysis as presented in Aim 1a.

2.4 Constitutive model of tissue viscoelasticity: Quasilinear viscoelastic fitting

We performed the same quasilinear viscoelastic fitting procedure as presented in Aim 1b.

4. Results

4.1 Diseased RV and healthy RV exhibit different stretch-rate dependent elasticity

First, we investigated the effect of stretch rate on the healthy and diseased RV elasticity (W_S) and viscosity (W_d). Increasing from a sub-physiological to a physiological stretch-rate did not influence healthy RV

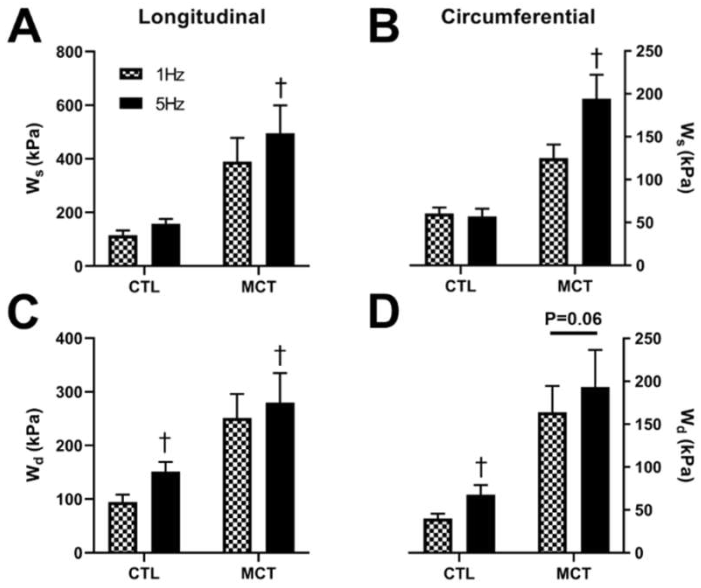

Figure 2.8. The elasticity (WS) (A&B) and viscosity (Wd) (C&D) of healthy and diseased RVFW in the longitudinal (left column) and circumferential (right column) directions at the sub-physiological (1Hz) and physiological (5Hz) stretch rates. † $p<0.05$ compared to to the sub-physiological stretch rate.

elasticity in either direction, but it significantly increased diseased RV elasticity in both directions (**Fig. 2.8A&B**). In contrast, when examining the stretch-rate's effect on tissue viscosity, we found that the viscosity of healthy and diseased RVs was increased significantly in both directions (**Fig. 2.8C&D**). The percentage of increase in W_d was more pronounced in the healthy RV (L=35%, C=42%) than diseased RV (L=11%, C=18%). Our results showed that the stretch-rate had a greater effect on the viscosity of healthy RVs and the elasticity of the diseased RVs.

3.2 Diseased RV and healthy RV exhibit similar strain dependent elasticity and viscosity

Additionally, we analyzed RVFW viscoelasticity at a physiological stretch rate and at early and end diastolic strain levels. As expected, we observed increased viscosity and elasticity of the RVFW from the early to the end diastolic strain levels (**Fig. 2.9**), indicating the strain stiffening and strain "thickening" effects of the tissue. This behavior was observed in both the healthy and the diseased RVFW, suggesting that the impact of strain level on myocardial mechanics is independent of health states.

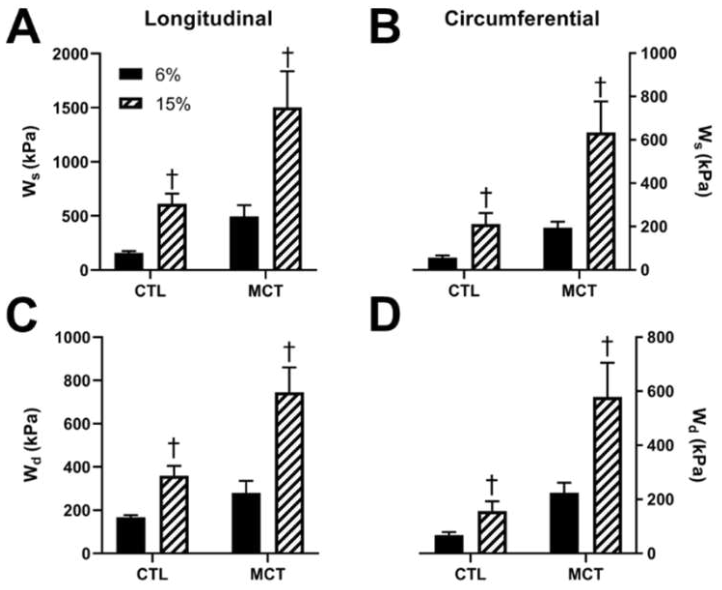

Figure 2.9. The elasticity (WS) (A&B) and viscosity (Wd) (C&D) of healthy and diseased RVFW in the longitudinal (left column) and circumferential (right column) directions at the early diastolic (6%) and end diastolic (15%) strain levels. † $p<0.05$ compared to the early diastolic strain level.

4.3 Removal of MT similarly weakens viscoelasticity of diseased RV and healthy RV at early diastolic strain

After examining how PH impacts on RVFW viscoelasticity, we investigated the contribution of the MT network to healthy and diseased RVs firstly at the early diastolic strain level. Because the mechanical behavior at physiological stretch rate is more relevant to organ performance, we only present the data obtained from this condition from now on. First, in both directions, the elasticity (W_S) and viscosity (W_d) were significantly reduced in both groups after MT removal (**Fig. 2.10A&B, D&E**), except for a moderate trend of reduction in the diseased RVFW in the longitudinal direction (p=0.1). Moreover, the V/E ratio was

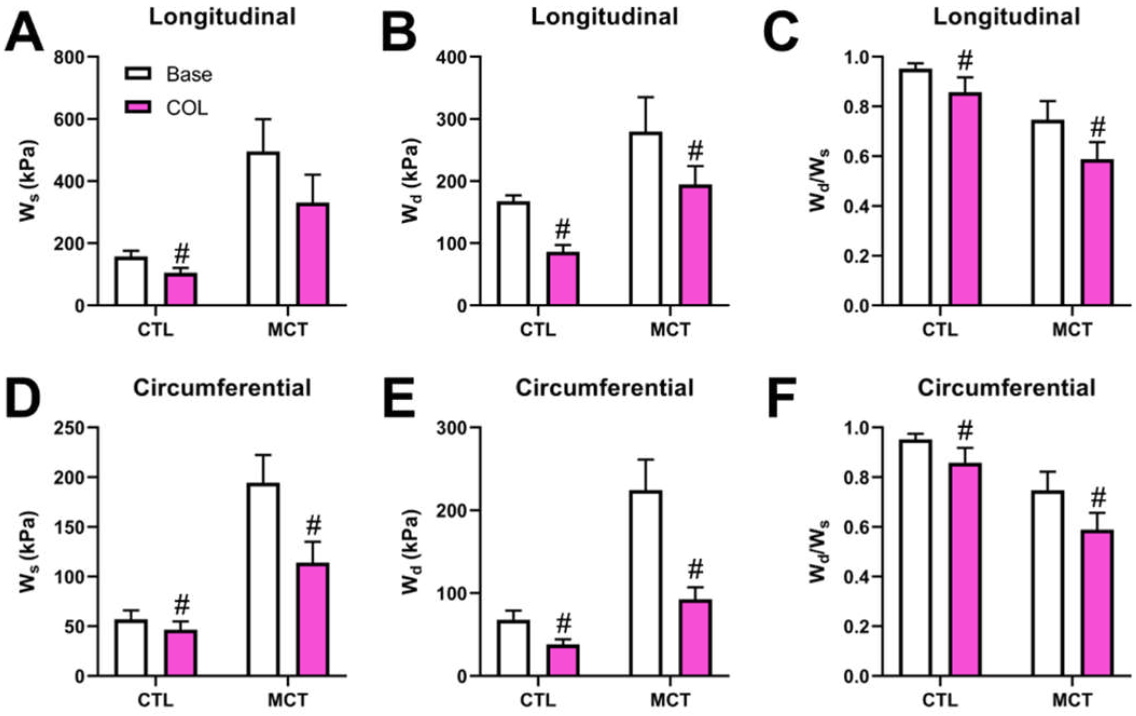

Figure 2.10. The elasticity (A&D), viscosity (B&E), and the V/E ratio (C&F) of healthy and diseased RVFW after the removal of the MT network (COL) under 6% strain and ramp speed corresponding to 5Hz. #p<0.05 compared to baseline in same direction and group.

reduced significantly in both directions and for both groups (**Fig. 2.10C, F**). This result is due to the greater reduction of viscosity than elasticity, indicating a stronger role of the MT network in tissue viscosity (**Fig. 2.10C**).

4.4 Removal of MT differently weakens viscoelasticity of diseased RV and healthy RV at end diastolic strain

It is found that the elastic behavior of myocardium is dominant by myofibers at small strains and by collagen fibers at large strains [6]. But whether and how much the MT network contributes to the tissue-level viscoelasticity at larger strains is unclear. To answer this question, we investigated the effects of MT removal on RV viscoelasticity at the end diastolic strain level. In contrast to the results at early diastolic strain, we observed a differential role of the MT network in the healthy and diseased RVs. First, in the longitudinal direction, both elasticity and viscosity were weakened after MT removal in the healthy RVs, but this change was not observed in the diseased RVs (**Fig. 2.11A&B**). Moreover, there was an absence of effect on the V/E ratio for both groups (**Fig. 2.11C**). In the circumferential direction, the effects of MT

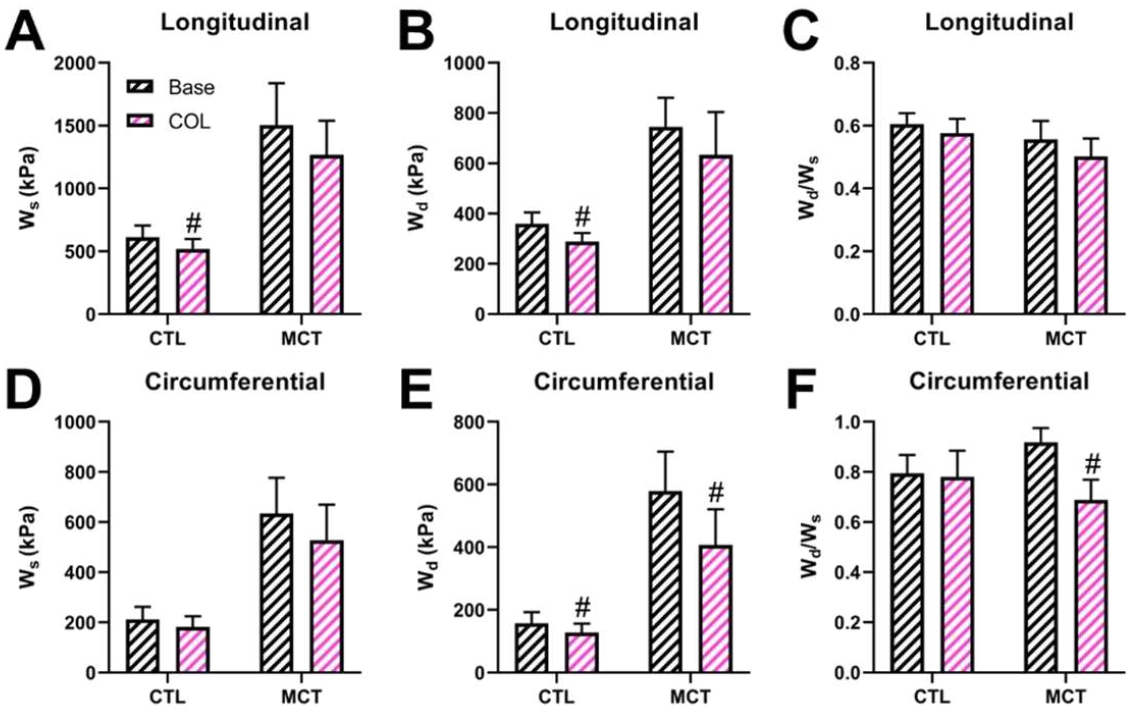

Figure 2.11. The elasticity (A&D), viscosity (B&E), and the V/E ratio (C&F) of healthy and diseased RVFW after the removal of the MT network (COL) under 15% strain and ramp speed corresponding to 5Hz. #$p<0.05$ compared to baseline in same direction and group.

removal on elasticity and viscosity were similar between healthy and diseased RVs – no change on elasticity but a decrease of viscosity were noted (**Fig. 2.11D&E**). Additionally, the MT removal led to a reduction in the V/E ratio in the diseased RVs only (**Fig. 2.11F**). These results suggest distinct contributions of MT network to the viscoelasticity of normotensive and hypertensive RVs after collagen recruitment.

4.5 QLV modeling reveals removal of MT network decreases RV relaxation strength (viscosity) at late time points of relaxation in healthy and diseased RVFW

Lastly, we applied a QLV model to characterize the role of MT in the relaxation behavior of the RVFW with disease progression and removal of MT. First, at the early diastolic strain level, tissue relaxation strength at a later time point (G_3) was reduced after the removal of the MT network in both directions and for both groups (**Fig. 2.12A&B**). Similar effects were observed at the end diastolic strain level (**Fig. 2.12C&D**). These data suggest that the G_3 coefficient is affected by the MT network, regardless of the strain levels or disease state. Moreover, we found that G_2 was reduced in the diseased RVs as well, and the reduction was in the longitudinal direction at early diastolic strain (**Fig. 2.12A**) and in the circumferential direction in the end diastolic strain (**Fig. 2.12D**).

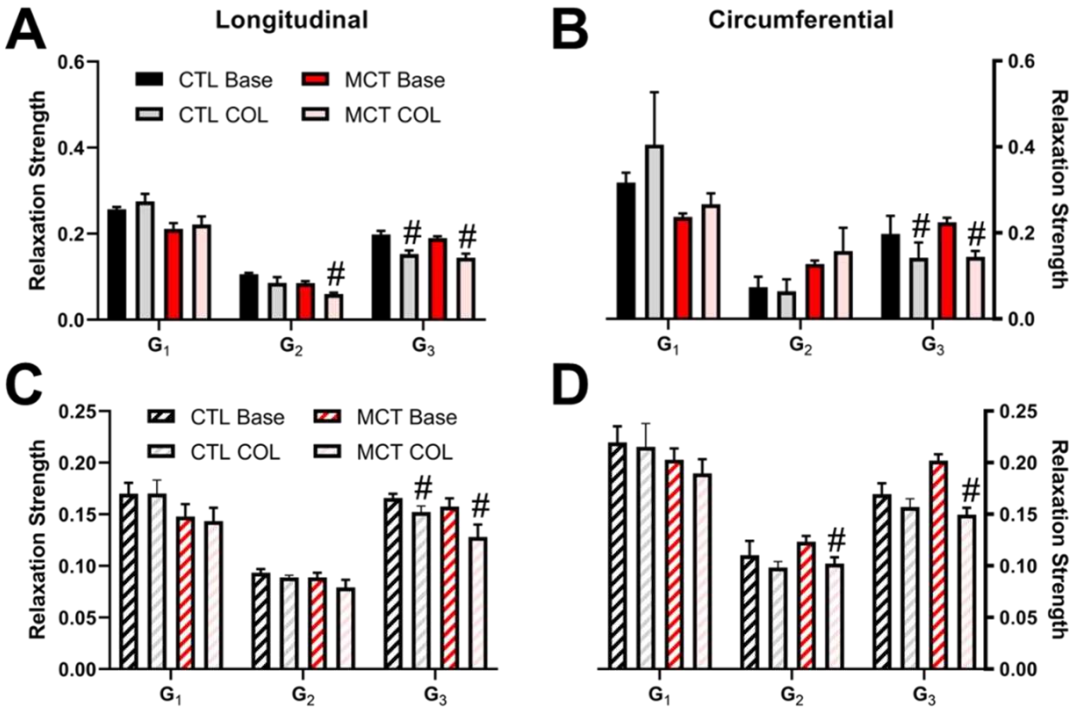

Figure 2.12. The relaxation strength (Gn) of healthy and diseased RVFW before and after the removal of the MT network at early (A&B) and end (C&D) diastolic strain levels. #p<0.05 compared to baseline in same group and direction.

5. Discussion

5.1 Altered stretch-rate dependent changes in RVFW elasticity and viscosity with PH progression

Biological tissues are viscoelastic, and this behavior can be either strain or strain-rate dependent [116]. Caporizzo et al. found at the cellular level that isolated healthy cardiomyocytes exhibit enhanced elastic modulus and stronger hysteresis behavior under a diastolic (10% over 5ms) compared to a sub-physiological stretch speed (10% over 200ms) [44]. While stretch-rate dependence has been reported in the healthy myocardium, [14], [16], [24], the observations are not consistent. Sommer et al. studied the mechanical behavior of human LV and RV and found that the viscosity (hysteresis loop area) is greater at the dynamic (30mm/min) stretch rate compared to the quasi-static (3mm/min) stretch rate [24]. However, the elastic modulus (slope of the loop), was unchanged between stretch rates. Our results here showed similar behavior in the healthy RVFW, with no change in elasticity (W_S) (**Fig. 2.8A&B**) but an increased viscosity (W_d) (**Fig. 2.8C&D**) with increasing stretch rate. However, there is a different story in the diseased RVFW, with both elasticity and viscosity increasing from the sub- to physiological stretch rates (**Fig. 2.8**). Our group has previously shown stronger stretch-rate dependent behavior in the diseased RV compared to the healthy RV [38]. Relaxation modulus, a metric of overall viscoelasticity, monotonically decreased with increasing frequency and this trend was stronger in the PH group. However, these measurements were taken at the beginning of relaxation (0.01s after peak stress), whereas our results here were obtained at the end of relaxation (100s after peak stress). Moreover, in the diseased RVs, there is an accumulation of collagen, and the enhanced contribution of collagen may be responsible for the stretch-rate dependent elasticity seen in the diseased RVs. Further investigation is needed to de-couple the roles of cellular and extracellular components in tissue mechanics.

5.2 Effects of MT network on RVFW elasticity and viscosity with disease progression at early diastolic strain

At the early diastolic strain level, we observed reduced elasticity and viscosity after MT removal in both directions and for both groups. This indicates that the MT network is an important component conferring the viscoelastic behavior of the tissue. Besides, we observed other interesting findings when comparing the reductions between directions and between groups. Firstly, we noted that in the healthy RVs, the reduction of viscosity was equivalent between directions (~43%), while the decrease in elasticity was stronger in the longitudinal direction (~34%) compared to the circumferential direction (~18%) (**Fig. 2.10A-C**). This suggests that the contribution of MT is isotropic for tissue viscosity but anisotropic for tissue elasticity. However, in the diseased RVs, the drops in viscosity (59%) and elasticity (24%) were both greater in the circumferential than longitudinal (30% and 5% for viscosity and elasticity, respectively) directions (**Fig. 2.10D-F**). Thus, the contribution of MT is anisotropic for both mechanical properties, and this indicates an altered MT microstructure or organization in the diseased RV, as reported by Prins et al [115]. In healthy cardiomyocytes, the MT network forms an orthogonal grid, where the cytoskeletons are predominantly aligned along the axis of the cell with interspersed transverse structures that run perpendicular to the cell axis [117]. With PH progression, though, the cardiomyocytes have a preferred alignment along the outflow tract (longitudinal) direction [6], [8], [23], and the MT network density is increased and less organized [115]. The disorganization of the MT network may lead to a failure of the cytoskeletons to keep aligned with the axis of the cell as in healthy state, and the transverse MT component becomes more prominent in the diseased RVs. Therefore, the greater reduction of viscosity and elasticity occurred in the circumferential direction after the MT depolymerization in these tissues. It should be acknowledged, too, that the alignment behavior of titin – a large sarcomeric protein – is altered with disease progression [23], [118] and may be adversely affected by the breakdown of the MT network. We cannot rule out this secondary effect of MT removal, which awaits further investigations. Overall, despite the same trend (reduction) found in healthy and diseased RVs after MT depolymerization, the accumulation and altered microstructure of MT network have resulted in distinct impacts on RVFW mechanics with disease progression.

5.3 Effects of MT network on RVFW elasticity and viscosity with disease progression at end diastolic strain

We have shown that the removal of MT network significantly reduced healthy and diseased RVFW elasticity and viscosity at the early diastolic strain level (**Fig. 2.10**), which is consistent with the results of isolated cardiomyocytes [29], [44], [105]. However, when examining the effects of MT network at the end diastolic strain level, the healthy and diseased RVFW exhibited different responses: the removal of MT network reduced viscosity and elasticity in healthy RVs, but it only reduced the circumferential viscosity and the ratio of viscosity to elasticity in diseased RVs. (**Fig. 2.11**).

When the mechanical characterization is mainly performed for cardiomyocytes (at cell or fiber levels), the behavior is mainly attributed to the cellular components such as MT or titin. However, when the mechanical characterization is performed at the tissue level, the deformation will incorporate other non-cellular components (especially at large strains) and the overall behavior is a combined contribution of all tissue components. It must be considered, at the higher strain level, that collagen is recruited and playing a more dominant role in myocardial mechanics [6], [69]. Therefore, we investigated the effects of MT at both 6% and 15% strains in this study to minimize (at 6%) and maximize (at 15%) the contribution of collagen fibers in the tissue behavior. Not surprisingly, we observed different effects of MT network at early (6%) and end (15%) diastolic strain levels. As we found and discussed above for the results at early diastolic strain, in the healthy RV, the axial MT may contribute more to the elasticity and viscosity than the transverse MT, resulting in a stronger role of the MT in the longitudinal direction. A similar effect of MT remains evident in the healthy RV even after collagen recruitment (**Fig. 2.11**). But the effects of MT on diseased RVs at the large strain were different than those at small strain. The viscoelasticity in the longitudinal direction was totally unchanged in these RVs, indicating a non-significant role of MT after collagen accumulation (due to PH) and recruitment (due to large strain). There were still some effects of MT in the circumferential viscosity and the V/E ratio (**Fig. 2.11E&F**), though. We speculate that this may be related to the increased transverse MT component (as discussed above) in the diseased RVs as well as the intrinsically larger

viscosity in MT network than collagen fibers. Nevertheless, the results suggest that the contribution of MT to tissue viscosity is significant, even after the collagen recruitment. As prior cell studies have shown an increased contractile function of cardiomyocytes with reduced cell viscoelasticity [30], the role of tissue viscosity should not be ignored in ventricular performance and new therapies may consider targeting on MT polymerization in RV failure patients [117].

5.4 QLV modeling shows the role of MT in RV relaxation strength in disease progression is strain-dependent

Besides our novel findings from the experimental data, the computational work provides further insights into the role of the MT network in the relaxation behavior of the RVFW. As established in our prior work [28], we used three terms of relaxation coefficients (G_n) to capture the relaxation strength of the RV. We observed that the removal of MT network significantly reduces RV relaxation strength (viscosity) at the late time point (G_3) in both healthy and diseased RVs and at both strain levels (**Fig. 2.12**). These results not only demonstrate a strong contribution of the MT to the RV tissue viscosity in both directions, but also delineate the specific time scale of its contribution. Unfortunately, although the Fung's QLV theory has been applied to various biological and non-biological materials, to our knowledge, how the G_n is correlated to specific component (e.g., MT, collagen) or microstructure (e.g., size of fiber, bonds) of a material remain largely unknown. Nordsletten et al. has proposed that the hierarchical structure of the extracellular matrix (mainly collagen) is responsible for the molecular mechanism of relaxation at different time scales– from fibrils, to fibers, to bundles to sheets – in human myocardium [63]. Our results suggest that MT is responsible for the G_3 in both healthy and diseased RVs. We did observe some changes in G_2 in the diseased RV as well. For instance, the longitudinal G_2 at small strain and the circumferential G_2 at large strain were reduced after MT removal. We do not exactly know the reason for these changes, and future study may investigate the microstructure and proliferation of MT under pressure overload to reveal the molecular mechanism.

6. Conclusions

This is the first study to investigate the role of the microtubules to the viscoelasticity of the RVFW in pulmonary hypertension progression. We originally showed that PH increases RVFW viscoelasticity at sub-

and physiological stretch rates and at early and diastolic strain levels. The stretch-rate dependent behavior of the RVFW is altered with disease progression, while the strain-dependent behavior is not. The removal of the MT network weakens healthy and diseased RVFW viscoelasticity at the early diastolic strain level, with a stronger reduction in viscosity than elasticity. Finally, at the end diastolic strain level, the removal of the MT network only reduces longitudinal viscoelasticity of the healthy RVFW and the circumferential viscosity of the diseased RVFW. Our results suggest distinct cytoskeletal roles in the mechanical behavior of the RVFW with disease progression. These findings will deepen our understanding of the microstructural contributions to myocardial mechanics.

CHAPTER 3 - Explore the impact of RV viscoelasticity on organ function

Aim 3a: Investigate the effect of reduced RV viscoelasticity on *in vivo* function.[5]

1. Background

Heart failure (HF) is the leading cause of death in the US and worldwide [114], and ventricular dysfunction is a primary contributor to HF. More specifically, right ventricular (RV) failure contributes significantly to the mortality and morbidity of multiple cardiovascular diseases. Including congenital heart disease, left ventricular failure with preserved ejection fraction, and pulmonary hypertension (PH). Unfortunately, there is still a lack of treatment options for such patients due in large part to the poor understanding of the physiology and pathology of RV failure. The mechanical behavior of RV tissue is known to contribute and significantly impact organ function. For example, Jang et al. found in a rodent study a significant correlation between RV passive stiffness and end-diastolic elastance [6]. Additionally, our own ovine study showed a positive correlation between RV elasticity and hemodynamics [7]. While these findings support the impact of RV elastic behavior on performance, the RV is viscoelastic. This implies that both elastic and viscous resistances are present during deformation. Thus, there is an incomplete understanding of the implication of RV mechanics to organ function.

There is increasing evidence of myocardial viscoelasticity in both the left and right ventricle (LV, RV), in neonatal porcine [16], human [30], [47], [48], ovine [28], [43], and rodent [40], [59], [119], [120] myocardium. The RV free wall (RVFW) is a complex, mesh-like tissue comprised of myofibers, collagen, vasculature, and other extracellular matrix (ECM) components, all of which contribute to the viscoelastic, anisotropic behavior of the tissue. Our own group observed a significant reduction in healthy and pressure-overloaded RV viscosity and elasticity after acute MT depolymerization [40], [59]. In these *ex vivo* studies, the decrease in viscosity was greater than that of elasticity, indicating distinct molecular mechanisms of

[5] (Sections adapted from "Distinct right ventricular performance in response to reduced viscoelasticity via microtubule depolymerization in healthy and diseased states" – In progress)

these mechanical properties. Moreover, the reduction in viscoelasticity was stronger in the pressure-overloaded than healthy tissue, probably due to denser MT network with RV remodeling. While these findings indicate a significant contribution to RV mechanical behavior, we only measured the passive mechanics, and the role of the MT in RV contractile function is not understood. Recently, Caporizzo et al. found that the depolymerization of the microtubule (MT) network, a cytoskeletal structure of the cardiomyocyte (CM), reduces cell viscoelasticity as well enhances shortening velocity in the healthy and failing LVs [30], [48], indicating a cytoskeletal role in cell mechanics and contractile function. Additionally, in the LV, Hancock et al. and Pietsch et al. have investigated the contribution of MT polymerization and tyrosination on organ function. It was found that depolymerizing the MT network via colchicine increases the myofiber work loop of the healthy LV [60], suggesting a cytoskeletal role in organ function. Moreover, in a mouse model of hypertrophic cardiomyopathy, Pietsch et al. detyrosinated the MT network and observed increased stroke volume and improved LV function with disease progression [61], indicating a potential therapeutic role of the MT network and its contribution to LV performance. However, the impact of RV viscoelasticity on RV function via MT deposition remains unknown.

2. Goal and hypothesis of my research

Therefore, the aim of this study is to **investigate the response of RV performance to reduced viscoelasticity via MT depolymerization.** We induced PH in adult rats and measured the *in vivo* pressure-volume relation of the RV before and after colchicine injections. The acute treatment has been demonstrated to reduce tissue viscoelasticity in our prior *ex vivo* studies, and we expect minimal biological effect of MT depolymerization in the RV due to the brief period. Thus, MT removal and viscoelasticity reduction are exchangeable in this study when referring to the drug effect. We originally found that reduced myocardial viscoelasticity improved ventricular function of the diseased RVs, while the healthy RVs' performance was negligibly affected. The findings deepen our understanding of the role of RV mechanics in pathophysiology and suggest the MT network as a potential therapeutic target for RV failure patients.

3. Methods

3.1 Animal model

All animal procedures were approved by the Colorado State University Institutional Animal Care and Use Committees (IACUC). 6-week-old male Sprague-Dawley (Charles River) rats (n=7) were administered a single subcutaneous injection (60 mg/kg) of monocrotaline (MCT) and housed in normal conditions for 3 weeks to induce PH. We followed the identical disease model protocol as described previously, in which we observed overt PH [119]. Healthy, age-matched rats (n=10) served as control (CTL).

3.2 In vivo assessment of right ventricular function

Animals were anesthetized via an intraperitoneal injection of urethane (1.2-1.5g/mL) and then were intubated. The chest was opened to expose the heart, and the RV was catheterized through the myocardium using a 1.9F admittance catheter (Transonic/Scisense). The stable pressure-volume (PV) relation was obtained and assessed by an RV end-systolic pressure between 30 and 40mmHg. After obtaining the stable PV relation (base), three intramyocardial injections of colchicine (0.3mM, 0.25mL total bolus [40], [59]) were administered along the long axis of the right ventricle. The PV relation (COL) was recorded within two minutes of drug treatment. A similar administration of saline was performed as the drug control.

Standard hemodynamic variables including heart rate (HR), RV end-systolic pressure (ESP), stroke volume (SV), stroke work (SW, estimated as the area within the PV loop), ejection fraction (EF), cardiac output (CO), end-systolic and end-diastolic volumes (ESV, EDV), chamber compliance (defined as $\Delta V/\Delta P$), end-diastolic pressure volume relation (EDPVR), pulmonary vascular resistance (PVR, estimated as ESP/CO), and effective arterial elastance (E_a) were exported directly using LabChart (AD Instruments, version 8) or calculated after data collection. Additionally, we derived contractile metrics such as the maximum rate of change of pressure (dP/dt max), and the end-systolic pressure-volume relation (ESPVR, derived using the single beat method [121]). Finally, the RV-pulmonary vascular interaction was evaluated by ventricular-vascular coupling, determined by the ratio of E_{es} to E_a [122].

3.3 Statistical analysis

We performed unpaired student t-tests to compare the healthy and diseased intact RV performance, and paired student t-tests to compare the performance of the RV before and after acute depolymerization of the MT in each group. Statistical analysis was performed using GraphPad Prism, version 10. Results are presented as mean ± SEM.

4. Results

4.1 Impaired RV function with PH progression

We first examined the PV relation of the healthy and pressure-overloaded RVs (**Fig. 3.1**). Overall, the PH RVs exhibited impaired organ function and overt RV failure. The RV ESP was significantly elevated, which is a hallmark of PH (**Fig. 3.2A**). Additionally, RV SV was significantly reduced (**Fig. 2B**), and the SW tended to decrease in the MCT animals (**Fig. 3.2C**, p=0.07). The dP/dt max was significantly enhanced, indicating a stronger contractile function (**Fig. 3.2E**). Finally, we observed a marked increase in RV EDPVR with PH progression (**Fig. 3.2F**), suggesting a stiffer myocardial wall. This result is consistent with our prior *ex vivo* mechanical studies using the same disease model [40], [119].

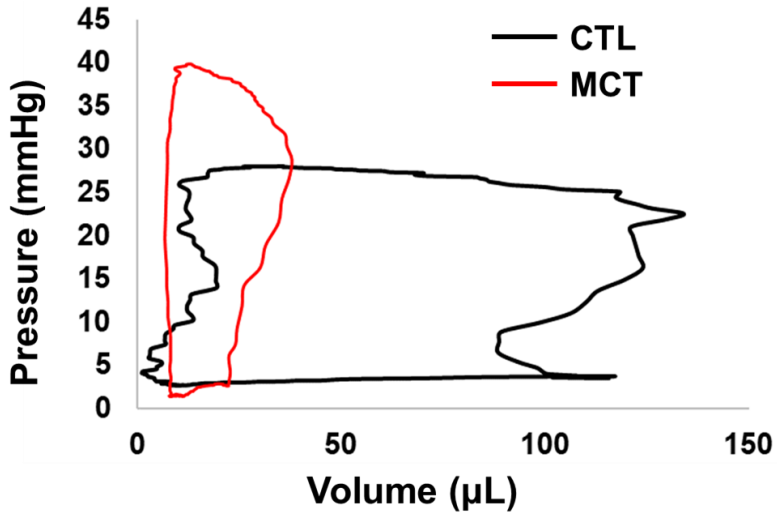

Figure 3.1. Healthy (CTL) and pressure-overloaded (MCT) RV pressure-volume relation.

4.2 MT depolymerization improves PH RV function, but does not affect healthy the RV

Next, we examined the effect of the MT removal on organ performance. In the healthy RV, reduced myocardial viscoelasticity did not impact the PV relation (**Fig. 3.3A**). However, the PH RV PV relation was markedly affected, with a notable change in end-systolic pressure and loop width (**Fig. 3.3B**). More specifically, after the treatment, we found that RV ESP was significantly reduced in diseased animals, with no effect on the healthy animal RV ESP (**Fig. 3.4A**). We observed in diseased RVs a significant increase in

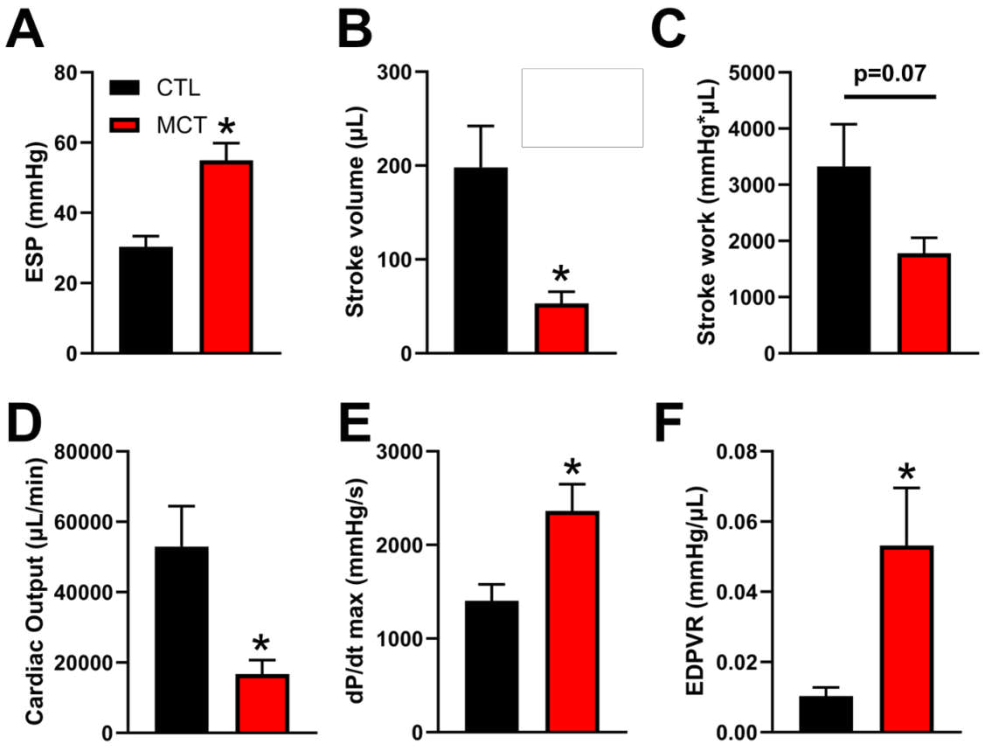

Figure 3.2. Healthy (CTL) and pressure-overloaded (MCT) RV end-systolic pressure (A), stroke volume (B), stroke work (C), cardiac output (D), dP/dt max (E), and EDPVR (F). * $p<0.05$ compared to CTL.

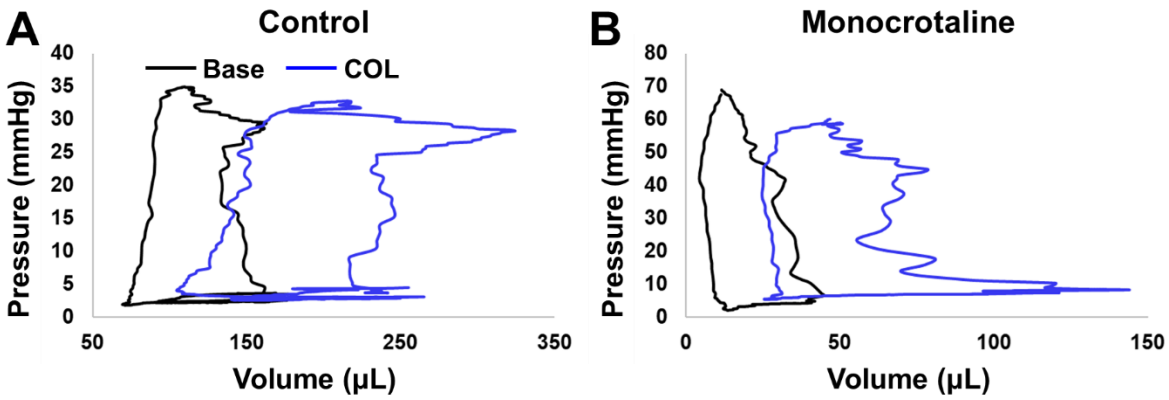

Figure 3.3. Healthy (A) and pressure-overloaded (B) RV pressure-volume relation before (base) and after MT depolymerization (COL).

SV (**Fig. 3.4B**), as well as CO (**Fig. 3.4C**), suggesting improved RV function after reduced viscoelasticity. Unexpectedly, RV contractility was weakened with a strong trend of decrease in ESPVR ($p=0.07$) and a significant reduction in dP/dt max (**Fig. 3.4D&E**) in this group, which may be a result of reduced afterload or demand of the ventricle Finally, the diseased RV showed reduced EDPVR after colchicine treatment, confirming a decrease in elasticity after MT depolymerization (**Fig. 3.4F**). In contrast, MT removal had no effects on these parameters in the healthy RVs. The RV PV relation was also measured before and after a

similar administration of saline in healthy RVs, and we did not observe a notable change after treatment (**Fig. 3.5**).

We further examined other hemodynamic parameters before and after colchicine treatment in the healthy and diseased RVs (**Table 3.1**). Overall, we observed similar trends of changes in these parameters between the healthy and diseased RVs. The changes were not significant in healthy RV but significant in the diseased RV. In the pressure-overloaded group, the end-systolic and end-diastolic volumes were increased,

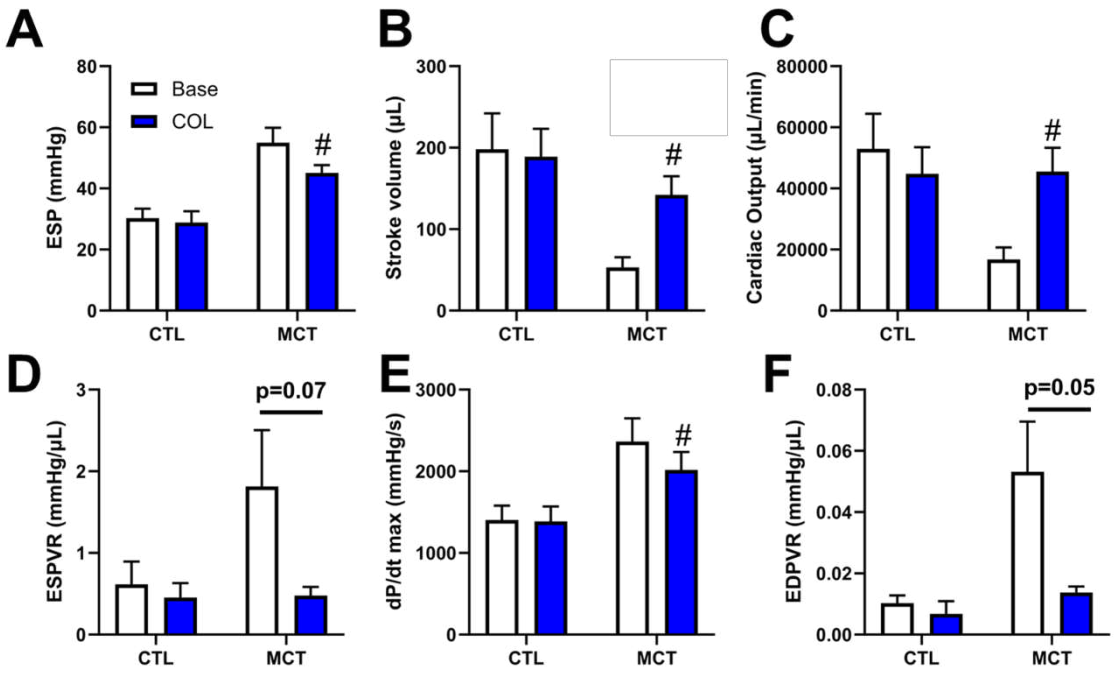

Figure 3.4. Healthy (CTL) and pressure-overloaded (MCT) RV end-systolic pressure (A), stroke volume (B), cardiac output (C), ESPVR (D), dP/dt max (E), and EDPVR (F) before (base) and after MT depolymerization (COL) # $p<0.05$ compared to base in the same group.

suggesting a dilated chamber after weakened viscoelasticity. Moreover, the SW and EF were significantly elevated, indicating improved RV performance with reduced viscoelastic resistance. RV compliance was

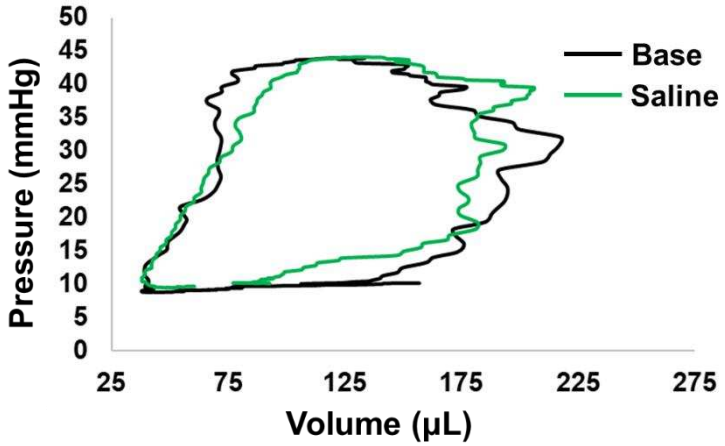

Figure 3.5. Healthy RV pressure-volume relation before (base) and after saline administration (saline).

markedly increased, suggesting a less stiff tissue as indicated by the change in EDPVR. Interestingly, the decrease in myocardial viscoelasticity caused a small but significant reduction in the heart rate.

Finally, we examined the effect of MT removal in the myocardium on the ventricular-vascular coupling. The RV afterload metrics, PVR and E_a, were significantly reduced in the diseased animals, indicating a weaker vascular opposition to the RV after decreased mechanical resistance. With both reductions in the ventricular and vascular elastances, the combined effect led to an overall increase in the ventricular-vascular coupling (E_{es}/E_a, p=0.08), and this effect was only observed in the diseased RV.

Table 3.1. Healthy (CTL) and pressure-overloaded (MCT) RV PV loop and hemodynamic parameters before (base) and after MT depolymerization (COL). #p<0.05 compared to baseline in same group.

	CTL			MCT		
PV Loop Parameter	**Base**	**COL**	**p-value**	**Base**	**COL**	**p-value**
ESV (µL)	131.1±34.3	151.5±39.6	0.16	42.17±12.1	90.4±27.9	0.05
EDV (µL)	329.2±70.7	340.4±65.5	0.80	95.24±23.1	232.6±44.2	#
EF (%)	61.6±4.3	56.2±5.3	0.32	60.3±5.8	67.4±5.6	#
SW (mmHg*µL)	3328±749	3094±404	0.75	1783±275	3717±436	#
HR (bpm)	290.4±26.3	259.9±28.7	0.19	329.8±31.7	320.0±31.3	#
RV compliance	9.27±2.59	9.61±2.22	0.85	1.06±0.28	3.71±0.64	#
PVR (mmHg*min/µL)	0.0008±0.0003	0.001±0.00003	0.25	0.004±0.001	0.001±0.00004	#
Ea (mmHg/µL)	0.26±0.11	0.26±0.1	0.98	1.01±0.23	0.21±0.03	#
Ees/Ea	2.24±0.44	2.39±0.55	0.31	2.39±0.43	3.44±0.8	0.08

5. Discussion

To our knowledge, this is the first study to investigate the role of the microtubule network in right ventricular physiology. In this study, we originally found that the reduction of myocardial viscoelasticity via MT depolymerization improves pressure-overloaded RV function with minimal effects on the performance of the healthy RV. Specifically, we observed enhanced stroke volume and ejection fraction after the removal of the MT network in the diseased RV, as well as reduced end-systolic pressure. In addition to alterations in ventricular performance, the removal of the MT network also impacted the vasculature, including a reduction in total pulmonary vascular resistance and effective arterial elastance. The findings from this study further our understanding of the role of myocardial mechanical behavior in RV pathophysiology and implicate the microtubule network as a potential therapeutic target for RV failure patients.

5.1 Removal of the MT network improves pressure-overloaded RV function

We firstly observed the establishment of RV failure secondary to PH. Stroke volume and stroke work were both markedly reduced with elevated end-systolic pressure (**Fig. 3.2**), which are the hallmark of RV failure [7], [119], [123]. Nevertheless, we observed non-significant changes in the ejection fraction (**Table 3.1**). While all other hemodynamic parameters point to the establishment of overt RV failure, the maintained ejection fraction suggests some common pathology as in the heart failure with preserved ejection fraction (HFpEF).

After MT depolymerization, SV and EF were both increased (**Fig. 3.4A&B**), indicating an improvement in RV function, although the treatment did not return the SV to the healthy level. Pietsch et al. recently measured the PV relation of the LV before and after the detyrosination the MT network in a mouse model of dilated cardiomyopathy [61]. They observed an increase in stroke volume and concluded that the acute removal of the MT network improved LV function. There was no report of changes in EF in this study. Therefore, it is consistently found that the removal of MT in hypertrophied ventricles (left or right) has beneficial effect on the systolic function.

We have reported previously that the acute removal of the MT network reduced both mechanical properties in the healthy and pressure-overloaded RVs in *ex vivo* studies [40], [59]. In the present work, we found reduced EDPVR (**Fig. 3.4F**) and increased RV compliance (**Table 3.1**) in the diseased RVs after acute MT

removal *in vivo* using the same dose as in our *ex vivo* studies, confirming a decreased ventricular stiffness. In the healthy RVs, the EDPVR showed the same but non-significant trend of changes as in diseased RVs. We attribute the less significant changes from the *in vivo* mechanical measurements to normal MT content in the healthy ventricles. In both hypertrophied LVs and RVs, the amount of MT is elevated, and denser MT network is evident [104], [115]. Thus, the drop in ventricular elasticity by MT removal is more significant in the diseased tissues.

The enhanced systolic function in diseased RVs may be partly explained by the Frank Starling mechanism. While the removal of MT weakened the mechanical resistance of the ventricle wall, the filling of the ventricle during diastole was improved, as evident by increased EDV. Thus, the SV was increased with a larger filing volume of the RV. Nevertheless, from the measurements of dP/dt max or ESPVR, we saw a decrease or trend of decrease, not increase, in the contractile properties after MT removal. The length-dependent activation (LDA) phenomenon at the cell level forms the basis of the Frank Starling mechanism, which is applied to the tissue level. However, LDA refers to the relation between the force during cell contraction and isometric cell length [124], whereas the Frank Starling mechanism refers to the relation between preload (length) and stroke volume. Thus, at the tissue level, preload may not directly translate to contractility. The increased stroke volume does not necessarily mean the strength of contractility is increased, which explains the discrepant trend between it and other metrics of contractility (dP/dt max, ESPVR). Moreover, diseased RV end-systolic pressure as well as dP/dt maximum were significantly decreased after reduced viscoelasticity. We hypothesize that the reduction in ESP is a result of reduced viscoelastic resistance, and the decreased pressure lowers the demand of the ventricle, causing a weaker dP/dt max. These trends could be attributed to a lowered HR, but whether heart rate leads to changes in ESP and dP/dt max or vice versa has yet to be elucidated.

5.2 Other effects of removal of the MT network

As we observed elevated SV in the diseased RV after colchicine, we also observed increased end-systolic and end-diastolic volumes with MT depolymerization (**Table 3.1**). Similar trends were observed in the healthy RVs as well, although the changes did not reach statistical significance. These findings indicate a

dilation of the chamber, and. we attribute these effects to the reduction in mechanical (elastic and viscous) resistance caused by MT depolymerization.

Interestingly, we observed a small but significant reduction in heart rate in the diseased RVs (**Table 3.1**). Various effects of colchicine on heart rate have been reported previously. An early cell study and preclinical study in rabbits have reported increased heart rate or ventricular fibrillation with colchicine treatment in a dose-dependent manner [125], [126], [127]. But the acute treatment of colchicine has also led to bradydysrhythmias with reduced heart rate [128].

There is growing evidence of microtubules' significant contribution to important functions of the nervous system [129], including providing structural support for axons and dendrites, serving as long-distance railways for proteins and organelles to be transported within axons and dendrites, and playing a role in the central nervous system by regulating cell migration [130]. The treatment of colchicine may not have only caused depolymerization of the MT network in the myocardium, but also in the neurons, impacting nervous system function. Reported neurotoxic effects of colchicine, though, occur at much higher (20x) doses than the prescribed dose in this study and, thus, we can rule out neurotoxicity of colchicine in this study [131], [132]. While MTs have not been directly linked to the behavior of the autonomic nervous system (ANS), their impact on axonal and dendritic function surely could affect the ANS (both para- and sympathetic) and lead to changes in HR. This hypothesis, though, awaits further investigation.

In addition to changes in ventricular performance, we also observed changes in vascular function of the diseased animals after MT depolymerization. Specifically, both pulmonary vascular resistance (PVR) and effective arterial elastance (E_a) were significantly reduced (**Table 3.1**). We suspect that the cause of the reductions may origin from the effect of colchicine on smooth muscle cells from the flush-out of the bolus. Endothelial MTs regulate centrifugal pull in the cell, which will ultimately regulate cell shape [133]. Ochoa et al. has previously found that microtubules in pulmonary endothelia exhibit cold-instable behavior, which means the MTs depolymerize (disassemble) upon cold exposure in the same manner as when they are exposed to colchicine [134]. The disassembly they observed greatly affected endothelial shape—elongated

shape to a round shape—which will confer altered vascular tone. The treatment of colchicine in the myocardium would lead to exposure of colchicine in the vasculature, too, thus reducing the vascular resistance. Similarly, Prins et al. observed a reduction in total pulmonary resistance after a 3-week treatment of colchicine [115]. Prins et al. attributed this response to the antimitotic effects of colchicine, and further observed enhanced ventricular-vascular coupling after the treatment. Of course, the weaker afterload supports our finding of reduced ESP and dP/dt max, as there is a lesser demand of the ventricle. This coupled behavior was exacerbated, too, after MT removal, as we observed a strong trend of increase in the ventricular-vascular coupling (VVC) parameter (**Table 3.1**).

5.3 Removal of the MT network impacts the diseased, not healthy RV

Our results show that the regulation of RV viscoelasticity via the MT network *in vivo* affects only the pressure-overloaded RV, and not the healthy RV. At the microstructural level, prior research has shown an increase in MT network density in PH RVs [115], as well as upregulated expression of the two subunits of the MT, α- and β-tubulin [104], [135], [136]. The conflicting response of the healthy and pressure-overloaded RV to MT depolymerization may be due to higher content of the MT in the diseased tissue. This is supported by previous *ex vivo* mechanical tests, too, which have shown a larger degree of change in diseased tissue mechanics after MT removal compared to the healthy RV [40]. Additionally, diseased RV tissue and LV myocardium has shown higher viscoelasticity compared to healthy tissue [27], [40], [48], [119], so we would expect a greater effect of MT removal in these tissues.

Considering only the mechanical behavior of the myocardium, prior *ex vivo* studies, including our own, have shown that the depolymerization of the MT network via colchicine significantly reduces the viscosity and elasticity of healthy myocardium, in both the LV and RV [27], [30], [48], [59], [60]. These studies, though, primarily focused on the independent changes of viscosity and elasticity, but not the relative change of the two parameters. We previously found that the ratio of viscosity to elasticity (V/E ratio) was unchanged in the healthy RV after MT removal via colchicine, suggesting a similar degree of reduction in the two mechanical properties [40]. However, in the diseased RV, the V/E ratio was significantly reduced after MT removal, suggesting that it is not individual elasticity or viscosity, but the V/E ratio, that is linked

to the organ function. Thus, it may be the interaction between and a varied contribution of the viscous and elastic response of the tissue that is dictating the role of mechanics in ventricular function. Moreover, as previous cell studies have shown, reduced viscosity and elasticity led to significant enhancements of cell contractility (extent of shortening and shortening velocity) [30], [48], [105], [107]. The individual impact of these two mechanical properties, though, on contractile function has not been studied. Thus, understanding how viscosity and elasticity each regulate ventricular function, though, awaits further investigation.

Limitations

There are a few limitations to our study. First, we induced a reduction of myocardial viscoelasticity via pharmaceutical interventions based on previous *ex vivo* studies. However, we are unable to measure viscoelasticity *in vivo* and only indirectly relate the removal of the MT network with reduced viscoelasticity. Additionally, the treatment of colchicine to remove the MT network was administered via intramyocardial injections. Thus, the washout of the drug would be quick. An improved approach would be to do an infusion of colchicine to induce prolonged treatment. Thirdly, we only included male subjects in this study. Prior studies have shown that estrogen has an 'anti-microtubule effect' and, thus, the *in vivo* response to colchicine in female subjects will likely be different than in males. It will be important to include both sexes in future work. Finally, because the washout of the drug was fast, we observed a short period of the drug effect in the PV relation. This resulted in an inability to perform a vena cava occlusion to derive the ESPVR from a series of loops. While this is a preferred metho, we were still able to measure this parameter using the single beat method.

6. Conclusions

To our knowledge, this is the first study to investigate the role of the MT network and myocardial viscoelasticity in RV pathophysiology. We originally found that the removal of the MT network led to significant improvements in RV performance, although these changes were only observed in the pressure-overloaded RV. Specifically, we measured increased SV, EF, and SW after MT removal, as well as reduced

ESP and dP/dt max. At the vascular level, we observed reduced pulmonary vascular resistance and effective arterial elastance. These novel findings indicate the significant role of myocardial viscoelasticity in RV performance and implicate the MT network as a potential therapeutic target for heart failure patients.

Aim 3b: Characterize the effect of RV viscoelasticity on organ function using multiscale constitutive modeling.

1. Overview - Multiscale biomechanics of the right ventricle: the relation of tissue structure, mechanics, and physiology[6]

Introduction

The right ventricle (RV) is historically an understudied organ compared to the left compartment of the heart. However, RV failure is prevalent in the US and worldwide and is a key contributor to the mortality of multiple cardiovascular diseases. During RV failure development, the tissue undergoes significant structural remodeling and mechanical changes, which lead to the alteration of overall organ function. Significant advancements have been achieved recently in the understanding of cell and tissue mechanical behavior, as well as RV function, using both experimental and computational approaches. This chapter aims to discuss the current methodologies and findings to expand our understanding of RV biomechanics and pathophysiology at multiple scales.

1.1 Classification of material mechanical behavior and mechanical type of right ventricles

1.1.1 Nonlinear elasticity

Elasticity describes the material's ability to deform and store energy under loadings. In other words, the applied forces are converted to mechanical energy and stored, and this energy can be fully released after the removal of external forces. Elasticity can be derived from the slope of the stress-strain curve. This is referred to as the elastic modulus or Young's modulus (**Fig. 3.6A**). There are two forms of elastic behavior: linear and nonlinear. A linear elastic material displays the same degree of elasticity regardless of the loading (stress) or deformation (strain) (**Fig. 3.6A**). In contrast, a nonlinear elastic material displays altered

[6] Section is adapted from "Multiscale biomechanics of the right ventricle: the relation of tissue structure, mechanics, and physiology" – in press

elasticity that depends on deformation (strain) (**Fig. 3.6B**). Like all biological tissues, the RV exhibits a nonlinear elastic behavior[6], [28], [57], [58].

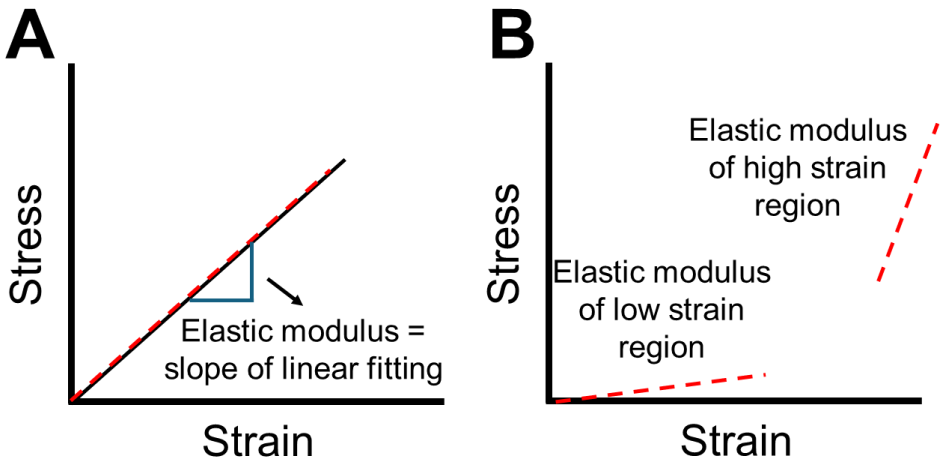

Figure 3.6. Stress-strain relations of a linear (A) and a nonlinear (B) elastic material.

1.1.2 Viscoelasticity

Viscoelasticity refers to the material's ability to store and dissipate energy under loadings. In other words, the applied forces cause both elastic and viscous resistances, and there is a certain loss of mechanical energy after the removal of external forces. The elastic resistance originates from the atomic bond energy of molecules and contributes to energy storage during deformation. On the other hand, viscous resistance originates from friction arising from the sliding of molecular bonds, and it contributes to the energy dissipation during deformation. The viscoelastic behavior can be evident or measured in three ways: creep (**Fig. 3.7A**), stress-relaxation (**Fig. 3.7B**), and the hysteresis loop during cyclic loadings (**Fig. 3.7C**).

Three forms of viscoelastic behavior exist: linear viscoelastic, quasilinear viscoelastic and fully nonlinear viscoelastic. A linear viscoelastic material exhibits a linear elastic response, as well as a linear time-dependent (viscous) response. In other words, both elasticity and viscosity are independent of strain or strain rate (**Fig. 3.8**). A quasilinear material exhibits a nonlinear elastic response but a linear viscous

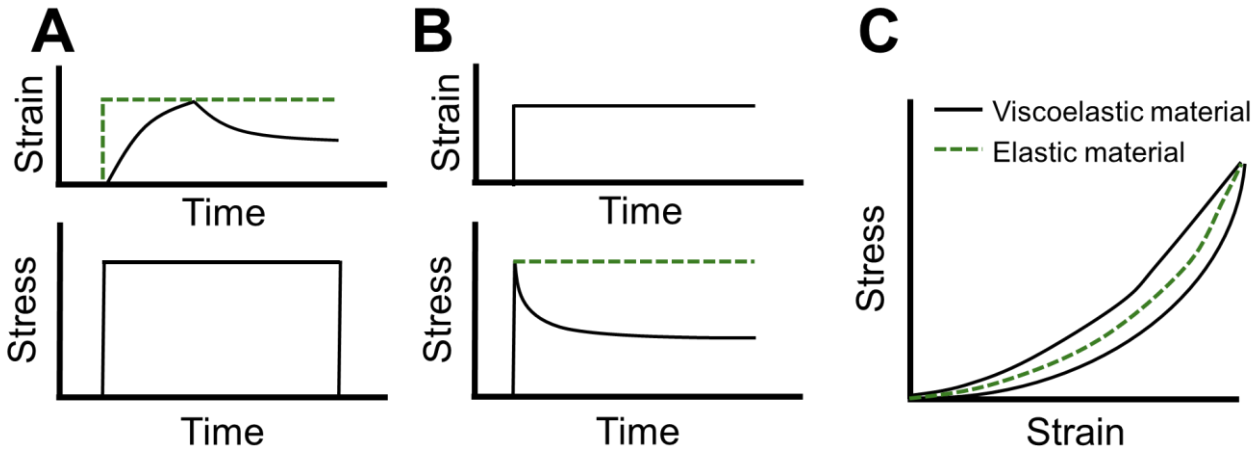

Figure 3.7. Creep (A), stress-relaxation (B), and cyclic loading (C) behavior of a viscoelastic (black solid line) material. The response of an elastic (green dash line) material is shown to illustrate the difference from the viscoelastic response.

response (**Fig. 3.9**). In the cases of both linear and quasilinear viscoelasticity, the elasticity and viscosity of the material are separable. In a fully nonlinear viscoelastic material, both the elastic and the viscous behaviors are nonlinear (strain- and strain-rate dependent) (**Fig. 3.10**). In this case, the viscosity and elasticity are non-separable (inter-dependent).

Fung developed the quasilinear viscoelastic theory in order to characterize the nonlinear stress-strain relationship of the tissue[137], and the formulation has been adopted in numerous studies of cardiac tissue mechanics[84], [138], [139]. Under a certain range of strains and strain rates, the RV tissue can be treated as a quasilinear viscoelastic material to characterize the mechanical behavior at a lower computational cost. Based on our recent studies on ovine hearts, however, the RV tissue exhibited nonlinear viscoelastic behavior in both longitudinal (apex-to-base axis) and circumferential directions[28].

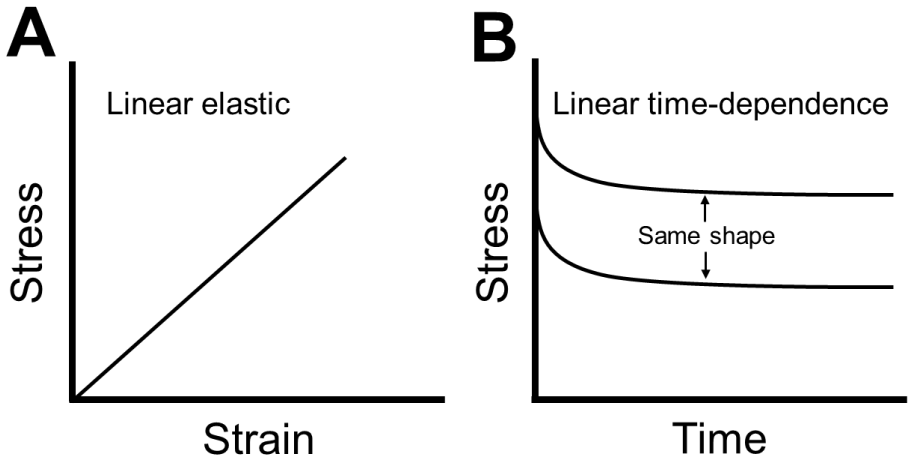

Figure 3.8 Stress-strain (A) and Stress relaxation (B) measurements of a linear viscoelastic material.

In myocardial tissues, elasticity and viscoelasticity are enhanced with elevated stretch rates[36], [59], [119], [140]. The strain-rate and strain dependency of RV tissue mechanics indicates the importance of measuring the tissue mechanical behavior under physiological conditions to capture the *in vivo* behavior. This means that in small animal hearts, a higher strain rate should be adopted than that of large animal hearts to mimic the higher heart rate. In most mechanical testing devices and/or protocols, the physiological strains can be readily achieved. However, the physiological strain-rates, as well as the data acquisition capability of the system, are not available to enable a physiological viscoelastic measurement in rodent hearts. This limit has impeded the complete understanding of the dynamic (viscoelastic) mechanical behavior of the RV[36].

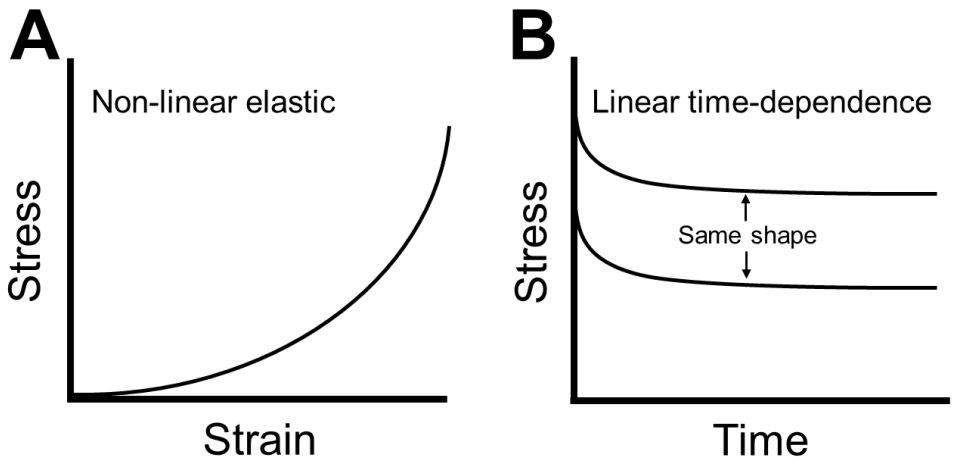

Figure 3.9 Stress-strain (A) and stress relaxation (B) measurements of a quasilinear viscoelastic material.

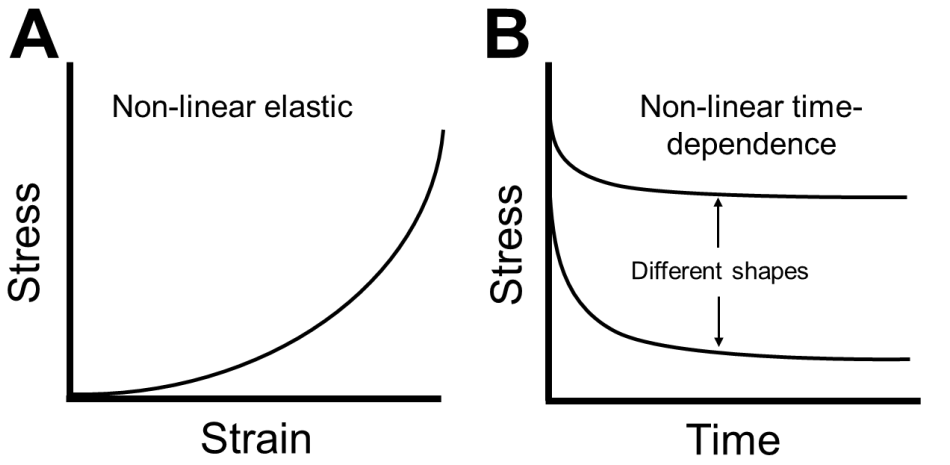

Figure 3.10. Stress-strain (A) and stress relaxation (B) measurements of a fully nonlinear viscoelastic material.

1.1.3 Isotropy and anisotropy

In an isotropic material, its mechanical properties are independent of direction. That is, the mechanical behavior is the same in all directions/orientations. On the other hand, an anisotropic material's mechanical properties depend on the direction/orientation. One needs to note that such classification is different than the definition of homogenous and heterogeneous materials, which refers to the uniformity of the material

properties throughout the volume. A homogenous material has the same mechanical behavior everywhere, whereas a heterogeneous material has different mechanical behaviors at distinct locations of the specimen.

The RV myocardium is anisotropic as a result of the amount and structural orientation of the tissue constituents, such as myo- and collagen fibers[23]. In general, the RV is treated as an orthotropic material, which is a subset of anisotropic materials. This means that its material properties are different in three perpendicular directions[47], [57], [62]. However, the RV is sometimes assumed and treated as a transversely anisotropic material for simplicity.

1.2 Mechanical assessments of RV at cell and tissue levels

Currently, RV mechanics have been investigated at various scales, ranging from isolated cardiomyocytes, trabeculae, papillary muscles and even the entire RV free wall. These methodologies have their own advantages and disadvantages. For instance, the loading of individual cells or papillary muscles can only be performed at one dimension, whereas the loading of RV free wall tissue can be performed at one (by uniaxial or indentation test), two (by biaxial tests) or three (by triaxial tests) dimensions. Thus, the latter measurements offer more comprehensive mechanical characterization of the myocardial wall. Alternatively, cell-level mechanics can be assessed in both active and passive states of the cardiac muscle, whereas tissue-level mechanics are mainly assessed in the passive state of the tissue. The active mechanical behavior (from the biomechanical engineering perspective) of myocardium is sometimes referred to as the contractile behavior or contractility of the muscle (from the physiology perspective). In this section, we will summarize current *ex vivo* mechanical testing methodologies at cellular and tissue levels.

1.2.1 *Ex vivo*, multi-axial mechanical tests

Cardiomyocytes (CM) are a major cell population of the myocardium and contribute significantly to the passive and active mechanical behaviors of the tissue. The CM consists of a cytoskeletal network, made up of the sarcomeric cytoskeleton such as actin, myosin and non-sarcomeric cytoskeleton such as titin, microtubules, and intermediate filaments[48]. These cytoskeletons are predominantly aligned axially in the

cell, with some transverse filaments interspersed[104]. Despite the 3D structure of the cell, only uniaxial (axial) cell mechanics are measured and reported. The RV free wall, however, is a complex tissue comprised of myofibers (CM), collagen, and other cells and extracellular matrix proteins, which contribute to the anisotropic mechanical behavior of the tissue. To date, uniaxial, biaxial and triaxial mechanical tests have all been reported for ventricular free wall tissues. Particularly, biaxial and triaxial mechanical tests provide more comprehensive measurements of the myocardium. Additionally, they better mimic the *in vivo* mechanical loading of the RV[6], [21], [23], [64], [141], [142], [143]. In such tests, a different degree of deformation or loading[47], [56], [144], [145] or the same degree of deformation or loading[7], [25], [39], [40], [43], [59], [91], [146], [147], [148] can be applied in each direction.

Because of the unique physiological motions (mainly planar deformation) and the thin wall of the RV, planar (biaxial) tests are often used to assess the anisotropic behavior of the tissue. Conventionally, the orientation of the tissue is defined by main-fiber and cross-fiber/sheet orientations of the heart[6], [23], [47], [57], [149]. But recent studies have oriented the tissue based on anatomic orientations. That is, the testing axes are defined by the apex to outflow-tract direction and the perpendicular direction[40], [43], [119], [147].

Biaxial and uniaxial mechanical tests apply normal tensile or compressive forces to the specimen and only planar deformation is induced in these tests. However, a few studies have suggested transmural changes in RV free wall microstructure and mechanical properties[57], [58]. To account for this, triaxial mechanical tests are performed to measure the shear and/or orthotropic properties of the tissue[47], [62], [150], [151]. These tests are more common for the left ventricle (LV). Some studies have used the combination of biaxial and shear tests to characterize the 3D mechanical behavior of the ventricle[14], [152].

1.2.2 Sample preparation

Multiple preparation steps must be taken to maintain the physiological behavior of cell or tissue samples. This includes harvest time and storage. Typically, fresh samples should be used (testing within several hours of harvest), and the sample is kept on ice prior to the test. To preserve cell viability, media such as Tyrode's

solution is used in isolated CM studies[30], [135], [153], and phosphate buffer or cardioplegic solutions are used in tissue studies[39], [135]. Moreover, to capture the passive behavior of the tissue, a relaxant solution is often used to break the actin-myosin cross-bridge in cardiac muscle cells, such as 2,3-butanedione monoxime[43], [56].

Before data acquisition, the samples should undergo a series of preconditioning cycles to achieve a stable mechanical response. This protocol was proposed and developed by Fung[137]. When the sample is excised, it moves from a loaded to an unloaded state, which may cause microstructural changes in the tissue and, consequently, affects the mechanical behavior. After it is mounted and reloaded for testing, the preconditioning cycles enable the tissue to re-adapt to reset the microstructural properties to those under *in vivo* loading conditions. A typical response to the preconditioning cycles is presented in **Fig. 3.11**. It often takes a few (~10-15) cycles of loading for the specimen to reach an equilibrium state.

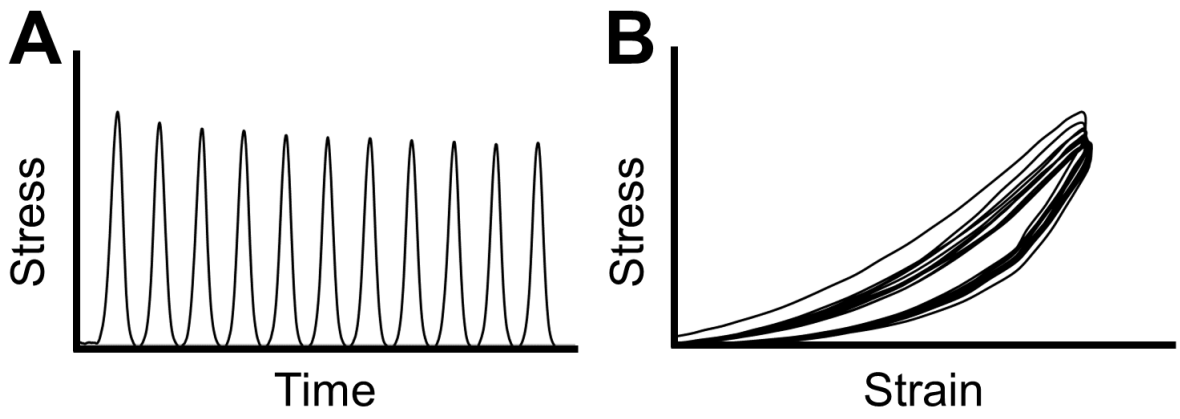

Figure 3.11. The stress-time (A) and stress-strain (B) curves obtained from preconditioning arise from viscoelastic behavior of the material.

1.2.3 Passive Mechanical Measurements

1.2.3.1 Cyclic tensile test

The cyclic tensile mechanical test is a common method to measure the passive, elastic behavior of CM[122], [154], [155] and free wall[7], [25], [39], [43], [91], [146], [147] of the RV. In isolated cell tests, the degree

of length extension is typically set by the resting (slack) and extended (tensioned) sarcomere length, for instance, from 1.4μm to 2.0μm, respectively[156]. In studies of RV free wall mechanics, the tissue is deformed to an *in vivo* strain level that is derived from medical images at end-systole and end-diastole. Thus, a range of 10-20% of strain is used depending on the animal species[23], [43], [57], [91], [147], [157].

Cyclic mechanical tests can also be used to measure the viscoelastic behavior of the cell or tissue. To derive the material elastic property, the elastic modulus or the stored energy is quantified from the hysteresis loop (**Fig. 3.7C**)[35], [36], [41], [43], [47]. The viscous property can be derived from various parameters, such as the loop width, loop area or dissipated energy[36], [48].

1.2.3.2 Nanoindentation test

Atomic force microscopy (AFM) indentation testing has been used for measuring cell[30], [158], [159], [160], [161], [162], [163], [164], [165], [166] and tissue [120], [167], [168], [169] mechanics. In such tests, a cantilever is actuated to push a nano-indenter to a certain depth, which deforms the cell. The material stiffness is derived as Young's modulus, using mathematical models such as the Hertz model[30], [170], [171], [172], [173]. The Young's modulus obtained using such tests is considered a tensile mechanical property, although the deformation is compressive. Another important assumption in AFM measurement is that the material is isotropic and homogeneous[174], which is not the case in cells or tissues. Moreover, the nanoindentation tests only provide the *local* (microscopic) mechanical behavior of the specimen, while the normal compressive or tensile mechanical test allows the experimentalist to obtain the *global* (macroscopic) mechanical behavior of the specimen. Thus, mechanical behaviors obtained from indentation tests are highly dependent on the spatial selection of the sample and may vary significantly from place to place in heterogenous materials. However, some groups have performed indentations at multiple locations in the RV tissue to obtain the mechanical behavior across the entirety of the material in an effort to overcome this limitation[120], [168].

AFM indentation can also be used to quantify the viscoelastic behavior of myocardium tissues. In these tests, the speed of compression is slow (0.6μm/s)[163], [167]. However, for viscoelastic materials such as ventricle walls, the mechanical behavior is dependent on the deformation rate, and it is appropriate to adopt the physiological stretch rates of the species to obtain physiologically relevant mechanical properties. To account for this, Caporizzo et al. applied a wide range of indentation speeds (0.1μm/s-150μm/s) and measured the elastic modulus of the cardiomyocyte at each speed. They found that the elastic modulus increased with increasing indentation speed, indicating a viscoelastic behavior of the cell (strain-rate dependent)[30]. Moreover, they attributed the low-speed indentation measures to a static (elastic) mechanical property, and the high-speed indentation measures to the dynamic (viscoelastic) mechanical behavior of the cell.

1.2.3.3 Stress relaxation

Finally, stress-relaxation is another mechanical testing method from which the viscoelastic mechanical properties of the material can be measured. In these tests, the material is quickly deformed to a specified length, and then held constant to observe the viscous decay (**Fig. 3.7B**)[28], [47], [48], [119], [164]. As in the cyclic mechanical tests, a physiological strain level is applied to the material to better mimic the *in vivo* mechanical behavior. However, the loading scheme applied in these tests is certainly not physiological as the material is held stretched for prolonged periods of time. From the stress-relaxation curve, relaxation modulus is derived as the stress at a given time divided by the applied strain[59], [119], [164]. Additionally, normalized stress is derived as the stress at a given time divided by the maximal stress and has been used previously as a metric of viscosity[43], [119]. As from the hysteresis loops, Liu et al. has derived stored and dissipated energies from the stress-relaxation curve as metrics of elasticity and viscosity, respectively[40], [59], [119]. In this method, elasticity is defined as the product of the input strain and the area beneath the raw stress-relaxation curve, and the dissipated energy as the product of the input strain and the area between the raw stress-relaxation curve and the theoretical purely elastic curve. We do not include studies/details of

creep tests in quantifying RV viscoelasticity. This is partly because the viscoelastic behavior of heart tissues is often negligible when quantified by such approaches.

1.2.4 Active Mechanical Measurements

In general, there are two techniques used to measure active force in isolated CM or cardiac muscles: the measurement of force under electrical stimulation[154], [175], and the measurement of force under altered calcium concentration[176]. Applying either stimulus, isometric contraction can be achieved at a fixed sarcomere length. Then, the length-dependent activation (Frank-Starling mechanism) of the cell can then be measured at varying sarcomere lengths. A more detailed review of cell active mechanics and organ function is provided here[177].

The measurement of active force in a larger scale of myocardium such as the entire free wall, though, is less established. When measuring the active behavior of myocardial tissue, though, many groups obtain these measurements in isolated papillary muscles, not integrated ventricular free walls[27], [178], [179], [180], [181]. However, Neelakantan et al. recently presented a method measuring the active mechanics of mouse left ventricular tissue[182]. LV free wall tissue was passively stretched up to 20% of strain and then submerged in an activation solution, in which the trabeculae or papillary muscles fully contract and the active force could be measured. Overall, the measurement of RV free wall active mechanics using *ex vivo* techniques is underdeveloped.

1.3. *In silico* models of myocardial mechanics

In silico models of cardiac mechanics at cellular or tissue levels are valuable tools for understanding the mechanical behavior and the structure-function relations of the material. Such models have constitutive relations based on physical elements or mathematical theory, and they can be used to model elastic or viscoelastic mechanical responses and passive or active mechanical behavior. In this section, we will provide a general picture of the modeling of myocardial (cellular and tissue) in passive and active states, with a focus on RV-relevant research and recent findings in RV viscoelastic modeling. For additional

reviews of *in silico* modeling in general biomechanics or ventricular biomechanics, please refer to the following references[183], [184].

1.3.1 Hyperelastic models

From cyclic mechanical tests, constitutive models have been used to fit the stress-strain curve to describe the elastic behavior of the RV. The traditional Fung-type model has been used extensively for the fitting of hyperelastic curves of the RV and other cardiovascular tissues[39], [56], [185], [186]. Studies have reported strong fitting capabilities of the Fung-type model, as well the ability of the model to capture the anisotropic behavior of the RV[56], [185], [187]. In this formulation, tissue elasticity is derived using the Fung exponential strain energy density function.

While the Fung-type model captures the anisotropic behavior of the tissue, it does not have the ability to distinguish the contributions of myo- and collagen fibers to the total elastic behavior. Thus, Avazmohammadi et al. incorporated the collagen and myofiber structure, including content and orientation, in a hyperelastic model of the RV[57], [58]. The model provided accurate fitting of the hyperelastic curve and elucidated distinct contributions of myo- and collagen fibers to the total elastic behavior of the RV. Additionally, this model attributed the low-strain elastic modulus to the contribution of myofibers, and the high strain elastic modulus to the contribution of collagen fibers, as described previously[6], [23]. Kakaletsis et al. implemented a similar approach in a modified Holzapfel model. The Holzapfel model incorporates tissue microstructural information (fiber orientation and dispersion). However, according to Kakaletsis et al., higher fidelity microstructural information in the Holzapfel model greatly improved its predictive capability[150]. While the fiber orientation is a principal factor to incorporate in a constitutive model to predict the elastic behavior of the anisotropic RV, Kakaletsis et al. also included the area fraction of myo- and collagen fibers, as well as the ground matrix to delineate the microstructural contributions to RV elasticity, as done recently by Li et al.[148].

1.3.2 Viscoelastic models

While tremendous efforts have been made and remain to be devoted in the hyperelastic modeling of the 3D, anisotropic composite material of myocardium, it is imperative to develop viscoelastic models at multiple scales and improve the understanding of the organ that is constantly under dynamic motions. The establishment of various viscoelastic models, including the phenomenological and constitutive models to describe the quasilinear viscoelastic (QLV) or fully nonlinear viscoelastic (NLV) behaviors, has been achieved in broad fields of materials science or biological tissues. Nevertheless, the application in myocardial cells or tissues, particularly in the context of the RV, has remained limited. Therefore, we will start our discussion with more simplistic approaches of viscoelastic modeling using the Maxwell and Kelvin-Voigt models and move to the more complex and robust QLV and NLV models.

1.3.2.1 Phenomenological models

A simplistic approach to describe the viscoelastic phenomenon of a material is to represent the elastic and viscous properties using spring and dashpot elements. Depending on the number of components and the relation between elastic and viscous components, the Maxwell and Kelvin-Voigt models have been used to model myocardial viscoelastic behavior. The Maxwell model simulates the material as a spring and dashpot in series, and the formulation for stress in the material is described as

$$\sigma_{total} = \eta\dot{\varepsilon} - \frac{\eta}{E}\dot{\sigma}, \qquad \text{Eq. 3.1}$$

where σ_{total} is the total stress in the material, η is the viscosity of the material, $\dot{\varepsilon}$ is the strain rate, E is the relaxation modulus (stiffness), and $\dot{\sigma}$ is rate of stress applied. In this model, the stress applied to the entire system is applied to both the spring and dashpot elements, but the total strain is the sum of the strain in the dashpot and in the spring elements. Unlike models of hyperelasticity, the elastic element is a *linear* spring, which is too simple in capturing the nonlinear elastic behavior of the RV.

The Kelvin-Voigt model simulates the material as a spring and dashpot in parallel, and the formulation for the total stress in the material is described as

$$\sigma_{total} = E\varepsilon + \eta\dot{\varepsilon}, \quad \text{Eq. 3.2}$$

where ε is the applied strain. In this model, the strain applied to the entire system is equivalent to the strain in the spring and dashpot elements, while the total stress is the sum of the stress of the spring and dashpot elements.

Many groups have combined the Kelvin Voigt and Maxwell models to improve accuracy of simulating the physical system. These models are referred to as standard linear solid (SLS) models. Such models have been used to describe stress relaxation or cyclic loading mechanical data in papillary muscles[27], [73] and ventricular tissue[62], [64], [120], [149], [188]. At the cell level, Caporizzo et al. modeled isolated CM stress relaxation and cyclic loading response as a combined Maxwell-Kelvin-Voigt model, with a spring and dashpot in parallel with a spring-dashpot series element[30]. Each element was related to a different portion of the loading regime: in stress relaxation, the individual dashpot element represented the ramp phase, the spring-dashpot series element represented the early relaxation phase, and the individual spring element represented the end-stage relaxation phase (equilibrium). Alternatively, in the cyclic loading regime, the individual spring element represents the low-strain-rate stiffness where viscous stress is negligible, the spring-dashpot series element represents the transition-strain-rate stiffness, and the dashpot element represents the high-strain-rate stiffness when viscous stress dominates the mechanical behavior. The rheological elements are added to better describe the physiological and rate-dependent response of the cell or tissue[183]. At the tissue level, Rubiano et al. has applied an SLS model to AFM indentation test data and predicted the viscous and elastic behavior of rodent myocardium[120]. Early uses of the Maxwell and Kelvin-Voigt models used linear elements, but the formulations have been improved by using nonlinear spring and dashpot elements to capture the nonlinear viscoelastic behavior of the myocardium[27], [74], [75], [189].

1.3.2.2 Quasilinear and nonlinear viscoelastic constitutive models

Unlike phenomenological models, constitutive models employ known physical and mathematical relations to formulate the governing equations. Depending on the type of viscoelasticity, various models have been used to predict the mechanical behavior of the myocardium. For a QLV material, the main governing equation is given as

$$\boldsymbol{S}(\boldsymbol{E},t) = \boldsymbol{S}_0 + \int_0^t \boldsymbol{G}(t-\tau)\frac{\partial \boldsymbol{S}^e}{\partial \boldsymbol{E}} : \frac{\partial \boldsymbol{E}(\tau)}{\partial \tau} d\tau, \quad \text{Eq. 3.3}$$

where **E** is the Green strain tensor, t is time, $\mathbf{S_0}$ is the initial stress obtained from the force in the zero-stress configuration, **G**(t) is the reduced relaxation function, $\mathbf{S^e}$ is the instantaneous elastic stress, and τ is a time variable of integration. Tissue viscosity is given by the reduced relaxation function, **G**(t), which is defined using a Prony series:

$$G(t) = G_\infty + \sum_{n=1}^{3} G_n e^{-t/\tau_n} \quad \text{Eq. 3.4}$$

In the QLV model, the sum of the relaxation constants, G_n, is sometimes constrained to be 1[28], [40], [59]. However, whether this constraint is necessary and whether varying numbers of G_n values can be used are unclear. The above Prony series was adopted because it provided optimal fitting to ovine and rat RV stress-relaxation experimental data. A similar approach has been applied to human myocardium tissues by Nordsletten et al.[149], but it is unclear whether the model would work well for the RV and the exact Prony series is not specified.

The traditional Fung-type QLV fitting scheme (Eq. 3), though, has offered strong fitting capabilities of stress-relaxation raw data of both ovine[28] and rodent[40], [59] RVFW tissue. Moreover, the QLV model elucidates further information regarding the viscous relaxation of the tissue that can be obtained via experimental approaches, such as the time-dependent relaxation strength at various time points. Liu et al. observed a stronger relaxation strength at late (30 seconds) rather than earlier (0.3 and 3) relaxation time points of the healthy ovine RV[28]. Alternatively, our own group observed equivalent relaxation strengths between the early (0.3 seconds) and late (30 seconds) relaxation time points of the healthy rodent RV[59].

As we introduced previously, the viscosity of a QLV material is independent of strain or strain history. Thus, the relaxation function (viscosity) and elastic stress (elasticity) are separated. However, this is not the case for nonlinear viscoelastic materials. The QLV formulation was unable to fit RV stress-relaxation raw data at multiple strain levels, suggesting a nonlinear viscoelastic response. Thus, to model a NLV material, the main governing equation becomes:

$$\boldsymbol{S}(\boldsymbol{E}(t),t) = \boldsymbol{S}_0 + \int_0^t \boldsymbol{M}(\boldsymbol{E}(\tau), t-\tau) : \frac{\partial \boldsymbol{E}(\tau)}{\partial \tau} d\tau, \quad \text{Eq. 3.5}$$

where **M** is the strain-dependent relaxation modulus. Due to the high computational cost, the first NLV model of the RV was developed with the assumptions of a step increase in strain (Heaviside function) and a power-law behavior in the relaxation modulus.

Liu et al. found that this NLV model had a higher capacity in predicting the stress-relaxation at multiple strain levels than the QLV model, thus, the NLV model formulation is better suited for describing RV viscoelasticity[28], [84]. This was the first study to treat the RV as a fully nonlinear viscoelastic material, and the study only investigated healthy ovine tissue. Future work should move towards the applications in other species or states and the use of a fully NLV model to capture the viscoelastic behavior of the RV.

1.3.2.3 Fractional viscoelastic models

Many of the viscoelastic models presented thus far consider the viscous and elastic components to be additive, which implies that the elasticity (spring) and viscosity (dashpot) are separate elements. But these models have their own disadvantages[190]. Recently, a new category of viscoelastic models (fractional viscoelastic models) has been developed to overcome these limitations. With the introduction of fractional calculus as a mathematical tool, it is possible to replace the convolution integrals used in a QLV modeling (see §3.2.2) with a Caputo derivative, with the assumption of isotropic, power-law behavior materials. The application of fractional derivatives to represent viscoelastic behavior was introduced by Suki et al. in a mechanical study of lung tissue[191]. The power-law assumption is mostly valid as it has been shown that

in a wide range of materials, including biological materials, the stress relaxation response follows a power-law signature, and this has been attributed to the complex microstructure of the material (please refer to the review of Bonfanti et al.[190]). As a result, the governing constitutive equation and the number of model parameters can be simplified or reduced[190]:

$$\sigma(t) = c_\beta \frac{d^\beta \varepsilon(t)}{dt^\beta} \quad \text{Eq. 3.6}$$

where c_β is a constant determined by the elastic and/or viscous properties and often interpreted as the 'firmness' of a material, and the fractional derivative is also called the Caputo derivative.

In the fractional viscoelastic model, a new spring-pot element (defined by the Caputo derivative) is introduced, in which the viscous and elastic components are not necessarily separate, additive components. This element can also be combined with spring or dashpot elements, and such models are referred to as generalized fractional viscoelastic models (see Table 1 in[190]). Depending on the power exponent β ($0 \leq \beta \leq < 1$), the fractional element (spring-pot) behaves as a spring (β=0) or a dashpot (β=1) and the stress in this element is derived using a Caputo derivative[183]. Recently, Nordsletten and colleagues have compared and evaluated over 4,000 viscoelastic models across different test conditions (uniaxial, biaxial, pure shear, simple shear, torsion tests with sinusoidal or sawtooth wave functions, as well as relaxation and creep tests)[149], [183]. Although all models are limited to isotropic materials, they found that different viscoelastic models should be chosen for different testing conditions, and the fractional Zener model is the most robust model for a wide range of tests and frequencies. To our knowledge, the use of fractional viscoelastic modeling on myocardial tissue is limited to the LV only[149]. It would be interesting to assess this model in describing the viscoelastic behavior of the RV.

1.3.3 Active cardiac mechanics models

At the subcellular and cellular levels, models incorporate myofilament mechanics, geometry, and interactions to capture the active mechanical behavior of isolated CM[177], such as the Huxley model[192]:

$$F(t) = k\sum_{-\infty}^{\infty} n(x,t)xdx \quad \text{Eq. 3.7}$$

where F is the contractile force, k is the stiffness of the actin-myosin cross-bridge, and the distribution function $n(x,t)$ describes the rate of connections between actin filaments and myosin heads[193]. Alternatively, Rice et al. developed a phenomenological model to predict CM activation and force generation using myofilament behaviors[194]. Using an experimental approach, they determined 8 key modulators of CM active mechanics, including steady-state force-sarcomere length relations, steady-state force-calcium relations, steady-state sarcomere length-calcium relations, as well as the effect of sarcomere length on the intracellular calcium transients. The model accurately fit the predictions of the well-established Hill model. Additionally, studies have incorporated calcium activation[195], as well as sarcomere dynamics, including calcium binding and length changes[196]. For example, Lumens et al. derived myofiber active mechanical stress using sarcomere length-dependent activation and the total active stress of the tissue[197]:

$$\sigma_{f,act} = \sigma_{act} C(L_{sc} - L_{sc0}) \frac{L_s - L_{sc}}{L_{se,iso}}, \quad \text{Eq. 3.8}$$

where σ_{act} is the total active stress in the tissue, C is the mechanical activation, L_{sc} is the contractile element length, L_{sc0} is the contractile element length with zero active stress, L_s is the sarcomere length, and $L_{se,iso}$ is the length of an isometrically stressed series elastic element. The time derivative of C is heuristically obtained, with separate terms describing the rise and decay of mechanical activation C:

$$\frac{dC}{dt} = \frac{1}{\tau_R} C_L(L_{sc}) F_{rise}(t) + \frac{1}{\tau_D} \frac{C_{rest} - C}{1 + e^{(T(L_{sc}) - t)/\tau_D}} \quad \text{Eq. 3.9}$$

where τ_R and τ_D are scaling rise and decay time parameters, respectively. Functions C_L, F_{rise}, and T refer to increase of activation with sarcomere length, rise of mechanical activation, and decrease of activation duration with decrease of sarcomere length, respectively. Finally, symbols t and C_L denote the time and diastolic resting level of activation, respectively.

All these above models have been validated by the cell-level experiments, and thus can be used to delineate the independent role of each factor (i.e., sarcomere length control) and to predict the active force at certain hypothetical conditions. However, except for the Hill model that incorporates the interactions of the muscle to extracellular component, the other models are microscopic models of muscle contraction and do not take extracellular factors into consideration. For instance, the interactions of the CM and extracellular matrix proteins, the orientation and network of fibrillar and non-fibrillar components in the ventricular wall, as well as the electrical conductivity of the tissue, all play a critical role to the overall contractive behavior of the tissue or entire organ. More importantly, the cell-level modeling is only 1D and does not have the capacity to capture the multi-dimensional feature of active constriction. As a result, the macroscopic active force at the tissue-level or organ-level is not well understood, and the total force or stress is a simple summation of passive and active mechanical force, mostly in a scaler format rather than a tensor format.

1.4. RV mechanics in physiology and pathophysiology

Heart failure (HF) is the leading cause of death in both the US and worldwide[114]. Ventricular dysfunction is the most common type of HF, including right-sided HF secondary to pulmonary hypertension (PH), heart failure with preserved ejection fraction (HFpEF) and congenital heart disease[198], [199], [200]. During HF failure development, significant cell and extracellular matrix (ECM) remodeling takes place, which contributes to overall changes in tissue mechanics and function. The initial remodeling occurs to compensate for altered hemodynamic loads (adaptive remodeling). However, in chronic disease, the tissue will reach a maladaptive remodeling state, and the structure and function of the cells and organ will be impaired. The mechanism of transitioning from an adaptive to a maladaptive state is not completely understood.

Historically, the RV was considered the ‘forgotten’ chamber, and the knowledge obtained from the LV is often considered true for the RV. However, the LV and RV are distinct in their physiology, pathology, and mechanical behavior. The systemic circulation operates in a high pressure, high resistance, and low compliance system, while the pulmonary circulation operates in a low pressure, low resistance, and high

compliance system[56]. Thus, the LV and RV experience drastically different hemodynamic loads. Furthermore, in the case of pressure overload, the RV experiences a significantly greater increase in afterload compared to the LV: 5-fold vs 1.5-fold, respectively[201], [202], [203]. At the cell level, the Ca2+ sensitivity and handling of CM are different between the LV and RV[204], and more discussions of CM function between these chambers can be found in[205], [206].

In addition, it has been shown that, unlike the LV, the passive mechanics of the RV are a key determinant of organ function[6], [7], as RV elasticity is closely correlated to the degree of RV failure and is associated with the prediction of systolic function[207], [208], [209]. Thus, it is imperative to investigate the RV biomechanics in disease development. The focus of this section is on the structural remodeling and alterations of tissue mechanics in RV failure progression. We will discuss biomechanical mechanisms of the RV at multiple scales (from molecules and cells to tissue and organ), which includes the alteration of RV mechanical properties and the implications in RV malfunction.

1.4.1 Intracellular components of the RV

The CM serves as the contractile machine of the myocardium. Microtubules, actin, and myosin are the three cytoskeletal filaments of CM, and the microtubules are the largest and stiffest of these three filaments[104]. Titin is a stiff, large sarcomeric protein, and is often viewed as the dominant protein determining cardiomyocyte stiffness. Thus, for the purposes of this review, we will focus on microtubules and titin.

1.4.1.1 Microtubules

1.4.1.1.1 Structure and assembly

Microtubules are comprised of two subunits: α- and β-tubulin, and the assembly and disassembly of microtubules are extremely dynamic, with a turnover of α- and β-tubulin that is dependent on the degree and rate of stretch[210]. Without loading, the microtubules grow at a rate of 0.2-0.4μm/s, with a much higher shrinking rate[211]. Individual microtubules with crosslinkers interspersed between them form what

is called the microtubule network. Under stretch, the crosslinkers engage, which causes the microtubules to become more aligned and induces a nonlinear stiffening behavior of the microtubule network in the cell[104]. Additionally, there are two processes that will alter its structure and mechanics: polymerization and tyrosination. These processes are heavily determined by temperature, rate of stretch, and can be altered via pharmaceutical treatment[30], [48], [104], [106], [212], [213].

1.4.1.1.2 Changes in RV failure progression

In the pressure-overloaded RV, microtubule density is increased in the hypertrophied CM, with elevated expressions in both α- and β-tubulin[104], [115], [135], [136]. Furthermore, during heart failure progression, microtubule network stability is weakened[214], [215]. It has been observed, too, that the microtubule network becomes disorganized in pressure-overloaded RV[115], and there is an upregulation of genetic expression associated with abnormal microtubule assembly[216], [217]. In addition, the accumulation of microtubules in PH patients are not the same between males and females. Xiong et al. reported significant elevations of α- and β-tubulin with PH in male rat RVs, while no significant change in α- and β-tubulin expression or microtubule polymerization was observed in female rat RVs[218].

1.4.1.1.3 Role in RV mechanics

Cooper and his colleagues have reported significant impact of MT removal on CM in the contractile function of CM or papillary muscles from healthy and pressure-overloaded LVs and RVs[29], [105], [107]. But the mechanics of the cells or muscles have not been quantified. This is the first evidence that suggests a linkage between cell mechanics and function, but the translation at the tissue level is unknown. Caporizzo et al. observed that depolymerization of the microtubule network via colchicine treatment reduced cardiomyocyte viscoelasticity and enhanced the extent of shortening[30], [48], which indicates the impact of microtubule on cell mechanics and contractile function. But this behavior was only observed in human CM from healthy and failing LVs. Recently, we applied a similar approach at the tissue level by exposing healthy and pressure-overloaded RV samples to colchicine treatment. In the healthy RV, we observed

significant reductions in tissue viscosity and elasticity (from stress-relaxation) in both longitudinal (outflow tract) and circumferential directions after depolymerization of the microtubules[59]. Moreover, the impact was different at different strains and directions of the tissue. First, these changes were more substantial at lower level of strain that corresponds to the early diastolic phase, where myofibers (CM) dominate RV mechanical behavior[6], [58]. Second, the reductions were stronger in the longitudinal than circumferential direction, indicating an anisotropic impact of microtubules. In the pressure-overloaded RV, we observed similar but stronger effects of colchicine than in healthy RVs[40]. The degree of reduction in elasticity and viscosity were not equivalent, though, as the ratio of viscosity to elasticity was significantly decreased. These findings indicate distinct molecular mechanisms of RV viscoelasticity.

1.4.1.2 Titin

1.4.1.2.1 Structure and assembly

Titin is a stiff, large sarcomeric protein, with its Z disk connected to the M-band region of the sarcomere[219], [220]. Titin is comprised of multiple segments along its structure, each acting as a distinct spring element[221]. There are multiple isoforms of titin, with two main titin isoforms expressed in cardiac muscle: N2A and N2BA[222]. N2A is the stiff isoform, and N2BA is the compliant isoform of titin[223], [224]. Like microtubules, titin's structure and mechanical property are heavily influenced by mechanical load. When the cell is stretched to a sarcomere length greater than 2.1μm, the Z-disk and the myofilaments become more aligned and increase the stiffness of titin and, therefore, the entire cell[212], [225], [226].

1.4.1.2.2 Changes in RV failure progression

Titin undergoes significant remodeling with RV failure progression. Rain et al. reported reduced titin phosphorylation in rats with mild RV dysfunction, but the reduction was not significant in rats with severe RV dysfunction[223]. However, they did not find marked change in the total expression of titin. Moreover, multiple studies have observed a shift in titin isoform expression, with alterations in the N2BA/N2Aratio[223], [224], [227], [228], [229], [230], [231], [232]. These changes are dependent on the

severity of disease, as well as pathology. For example, in PH, the N2BA/N2A ratio is increased in the RV, suggesting a more compliant muscle in the chamber wall[223], [224], whereas in dilated cardiomyopathy and tachycardia, the ratio is reduced, suggesting a shift to a stiffer muscle[227], [228], [229]. Interestingly, though, in end-stage dilated cardiomyopathy, an increase in the N2BA/N2A ratio has been reported[230], [231], [232]. While the increase in N2BA/N2A ratio is viewed as a compensatory mechanism, significant myofiber stiffening is still observed in severe RV dysfunction[223], which may be due to other molecular mechanisms. Thus, the alteration in titin is unlikely to account for the increase in RVFW stiffness.

1.4.1.2.3 Role in RV mechanics

In isolated muscle fiber bundles from the LV, Loescher et al. cleaved titin via HaloTag-Tobacco Etch Virus protease and observed marked elastic *and* viscous force reductions at multiple strain levels (5%-25%)[233]. The contribution of titin was more marked at a higher strain level, with an approximate 73% reduction in elastic force at 10% of strain. After the breakdown of titin via KCl/KI, Granzier et al. observed a 70% reduction in passive tension, and this response was stronger with a higher sarcomere slack length[234]. Interestingly, there was no difference in the response of the trabeculae from the LV or RV. Moreover, Rain et al. investigated the role of titin phosphorylation on myocardial stiffness in the pressure-overloaded RV[223]. In the muscle with phosphorylated titin, myocardial stiffness was significantly reduced in both moderate and severe RV dysfunction samples. Similarly, in skinned rat RV muscles, Fukuda et al. observed a decrease in magnitude of peak force (elasticity) and a weakened stress-relaxation response (viscosity) after titin phosphorylation[235]. Although it is unclear how phosphorylation alters the cellular structure and then mechanics, these studies suggest a significant role of titin in RV myocardial mechanics. Unfortunately, the contribution of titin to the tissue-level mechanical behavior of the RV has not yet been elucidated.

1.4.2 Extracellular components of the RV

Collagen and fibronectin are two of the most predominant ECM proteins in the ventricular free wall[236]. The content of these two proteins is heavily influenced by mechanical load[237], [238], [239]. This

regulation occurs via the mechanosensing cardiac fibroblast, which is responsible for the increased synthesis of collagen and fibronectin under elevated loading environment[55], [236], [240]. Due to the lack of data in the role of fibronectin in RV mechanics, we will mainly discuss the findings related to collagen in this section.

1.4.2.1 Structure and assembly

Collagen is the most prevalent structural ECM protein in the RV. It is formed from the base unit called tropocollagen[241]. Tropocollagens twist together, making a triple helix structure, which forms the procollagen fibril. Procollagen fibrils then crosslink to form mature collagen fibers, bundles, or sheets. [148]. To date, over 25 types of collagen have been reported in biological tissues, and type I and type III collagen are the most predominant type in the heart to display a unique structure and mechanical behavior[242].

1.4.2.2 Changes in RV failure progression

In pressure-overloaded RVs, elevated collagen content (fibrosis) is reported in small and large animal models, as well as in early- and late-stage RV failure[53], [204], [243], [244]. Both Bogaard et al. as well as Borgdorff et al. have reported a marked fibrotic response of RVs in experimental models of PH[245], [246]. It is not well understood, though, whether certain collagen subtypes are more upregulated in diseased states than others. Golob et al. reported that, in a mouse model of PH (Sugen + hypoxia), the ratio of collagen type I to collagen type III was increased, and this alteration was primarily contributed by type I collagen[53]. Rain et al. observed the same trend in a rat model of PH (pulmonary arterial banding)[223].

In addition to collagen deposition, alterations in collagen morphology and alignment have also been reported in diseased RVs. Rain et al. observed increased collagen cross-linking in the RVs four weeks after PH development, and this increase was correlated with elevated diastolic pressures[223]. But the crosslinking formation may not form in early remodeling as Baicu et al. did not observe a change in insoluble collagen expression or diastolic pressures two weeks post pulmonary arterial banding[247].

However, collagen content was elevated, suggesting new collagen fibers were deposited but not yet cross-linked at this time point. These results further suggest that the increased diastolic pressure is associated with collagen cross-linking, not content. It is speculated that the increased cross-linking stiffens the RV myocardium and prevents overstretch of the tissue, which leads to a fatal pathological condition[248].

Finally, alterations in myofiber and collagen alignment in the RV have been reported in PH development. Fibers have been found to become more aligned (organized), and their preferred direction is altered toward the long axis (apex-to-outflow tract direction) in several rodent studies, including our own work[23], [57], [58]. Interestingly, though, there is no significant change in fiber orientation in an ovine model of RV failure secondary to PH[249], with a preferred alignment of 60º in the healthy ovine RV. Park et al., though, observed significant fiber orientation change in pressure-overloaded rat RVs at both the endocardial and epicardial side of the free wall[250]. Moreover, the transmural change in the fiber orientation of the pressure-overloaded RV was significantly smaller than that of the healthy RV, suggesting a small transmural fiber orientation distribution with PH progression. It has also been shown that RV collagen fiber preferred orientation moves towards the circumferential direction during growth and development[251], [252], although these measurements were performed only in porcine RV samples. Whether the collagen fiber orientation of human RV changes with growth and disease progression is unknown.

1.4.2.3 Role in RV mechanics

In the pressure-overloaded rat RV, Hill et al. reported no change in individual collagen fiber stiffness with PH progression, which was quantified using a constitutive model[23]. Hence, their findings suggest that it is the remodeling of collagen structure and morphology, not the intrinsic mechanical properties of the protein that contributes to the changes in mechanical behavior in PH development. In general, fibrillar (type I) collagen is more dominant in high strain regions, as it recruits during deformation. In an ovine model of PH, Liu et al. reported that type III collagen, not myofiber hypertrophy, is strongly correlated with the longitudinal low-strain elastic modulus of the RV, whereas the total collagen content is correlated with the high-strain elastic modulus[56]. We speculate the discrepant contributions between low and high strain

regions are most likely influenced by the different recruitment and mechanical behaviors of type I and III collagen. Fibrillar type I collagen is stiffer compared to the non-fibrillar, mesh-like type III collagen[253]. Typically, the collagen fibers are thought to be recruited at larger strains and thus contribute to the nonlinear elastic behavior of the RV. The findings in the ovine PH RVs suggest a new role of type III collagen in the low-strain RV mechanical behavior, which needs further investigations.

1.5. Translation from RV Mechanics to Organ Physiology

1.5.1 Implications of RV mechanics to organ function from *ex vivo* studies

As previously discussed, there are marked biological remodeling and mechanical alterations in the RV with disease progression. While many *ex vivo* studies have been performed to thoroughly characterize the mechanical behavior of the RV tissue, only a few directly examined the physiological relevance of the measured mechanical properties. For instance, Trip et al. and Rain et al. found that the RV diastolic stiffness measured by the end-diastolic pressure-volume relation (EDPVR) was related with clinical progression of both healthy and pulmonary arterial hypertension human patients, as an elevated stiffness was associated with worse prognosis[209]. Additionally, Jang et al. reported that the rat longitudinal RV elastic modulus was correlated with the EDPVR, indicating a correlation of *ex vivo* and *in vivo* measurements[6]. Later, Liu et al. found in an ovine model of RV failure that the longitudinal elastic modulus at high strain was positively and significantly correlated with ejection time, a metric of systolic function[7].

Furthermore, as the viscoelastic behavior of ventricular wall raises more attention in recent studies[16], [28], [36], [40], [47], [59], [120], the changes in RV viscoelastic properties with disease progression and their implications in RV dysfunction have been noted. In a rat model of PH, elevated RV tissue elasticity and viscosity, as well as enhanced anisotropy in both parameters were reported with disease progression[40], [119]. In both studies, it was observed that the relative changes of viscosity and elasticity were different, evidenced by an impaired damping capacity (ratio of dissipated energy to total energy)[119] as well as a reduced ratio of dissipated energy over stored energy (i.e., V/E ratio)[40] with PH. These

findings suggest distinct viscous and elastic responses of the RV in disease progression. Furthermore, it was observed that RV's circumferential damping capacity was significantly correlated with acceleration time and the ratio of acceleration time/ejection time, both of which are metrics of systolic function[119]. These findings suggest the roles of both RV elasticity and viscosity in organ performance. It is unclear, though, whether a homeostasis of these two parameters should be maintained in compensated RV hypertrophy.

The regulation of mechanical behavior via the microtubule network may offer some insights into the role of tissue viscoelasticity in organ function. Hancock et al. depolymerized the microtubules via colchicine in LV myocardial slices and observed improved diastolic performance by assessment of *ex vivo* work loops[60]. Moreover, in a mouse model of hypertrophic cardiomyopathy, Pietsch et al. observed improved LV systolic performance after microtubule destabilization using *in vivo* pressure-volume measurements[254]. In both studies, an increased loop width (stroke volume) was observed after the removal of microtubule network. Considering the Frank-Starling mechanism, it can be inferred that the reduced viscoelastic resistance by the destabilization of the microtubule network leads to this enhanced stroke volume and improved performance. Additionally, the effect of chronic microtubule destabilization on RV function in a rat model of PH has been investigated by Prins et al. RV performance was significantly improved after microtubule depolymerization, although this result is attributed to t-tubule architecture enhancement and reduced adverse pulmonary vascular remodeling[115]. Overall, a complete assessment of the dependence of RV function on tissue mechanics remains a knowledge gap. Moreover, these prior studies did not investigate the separate roles of tissue viscosity and elasticity but treated the 'viscoelastic resistance' as a whole to impact the ventricular function. Since Liu et al. has observed distinct changes in RV viscosity and elasticity with PH progression[119], it is possible that these mechanical properties may contribute differently to RV failure development.

1.5.2 Implications of RV mechanics to organ function from *in vivo* studies

The advancement in medical imaging has enabled *in vivo* assessments of RV from various imaging modalities. The utilization of these methods offers different mechanical and physiological metrics, as we

will briefly discuss below. Moreover, the imaging data can be used to develop shape models of the RV, which are useful inputs for multiscale computational models as discussed in §5.3.

1.5.2.1 Echocardiography

Echocardiography is a common, noninvasive approach to assess ventricular performance, often used in clinical settings. This technique uses imaging data to derive certain metrics of contractility, such as fractional shortening (FS), acceleration time (AT), ejection time (ET), and tricuspid annular plane systolic excursion (TAPSE). Echocardiography also offers information about ventricular and atrial geometry, which provides insight into the health of the organ. Using 3D echocardiography, strain mapping can be performed to track tissue stretch and contraction during the cardiac cycle[255]. This method is referred to as speckle-tracking echocardiography (STE). However, STE has mainly been performed in the LV and is limited in the RV due to its irregular geometry and thin wall. Recently, though, 2D STE of the RV has been performed and the strain parameters were found to be prognostic of the mortality of HF with reduced ejection fraction (HFrEF)[256].

1.5.2.2 Cardiac MRI

Cardiac magnetic resonance (CMR) imaging is another noninvasive method for measuring ventricular and vascular geometry, as well as flow parameters and myocardial relaxation[257]. RV strain quantification has been performed from CMR images. Using a hyperelastic warping method, which is a finite element method, RV strains were derived in a single ventricular model[258] as well as a bi-ventricular model[259]. Strain encoded (SENC) MRI is another effective tool in strain-mapping of the RV[260], [261], and it has been validated against conventional tagged images[262]. The RV strains derived from CMR have been shown to be indicative of systolic function[260], [261], [262].

1.5.2.3 CT

Computed tomography (CT) is an x-ray imaging technique in which x-ray beams are directed at the patient to compile 3D images of the area of interest. Cardiac CT is a powerful tool in cardiovascular disease diagnosis. Additionally, strain analysis can be performed from CT images. As described by Xiong et al., strain tensors are derived from subsequent 3D images throughout the cardiac cycle[263]. Strain mapping from CT scans, though, is not standard. The time-resolution of CT is low, which results in inaccurate strain-time wave form, though the spatial resolution is high. Thus, strain measurements from echocardiography or CMR are better options.

1.5.3 Implications of RV mechanics to organ function from multiscale modeling

While current medical imaging modalities offer great tools in assessing RV geometry and function, the evaluation of RV mechanics with *in vivo* methods is limited compared to the *ex vivo* measurements. Furthermore, the experimental approaches are often time and cost expensive, and it is difficult to rule out individual factors' influence on the overall organ performance. Recent development in multiscale computational modeling has the potential to overcome these obstacles and provide novel insights on the translation from RV mechanics to organ physiology.

Multiscale computational models of the cardiovascular system, including both ventricular and vascular components, can incorporate multiple physical and physiological processes at different scales, such as (vascular) hemodynamic loads, ventricular geometry, tissue mechanical behavior, and cardiac muscle cell contractility, into the organ-level performance and function (**Fig. 3.12**). The researcher can adjust the model by choosing the necessary components and processes and varying from 0D to 3D modeling for each component. Such computational frameworks offer a powerful tool capable of delineating specific modulators (e.g., RV mechanical behavior) and their involvement in multi-scale processes as well as predicting the ventricular performance in specific processes and pathologies[264], [265], [266], [267]. Below, we will provide a summary of the model components (**Fig. 3.12**) and their applications in RV research. More general reviews on the multiscale modeling of the RV and/or pulmonary circulation system can be found here[72], [268], [269].

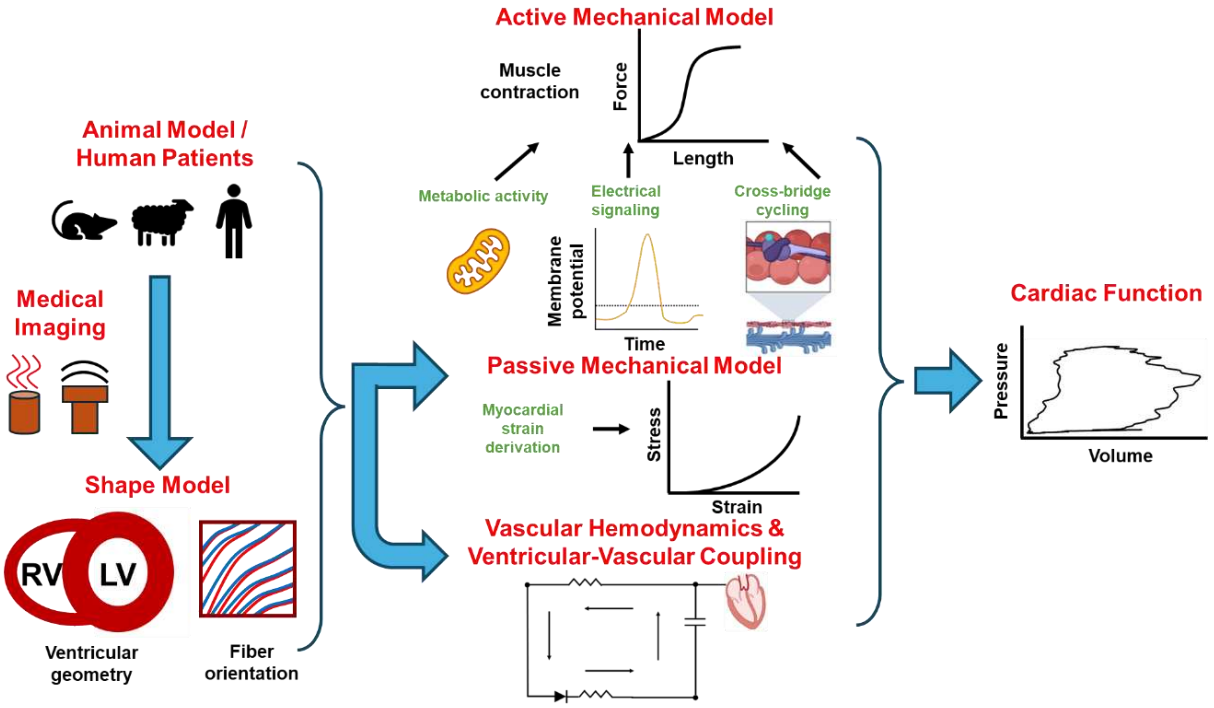

Figure 3.12. Functional diagram of multiscale computational modeling framework inputs in organ function prediction.

1.5.3.1 Shape model as inputs for multiscale modeling

Accurate modeling of ventricular geometry is critical in the development of multiscale computational models, as chamber geometry and myocardial strain information are direct inputs to the passive mechanical and vascular hemodynamic components of the framework. The ventricular chamber is often simulated using a so-called 'shape model' that includes anatomy and geometry. A well-known shape model, CircAdapt, developed by Arts et al.,[270], is a 4-chamber model coupled to the vasculature that can simulate beat-to-beat dynamics. The CircAdapt model can also simulate geometric and structural remodeling of the ventricles in response to mechanical load. The independence of the two ventricles, though, was not considered as the ventricular shapes are simulated as one large outer chamber encapsulating a small inner chamber. The septum was also not considered. The TriSeg model was, thus, developed to counter these limitations. Developed by Lumens et al., the TriSeg model simulates the LV, RV, and septum as three thick-walled segments[197] and has been used previously in studies of the RV[271], [272]. Both the TriSeg and

CircAdapt models are considered bi-ventricular models. The TriSeg and CircAdapt models assume a homogeneous material, which is a simplistic approach to modeling the myocardium that only includes the overall chamber geometry. Pourmodheji et al., though, developed a single chamber shape model of the RV with an assumed geometry of a quarter prolate spheroid[265].

While these shape models use an idealized geometry of the ventricles, medical imaging modalities can be used to construct patient-specific 3D finite element (FE) models of the heart. For example, Xi et al. developed a patient-specific bi-ventricular model of a healthy a pressure-overloaded RV to assess the ventricular interactions during disease progression[273]. The FE mesh was developed from CINE MRI scans in healthy and PAH patients, and fit contours of the LV and RV endocardium, and epicardium at various short- and long-axis views to obtain 3D endocardial and epicardial surfaces of the LV and RV. Similarly, Gomez et al., obtained the geometry for a bi-ventricular FE model from CINE MRI scans of healthy adult rabbits[274]. The study was interested in the effect of myofiber alignment during PH progression. Thus, DT-MRI scans were performed to incorporate transmural myofiber architecture and obtain different FE meshes at the healthy and pressure-overloaded state. Similarly, Avazmohammadi et al. and Finsburg et al. have developed patient-specific bi-ventricular FE models in rat and human[275], [276]. Because the FE modeling framework incorporates the morphological and mechanical changes of the RV, it is widely considered the most versatile modeling method for predicting myocardial mechanics[269], [277], [278].

While the development of FE models of the heart is more computational demanding than using an idealized geometry, the former offers the ability to incorporate microstructural information into the framework, which is critical in understanding RV remodeling. Recently, though, the MultiPatch module was developed by Walmsley et al. to allow modeling of the heterogeneity in the RV tissue, which improves its capabilities of capturing structural properties of the RV free wall[279].

1.5.3.2 Active mechanics modeling (contraction model)

Many models of myocardial active mechanics incorporated in multiscale computational frameworks are at cellular levels and only one-dimensional. We have previously reviewed the constitutive models of cellular contractility in §3.3, and such models have been applied to the multiscale modeling framework. Common formulations of active stress include those presented by Kim et al. and Lumens et al., where active stress is a function of sarcomere mechanics (length under zero tension and under stress, shortening velocity) and mechanical activation[197], [271], [280]. Alternatively, instead of using a description of sarcomere kinetics, Tözeren et al. proposed a modified Hill model to describe the muscle active tension as a function of intracellular calcium concentration and length-dependent calcium sensitivity[281], [282]. Tossas-Betancourt applied this model in a bi-ventricular model of pulmonary arterial hypertension to describe the active stress in a single myocardial muscle fiber of the RV[283].

The modeling of tissue-level active mechanics is not a common approach. Thus, unlike the passive mechanics modeling of the RV, the active mechanics of the tissue is often reduced to 1D that aligns with the muscle fiber's long axis. When the total stress (i.e., the summation of the passive and active stress) is derived, the passive stress in the fiber direction is used[47], [57], [265]. The lack of a 2D or 3D description of the active mechanical behavior of the tissue remains a major knowledge gap in the field.

1.5.3.3 Passive mechanics modeling

As we discussed in §3.1 and §3.2, a variety of constitutive formulations are established to describe the passive stress within the RV. Some of them have been adapted to the multiscale modeling of the RV. For example, Colebank et al. modeled the passive stress (1D) generated as a sum of stresses in the ECM (G_{ECM}) and titin (G_{titin}), using a structurally informed approach[272], where the stress in the ECM and titin is a function of sarcomere length, L_s:

$$G_{pas} = G_{ECM}(L_s) + G_{titin}(L_s) \quad \text{Eq. 3.10}$$

Similarly, in a bi-ventricular model of HFpEF, Kim et al. treated the passive stress (1D) as a function of the time-dependent sarcomere length based on myocardial strain (L_i) and the sarcomere length at zero active stress ($L_{c,0}$)[271]:

$$\sigma_{pas,i} = (\nu_L(L_i - L_{c,0}))^{\gamma} \quad \text{Eq. 3.11}$$

where ν_L is a unit conversion factor. The model accurately predicted the RV pressure-volume relation and revealed the role of RV compensation in the progression of LV failure.

The constitutive relations used in the above studies derive the passive stress at the sarcomeric level and is only one-dimensional. However, other groups determine the passive mechanics at tissue level based on material parameters of the entire tissue. For example, in a bi-ventricular mode of pediatric pulmonary arterial hypertension, Tossas-Betancourt et al. derived the RV passive stress (3D) from a modified Ogden-Holzapfel strain energy density function[273], [283]:

$$W = \frac{1}{2}c(e^{Q} - 1) \quad \text{Eq. 3.12}$$

where Q is a quadratic function of the strain components defined in the material directions:

$$Q = b_{ff}E_{ff}^2 + b_{xx}(E_{ss}^2 + E_{nn}^2 + E_{sn}^2 + E_{ns}^2) + b_{fx}(E_{fn}^2 + E_{nf}^2 + E_{fs}^2 + E_{sf}^2) \quad \text{Eq. 3.13}$$

where E_{ij} is the Green-Lagrange strain tensor with components $(i,j) \in (f,s,n)$ that denote the myocardial fiber (f), sheet (s), and sheet normal (n) directions, and b_{ff}, b_{xx}, and b_{fx} are material constants. In this model, the ventricular and vascular hemodynamics (i.e., pressures and flows in the RV and pulmonary vessels) were predicted, and several model-derived metrics were strongly correlated with clinically assessed disease severity. Gomez et al. applied the same formulation for passive stress in a patient-specific bi-ventricular model of PH and found that the longitudinal alignment of myofibers was related to an enhanced RV ejection fraction[274]. This response was more pronounced in the pressure-overloaded RV. Thus, the

re-orientation of the myofibers to the long axis of the RV may serve as a compensatory mechanism. Such findings provide critical knowledge of RV pathophysiology that cannot be obtained *in vivo*.

In addition, Pourmodheji et al. incorporated a growth and remodeling (G&R) component of RV in pulmonary arterial hypertension patients with the same strain energy density function shown in Eq. 12 [265]. Then, the RV passive fiber stress (1D) was given as:

$$\sigma_{RV,p}(s,t) = 2C(s)b_f E_f(s,t)\lambda_f^2(s,t)e^{Q(s,t)} \quad \text{Eq. 3.14}$$

where Q, C and b_f are material parameters associated with the strain energy density function. Because this is a model of G&R, the passive stress is given as a function of time, where t refers to the short timescale (defined by the duration of a single heartbeat), and s refers to the long timescale (defined by the duration of time during disease progression). This is one of the first computational models to consider the G&R of tissues in the context of coupling between the pulmonary circulation and the RV in a closed-loop circulation. It was predicted that progressive RV stiffening led to a large increase in RV end-diastolic pressure but a small increase in end-diastolic volume. Moreover, RV stiffening resulted in an enhanced pulmonary arterial pressure and an upregulation of pulmonary arterial mass.

In another bi-ventricular model of PH, Odeigah et al. applied the Ogden strain energy density function to derive the passive mechanical behavior of the RV[284]. A shape model was developed using a FE framework to match experimentally measured RV wall thickness and inflated both ventricles to match the cavity volumes. The fiber angle architecture was prescribed to vary transmurally from +60º at the endocardium to -60º at the epicardium. The model predicted an increase in myocardial wall stress in the fiber, cross-fiber, and apex-to-outflow directions, which was consistent with previous experimental findings. Moreover, the authors attributed these increases to the enhanced wall thickening of the RV during PH progression.

Pourmodheji et al., Tossas-Betancourt et al. and Odeigah et al. all applied a transversely isotropic form of the hyperelastic strain energy density function to derive the passive stress of the RV. However, an

orthotropic model may better represent RV mechanics, as the RV tissue has shown transmural changes in mechanical behavior. Moreover, recent works have suggested a significant viscoelastic behavior of the RV, and thus a viscoelastic model would more comprehensively capture the dynamic mechanical behavior than the hyperelastic model. Future modeling work may consider an improvement in these aspects.

1.5.3.4 Vascular hemodynamics & ventricular-vascular coupling

In a multiscale model, the vasculature component is often incorporated using a lumped parameter approach. The hemodynamic loads are represented by the resistance and compliance of the vessels (arteries and veins), and both proximal and distal vessels can be included. Next, the hemodynamics are determined by simple physical laws (e.g., resistance = mean arterial pressure / mean flow, compliance = volume change / pressure change) and then used as the input pressure and volume of the RV chamber. A common approach using simple flow calculations to derive the arterial, venous, and valvular pressure and volumes has been documented in previous studies[265], [272], [283], [284], [285]. The lumped parameter approach is also called 0D modeling. Using more sophisticated computational fluid dynamic (CFD) modeling, 1D to 3D hemodynamics from the vasculature can be obtained and used for the multiscale model, as done previously[286], [287]. A thorough review of pulmonary vasculature modeling can be found in Vélez-Rendón et al.[288], [289]. In this chapter, we will focus on the coupling of vasculature with the RV using the lumped parameter approach.

Typically, clinical (human) or preclinical (large animal) data is used to determine baseline ventricular and vasculature pressure[284], or volume[265]. The lumped parameter model is then connected to a model of a single or two ventricular chambers. This method is typically used in shape models of idealized ventricular geometry. In FE models of the RV, the pulmonary circulation can be simulated using a lumped-parameter model, or the vasculature can be included as the boundary conditions of the FE simulation[290]. Alternatively, Xi et al. have used direct hemodynamic measures of the RV and LV instead of using 0D modeling[273]. Pressure and volume waveforms were obtained via pressure-volume loop acquisition, and

the waveforms were then synchronized with CINE MR images of the LV and RV, using the end-diastolic stage as the reference point. Thus, the true *in vivo* hemodynamic condition was used in this study.

The ability to combine developed models of the ventricle and the vascular system allows us to better understand the ventricular-vascular coupling (VVC) in RV pathophysiology. Experimentally, the VVC is quantified via a single parameter, defined as the ratio of end-systolic elastance (E_{es}) to effective arterial elastance (E_a) (E_{es}/E_a). However, the coupling mechanism may involve more aspects than what a single parameter can measure. In a computational model, the VVC can be comprehensively assessed by a metric of model parameters and easily obtained in different pathologies[264], [283] and at multiple time points of disease progression[265]. Moreover, multiscale models provide further insight into the relationship between vascular and ventricular remodeling[197], [265].

1.5.3.5 Future work to link RV mechanics to organ function

The incorporation of RV mechanics in multiscale modeling frameworks is imperative in accurately predicting ventricular function. Current computational frameworks primarily incorporate the *elastic* behavior of the RV tissue and often only in 1D. However, as we have discussed previously, the RV exhibits marked viscoelastic and anisotropic mechanical behavior, and the neglect of these key features will impede a full understanding of the translational role of RV mechanics to organ function. Furthermore, the distinct alterations of tissue viscosity and elasticity during PH progression and their contributions to RV dysfunction have yet to be elucidated. Finally, a transmural mechanical difference has been reported in the ovine septum [39], and septal wall remodeling and geometrical changes with PH progression have been observed widely. A further investigation incorporating the shape and mechanics of the septum tissue will be valuable to shed new lights on the bi-ventricular interactions and RV failure.

Conclusions

RV mechanical behavior, including both elastic and viscous properties, is a critical factor in the progression of RV failure. Our review highlights current experimental and *in silico* approaches to characterize passive

and active mechanics of the RV myocardium. In addition, we have shown a significant contribution of both intra- and extracellular components to the cell and tissue level viscoelasticity, the distinct alterations of viscosity and elasticity in disease progression, and implications of the RV mechanics to organ function. While the delineation of these multi-temporal, multiscale remodeling processes and hemodynamics/mechanics are not always feasible via experimental approaches, the implementation of multiscale modeling opens new ways to incorporate multiple or individual mechanical factors that will inform RV function. Further achievement in the multiscale computational framework will offer a promising tool to capture the biomechanical mechanism of the RV in different pathologies.

2. Multiscale computational modeling in RV pathophysiology – critical knowledge gaps and the strength of *in silico* modeling

2.1. Implications of ventricular viscoelasticity in the physiological function and the current gap

There is recent evidence of microtubule contribution to myocardial viscoelasticity at both cellular and tissue levels. Cardiomyocytes (CM) have been shown to be viscoelastic and are a key determinant of the contractile function of the myocardium [30], [44], [104], [106], [113]. Moreover, Caporizzo et al. and Cooper et al. have demonstrated that the disruption of the microtubule (MT) network, a cytoskeletal component, weakens the cell viscosity and elasticity and strengthens the extent of shortening [30], [44], [107], suggesting a key role of the MT in CM mechanics and contractile function. The effect of the MT network on the tissue level mechanics is also evident. My recent work has established that the acute removal of the MT network by colchicine treatment significantly reduces the passive viscoelastic behavior of the RV free wall (RVFW). Specifically, I found that the MT network differentially regulates RV viscosity and elasticity, indicating distinct molecular mechanisms for tissue viscosity and elasticity [291]. In addition, in a rat model of pulmonary hypertension, Prins et al. assessed RV functional characteristics after the chronic colchicine treatment and observed that the treatment attenuated disease progression [115]. In the pressure-overloaded CM, too, contractile function is restored after the treatment of colchicine[44], although these effects were only observed after an acute treatment. Such findings suggest the MT network as a therapeutic target in RV failure. However, this study did not measure the mechanical properties of the RV before and after colchicine treatment and, thus, there remains an incomplete understanding of how RV viscoelastic modulation via the MT network contributes to RV pathophysiology.

During RV failure progression, the tissue undergoes significant remodeling that adversely affects the mechanical properties of the tissue, such as stiffening of the myocardium and enhanced anisotropy [6], [7], [292]. It is found that the longitudinal (i.e., in outflow tract direction) elasticity of the RV is correlated with the organ function [6], [7], indicating a key physiological role of myocardial viscoelasticity. Additionally, multiple cell studies have shown that isolated pressure-overloaded CM exhibit greater viscosity (hysteresis

loop area), elasticity (slope of the hysteresis loop), as well as impaired contractile function [44], [67], [105], [107]. Moreover, our group established that both the tissue elasticity and viscosity are significantly elevated in the pressure-overloaded RV [38]. The degree of change in these parameters with PH progression were not equal, and the increases in viscosity and elasticity were not identical between directions. While the contribution of elasticity to organ function is frequently studied, the contribution of tissue viscosity is completely unknown. Therefore, this calls for a deeper understanding of the role of viscosity in RV failure progression. To address this critical need, in the proposed work, an innovative experimental approach has been developed to quantify the functional outcomes of the RV with acute reduction of viscoelasticity via removal of MT network. The further study plan will be addressed in the following sections.

Moreover, at either the cell or tissue level, the contributions of elasticity and viscosity cannot be separated experimentally, and it remains unclear if and how these mechanical behaviors independently inform the RV function. Therefore, the development of multiscale constitutive modeling for cardiopulmonary circulation provides a great potential to delineate the individual roles of viscosity and elasticity in RV performance. This will be discussed in the next section.

2.2. Power of multiscale, multiphysics modeling and the current gap

The pressure-volume (PV) relation offers a metric of functional parameters of the ventricles including the vascular-ventricular interaction of the cardiovascular system [23], [25], [293], [294]. The PV relation is obtained from a catheterization of the ventricle, in which blood volume and pressure are measured and plotted on the horizontal axis and vertical axis, respectively. The functional parameters obtained from such experiments provide critical information about the contractility, efficiency, and stiffness of the organ. Metrics such as end-systolic pressure and volume, end-diastolic pressure and volume, stroke volume (volume of blood ejected during contraction), ejection fraction (percentage of the total blood volume ejected during contraction), cardiac output (total volume of blood ejected over time), and the end-systolic pressure-volume relation (metric of organ contractility) are key indicators of the overall health of the organ. However, such *in vivo* measurements are invasive and only assess the entire organ performance, as a combined

outcome of the tissue-level, cell-level, or sub-cellular functions. Multiscale computational models provide the advantage of isolating individual factors that inform the function of the organ, such as (vascular) hemodynamic loads, cardiac muscle cell contractility, ventricular geometry, and tissue passive mechanical behavior.

A computational framework can incorporate the remodeling processes at different levels into the organ-level function, making it a powerful tool in delineating specific modulators at multi-scale processes and predicting the ventricular performance in specific processes and pathologies [264], [265], [266], [267]. Pourmodheji et al. applied a multiscale computational framework to predict the PV relation of the RV in growth and remodeling [265]. In this study, the remodeling of the microstructure of the pulmonary artery over time was incorporated to predict the functional outcome of the RV. Moreover, some studies have modulated multiple factors at a variety of scales to predict functional outcomes of the ventricle. In the LV, Shavik et al. applied a multiscale model to predict organ function in HFpEF patients. This study examined the changes of ventricular geometry, muscle contractility and hemodynamic loads in disease progression and their effect on organ performance [264].

However, in the characterization of the mechanical behavior in such models, only the elastic behavior of the myocardium is incorporated, and the viscous behavior is ignored. This leads to an incomplete understanding of the role of ventricular mechanical properties in organ performance. The establishment of a model that includes both tissue elasticity and viscosity will significantly advance the knowledge of tissue mechanical properties in organ function. Moreover, it allows us to uncover the distinct contribution of viscosity and elasticity to organ function. The computational framework provides us with the advantage to separately alter the myocardial viscosity and elasticity and predict the functional outcome of the ventricle, which cannot be done by *in vivo* experimental designs.

3. Goal and hypothesis of my research

Therefore, the primary goal of my research in Aim 3b is to develop a new model of the cardiopulmonary circulation system incorporating viscoelastic modeling of the tissue's passive stress. Using this model, I

will achieve my goal in Aim 3b to explore the distinct impact of myocardial elasticity and viscosity on RV organ function via computational approaches. I hypothesize that the passive tissue viscosity contributes more notably to RV systolic function while the tissue elasticity contributes more to RV diastolic function.

4. Methods

The computational framework consists of the RV, right atrium, pulmonary artery (PA), pulmonary veins and the heart valves in the pulmonary circulation, and it was adapted from previously established multiscale circulation models [264], [265]. In the revised model, I made multiple modifications in the hemodynamic loads, cell contractility, the pressure-tension relation of the RV, and the chamber pressure formulation. First, I updated the hemodynamic parameters to reflect the pulmonary arterial system, and made improvements to more accurately capture the venous return by incorporating resistance and compliance metrics for the right atrium and tricuspid valve. Additionally, I separated the pulmonary artery into proximal and distal components to better characterize arterial flow, whereas the previous model only included the proximal component. I then modified the peak calcium concentration and the sarcomere length to reflect that of the RV. Additionally, I modified the formulation for the chamber tension and pressure based on the correct geometry of the RV. The model for the systemic circulation modeled the LV as a half sphere, whereas we model the RV as a quarter sphere, thus necessitating a different form for the pressure and Law of Laplace relationship. Finally, I improved the formulation of passive stress such that it is simulated using a Kelvin-Voigt model, thus including both viscous and elastic stress components. Key components that were modified or added are bolded throughout the methods.

We coupled the RV and PA with the other pulmonary circulation components using a lumped parameter approach (**Fig. 3.13**) [265].

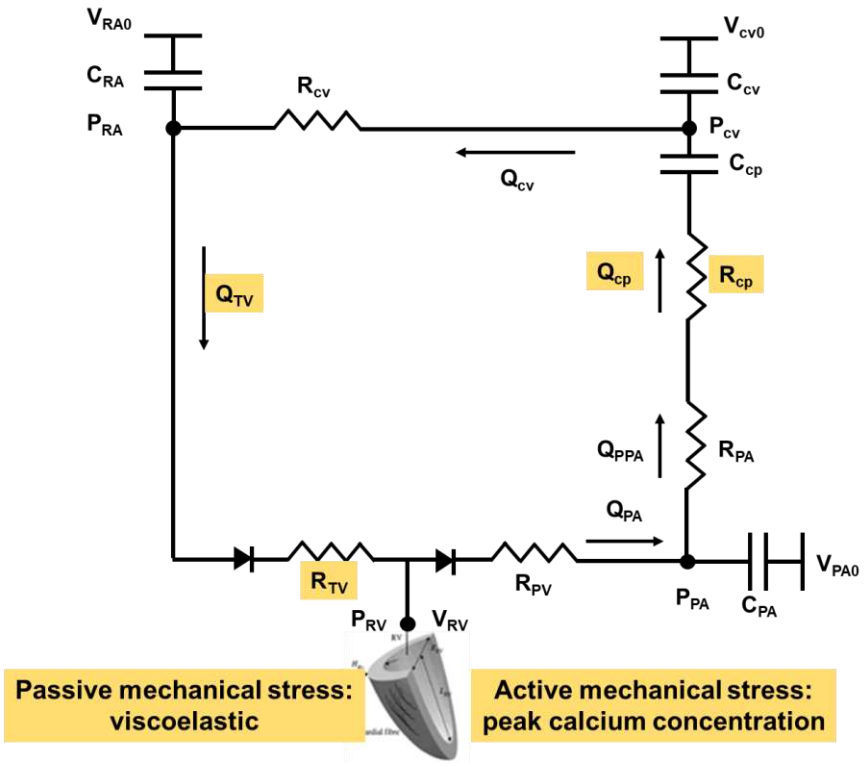

Figure 3.13 Schematic showing the computational framework for the developed RV model (pulmonary circulation). V_{RA0}: resting right atrium volume; C_{RA}: right atrium compliance; P_{RA}: right atrium pressure; Q_{TV}: flow through tricuspid valve; R_{TV}: tricuspid valve resistance; P_{RV}: right ventricle pressure; V_{RV}: right ventricle chamber volume; R_{PV}: pulmonary valve resistance; Q_{PA}: flow through main pulmonary artery; C_{PA}: main pulmonary artery compliance; P_{PA}: main pulmonary arterial pressure; V_{PA0}: main pulmonary artery resting volume; R_{PA}: main pulmonary arterial resistance; Q_{PPA}: flow through branching pulmonary artery; Q_{cp}: flow through distal pulmonary artery; R_{cp}: distal pulmonary artery resistance; C_{cp}: distal pulmonary artery compliance; C_{cv}: central venous compliance; P_{CV}: venous pressure; V_{CV0}: resting venous volume; Q_{CV}: flow through veins; R_{CV}: venous resistance.

3.1 Closed loop cardiopulmonary circulation model

The PA was modeled as a thin-walled cylinder, and we used a closed-loop system to develop the cardiopulmonary circulation constituents. The governing equations of the closed-loop system are given as follows,

$$\frac{dV_{RV}}{dt} = q_{tv} - q_{PA} \quad \text{Eq. 3.15}$$

$$\frac{dV_{PA}}{dt} = q_{PA} - q_{ppa} \quad \text{Eq. 3.16}$$

$$\frac{dV_{cp}}{dt} = q_{ppa} - q_{cp} \quad \text{Eq. 3.17}$$

$$\frac{dV_{cv}}{dt} = q_{cp} - q_{cv} \quad \text{Eq. 3.18}$$

where subscripts RV, PA, tv, ppa, cv, cp, and pv denote the right ventricle, main pulmonary artery, tricuspid vale, proximal pulmonary artery, distal venous and arterial vessels, and the pulmonary valve, respectively. Additionally, q_{cv}, q_{pv}, q_{PA}, and q_{cp} denote the flow rates connecting each cardiopulmonary segment (**Fig. 3.13**). The initial ventricular, venous, and arterial volume values, as well as vascular resistances and compliances are given in **Table 3.2**.

Table 3.2 Geometry, circulatory, and passive mechanics model parameters used in the formulation of the right ventricle pressure-volume relation. Values based on data from human/large animal. Adapted from Pourmodheji et al. [265]

	Parameter	Value	
Geometry (during diastole)	Proximal pulmonary artery (mL)	1.0	
	Distal pulmonary artery (mL)	2.0	
	Venous component (mL)	10	
	Right atrium (mL)	70	
	Right ventricle (mL)	100	
		Healthy	**Diseased**
Circulatory System	R_{pa} (MPa*ms^{-1}*mL^{-1})	0.2	0.5
	R_{pv} (MPa*ms^{-1}*mL^{-1})	0.002	0.002
	R_{cp} (MPa*ms^{-1}*mL^{-1})	0.05	0.05
	R_{cv} (MPa*ms^{-1}*mL^{-1})	0.004	0.004
	R_{tv} (MPa*ms^{-1}*mL^{-1})	0.2	0.2
	C_{pa} (mL*Mpa^{-1})	4.4x10^3	3x10^3
	C_{cp} (mL*Mpa^{-1})	6.5x10^3	6.5x10^3
	C_{cv} (mL*Mpa^{-1})	280x10^3	200x10^3
	C_{ra} (mL*Mpa^{-1})	50x10^3	10x10^3
Passive stress properties	C (passive stiffness, kPa)	0.18	0.88
Active stress properties	T_{max} (time to maximum tension, MPa)	0.145	0.145
	Ca_0 (Calcium concentration, μM)	4.35	4.35
	l_r (stress-free sarcomere length, μm)	1.85	1.85
	l_0 (sarcomere length at zero active stress, μm)	1.58	1.58
	B (μm^{-1})	4.75	4.75
	t_0 (time to peak tension, ms)	250	250
	t_{tr} (time of start of relaxation, ms)	300	300
	τ_r (relaxation constant, ms)	25	25

The flow rates depend on its pressure gradient and prescribed flow resistance:

$$q_{PA} = \begin{cases} 0 \; when \; P_{RV} < P_{PA} \\ \frac{P_{RV} - P_{PA}}{R_{pv}} \; when \; P_{RV} \geq P_{PA} \end{cases} \quad \text{Eq. 3.19}$$

$$\boldsymbol{q_{tv} = \begin{cases} 0 \; when \; P_{RV} \geq P_{cv} \\ \frac{P_{cv} - P_{RV}}{R_{cv}} \; when \; P_{RV} < P_{cv} \end{cases}} \quad \text{Eq. 3.20}$$

$$q_{cv} = \frac{P_{cv} - P_{ra}}{R_{cv}} \quad \text{Eq. 3.21}$$

$$\boldsymbol{q_{ppa} = \frac{P_{PA} - P_{cp}}{R_{PA}}} \quad \text{Eq. 3.22}$$

$$\boldsymbol{q_{cp} = \frac{P_{cp} - P_{cv}}{R_{cp}}} \quad \text{Eq. 3.23}$$

where R_{pv}, R_{cv}, R_{PA}, and R_{cp} are the resistances corresponding to the flow through the pulmonary valve, distal veins, pulmonary artery, and distal pulmonary artery, respectively. We assumed flow in the pulmonary artery was the same as that of the pulmonary valve (PV). To ensure a smooth transition from the open to closed position of the valve (deriving stable flow), we applied a softplus function, as previously described [295]. The updated formulation for the main PA (PV) flow is as follows:

$$\boldsymbol{q_{PA} = \begin{cases} \frac{1}{\alpha R_{pv}} \ln\left(1 + e^{\alpha(P_{RV} - P_{PA})}\right) \; when \; \alpha(P_{RV} - P_{PA}) \leq 20 \\ \frac{P_{RV} - P_{PA}}{R_{pv}} \; when \; P_{RV} \geq P_{PA} \end{cases}} \quad \text{Eq. 3.24}$$

where α is set to 1.0 and is decreased as necessary to improve smoothing of the predicted curve.

Pressure in the cardiopulmonary circulation is formulated using the volume differential and the corresponding vascular compliance:

$$P_{PA} = \frac{V_{PA} - V_{PA,o}}{C_{PA}} \quad \text{Eq. 3.25}$$

$$P_{cv} = \frac{V_{cv} - V_{cv,o}}{C_{cv}}$$ Eq. 3.26

$$P_{ra} = \frac{V_{ra} - V_{ra,o}}{C_{ra}}$$ Eq. 3.27

$$\boldsymbol{P_{cp} = \frac{V_{cp} - V_{cp,o}}{C_{cp}}}$$ Eq. 3.28

where $V_{PA,o}$, $V_{cv,o}$, $V_{ra,o}$, $V_{cp,o}$, are the volumes of the pulmonary artery, distal veins, right atrium, and distal pulmonary artery at rest (time of zero pressure).

3.2 Right ventricle constitutive formula

The RV was modeled as an idealized quarter prolate spheroid [265]. The RV cavity volume and wall volume are given as

$$V_{RV} = \frac{1}{3}\pi\gamma r_{RV}^3$$ Eq. 3.29

and

$$v_{RV} = \frac{1}{3}\pi[(\gamma r_{RV}^3 + h_{RV})(r_{RV} + h_{RV})^2 - \gamma r_{RV}^3]$$ Eq. 3.30

where γr_{RV} is the deformed long-axis radius, and h_{RV} is the deformed wall thickness.

Fiber strain was defined using Greens strain and is given as

$$E_f = \frac{1}{2}(\lambda_f^2 - 1)$$ Eq. 3.31

where λ_f is fiber stretch and is assumed to be distributed uniformly in two circumferential directions.

As the initial attempt to introduce viscoelasticity of the RV, the RV passive stress is given by a modified Kelvin Voigt model. We assume the elastic and viscous components to be working in parallel, thus resulting

in a summation of the two stresses (elastic and viscous) as the total passive stress. The elastic contribution to the total passive stress is given by a modified Fung type model

$$\sigma_{elastic} = 2Cb_{ff}E_f\lambda_f^2 e^Q \quad \text{Eq. 3.32}$$

where C, b_{ff}, and Q are model fit parameters, and E_f and λ_f are strain and stretch in the fiber direction, respectively. The Fung-type model fit parameters used to derive the healthy and diseased PV relations are given in **Table 3.2.** The viscous contribution to passive stress is given as

$$\boldsymbol{\sigma_{viscous} = -1.0 * sign(\dot{V}) * 1000 * \eta \frac{1}{3} * \left(\frac{1}{v}^{\frac{2}{3}} V_{RV}^{-\frac{2}{3}}\right) * |\dot{V}|} \quad \text{Eq. 3.33}$$

where $\dot{V}$ is the rate of change of volume, η is a viscous parameter (kPa*s), v is the unloaded chamber volume, and V_{RV} is the loaded chamber volume. The viscous stress has a modifier of negative one (change of sign) because the viscous stress opposes the elastic stress. The η values used to derive the healthy and diseased RV PV loop are 0.8kPa*s and 1.8kPa*s, respectively. Because of the lack of viscous measurement in large animal myocardial tissues, these values are based on a cell study from the human left ventricle [30]. Therefore, the total passive stress is calculated as the summation of the passive elastic and viscous stresses.

The active stress component is defined as

$$\sigma_{active} = T_{max}\frac{Ca_0^2}{Ca_0^2 + ECa_{50}^2}C_t \quad \text{Eq. 3.34}$$

where T_{max} is the isometric tension reached at the longest sarcomere length, Ca_0 denotes and the peak intracellular calcium concentration, and ECa_0 is the length-dependent calcium sensitivity.

Finally, right ventricular pressure is prescribed using as the intraluminal pressure and is given as

$$P_{RV} = \frac{1}{3}\sigma_{RV}\ln\left(1 + \frac{v_{RV}}{V_{RV}}\right) \quad \text{Eq. 3.35}$$

where σ_{RV} is the total stress in the RV (active and passive), v_{RV} is the unloaded chamber volume and V_{RV} is the loaded chamber volume.

5. Results and Discussion

5.1 The updated circulation framework without viscous component predicts the PV relations of the healthy and diseased RV

We first assessed the ability of the model to predict the pressure-volume (PV) relation of the healthy and diseased RV using the elastic model of passive stress. We observed physiological pressure and volume ranges of the RV for both conditions (**Fig. 3.14**). From the healthy to diseased state, we observed a rightward shift of the PV loop, suggesting a dilated chamber. Additionally, we observed an elevated end-systolic pressure (ESP), indicating pressure-overload state of the RV, as well as a narrowing of the loop indicating reduced SV. (**Fig. 3.14**). Upon further assessment of the hemodynamics, we further observed reduced EF and CO from healthy to diseased state, which suggests impaired systolic function (**Table 3.3**). In terms of contractile function of the muscle, dP/dt max and dP/dt min, were increased from the healthy to diseased state, suggesting an enhanced contractility under the pressure overload. Finally, EDPVR was notably increased, as well end-diastolic volume (EDV), suggesting diastolic dysfunction of the RV (**Table 3.3**). These findings indicate that the revised model was able to characterize the RV behavior at physiological and pathophysiological conditions.

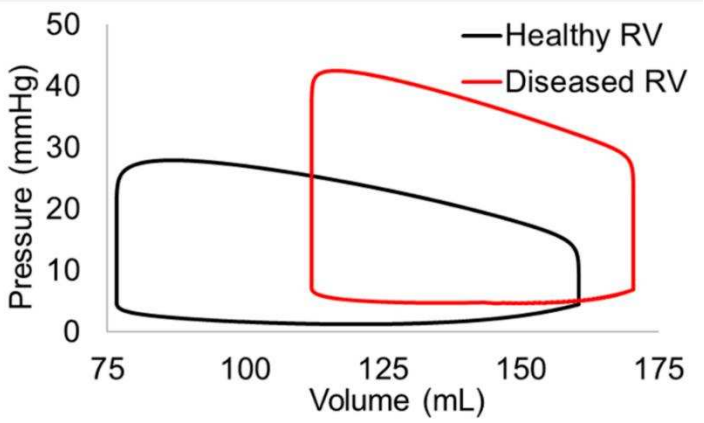

Figure 3.14. Healthy and diseased RV pressure volume relation derived from the multiscale computational model using purely elastic stress formulation.

Table 3.3 Healthy and diseased RV hemodynamics derived from the multiscale model using only elastic stress formulation.

	Healthy	Diseased	% Change
ESV (mL)	76	112	32
EDV (mL)	160	170	5.9
ESP (mmHg)	28	43	34
EDP (mmHg)	4.5	6.9	34
SV (mL)	84	58	-43
SW (mmHg*mL)	2347	2489	5.7
EF (%)	52.3	34.3	-52
CO (L/min)	5.0	3.5	-43
dP/dt max (mmHg/min)	0.35	0.43	19
dP/dt min (mmHg/min)	-0.85	-1.4	40
ESPVR (mmHg/mL)	0.37	0.38	3.7
EDPVR (mmHg/mL)	0.08	0.11	27

5.2. The change of PV relation with the addition of viscous component differs between healthy and diseased states

Next, we examined the PV relation in a healthy RV after the modeling of viscoelastic passive stress. We compared the new PV loop with that obtained with purely elastic stress formulation (**Fig. 3.15**). The addition of the viscous stress component produced a PV loop with similar position (ESV and EDV) and width (SV) as predicted by the elastic model (**Fig. 3.15**). Overall, there were minimal changes in SV, EF, and CO from an elastic to viscoelastic material modeling (**Table 3.4**).

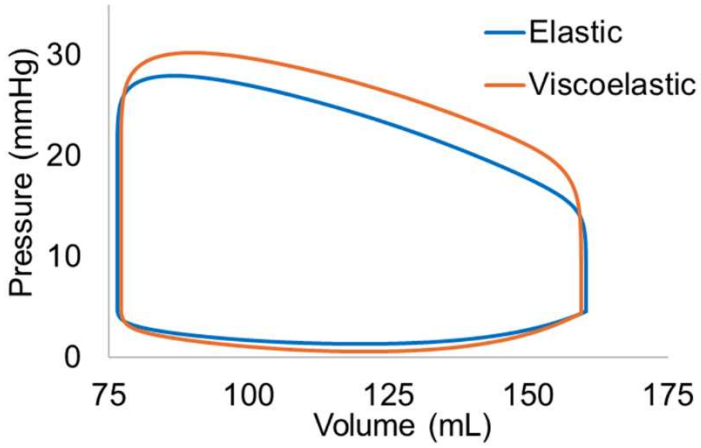

Figure 3.15 Healthy RV pressure volume relation derived from the multiscale computational model using elastic stress (blue) and viscoelastic stress (orange).

Table 3.4 Healthy RV hemodynamics obtained from the multiscale model using elastic and viscoelastic passive stress.

	Elastic	Viscoelastic	% Change
ESV (mL)	76	77	0.92
EDV (mL)	160	159	-0.55
ESP (mmHg)	28	30	7.4
EDP (mmHg)	4.5	4.3	-5.0
SV (mL)	84	82	-1.9
SW (mmHg*mL)	2347	2486	5.6
EF (%)	52	51	-1.4
CO (L/min)	5.0	4.9	-1.9
dP/dt max (mmHg/min)	0.35	0.42	17.4
dP/dt min (mmHg/min)	-0.85	-0.89	4.9
ESPVR (mmHg/mL)	0.37	0.39	6.4
EDPVR (mmHg/mL)	0.08	0.1	18.67

However, despite the identical active stress in the modeling, we saw notable changes in the ejection phase of the RV including a 7% increase of ESP (loop height). We found a 17% of increase in dP/dt max but only 5-6% of increase in dP/dt min and ESPVR. These data suggests some degree of improved systolic function with the addition of viscous stress. It is not surprising that ESPVR (a load-independent contractility index) was minimally altered as we did not change the active stress properties in the model. But the discrepant changes in dP/dt max and dP/dt min were not expected, as usually these two parameters follow a similar

trend of changes in *in vivo* measurements. Our results suggest that dP/dt max and dP/dt min may be affected by different factors (such as passive viscoelastic stress) and the exact meaning of contractility measured from dP/dt max, dP/dt min and ESPVR should be further investigated.

Finally, although the shape of the PV loop in the diastolic filling was not noticeable changed, there was a 19% of increase in EDPVR with the addition of viscous stress formulation (**Table 3.4**). The increase in EDPVR is usually interpreted as a "stiffening" of the tissue. But we used the same RV elastic modulus in the viscoelastic formulation, and this result is unexpected. Such data suggests that EDPVR is not only affected by the elastic property but also affected by the viscous property of the ventricle wall. A better interpretation of this parameter might be viewing it as the total passive (elastic and viscous) resistance of the ventricle in the diastolic filling stage.

We further examined the individual stresses in the passive stress profiles and found that the peak viscous stress is approximately 20% of the peak total passive stress (**Fig. 3.16**). Thus, despite a relatively smaller contribution of viscosity than elasticity in the total passive stress, there were notable impacts on the healthy RV's systolic and diastolic function. Our computational modeling results suggest that the inclusion of viscous mechanical behavior of RV is important to fully characterize the ventricular function.

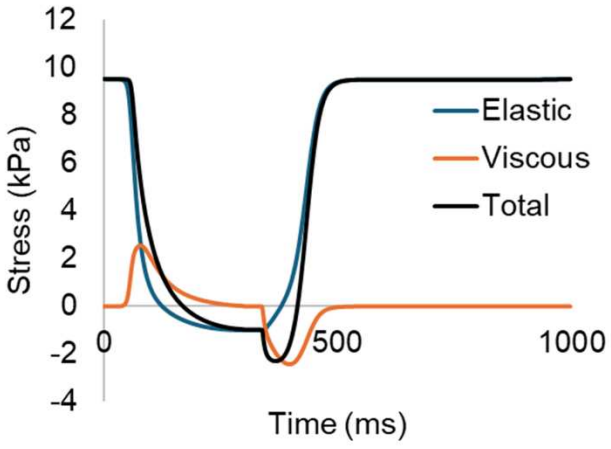

Figure 3.16 Healthy RV elastic, viscoelastic and total passive stress profiles derived from the multiscale computational model. η=0.8kPa*s, C=0.18kPa.

Next, we examined the PV relation in a diseased RV after the modeling of viscoelastic passive stress. As for the healthy RV, we compared the new PV relation with that obtained with purely elastic stress formulation. The addition of viscous component produced a similar PV loop (**Fig. 3.17**). There were no major changes in the overall performance of the RV as indicated by SV, SW, EF, and CO (**Table 3.5**). Unlike as observed in a healthy RV, the contractile behavior of the RV was largely unchanged with the addition of viscous stress, which is evident by small changes of dP/dt max (5% increase) and dP/dt min (0% change), and ESPVR (2% increase) between the purely elastic and viscoelastic conditions (**Table 3.5**). EDPVR was increased by 7% with the addition of viscous stress (**Table 3.5**). Therefore, the viscoelastic modeling leads to small and negligible changes of dP/dt max and EDPVR in diseased condition, which is in contrast to the significant elevations of these parameters in healthy condition.

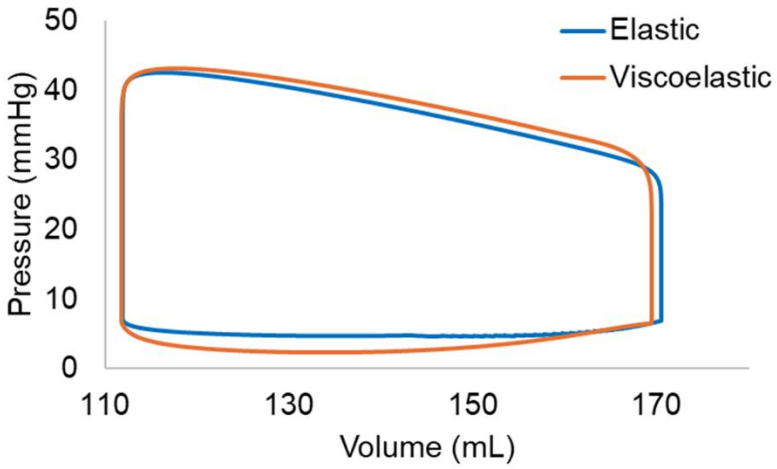

Figure 3.17 Diseased RV pressure volume relation derived from the multiscale computational model using passive elastic stress (blue) and viscoelastic passive stress (orange).

Table 3.5 Diseased RV hemodynamics obtained from the multiscale model using elastic and viscoelastic passive stress.

	Elastic	Viscoelastic	% Change
ESV (mL)	112	111	-0.15
EDV (mL)	170	169	-0.59
ESP (mmHg)	42	43	1.422
EDP (mmHg)	6.9	6.6	-4.4
SV (mL)	58	57	-1.5
SW (mmHg*mL)	2489	2489	-0.02
EF (%)	34	34	-0.86
CO (L/min)	3.5	3.4	-1.5
dP/dt max (mmHg/min)	0.43	0.45	5.2
dP/dt min (mmHg/min)	-1.4	-1.4	-0.02
ESPVR (mmHg/mL)	0.38	0.39	1.5
EDPVR (mmHg/mL)	0.11	0.12	6.7

Finally, we presented and compared the predicted PV relations in healthy and diseased states using viscoelastic formulation (**Fig. 3.18**). From the healthy to the failing RV, we observed an increase in loop height, indicative of elevated end-systolic pressure. Additionally, the loop was shifted rightward and narrowed, suggesting a dilated chamber with impaired stroke volume. Hemodynamic parameters revealed impaired RV diastolic and systolic function with disease progression (**Table 3.6**). These results indicate the ability of our viscoelastic modeling to capture the RV physiological and pathological behaviors.

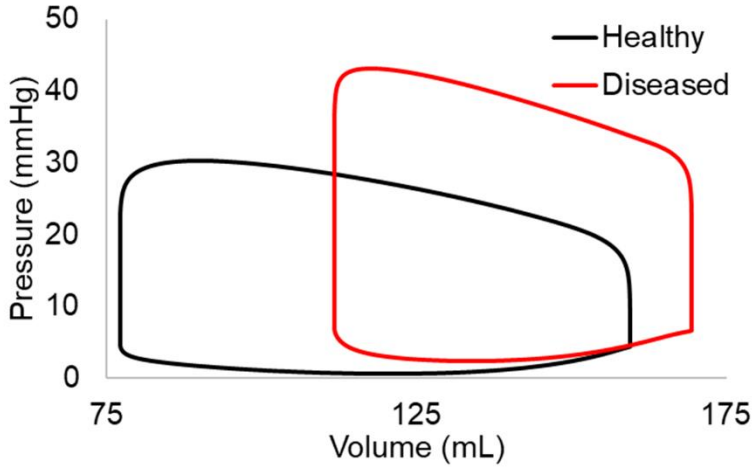

Figure 3.18 Healthy and diseased RV pressure volume relation derived from the multiscale computational model using **purely passive viscoelastic stress**.

Table 3.6 Healthy and diseased RV hemodynamics obtained from the multiscale model using viscoelastic passive stress.

	Healthy	Diseased	% Change
ESV (mL)	77	112	30.9
EDV (mL)	160	169	5.8
ESP (mmHg)	30	43	30
EDP (mmHg)	4.3	6.6	34
SV (mL)	82	58	-42
SW (mmHg*mL)	2486	2489	0.11
EF (%)	51	34	-52
CO (L/min)	4.9	3.4	-43
dP/dt max (mmHg/min)	0.42	0.46	7.4
dP/dt min (mmHg/min)	-0.89	-1.4	37
ESPVR (mmHg/mL)	0.39	0.39	-1.3
EDPVR (mmHg/mL)	0.01	0.12	17

5.3 Independent contributions of passive viscous and elastic stresses

We then investigated how independent changes of elasticity and viscosity impact the RV function (**Table 3.7**). We applied four combinations of varying properties of elasticity and viscosity: the mechanical behavior in the healthy condition (C=0.18kPa, η=0.8kPa*s); increased elasticity with a healthy viscosity (C=0.88kPa, η=0.8kPa*s); increased viscosity with a healthy elasticity (C=0.18kPa, η=1.8kPa*s); and increased elasticity and viscosity to mimic the mechanical behavior in the diseased state (C=0.88kPa, η=1.8kPa*s). It should be noted that the de-coupled change in elasticity or viscosity is hypothetical only as the two mechanical properties are altered concomitantly in living tissues. We fixed the vascular properties in the healthy state so that the changes in PV loop are only due to changes in ventricular mechanics (viscosity or elasticity).

We examined the hemodynamics in these four mechanical conditions. First, changes in elasticity or viscosity did not have large impacts on the ESV (5% reduction) (**Table 3.7**). However, an increase in elasticity, not viscosity, resulted in a 21% reduction of EDV (**Table 3.8**). When both elasticity and viscosity were increased, there was still a 21% reduction of EDV, suggesting elasticity is a stronger determinant of EDV. This result can be explained by the fact that a stiffer ventricular wall prevents the volume expansion

during diastolic filling. Next, enhanced elasticity resulted in a 40% reduction in ESP, while increased viscosity resulted in a less than 1% change of ESP (**Table 3.8**). When both elasticity and viscosity were increased, there was still a 40% reduction of ESP, suggesting elasticity is a stronger determinant of ESP. It is expected and has been observed *in vivo* studies that a stiffening RV is associated with elevated RV pressure. However, we do not see this trend here. Considering that we keep the vascular properties in healthy state in the modeling, the heightened pressure observed in diseased condition, then, may be a result of increased resistance or afterload in the vasculature.

The strengthened elasticity not only resulted in a constricted RV (reduced EDV) but also reducing SV. As other physiological conditions remain the same in the modeling, the decreased SV is a result of the increased mechanical (elastic) resistance, which is consistent with the Frank Starling mechanism (i.e., reduced filling results in reduced SV). Interestingly, though, strengthened viscosity did not have a notable impact on SV (0.07%). Likewise, EF, CO, and SW were only impacted when elastic stress and viscoelastic stress were increased (**Table 3.8**), suggesting elasticity, not viscosity, is playing a dominant role in these parameters.

Table 3.7 Hemodynamic parameters derived from the multiscale computational model with de-coupled elastic (C) and viscous (η) changes.

	C=0.18kPa, η=0.8kPa*s	C=0.88kPa, η=0.8kPa*s	C=0.18kPa, η=1.8kPa*s	C=0.88kPa, η=1.8kPa*s
ESV (mL)	77	73	77	73
EDV (mL)	159	131	159	131
ESP (mmHg)	30	21	30	21
EDP (mmHg)	4.3	4.5	4.3	4.5
SV (mL)	82	57	82	57
SW (mmHg*mL)	2486	1237	2486	1237
EF (%)	51	44	51	44
CO (m/min)	4.9	3.4	4.9	3.4
dP/dt max (mmHg/min)	0.42	0.29	0.55	0.35
dP/dt min (mmHg/min)	-0.89	-0.69	-0.89	-0.69
ESPVR (mmHg/mL)	0.39	0.29	0.39	0.29
EDPVR (mmHg/mL)	0.01	0.09	0.13	0.11

Metrics representative of RV contractility tell a different story about elasticity and viscosity. dP/dt max was reduced with an elevated elasticity but was increased with an elevated viscosity. In terms of dP/dt min, it was reduced with an elevated elasticity but was not altered with an elevated viscosity. Moreover, weakened

dP/dt max and dP/dt min were observed with increases in both elasticity and viscosity (the diseased state), but the reduction from the healthy state is not as great as that in the purely stiffened tissue (elevated elasticity alone). These results suggest that elasticity and viscosity have opposite impacts on contractility. The elevation in viscosity seems "damping" the reduction in dP/dt max and min caused by elevated elasticity. We observe a similar response in ESPVR. When elasticity was increased, ESPVR was reduced (33.5%). However, an increase in viscosity resulted in no change in ESPVR. This enhancement, though, only occurs when viscosity is independently strengthened. ESPVR represents tissue elastance at the end-systolic phase, not necessarily the strength of contraction. dP/dt max, though, is purely a metric of contractility, which may be the reason for their different response to the combined increase of elasticity and viscosity.

Finally, EDPVR showed distinct sensitivity to viscosity and elasticity. EDPVR was more or less unchanged by an independent increase in elasticity (6% reduction). However, enhanced viscosity resulted in a notable increase in EDPVR (27% increase). Moreover, when both elastic and viscous properties are enhanced, EDPVR is strengthened but to a less degree as in the case of an independent increase in viscosity. EDPVR represents the total mechanical resistance, and these results suggest viscosity contributes more strongly to the mechanical resistance during diastolic filling rather than elasticity. ESPVR, on the other hand, was only changed with increases in elasticity, suggesting elasticity is the main contributor to this parameter.

Table 3.8 Percent change of hemodynamic parameters after independent and combined increases to elasticity and viscosity.

	⬆Elasticity	⬆Viscosity	⬆ VE
ESV (mL)	-5.2	-0.08	-5.2
EDV (mL)	-22	0.002	-22
ESP (mmHg)	-40	-0.08	-41
EDP (mmHg)	3.4	-0.01	3.4
SV (mL)	-43	0.07	-43
SW (mmHg*mL)	-101	0.00	-101
EF (%)	-17	0.07	-17
CO (mL/min)	-43	0.07	-43
dP/dt max (mmHg/min)	-45	23	-22
dP/dt min (mmHg/min)	-30	0.05	-30
ESPVR (mmHg/mL)	-33	0.00	-33
EDPVR (mmHg/mL)	-6.5	26.9	10.9

Finally, we compared the viscous and elastic stress profiles with these independent changes to the mechanical properties. When only elasticity was increased, the viscous stress and the maximum elastic stress were unchanged, but the minimum elastic stress and profile were markedly changed (**Fig. 3.19A&B**). When only viscosity was increased, the elastic stress was unchanged but both peak and minimal viscous stress increased (**Fig. 3.19A&C**). When both viscosity and elasticity were strengthened, we saw a similar response of the elastic stress profile as observed in panel B and a similar response of the viscous stress profile as in panel C (**Fig. 3.19D**). However, the increases in peak and minimal viscous stresses were not as marked as observed in panel C. These results suggest that the concomitant increases in viscosity and elasticity have an impact on the viscous stress, not elastic stress. The impact may be related to the coupling of the RV and PA circulation components or other mechanisms, which awaits further investigation. This may give some insight into the relative behavior or interaction between viscosity and elasticity in organ function.

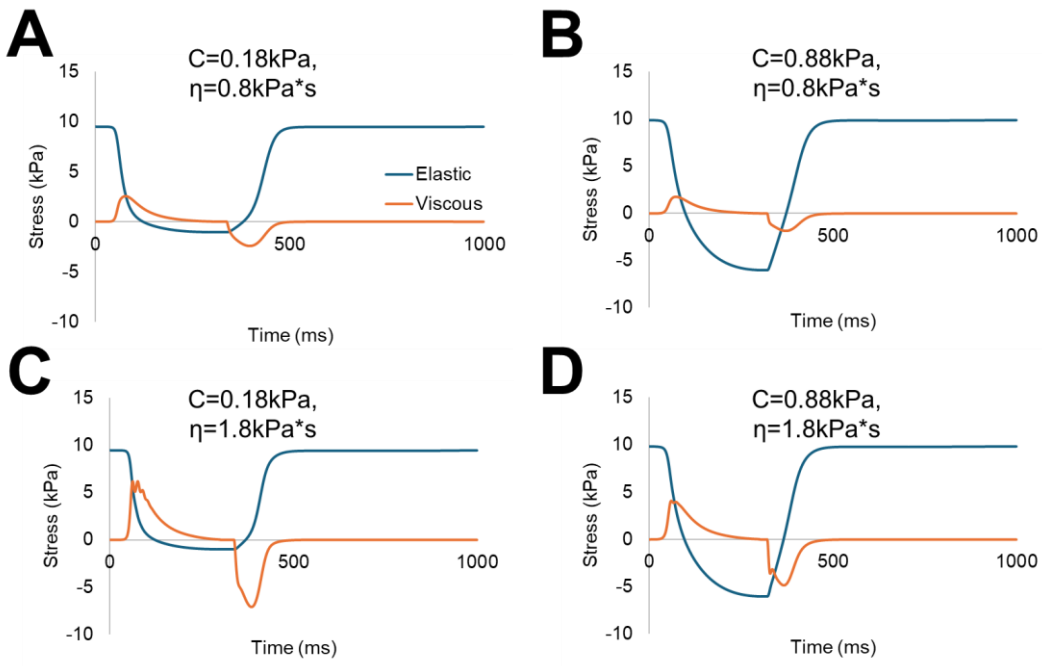

Figure 3.19 Healthy RV passive stress profiles for a fixed elastic contribution to passive stress and varying viscous contribution to passive stress.

Limitations

This study has a few limitations. First, the contractile function (active component) is surely altered in disease progression. However, we left the active stress formulation and inputs unchanged between healthy and diseased states. A future study incorporating contractile parameters representative of the diseased state will lead to further insights and improve the multiscale model. Second, the multiscale model framework is based on human/large animal species. But we do not have direct measurements of η from large animal right ventricular tissue. Instead, we used model fit parameters from a cell study of rat LV myocardium. Moreover, this study only provided η values from healthy myocardium, not failing. Thus, the η values selected for both states may not fully capture the physiological range. Finally, we did not implement a system to validate the model. We assessed the efficacy of the model by comparing the PV loop and hemodynamic parameters to prior and existing *in vivo* studies and data. A validation system or a method to evaluate the results evaluation would greatly improve the strength of the model.

6. Conclusions and Future Directions

In this study, we originally found that (1) the multiscale computational model using purely elastic stress accurately predicts the healthy and diseased RV physiological conditions; (2) with the addition of viscous stress, the physiological behavior of the healthy and diseased RV is still captured; (3) the addition of viscous stress impacts the systolic function of the healthy RV while it impacts the diastolic function of the diseased RV; (4) independent and combined increases of elasticity and viscosity revealed viscosity contributes primarily to parameters representative of RV ejection while elasticity has a more marked effect on other metrics of RV performance (SV, EF, CO).

Additionally, we used the Kelvin-Voigt model to derive viscoelastic stress. However, using this formulation, the viscous stress is dependent on strain rate, which is zero during the isovolumetric phases. The viscous stress during these phases, though, is not necessarily zero. Thus, the formulation for the total passive stress should be improved to better reflect the true mechanical loading during the cardiac cycle. For example, using the QLV formulation presented in Chapters 1&2.

Finally, the model is currently based on the human or large animal cardiopulmonary system. An important next step would be to develop this model for the small animal cardiopulmonary system to incorporate more experimental data available in the literature. Furthermore, using the viscoelastic formulation established here in a model of the systemic circulatory system would greatly improve the modeling capabilities for left side heart failure pathologies.

References

[1] N. F. Voelkel *et al.*, "Right ventricular function and failure: Report of a National Heart, Lung, and Blood Institute working group on cellular and molecular mechanisms of right heart failure," *Circulation*, vol. 114, no. 17, pp. 1883–1891, Oct. 2006, doi: 10.1161/CIRCULATIONAHA.106.632208.

[2] F. Haddad, S. A. Hunt, D. N. Rosenthal, and D. J. Murphy, "Right ventricular function in cardiovascular disease, part I: Anatomy, physiology, aging, and functional assessment of the right ventricle," Mar. 2008, *Circulation*. doi: 10.1161/CIRCULATIONAHA.107.653576.

[3] T. Lahm *et al.*, "Assessment of right ventricular function in the research setting: Knowledge gaps and pathways forward an official American thoracic society research statement," Aug. 15, 2018, *American Thoracic Society*. doi: 10.1164/rccm.201806-1160ST.

[4] D. Kohler, R. Arnold, T. Loukanov, and M. Gorenflo, "Right ventricular failure and pathobiology in patients with congenital heart disease – implications for long-term follow-up," *Front Pediatr*, vol. 1, no. 37, Nov. 2013.

[5] M. A. Konstam *et al.*, "On behalf of the American Heart Association Coun-cil on Clinical Cardiology; Council on Cardiovas-cular Disease in the Young; and Council on Cardiovascular Surgery and Anesthesia," *Circulation*, vol. 137, pp. 578–622, 2018.

[6] S. Jang *et al.*, "Biomechanical and hemodynamic measures of right ventricular diastolic function: Translating tissue biomechanics to clinical relevance," *J Am Heart Assoc*, vol. 6, no. 9, Sep. 2017, doi: 10.1161/JAHA.117.006084.

[7] W. Liu *et al.*, "Correlations between the right ventricular passive elasticity and organ function in adult ovine," *J Integr Cardiol*, vol. 6, pp. 1–6, 2020, doi: 10.15761/JIC.1000294.

[8] W. Liu and Z. Wang, "Current Understanding of the Biomechanics of Ventricular Tissues in Heart Failure," *Bioengineering 2020, Vol. 7, Page 2*, vol. 7, no. 1, p. 2, Dec. 2019, doi: 10.3390/BIOENGINEERING7010002.

[9] L. N. Diebel, R. F. Wilson, M. G. Tagett, and R. A. Kline, "End-diastolic volume. A better indicator of preload in the critically ill," *Archives of surgery*, vol. 127, no. 7, pp. 817–821, Jul. 1992.

[10] R. Durham, K. Neunaber, G. Vogler, M. Shapiro, and J. Mazuski, "Right ventricular end-diastolic volume as a measure of preload," *Journal of Trauma*, vol. 39, no. 2, pp. 218–223, Aug. 1995.

[11] M. L. Cheatham, L. D. Nelson, M. C. Chang, and K. Safcsak, "Right ventricular end-diastolic volume index as a predictor of preload status in patients on positive end-expiratory pressure," *Crit Care Med*, vol. 26, no. 11, pp. 1801–1806, Nov. 1998.

[12] S. Zhang *et al.*, "Assessing right ventricular function in patients with hypertrophic cardiomyopathy with cardiac MRI: correlation with the New York Heart Function Assessment (NYHA) classification," *PLoS One*, vol. 9, no. 9, Sep. 2017.

[13] A. Vonk Noordegraaf, B. E. Westerhof, and N. Westerhof, "The Relationship Between the Right Ventricle and its Load in Pulmonary Hypertension," *J Am Coll Cardiol*, vol. 69, no. 2, pp. 236–243, Jan. 2017.

[14] S. Dokos, B. H. Smaill, A. A. Young, and I. J. LeGrice, “Shear properties of passive ventricular myocardium,” *Heart and Circulatory Physiology*, vol. 283, no. 6, pp. 2650–2659, Dec. 2002.

[15] Z. Wang, M. J. Golob, and N. C. Chesler, “Viscoelastic Properties of Cardiovascular Tissues,” *Viscoelastic and Viscoplastic Materials*, Sep. 2016.

[16] F. Ahmad *et al.*, “Biomechanical properties and microstructure of neonatal porcine ventricles,” *Journal of the Mechanical Behavior of Biomedical Materials*, vol. 88, pp. 18–28, Dec. 2018.

[17] L. W, N.-T. M, A. M, L. KM, P. CM, and W. Z, “Different Passive Viscoelastic Properties Between the Left and Right Ventricles in Healthy Adult Ovine,” *J Biomech Eng*, vol. 143, no. 12, Dec. 2021, doi: 10.1115/1.4052004.

[18] M. S. Sirry *et al.*, “Characterisation of the mechanical properties of infarcted myocardium in the rat under biaxial tension and uniaxial compression,” *J Mech Behav Biomed Mater*, vol. 63, pp. 252–264, Oct. 2016.

[19] G. A. Holzapfel and R. W. Ogden, “Constitutive modelling of passive myocardium: a structurally based framework for material characterization,” *Philos Trans A Math Phys Eng Sci*, vol. 367, no. 1902, pp. 3445–3475, Sep. 2009.

[20] H. Ghaemi, K. Behdinan, and A. D. Spence, “In vitro technique in estimation of passive mechanical properties of bovine heart part I. Experimental techniques and data,” *Med Eng Phys*, vol. 31, no. 1, pp. 76–82, Jan. 2009.

[21] M. S. Sacks and C. J. Chuong, “Biaxial mechanical properties of passive right ventricular free wall myocardium,” *J Biomech Eng*, vol. 115, no. 2, pp. 202–205, May 1993.

[22] J. D. Humphrey, R. K. Strumpf, and F. C. Yin, “Biaxial mechanical behavior of excised ventricular epicardium,” *American Journal of Physiology*, vol. 259, pp. 101–108, Jul. 1990.

[23] M. R. Hill, M. A. Simon, D. Valdez-Jasso, W. Zhang, H. C. Champion, and M. S. Sacks, “Structural and Mechanical Adaptations of Right Ventricle Free Wall Myocardium to Pressure Overload,” *Ann Biomed Eng*, vol. 42, no. 12, pp. 2451–2465, Nov. 2014, doi: 10.1007/s10439-014-1096-3.

[24] S. G *et al.*, “Biomechanical properties and microstructure of human ventricular myocardium,” *Acta Biomater*, vol. 24, pp. 172–192, Sep. 2015, doi: 10.1016/J.ACTBIO.2015.06.031.

[25] D. Valdez-Jasso, Marc. A. Simon, H. C. Champion, and M. S. Sacks, “A murine experimental model for the mechanical behaviour of viable right-ventricular myocardium,” *J Physiol*, Aug. 2012.

[26] A. Rubiano *et al.*, “Stem cell therapy restores viscoelastic properties of myocardium in rat model of hypertension,” *J Mech Behav Biomed Mater*, vol. 59, pp. 71–77, Jun. 2016.

[27] J. D. Stroud, C. F. Baicu, M. A. Barnes, F. G. Spinale, and M. R. Zile, “Viscoelastic properties of pressure overload hypertrophied myocardium: effect of serine protease treatment,” *https://doi.org/10.1152/ajpheart.00711.2001*, vol. 282, no. 6 51-6, 2002, doi: 10.1152/AJPHEART.00711.2001.

[28] W. Liu *et al.*, “Strain-dependent stress relaxation behavior of healthy right ventricular free wall,” *Acta Biomater*, vol. 152, pp. 290–299, Oct. 2022, doi: 10.1016/J.ACTBIO.2022.08.043.

[29] G. Cooper, “Cytoskeletal networks and the regulation of cardiac contractility: microtubules, hypertrophy, and cardiac dysfunction,” *Heart and Circulatory Physiology*, vol. 291, no. 3, pp. 1003–1014, Sep. 2006.

[30] M. A. Caporizzo, C. Y. Chen, A. K. Salomon, K. B. Margulies, and B. L. Prosser, “Microtubules Provide a Viscoelastic Resistance to Myocyte Motion,” *Biophys J*, vol. 115, no. 9, pp. 1796–1807, Nov. 2018, doi: 10.1016/j.bpj.2018.09.019.

[31] C. Schubert, M. Lambertz, R. A. Nelesen, W. Bardwell, J.-B. Choi, and J. E. Dimsdale, “Effects of stress on heart rate complexity--a comparison between short-term and chronic stress,” *Biol Psychol*, vol. 80, no. 3, pp. 325–332, Mar. 2009.

[32] C.-J. Huang, H. E. Webb, M. C. Zourdos, and E. O. Acevedo, “Cardiovascular reactivity, stress, and physical activity,” *Front Physiol*, vol. 4, no. 314, Nov. 2013.

[33] B. A. Borlaug, G. C. Kane, V. Melenovsky, and T. P. Olson, “Abnormal right ventricular-pulmonary artery coupling with exercise in heart failure with preserved ejection fraction,” *Eur Heart J*, vol. 37, no. 43, pp. 3293–3302, Nov. 2016.

[34] M. Guazzi *et al.*, “Right Ventricular Contractile Reserve and Pulmonary Circulation Uncoupling During Exercise Challenge in Heart Failure: Pathophysiology and Clinical Phenotypes,” *JACC Heart Fail*, vol. 4, no. 8, pp. 625–635, Aug. 2016.

[35] Z. Wang, R. S. Lakes, M. Golob, J. C. Eickhoff, and N. C. Chesler, “Changes in Large Pulmonary Arterial Viscoelasticity in Chronic Pulmonary Hypertension,” *PLoS One*, Nov. 2013.

[36] K. Roth, W. Liu, K. LeBar, M. Ahern, and Z. Wang, “Establishment of a Biaxial Testing System for Characterization of Right Ventricle Viscoelasticity Under Physiological Loadings,” *Cardiovasc Eng Technol*, pp. 1–13, Mar. 2024, doi: 10.1007/S13239-024-00722-5/METRICS.

[37] L. W, N.-T. M, A. M, L. KM, P. CM, and W. Z, “Different Passive Viscoelastic Properties Between the Left and Right Ventricles in Healthy Adult Ovine,” *J Biomech Eng*, vol. 143, no. 12, Dec. 2021, doi: 10.1115/1.4052004.

[38] W. Liu *et al.*, “Alterations of biaxial viscoelastic properties of the right ventricle in pulmonary hypertension development in rest and acute stress conditions,” *Front Bioeng Biotechnol*, vol. 11, May 2023.

[39] M. Nguyen-Truong *et al.*, “The Interventricular Septum Is Biomechanically Distinct from the Ventricular Free Walls,” *Bioengineering 2021, Vol. 8, Page 216*, vol. 8, no. 12, p. 216, Dec. 2021, doi: 10.3390/BIOENGINEERING8120216.

[40] K. LeBar, W. Liu, J. Pang, A. Chicco, and Z. Wang, “Role of the Microtubule Network in the Passive Anisotropic Viscoelasticity of Right Ventricle with Pulmonary Hypertension Progression,” *Acta Biomater*, 2024.

[41] Z. Wang and N. C. Chesler, “Role of collagen content and cross-linking in large pulmonary arterial stiffening after chronic hypoxia,” *Biomech Model Mechanobiol*, vol. 11, no. 1–2, pp. 279–289, Jan. 2012, doi: 10.1007/s10237-011-0309-z.

[42] Z. Wang, R. S. Lakes, J. C. Eickhoff, and N. C. Chesler, “Effects of collagen deposition on passive and active mechanical properties of large pulmonary arteries in hypoxic pulmonary hypertension,” *Biomech Model Mechanobiol*, vol. 12, pp. 1115–1125, Feb. 2013.

[43] W. Liu, M. Nguyen-Truong, M. Ahern, K. M. Labus, C. M. Puttlitz, and Z. Wang, “Different Passive Viscoelastic Properties between the Left and Right Ventricles in Healthy Adult Ovine,” *J Biomech Eng*, vol. 143, no. 12, Dec. 2021, doi: 10.1115/1.4052004.

[44] M. A. Caporizzo, C. Y. Chen, K. Bedi, K. B. Margulies, and B. L. Prosser, “Microtubules Increase Diastolic Stiffness in Failing Human Cardiomyocytes and Myocardium,” *Circulation*, pp. 902–915, Mar. 2020, doi: 10.1161/CIRCULATIONAHA.119.043930.

[45] M. W. Curtis and B. Russell, “Cardiac tissue engineering,” *Journal of Cardiovascular Nursing*, vol. 24, no. 2, pp. 87–92, Mar. 2009.

[46] A. J. Ryan and F. J. O’brien, “Insoluble elastin reduces collagen scaffold stiffness, improves viscoelastic properties, and induces a contractile phenotype in smooth muscle cells,” *Biomaterials*, vol. 73, pp. 296–307, Dec. 2015.

[47] G. Sommer *et al.*, “Biomechanical properties and microstructure of human ventricular myocardium,” *Acta Biomater*, vol. 24, pp. 172–192, Sep. 2015, doi: 10.1016/j.actbio.2015.06.031.

[48] M. A. Caporizzo, C. Y. Chen, K. Bedi, K. B. Margulies, and B. L. Prosser, “Microtubules Increase Diastolic Stiffness in Failing Human Cardiomyocytes and Myocardium,” *Circulation*, vol. 141, no. 11, pp. 902–915, Mar. 2020, doi: 10.1161/CIRCULATIONAHA.119.043930.

[49] B. M. Learoyd and M. G. Taylor, “Alterations with Age in the Viscoelastic Properties of Human Arterial Walls.” [Online]. Available: http://ahajournals.org

[50] L. G. Gamero, R. L. Armentano, J. G. Barra, A. Simon, and J. Levenson, “Identification of arterial wall dynamics in conscious dogs,” *Exp Physiol*, vol. 86, no. 4, pp. 519–528, 2001, doi: 10.1113/eph8602172.

[51] R. H. Cox, “Viscoelastic properties of canine pulmonary arteries,” *American Journal Physiology*, vol. 1, no. 246, pp. H90-96, Jan. 1984.

[52] D. H. Bergel, “The dynamic elastic properties of the arterial wall,” *J. Physiology*, vol. 156, pp. 458–469, Nov. 1961.

[53] M. J. Golob, Z. Wang, A. J. Prostrollo, T. A. Hacker, and N. C. Chesler, “Limiting collagen turnover via collagenase-resistance attenuates right ventricular dysfunction and fibrosis in pulmonary arterial hypertension,” *Physiol Rep*, vol. 4, no. 11, 2016, doi: 10.14814/phy2.12815.

[54] J. J. Ryan and S. L. Archer, “The Right Ventricle in Pulmonary Arterial Hypertension: Disorders of metabolism, angiogenesis and adrenergic signaling in right ventricular failure,” *Circ Res*, vol. 115, no. 1, pp. 176–188, Jun. 2015.

[55] K. LeBar and Z. Wang, “Extracellular Matrix in Cardiac Tissue Mechanics and Physiology: Role of Collagen Accumulation,” *Extracellular Matrix - Developments and Therapeutics [Working Title]*, Mar. 2021, doi: 10.5772/INTECHOPEN.96585.

[56] W. Liu *et al.*, “Multiscale Contrasts Between the Right and Left Ventricle Biomechanics in Healthy Adult Sheep and Translational Implications,” *Front Bioeng Biotechnol*, vol. 10, Apr. 2022, doi: 10.3389/FBIOE.2022.857638.

[57] R. Avazmohammadi, M. Hill, M. Simon, and M. Sacks, “Transmural remodeling of right ventricular myocardium in response to pulmonary arterial hypertension,” *APL Bioeng*, Dec. 2017.

[58] R. Avazmohammadi, M. R. Hill, M. A. Simon, W. Zhang, and M. S. Sacks, “A novel constitutive model for passive right ventricular myocardium: evidence for myofiber–collagen fiber mechanical coupling,” *Biomech Model Mechanobiol*, vol. 16, no. 2, pp. 561–581, Apr. 2017, doi: 10.1007/S10237-016-0837-7.

[59] K. LeBar, W. Liu, A. J. Chicco, and Z. Wang, “Role of Microtubule Network in the Passive Anisotropic Viscoelasticity of Healthy Right Ventricle ,” *J Biomech Eng*, 2023.

[60] E. N. Hancock, B. M. Palmer, and M. A. Caporizzo, “Microtubule destabilization with colchicine increases the work output of myocardial slices,” *Journal of Molecular and Cellular Cardiology Plus*, vol. 7, p. 100066, Mar. 2024, doi: 10.1016/j.jmccpl.2024.100066.

[61] N. Pietsch *et al.*, “Chronic activation of tubulin tyrosination in HCM mice and in human iPSC-engineered 1 heart tissues improves heart function 2”, doi: 10.1101/2023.05.25.542365.

[62] O. Gültekin, G. Sommer, and G. A. Holzapfel, “An orthotropic viscoelastic model for the passive myocardium: continuum basis and numerical treatment,” *Comput Methods Biomech Biomed Engin*, vol. 19, no. 15, pp. 1647–1664, Nov. 2016, doi: 10.1080/10255842.2016.1176155.

[63] D. Nordsletten *et al.*, “A viscoelastic model for human myocardium,” *Acta Biomater*, vol. 135, pp. 441–457, Nov. 2021.

[64] L. L. Demer and F. C. Yin, “Passive biaxial mechanical properties of isolated canine myocardium.,” *J Physiol*, Jun. 1983.

[65] M. A. Caporizzo and B. L. Prosser, “Need for Speed: The Importance of Physiological Strain Rates in Determining Myocardial Stiffness,” *Front Physiol*, vol. 12, Jul. 2021, doi: 10.3389/FPHYS.2021.696694.

[66] C. S. Chung *et al.*, “Titin based viscosity in ventricular physiology: An integrative investigation of PEVK-actin interactions,” *J Mol Cell Cardiol*, vol. 51, no. 3, pp. 428–434, Sep. 2011, doi: 10.1016/j.yjmcc.2011.06.006.

[67] G. Cooper, “Proliferation Cardiac Microtubules,” *Heart and Circulatory Physiology*, Aug. 2009.

[68] T. S. Harris *et al.*, “Constitutive properties of hypertrophied myocardium: cellular contribution to changes in myocardial stiffness,” *Am J Physiol Heart Circ Physiol*, vol. 282, no. 6, 2002, doi: 10.1152/AJPHEART.00480.2001.

[69] A. R, H. MR, S. MA, Z. W, and S. MS, “A novel constitutive model for passive right ventricular myocardium: evidence for myofiber-collagen fiber mechanical coupling,” *Biomech Model Mechanobiol*, vol. 16, no. 2, pp. 561–581, Apr. 2017, doi: 10.1007/S10237-016-0837-7.

[70] R. Avazmohammadi, J. S. Soares, D. S. Li, S. S. Raut, R. C. Gorman, and M. S. Sacks, “A Contemporary Look at Biomechanical Models of Myocardium,” *Annu Rev Biomed Eng*, vol. 21, pp. 417–442, Jun. 2019.

[71] A. Propp, A. Gizzi, F. Levrero-Florencio, and R. Ruiz-Baier, “An orthotropic electro-viscoelastic model for the heart with stress-assisted diffusion,” *Biomech Model Mechanobiol*, vol. 19, no. 2, pp. 633–659, Apr. 2020, doi: 10.1007/S10237-019-01237-Y.

[72] D. Sharifi Kia, K. Kim, and M. A. Simon, “Current Understanding of the Right Ventricle Structure and Function in Pulmonary Arterial Hypertension,” *Front Physiol*, vol. 12, May 2021, doi: 10.3389/FPHYS.2021.641310.

[73] L. Loeffler and K. Sagawa, “A one dimensional viscoelastic model of cat heart muscle studied by small length perturbations during isometric contraction,” *Circ Res*, vol. 36, no. 4, pp. 498–512, 1975, doi: 10.1161/01.RES.36.4.498.

[74] O. M. Hess, J. Schneider, R. Koch, C. Bamert, J. Grimm, and H. P. Krayenbuehl, “Diastolic function and myocardial structure in patients with myocardial hypertrophy. Special reference to normalized viscoelastic data,” *Circulation*, vol. 63, no. 2, pp. 360–371, 1981, doi: 10.1161/01.CIR.63.2.360.

[75] C. O. Olsen, D. D. Glower, K. L. Lee, P. A. McHale, and J. S. Rankin, “Diastolic anisotropic properties of the left ventricle in the conscious dog,” *Circ Res*, vol. 69, no. 3, pp. 765–778, 1991, doi: 10.1161/01.RES.69.3.765.

[76] M. Yang and L. A. Taber, “The possible role of poroelasticity in the apparent viscoelastic behavior of passive cardiac muscle,” *J Biomech*, vol. 24, no. 7, pp. 587–597, 1991, doi: 10.1016/0021-9290(91)90291-T.

[77] J. M. Huyghe, D. H. van Campen, T. Arts, and R. M. Heethaar, “A two-phase finite element model of the diastolic left ventricle,” *J Biomech*, vol. 24, no. 7, pp. 527–538, 1991, doi: 10.1016/0021-9290(91)90286-V.

[78] J. M. Huyghe, D. H. Van Campen, T. Arts, and R. M. Heethaar, “The constitutive behaviour of passive heart muscle tissue: a quasi-linear viscoelastic formulation,” *J Biomech*, vol. 9, no. 24, pp. 841–849, 1991.

[79] Y.-C. Fung, “Biomechanics,” 1993, doi: 10.1007/978-1-4757-2257-4.

[80] C. E. Miller, M. A. Vanni, and B. B. Keller, “Characterization of passive embryonic myocardium by quasi-linear viscoelasticity theory,” *J Biomech*, vol. 30, no. 9, pp. 985–988, Sep. 1997, doi: 10.1016/S0021-9290(97)00048-1.

[81] J. Yao, V. D. Varner, L. L. Brilli, J. M. Young, L. A. Taber, and R. Perucchio, “Viscoelastic material properties of the myocardium and cardiac jelly in the looping chick heart,” *J Biomech Eng*, vol. 134, no. 2, 2012, doi: 10.1115/1.4005693.

[82] J. G. Pinto and Y. C. Fung, “Mechanical properties of the heart muscle in the passive state,” *J Biomech*, vol. 6, no. 6, 1973, doi: 10.1016/0021-9290(73)90017-1.

[83] K. L. Troyer and C. M. Puttlitz, “Human cervical spine ligaments exhibit fully nonlinear viscoelastic behavior,” *Acta Biomater*, vol. 7, no. 2, pp. 700–709, Feb. 2011, doi: 10.1016/J.ACTBIO.2010.09.003.

[84] K. L. Troyer and C. M. Puttlitz, “Nonlinear viscoelasticity plays an essential role in the functional behavior of spinal ligaments,” *J Biomech*, vol. 45, no. 4, pp. 684–691, Feb. 2012, doi: 10.1016/j.jbiomech.2011.12.009.

[85] N. L. Ramo, K. L. Troyer, and C. M. Puttlitz, “Viscoelasticity of spinal cord and meningeal tissues,” *Acta Biomater*, vol. 75, pp. 253–262, Jul. 2018, doi: 10.1016/j.actbio.2018.05.045.

[86] S. S. Shetye *et al.*, “Nonlinear viscoelastic characterization of the porcine spinal cord,” *Acta Biomater*, vol. 10, no. 2, pp. 792–797, 2014, doi: 10.1016/j.actbio.2013.10.038.

[87] S. Reddy and D. Bernstein, “Molecular mechanisms of right ventricular failure,” *Circulation*, vol. 132, no. 18, pp. 1734–1742, Nov. 2015, doi: 10.1161/CIRCULATIONAHA.114.012975.

[88] D. S. Kia, E. Benza, T. N. Bachman, C. Tushak, K. Kim, and M. A. Simon, “Angiotensin receptor-neprilysin inhibition attenuates right ventricular remodeling in pulmonary hypertension,” *J Am Heart Assoc*, vol. 9, no. 13, Jul. 2020, doi: 10.1161/JAHA.119.015708.

[89] S. Andersen *et al.*, “Pressure overload induced right ventricular remodeling is not attenuated by the anti-fibrotic agent pirfenidone,” *Pulm Circ*, May 2019.

[90] D. Pfau *et al.*, “Angiotensin Receptor Neprilysin Inhibitor Attenuates Myocardial Remodeling and Improves Infarct Perfusion in Experimental Heart Failure,” *Sci Rep*, vol. 9, no. 1, Apr. 2019.

[91] C. Witzenburg, R. Raghupathy, S. M. Kren, D. A. Taylor, and V. H. Barocas, “Mechanical changes in the rat right ventricle with decellularization,” *J Biomech*, vol. 45, no. 5, pp. 842–849, Mar. 2012, doi: 10.1016/J.JBIOMECH.2011.11.025.

[92] K. M. Labus and C. M. Puttlitz, “An anisotropic hyperelastic constitutive model of brain white matter in biaxial tension and structural-mechanical relationships,” *J Mech Behav Biomed Mater*, vol. 62, pp. 195–208, Sep. 2016, doi: 10.1016/J.JMBBM.2016.05.003.

[93] K. L. Troyer, D. J. Estep, and C. M. Puttlitz, “Viscoelastic effects during loading play an integral role in soft tissue mechanics,” *Acta Biomater*, vol. 8, no. 1, pp. 234–243, Jan. 2012, doi: 10.1016/J.ACTBIO.2011.07.035.

[94] K. M. Labus and C. M. Puttlitz, “Viscoelasticity of brain corpus callosum in biaxial tension,” *J Mech Phys Solids*, vol. 96, pp. 591–604, Nov. 2016, doi: 10.1016/J.JMPS.2016.08.010.

[95] W. Liu *et al.*, “Multiscale Contrasts Between the Right and Left Ventricle Biomechanics in Healthy Adult Sheep and Translational Implications,” *Front Bioeng Biotechnol*, vol. 10, p. 588, Apr. 2022, doi: 10.3389/FBIOE.2022.857638/BIBTEX.

[96] K. M. Labus, J. P. Kuiper, J. Rawlinson, and C. M. Puttlitz, “Mechanical characterization and viscoelastic model of the ovine temporomandibular joint Disc in indentation, uniaxial tension, and biaxial tension,” *J Mech Behav Biomed Mater*, vol. 116, Apr. 2021.

[97] K. Bertula *et al.*, “Strain-Stiffening of Agarose Gels,” *ACS Macro Lett*, vol. 8, no. 6, pp. 670–675, Jun. 2019, doi: 10.1021/ACSMACROLETT.9B00258.

[98] R. S. Lakes, “Viscoelastic solids,” *Viscoelastic Solids*, pp. 1–476, Jan. 1998, doi: 10.1201/9781315121369.

[99] M. Nguyen-Truong *et al.*, “Establishment of adult right ventricle failure in ovine using a graded, animal-specific pulmonary artery constriction model,” *Animal Model Exp Med*, vol. 3, no. 2, pp. 182–192, Jun. 2020, doi: 10.1002/ame2.12124.

[100] W. Liu *et al.*, “Correlations between the right ventricular passive elasticity and organ function in adult ovine,” *J Integr Cardiol*, vol. 6, no. 3, 2020, doi: 10.15761/JIC.1000294.

[101] B. A. Borlaug *et al.*, “Longitudinal changes in left ventricular stiffness: a community-based study,” *Circ Heart Fail*, vol. 6, no. 5, pp. 944–952, Sep. 2013.

[102] W. Liu *et al.*, “Strain-dependent stress relaxation behavior of healthy right ventricular free wall,” *Acta Biomater*, vol. 152, pp. 290–299, Oct. 2022, doi: 10.1016/J.ACTBIO.2022.08.043.

[103] W. Liu, M. Nguyen-Truong, M. Ahern, K. M. Labus, C. M. Puttlitz, and Z. Wang, “Different Passive Viscoelastic Properties Between the Left and Right Ventricles in Healthy Adult Ovine,” *J Biomech Eng*, vol. 143, no. 12, Dec. 2021, doi: 10.1115/1.4052004.

[104] M. A. Caporizzo and B. L. Prosser, “The microtubule cytoskeleton in cardiac mechanics and heart failure,” *Nat Rev Cardiol*, vol. 19, no. 6, pp. 364–378, Jun. 2022, doi: 10.1038/S41569-022-00692-Y.

[105] M. R. Zile *et al.*, “Role of microtubules in the contractile dysfunction of hypertrophied myocardium,” *J Am Coll Cardiol*, vol. 33, no. 1, pp. 250–260, Jan. 1999, doi: 10.1016/S0735-1097(98)00550-6.

[106] H. Tsutsui, K. Ishihara, and G. Cooper IV, “Cytoskeletal role in the contractile dysfunction of hypertrophied myocardium,” *Science*, vol. 260, no. 5108, pp. 682–687, 1993, doi: 10.1126/SCIENCE.8097594.

[107] H. Tsutsui *et al.*, “Role of microtubules in contractile dysfunction of hypertrophied cardiocytes,” *Circulation*, vol. 90, no. 1, pp. 533–555, 1994, doi: 10.1161/01.CIR.90.1.533.

[108] R. H. Cox, “Viscoelastic properties of canine pulmonary arteries,” *Heart and Circulatory Physiology*, vol. 246, no. 1, pp. 90–96, Jan. 1984.

[109] H. Xiao, I. Tan, M. Butlin, D. Li, and A. P. Avolio, “Arterial viscoelasticity: role in the dependency of pulse wave velocity on heart rate in conduit arteries,” *Heart and Circulatory Physiology*, vol. 312, no. 6, pp. 1185–1194, Jun. 2017.

[110] A. Anssari-Benam, Y.-T. Tseng, G. A. Holzapfel, and A. Bucchi, “Rate-dependency of the mechanical behaviour of semilunar heart valves under biaxial deformation,” *Acta Biomaterilia*, vol. 88, pp. 120–130, Apr. 2019.

[111] A. Anssari-Benam, Y.-T. Tseng, G. A. Holzapfel, and A. Bucchi, “Rate-dependent mechanical behaviour of semilunar valves under biaxial deformation: From quasi-static to physiological loading rates,” *Journal of the Mechanical Behavior of Biomedical Materials*, vol. 104, Apr. 2020.

[112] J. D. Humphrey, R. K. Strumpf, and F. C. Yin, “Biaxial mechanical behavior of excised ventricular epicardium,” *American Journal of Physiology*, no. 259, pp. 101–108, Jul. 1990.

[113] G. Cooper, “Cardiocyte cytoskeleton in hypertrophied myocardium,” *Heart Fail Rev*, vol. 5, no. 3, pp. 187–201, 2000, doi: 10.1023/A:1009836918377.

[114] S. S. Virani and Connie. W. Tsao, “Heart Disease and Stroke Statistics-2020 Update: A Report from the American Heart Association,” *Circulation*, vol. 141, no. 9, Jan. 2020.

[115] K. W. Prins, L. Tian, D. Wu, T. Thenappan, J. M. Metzger, and S. L. Archer, “Colchicine Depolymerizes Microtubules, Increases Junctophilin-2, and Improves Right Ventricular Function in Experimental Pulmonary Arterial Hypertension,” *J Am Heart Assoc*, vol. 6, no. 6, Jun. 2017, doi: 10.1161/JAHA.117.006195.

[116] Z. Wang, M. J. Golob, and N. C. Chesler, “Viscoelastic Properties of Cardiovascular Tissues,” in *Viscoelastic and Viscoplastic Materials*, InTech, 2016. doi: 10.5772/64169.

[117] P. Robison and B. L. Prosser, “Microtubule mechanics in the working myocyte,” *Journal of Physiology*, vol. 595, no. 12, pp. 3931–3937, Jun. 2017.

[118] Y.-H. Lin *et al.*, “HDAC6 modulates myofibril stiffness and diastolic function of the heart,” *J Clin Invest*, vol. 132, no. 10, May 2022.

[119] W. Liu *et al.*, “Alterations of biaxial viscoelastic properties of the right ventricle in pulmonary hypertension development in rest and acute stress conditions,” *Front Bioeng Biotechnol*, vol. 11, 2023, doi: 10.3389/FBIOE.2023.1182703.

[120] A. Rubiano, Y. Qi, D. Guzzo, K. Rowe, C. Pepine, and C. Simmons, “Stem cell therapy restores viscoelastic properties of myocardium in rat model of hypertension,” *J Mech Behav Biomed Mater*, vol. 59, pp. 71–77, Jun. 2016, doi: 10.1016/j.jmbbm.2015.11.041.

[121] D. M. Tabima, J. L. Philip, and N. C. Chesler, “Right Ventricular-Pulmonary Vascular Interactions,” *PHYSIOLOGY*, vol. 32, pp. 346–356, 2017, doi: 10.1152/physiol.00040.2016.

[122] X. Zhijie Wang, J. R. Patel, D. A. Schreier, T. A. Hacker, R. L. Moss, and N. C. Chesler, “Organ-level right ventricular dysfunction with preserved Frank-Starling mechanism in a mouse model of pulmonary arterial hypertension,” *J Appl Physiol*, vol. 124, pp. 1244–1253, 2018, doi: 10.1152/japplphysiol.00725.2017.-Pulmonary.

[123] M. Nguyen-Truong *et al.*, “Establishment of adult right ventricle failure in ovine using a graded, animal-specific pulmonary artery constriction model,” *Animal Model Exp Med*, vol. 3, no. 2, pp. 182–192, Jun. 2020.

[124] S. Kosta and P. C. Dauby, “Frank-Starling mechanism, fluid responsiveness, and length-dependent activation: Unravelling the multiscale behaviors with an in silico analysis,” *PLoS Comput Biol*, vol. 17, no. 10, Oct. 2021, doi: 10.1371/journal.pcbi.1009469.

[125] Y. Zhan, H. Yue, X. Zhao, J. Tang, and Z. Wu, “Colchicine in atrial fibrillation: are old trees in bloom?,” 2023, *Frontiers Media SA*. doi: 10.3389/fphys.2023.1260774.

[126] I. Klein, “Colchicine stimulates the rate of contraction of heart cells in culture,” 1983. [Online]. Available: https://academic.oup.com/cardiovascres/article/17/8/459/337669

[127] G. Frommeyer *et al.*, “Colchicine Increases Ventricular Vulnerability in an Experimental Whole-Heart Model,” *Basic Clin Pharmacol Toxicol*, vol. 120, no. 5, pp. 505–508, May 2017, doi: 10.1111/bcpt.12702.

[128] L. Mubayed, B. A. A. Muller, J. L. Jacobson, H. A. Hast, and H. H. Nguyen, “Acute Pediatric Colchicine Toxicity is Associated with Marked Bradydysrhythmias,” *Journal of Emergency Medicine*, vol. 55, no. 3, pp. e65–e69, Sep. 2018, doi: 10.1016/j.jemermed.2018.03.004.

[129] A. J. Matamoros and P. W. Baas, “Microtubules in health and degenerative disease of the nervous system,” *Brain Res Bull*, vol. 126, pp. 217–225, Sep. 2016, doi: 10.1016/j.brainresbull.2016.06.016.

[130] L. Penazzi, L. Bakota, and R. Brandt, “Microtubule Dynamics in Neuronal Development, Plasticity, and Neurodegeneration,” in *International Review of Cell and Molecular Biology*, vol. 321, Elsevier Inc., 2016, pp. 89–169. doi: 10.1016/bs.ircmb.2015.09.004.

[131] B. Y. Choi *et al.*, “Colchicine induced intraneuronal free zinc accumulation and dentate granule cell degeneration,” *Metallomics*, vol. 6, no. 8, pp. 1513–1520, 2014, doi: 10.1039/c4mt00067f.

[132] B. Y. Choi and S. W. Suh, “Antimicrotubule Agent-Induced Zinc Neurotoxicity,” 1001.

[133] T. Y. J. Lee and A. I. Gotlieb, “Microfilaments and microtubules maintain endothelial integrity,” Jan. 01, 2003, *Wiley-Liss Inc.* doi: 10.1002/jemt.10250.

[134] C. D. Ochoa, T. Stevens, and R. Balczon, “Cold exposure reveals two populations of microtubules in pulmonary endothelia,” *Am J Physiol Lung Cell Mol Physiol*, vol. 300, p. 22, 2011, doi: 10.1152/ajplung.00185.2010.-Microtubules.

[135] C. Y. Chen *et al.*, “Suppression of detyrosinated microtubules improves cardiomyocyte function in human heart failure,” *Nat Med*, vol. 24, no. 8, pp. 1225–1233, Aug. 2018, doi: 10.1038/s41591-018-0046-2.

[136] M. Schuldt *et al.*, “Proteomic and Functional Studies Reveal Detyrosinated Tubulin as Treatment Target in Sarcomere Mutation-Induced Hypertrophic Cardiomyopathy,” *Circ Heart Fail*, vol. 14, no. 1, p. E007022, Jan. 2021, doi: 10.1161/CIRCHEARTFAILURE.120.007022.

[137] Y. C. Fung, “Biomechanics: Mechanical Properties of Living Tissues,” *J Appl Mech Eng*, vol. 49, no. 2, pp. 464–465, Jun. 1982.

[138] K. M. Labus and C. M. Puttlitz, “Viscoelasticity of brain corpus callosum in biaxial tension,” *J Mech Phys Solids*, vol. 96, pp. 591–604, Nov. 2016, doi: 10.1016/j.jmps.2016.08.010.

[139] K. L. Troyer and C. M. Puttlitz, “Human cervical spine ligaments exhibit fully nonlinear viscoelastic behavior,” *Acta Biomater*, vol. 7, no. 2, pp. 700–709, 2011, doi: 10.1016/j.actbio.2010.09.003.

[140] W. Liu *et al.*, “Effects of Pulmonary Hypertension on Biaxial Viscoelastic Properties of the Right Ventricle at Rest and Exercise Conditions,” in *Experimental Biology*, Philadelphia: The Federation of American Societies for Experimental Biology, Apr. 2022.

[141] M. S. Sacks, “Biaxial Mechanical Evaluation of Planar Biological Materials,” 2000.

[142] H. Ghaemi, K. Behdinan, and A. D. Spence, “In vitro technique in estimation of passive mechanical properties of bovine heart. Part I. Experimental techniques and data,” *Med Eng Phys*, vol. 31, no. 1, pp. 76–82, Jan. 2009, doi: 10.1016/j.medengphy.2008.04.008.

[143] M. Nguyen-Truong and Z. Wang, “Biomechanical Properties and Mechanobiology of Cardiac ECM,” in *Cardiac Extracellular Matrix. Advances in Experimental Medicine and Biology*, vol. 1098, E. Shmuck, P. Hematti, and A. Raval, Eds., Springer, Cham, 2018, pp. 1–19.

[144] M. S. Sacks and C. J. Chuong, “Orthotropic Mechanical Properties of Chemically Treated Bovine Pericardium,” 1998.

[145] M. S. Sacks and W. Sun, “Multiaxial mechanical behavior of biological materials,” 2003. doi: 10.1146/annurev.bioeng.5.011303.120714.

[146] M. S. Sacks and C. J. Chuong, “Biaxial Mechanical Properties of Passive Right Ventricular Free Wall Myocardium,” *J Biomech Eng*, vol. 115, no. 2, pp. 202–205, May 1993.

[147] D. Vélez-Rendón, E. R. Pursell, J. Shieh, and D. Valdez-Jasso, “Relative Contributions of Matrix and Myocytes to Biaxial Mechanics of the Right Ventricle in Pulmonary Arterial Hypertension,” *J Biomech Eng*, vol. 141, no. 9, Sep. 2019, doi: 10.1115/1.4044225.

[148] D. S. Li, E. A. Mendiola, R. Avazmohammadi, F. B. Sachse, and M. S. Sacks, “A multi-scale computational model for the passive mechanical behavior of right ventricular myocardium,” *J Mech Behav Biomed Mater*, vol. 142, Jun. 2023, doi: 10.1016/j.jmbbm.2023.105788.

[149] D. Nordsletten *et al.*, “A viscoelastic model for human myocardium,” *Acta Biomater*, vol. 135, pp. 441–457, Nov. 2021, doi: 10.1016/j.actbio.2021.08.036.

[150] S. Kakaletsis *et al.*, “Right ventricular myocardial mechanics: Multi-modal deformation, microstructure, modeling, and comparison to the left ventricle,” *Acta Biomater*, vol. 123, pp. 154–166, Mar. 2021, doi: 10.1016/j.actbio.2020.12.006.

[151] D. S. Li *et al.*, “Insights into the passive mechanical behavior of left ventricular myocardium using a robust constitutive model based on full 3D kinematics,” *J Mech Behav Biomed Mater*, vol. 103, Mar. 2020, doi: 10.1016/j.jmbbm.2019.103508.

[152] R. Avazmohammadi *et al.*, “An integrated inverse model-experimental approach to determine soft tissue three-dimensional constitutive parameters: application to post-infarcted myocardium,” *Biomech Model Mechanobiol*, vol. 17, no. 1, pp. 31–53, Feb. 2018, doi: 10.1007/S10237-017-0943-1.

[153] G. M. Roth, D. M. Bader, D. M. Bader, and E. R. Pfaltzgraff, “Isolation and physiological analysis of mouse cardiomyocytes,” *Journal of Visualized Experiments*, no. 91, Jul. 2014, doi: 10.3791/51109.

[154] G. Iribe, M. Helmes, and P. Kohl, “Force-length relations in isolated intact cardiomyocytes subjected to dynamic changes in mechanical load,” *Am J Physiol Heart Circ Physiol*, vol. 292, no. 3, Mar. 2007, doi: 10.1152/ajpheart.00909.2006.

[155] W. K. K. Weiwad, W. A. Linke, and M. H. P. Wussling, “Sarcomere length-tension relationship of rat cardiac myocytes at lengths greater than optimum,” *J Mol Cell Cardiol*, vol. 32, no. 2, pp. 247–259, 2000, doi: 10.1006/jmcc.1999.1069.

[156] C. Crocini and M. Gotthardt, “Cardiac sarcomere mechanics in health and disease”, doi: 10.1007/s12551-021-00840-7/Published.

[157] D. Rappaport, D. Adam, P. Lysyansky, and S. Riesner, “Assessment of myocardial regional strain and strain rate by tissue tracking in B-mode echocardiograms,” *Ultrasound Med Biol*, vol. 32, no. 8, pp. 1181–1192, Aug. 2006, doi: 10.1016/j.ultrasmedbio.2006.05.005.

[158] J. C. Benech *et al.*, “Diabetes increases stiffness of live cardiomyocytes measured by atomic force microscopy nanoindentation,” *J Physiol Cell Physiol*, vol. 307, pp. 910–919, 2014, doi: 10.1152/ajpcell.00192.2013.-Stiffness.

[159] L. Lou, A. Sesena Rubfiaro, J. He, and A. Agarwal, “Understanding spatiotemporal mechanical behavior, viscoelasticity, and functions of stem cell-derived cardiomyocytes,” *Nanoscale*, vol. 15, no. 24, pp. 10360–10370, Jun. 2023, doi: 10.1039/d3nr01553j.

[160] B. W. Lee *et al.*, “Adult human cardiomyocyte mechanics in osteogenesis imperfecta,” *Am J Physiol Heart Circ Physiol*, vol. 325, no. 4, pp. H814–H821, Oct. 2023, doi: 10.1152/ajpheart.00391.2023.

[161] D. Borin, I. Pecorari, B. Pena, and O. Sbaizero, “Novel insights into cardiomyocytes provided by atomic force microscopy,” Jan. 01, 2018, *Elsevier Ltd*. doi: 10.1016/j.semcdb.2017.07.003.

[162] J. Zhu, T. Sabharwal, A. Kalyanasundaram, L. Guo, and G. Wang, “Topographic mapping and compression elasticity analysis of skinned cardiac muscle fibers in vitro with atomic force microscopy and nanoindentation,” *J Biomech*, vol. 42, no. 13, pp. 2143–2150, Sep. 2009, doi: 10.1016/j.jbiomech.2009.05.031.

[163] S. C. Lieber, N. Aubry, J. Pain, G. Diaz, S. J. Kim, and S. F. Vatner, “Aging increases stiffness of cardiac myocytes measured by atomic force microscopy nanoindentation,” *Am J Physiol Heart Circ Physiol*, vol. 287, no. 2 56-2, pp. 645–651, Aug. 2004, doi: 10.1152/AJPHEART.00564.2003/ASSET/IMAGES/LARGE/ZH40080431910007.JPEG.

[164] S. Deitch, B. Z. Gao, and D. Dean, “Effect of Matrix on Cardiomyocyte Viscoelastic Properties in 2D Culture.”

[165] R. Peyronnet *et al.*, “Simultaneous assessment of radial and axial myocyte mechanics by combining atomic force microscopy and carbon fibre techniques,” *Philosophical Transactions of the Royal Society B: Biological Sciences*, vol. 377, no. 1864, Nov. 2022, doi: 10.1098/rstb.2021.0326.

[166] C. Zhang, W. Wang, W. He, N. Xi, Y. Wang, and L. Liu, “Dynamic Model for Characterizing Contractile Behaviors and Mechanical Properties of a Cardiomyocyte,” *Biophys J*, vol. 114, no. 1, pp. 188–200, Jan. 2018, doi: 10.1016/j.bpj.2017.11.002.

[167] J. C. Benech and G. Romanelli, “Atomic force microscopy indentation for nanomechanical characterization of live pathological cardiovascular/heart tissue and cells,” *Micron*, vol. 158, Jul. 2022, doi: 10.1016/j.micron.2022.103287.

[168] I. Andreu *et al.*, “Heterogeneous micromechanical properties of the extracellular matrix in healthy and infarcted hearts,” *Acta Biomater*, vol. 10, no. 7, pp. 3235–3242, 2014, doi: 10.1016/j.actbio.2014.03.034.

[169] K. Genovese, A. Montes, A. Martínez, and S. L. Evans, “Full-surface deformation measurement of anisotropic tissues under indentation,” *Med Eng Phys*, vol. 37, no. 5, pp. 484–493, May 2015, doi: 10.1016/j.medengphy.2015.03.005.

[170] T. Lanzicher *et al.*, “The cardiomyopathy lamin A/C D192G mutation disrupts whole-cell biomechanics in cardiomyocytes as measured by atomic force microscopy loading-unloading curve analysis,” *Sci Rep*, vol. 5, Sep. 2015, doi: 10.1038/srep13388.

[171] E. Dague *et al.*, “Atomic force and electron microscopic-based study of sarcolemmal surface of living cardiomyocytes unveils unexpected mitochondrial shift in heart failure,” *J Mol Cell Cardiol*, vol. 74, pp. 162–172, 2014, doi: 10.1016/j.yjmcc.2014.05.006.

[172] J. R. Tangney *et al.*, “Novel role for vinculin in ventricular myocyte mechanics and dysfunction,” *Biophys J*, vol. 104, no. 7, pp. 1623–1633, Apr. 2013, doi: 10.1016/j.bpj.2013.02.021.

[173] X. Shi *et al.*, “Elasticity of cardiac cells on the polymer substrates with different stiffness: An atomic force microscopy study,” *Physical Chemistry Chemical Physics*, vol. 13, no. 16, pp. 7540–7545, Apr. 2011, doi: 10.1039/c1cp20154a.

[174] L. Qian and H. Zhao, “Nanoindentation of soft biological materials,” Dec. 11, 2018, *MDPI AG*. doi: 10.3390/mi9120654.

[175] G. Iribe, T. Kaneko, Y. Yamaguchi, and K. Naruse, “Load dependency in force-length relations in isolated single cardiomyocytes,” *Prog Biophys Mol Biol*, vol. 115, no. 2–3, pp. 103–114, Aug. 2014, doi: 10.1016/j.pbiomolbio.2014.06.005.

[176] A. Borbély *et al.*, “Cardiomyocyte stiffness in diastolic heart failure,” *Circulation*, vol. 111, no. 6, pp. 774–781, Feb. 2005, doi: 10.1161/01.CIR.0000155257.33485.6D.

[177] M. Golob, R. L. Moss, and N. C. Chesler, “Cardiac Tissue Structure, Properties, and Performance: A Materials Science Perspective,” Oct. 01, 2014, *Kluwer Academic Publishers*. doi: 10.1007/s10439-014-1071-z.

[178] T. Shibata *et al.*, “Metabolic and functional consequences of barium-induced contracture in rabbit myocardium.”

[179] Y. Saeki, K. Sagawa, and H. Suga, “Transient tension responses of heart muscle in Ba2+ contracture to step length changes.”

[180] E. Marban, H. Kusuoka, D. T. Yue, M. L. Weisfeldt, and W. G. Wier, “Maximal Ca2+-activated force elicited by tetanization of ferret papillary muscle and whole heart: mechanism and characteristics of steady contractile activation in intact myocardium.,” *Circ Res*, vol. 59, no. 3, pp. 262–269, 1986.

[181] T. Shibata, W. C. Hunter, and K. Sagawa, “Dynamic Stiffness of Barium-Contractured Cardiac Muscles With Different Speeds of Contraction.” [Online]. Available: http://ahajournals.org

[182] S. Neelakantan *et al.*, “Multiscale characterization of left ventricle active behavior in the mouse,” *Acta Biomater*, vol. 162, pp. 240–253, May 2023, doi: 10.1016/j.actbio.2023.03.022.

[183] W. Zhang, A. Capilnasiu, and D. Nordsletten, “Comparative Analysis of Nonlinear Viscoelastic Models Across Common Biomechanical Experiments,” *J Elast*, vol. 145, no. 1–2, pp. 117–152, Aug. 2021, doi: 10.1007/s10659-021-09827-7.

[184] R. Avazmohammadi, J. S. Soares, D. S. Li, S. S. Raut, R. C. Gorman, and M. S. Sacks, “A Contemporary Look at Biomechanical Models of Myocardium,” *Annu Rev Biomed Eng*, vol. 21, pp. 417–442, 2019, doi: 10.1146/ANNUREV-BIOENG-062117-121129.

[185] S. Javani, M. Gordon, and A. N. Azadani, “Biomechanical Properties and Microstructure of Heart Chambers: A Paired Comparison Study in an Ovine Model,” *Ann Biomed Eng*, vol. 44, no. 11, pp. 3266–3283, Nov. 2016, doi: 10.1007/s10439-016-1658-7.

[186] T. Matsumoto *et al.*, “Biaxial Tensile Properties of Thoracic Aortic Aneurysm Tissues,” *Journal of Biomechanical Science and Engineering*, vol. 4, no. 4, pp. 518–529, 2009, doi: 10.1299/JBSE.4.518.

[187] D. Pfau *et al.*, “Angiotensin Receptor Neprilysin Inhibitor Attenuates Myocardial Remodeling and Improves Infarct Perfusion in Experimental Heart Failure,” *Sci Rep*, vol. 9, no. 1, Dec. 2019, doi: 10.1038/S41598-019-42113-0.

[188] A. Propp, A. Gizzi, F. Levrero-Florencio, and R. Ruiz-Baier, “An orthotropic electro-viscoelastic model for the heart with stress-assisted diffusion,” *Biomech Model Mechanobiol*, vol. 19, no. 2, pp. 633–659, Apr. 2020, doi: 10.1007/s10237-019-01237-y.

[189] H. Pouleur, J. S. Karliner, M. M. Lewinter, and J. W. Covell, “Diastolic Viscous Properties of the Intact Canine Left Ventricle,” 1979. [Online]. Available: http://ahajournals.org

[190] A. Bonfanti, J. L. Kaplan, G. Charras, and A. Kabla, “Fractional viscoelastic models for power-law materials,” Jul. 14, 2020, *Royal Society of Chemistry*. doi: 10.1039/d0sm00354a.

[191] B. Suki, K. R. Lutchen, and A.-L. Barabhsi, “Lung tissue viscoelasticity: a mathematical framework and its molecular basis.”

[192] J. M. Guccione and A. D. McCulloch, “Mechanics of Active Contraction in Cardiac Muscle: Part I—Constitutive Relations for Fiber Stress That Describe Deactivation,” *J Biomech Eng*, vol. 115, no. 1, pp. 72–81, Feb. 1993, doi: 10.1115/1.2895473.

[193] B. Milićević, M. Ivanović, B. Stojanović, M. Milošević, M. Kojić, and N. Filipović, “Huxley muscle model surrogates for high-speed multi-scale simulations of cardiac contraction,” *Comput Biol Med*, vol. 149, Oct. 2022, doi: 10.1016/j.compbiomed.2022.105963.

[194] J. J. Rice, F. Wang, D. M. Bers, and P. P. De Tombe, “Approximate model of cooperative activation and crossbridge cycling in cardiac muscle using ordinary differential equations,” *Biophys J*, vol. 95, no. 5, pp. 2368–2390, Sep. 2008, doi: 10.1529/biophysj.107.119487.

[195] N. A. Trayanova and J. J. Rice, “Cardiac electromechanical models: From cell to organ,” *Front Physiol*, vol. 2 AUG, 2011, doi: 10.3389/fphys.2011.00043.

[196] T. Washio, J. I. Okada, S. Sugiura, and T. Hisada, “Approximation for cooperative interactions of a spatially-detailed cardiac sarcomere model,” *Cell Mol Bioeng*, vol. 5, no. 1, pp. 113–126, Mar. 2012, doi: 10.1007/s12195-011-0219-2.

[197] J. Lumens, T. Delhaas, B. Kirn, and T. Arts, “Three-wall segment (TriSeg) model describing mechanics and hemodynamics of ventricular interaction,” *Ann Biomed Eng*, vol. 37, no. 11, pp. 2234–2255, Nov. 2009, doi: 10.1007/s10439-009-9774-2.

[198] C. Yancy, “2013 ACCF/AHA Guideline for the Management of Heart Failure: Executive Summary: A Report of the American College of Cardiology Foundation/American Heart Association Task Force on Practice Guidelines,” *J Am Coll Cardiol*, vol. 128, no. 16, 2013.

[199] A. Dhingra *et al.*, “Epidemiology of Heart Failure with Preserved Ejection Fraction,” *Curr Heart Fail Rep*, vol. 11, pp. 354–365, Sep. 2014.

[200] O. E. Theophilus, D. O. Hodge, R. M. Herges, S. J. Jacobsen, V. L. Roger, and M. M. Redfield, “Trends in Prevalence and Outcome of Heart Failure with Preserved Ejection Fraction,” *N Engl J Med*, vol. 355, pp. 251–259, Jul. 2006.

[201] F. L. Abel, “Effects of alterations in peripheral resistance on left ventricular function,” *Proceedings of the Society of Experimental Biology and Medicine*, vol. 120, no. 1, pp. 52–56, Oct. 1965.

[202] S. Andersen, J. E. Nielsen-Kudsk, A. Vonk Noordegraaf, and F. S. de Man, “Right Ventricular Fibrosis,” *Circulation*, vol. 139, no. 2, pp. 269–285, Jan. 2019.

[203] M. Pahuja and D. Burkhoff, “Right Ventricular Afterload Sensitivity Has Been on My Mind,” *Circ Heart Fail*, vol. 12, no. 9, Sep. 2019.

[204] W. Liu and Z. Wang, “Current understanding of the biomechanics of ventricular tissues in heart failure,” *Bioengineering*, vol. 7, no. 1, Mar. 2020, doi: 10.3390/BIOENGINEERING7010002.

[205] J. Bernal-Ramirez *et al.*, “Exploring Functional Differences between the Right and Left Ventricles to Better Understand Right Ventricular Dysfunction,” *Oxid Med Cell Longev*, vol. 2021, 2021, doi: 10.1155/2021/9993060.

[206] C. E. Molina, J. Heijman, and D. Dobrev, “Differences in Left Versus Right Ventricular Electrophysiological Properties in Cardiac Dysfunction and Arrhythmogenesis,” *Arrhthm Electrophysiol Rev.*, vol. 5, no. 1, pp. 14–19, May 2016.

[207] S. Rain *et al.*, “Right ventricular diastolic impairment in patients with pulmonary arterial hypertension,” *Circulation*, vol. 128, no. 18, pp. 2016–2025, Oct. 2013, doi: 10.1161/CIRCULATIONAHA.113.001873.

[208] M. Murayama *et al.*, “Simple and noninvasive method to estimate right ventricular operating stiffness based on echocardiographic pulmonary regurgitant velocity and tricuspid annular plane movement measurements during atrial contraction,” *International Journal of Cardiovascular Imaging*, vol. 35, no. 10, pp. 1871–1880, Oct. 2019, doi: 10.1007/s10554-019-01637-2.

[209] P. Trip *et al.*, “Clinical relevance of right ventricular diastolic stiffness in pulmonary hypertension,” *European Respiratory Journal*, vol. 45, no. 6, pp. 1603–1612, Jun. 2015, doi: 10.1183/09031936.00156714.

[210] G. A. Buxton, S. L. Siedlak, G. Perry, and M. A. Smith, “Mathematical modeling of microtubule dynamics: Insights into physiology and disease,” *Prog Neurobiol*, vol. 92, no. 4, pp. 478–483, Dec. 2010, doi: 10.1016/J.PNEUROBIO.2010.08.003.

[211] A. J. Zwetsloot, G. Tut, and A. Straube, “Measuring microtubule dynamics,” *Essays Biochem.*, vol. 62, no. 6, pp. 725–735, Oct. 2018.

[212] M. A. Caporizzo and B. L. Prosser, “Need for Speed: The Importance of Physiological Strain Rates in Determining Myocardial Stiffness,” *Front Physiol*, vol. 12, Jul. 2021, doi: 10.3389/FPHYS.2021.696694.

[213] H. Sato *et al.*, “Microtubule Stabilization in Pressure Overload Cardiac Hypertrophy,” *J Cell Biol*, vol. 139, no. 4, pp. 963–973, 1997, Accessed: Sep. 04, 2023. [Online]. Available: http://www.jcb.org

[214] C. Zhang *et al.*, “Microtubule-mediated defects in junctophilin-2 trafficking contribute to myocyte transverse-tubule remodeling and Ca2+ handling dysfunction in heart failure,” *Circulation*, vol. 129, no. 17, pp. 1742–1750, Apr. 2014, doi: 10.1161/CIRCULATIONAHA.113.008452.

[215] B. S. Scopacasa, V. P. A. Teixeira, and K. G. Franchini, “Colchicine attenuates left ventricular hypertrophy but preserves cardiac function of aortic-constricted rats,” *J Appl Physiol*, vol. 94, no. 4, pp. 1627–1633, Apr. 2003, doi: 10.1152/japplphysiol.00744.2002.

[216] J. Luo *et al.*, “Integrative analyses of gene expression profile reveal potential crucial roles of mitotic cell cycle and microtubule cytoskeleton in pulmonary artery hypertension,” *BMC Med Genomics*, vol. 13, no. 1, p. 86, Jun. 2020, doi: 10.1186/s12920-020-00740-x.

[217] Q. Li, L. B. Meng, and D. P. Liu, “Screening and Identification of Therapeutic Targets for Pulmonary Arterial Hypertension Through Microarray Technology,” *Front Genet*, vol. 11, Jul. 2020, doi: 10.3389/fgene.2020.00782.

[218] P. Y. Xiong, S. L. Archer, and K. W. Prins, “Sex Hormones Directly Regulate Microtubules: New Insights Into Sex-Differences in Right Ventricular Function in Pulmonary Arterial Hypertension,” *Circulation*, vol. 140, no. 1, Nov. 2019.

[219] M. M. LeWinter, Y. Wu, S. Labeit, and H. Granzier, “Cardiac titin: Structure, functions and role in disease,” Jan. 2007. doi: 10.1016/j.cca.2006.06.035.

[220] M. M. Lewinter and H. Granzier, “Cardiac titin: A multifunctional giant,” May 18, 2010. doi: 10.1161/CIRCULATIONAHA.109.860171.

[221] M. Helmes *et al.*, “Mechanically Driven Contour-Length Adjustment in Rat Cardiac Titin’s Unique N2B Sequence Titin Is an Adjustable Spring,” 1999. [Online]. Available: http://www.circresaha.org

[222] W. A. Linke, “Titin Gene and Protein Functions in Passive and Active Muscle,” 2017, doi: 10.1146/annurev-physiol-021317-121234.

[223] S. Rain *et al.*, “Right ventricular myocardial stiffness in experimental pulmonary arterial hypertension,” *Circ Heart Fail*, vol. 9, no. 7, Jul. 2016, doi: 10.1161/CIRCHEARTFAILURE.115.002636.

[224] K. Stam *et al.*, “Cardiac remodelling in a swine model of chronic thromboembolic pulmonary hypertension: comparison of right vs. left ventricle,” *Journal of Physiology*, vol. 597, no. 17, pp. 4465–4480, Jun. 2019.

[225] M. R. Zile *et al.*, “Myocardial stiffness in patients with heart failure and a preserved ejection fraction contributions of collagen and titin,” *Circulation*, vol. 131, no. 14, pp. 1247–1259, 2015, doi: 10.1161/CIRCULATIONAHA.114.013215.

[226] W. A. Linke and J. M. Fernandez, “Cardiac titin: molecular basis of elasticity and cellular contribution to elastic and viscous stiffness components in myocardium,” *Mechanics of Elastic Biomolecules*, vol. 23, pp. 483–497, 2003, doi: 10.1007/978-94-010-0147-2_9.

[227] S. P. Bell, L. Nyland, M. D. Tischler, M. Mcnabb, H. Granzier, and M. M. Lewinter, “Alterations in the Determinants of Diastolic Suction During Pacing Tachycardia Integrative Physiology,” 2000. [Online]. Available: http://www.circresaha.org

[228] Y. Wu *et al.*, “Changes in titin isoform expression in pacing-induced cardiac failure give rise to increased passive muscle stiffness,” *Circulation*, vol. 106, no. 11, pp. 1384–1389, Sep. 2002, doi: 10.1161/01.CIR.0000029804.61510.02.

[229] W. A. Jaber *et al.*, “Titin isoforms, extracellular matrix, and global chamber remodeling in experimental dilated cardiomyopathy: functional implications and mechanistic insight.,” *Circ Heart Fail*, vol. 1, no. 3, pp. 192–199, 2008, doi: 10.1161/CIRCHEARTFAILURE.108.768465.

[230] S. F. Nagueh *et al.*, “Altered titin expression, myocardial stiffness, and left ventricular function in patients with dilated cardiomyopathy,” *Circulation*, vol. 110, no. 2, pp. 155–162, Jul. 2004, doi: 10.1161/01.CIR.0000135591.37759.AF.

[231] C. Neagoe *et al.*, “Titin isoform switch in ischemic human heart disease,” *Circulation*, vol. 106, no. 11, pp. 1333–1341, Sep. 2002, doi: 10.1161/01.CIR.0000029803.93022.93.

[232] I. Makarenko *et al.*, “Passive stiffness changes caused by upregulation of compliant titin isoforms in human dilated cardiomyopathy hearts,” *Circ Res*, vol. 95, no. 7, pp. 708–716, Oct. 2004, doi: 10.1161/01.RES.0000143901.37063.2f.

[233] C. M. Loescher *et al.*, “Titin governs myocardial passive stiffness with major support from microtubules and actin and the extracellular matrix,” *Nature Cardiovascular Research*, vol. 2, no. 11, pp. 991–1002, Nov. 2023, doi: 10.1038/s44161-023-00348-1.

[234] H. L. Granzier and T. C. Irving, “Passive Tension in Cardiac Muscle: Contribution of Collagen, Titin, Microtubules, and Intermediate Filaments,” 1995.

[235] N. Fukuda, Y. Wu, P. Nair, and H. L. Granzier, “Phosphorylation of titin modulates passive stiffness of cardiac muscle in a titin isoform-dependent manner,” *Journal of General Physiology*, vol. 125, no. 3, pp. 257–271, Mar. 2005, doi: 10.1085/jgp.200409177.

[236] D. Mackenna, S. R. Summerour, and F. J. Villarreal, “Role of mechanical factors in modulating cardiac fibroblast function and extracellular matrix synthesis,” 2000. [Online]. Available: www.elsevier.com/locate/cardioreswww.elsevier.nl/locate/cardiores

[237] F. J. Villarreal and W. H. Dillmann, “Cardiac hypertrophy-induced changes in mRNA levels for TGF-P, fibronectin, and collagen,” 1992.

[238] F. J. Villarreal, N. N. Kim, and F. J. Villareal, “Regulation of Myocardial Extracellular Matrix Components by Mechanical and Chemical Growth Factors.”

[239] W. Carver, L. Terracio, and T. K. Borg, “Expression and accumulation of interstitial collagen in the neonatal rat heart,” *Anat Rec*, vol. 236, no. 3, pp. 511–520, 1993, doi: 10.1002/ar.1092360311.

[240] D. A. MacKenna, S. M. Vaplon, and A. D. McCulloch, “Microstructural model of perimysial collagen fibers for resting myocardial mechanics during ventricular filling,” 1997.

[241] J. Parvizi and G. K. Kim, “Collagen,” in *High Yield Orthopaedics*, 2010, pp. 107–109.

[242] J. Rodriguez-Feo, J. Sluijter, D. Kleijn, and G. Pasterkamp, “Modulation of Collagen Turnover in Cardiovascular Disease,” *Curr Pharm Des*, vol. 11, no. 19, pp. 2501–2514, Jul. 2005, doi: 10.2174/1381612054367544.

[243] Z. Wang, D. A. Schreier, T. A. Hacker, and N. C. Chesler, “Progressive right ventricular functional and structural changes in a mouse model of pulmonary arterial hypertension,” *Physiol Rep*, vol. 1, no. 7, p. e00184, Dec. 2013, doi: 10.1002/PHY2.184.

[244] L. Todorovich-Hunter, D. J. Johnson, P. Ranger, and M. Rabinovitch, “Altered Elastin and Collagen Synthesis Associated with Progressive Pulmonary Hypertension Induced by Monocrataline. A Biochemical and Ultrastructural Study,” *Lab Invest.*, vol. 58, no. 2, pp. 184–195, 1988.

[245] H. J. Bogaard *et al.*, “Chronic pulmonary artery pressure elevation is insufficient to explain right heart failure,” *Circulation*, vol. 120, no. 20, pp. 1951–1960, Nov. 2009, doi: 10.1161/CIRCULATIONAHA.109.883843.

[246] M. A. J. Borgdorff *et al.*, “Distinct loading conditions reveal various patterns of right ventricular adaptation,” *Am J Physiol Heart Circ Physiol*, vol. 305, pp. 354–364, 2013, doi: 10.1152/ajpheart.00180.2013.-Right.

[247] C. F. Baicu *et al.*, “Time course of right ventricular pressure-overload induced myocardial fibrosis: relationship to changes in fibroblast postsynthetic procollagen processing,” *Am J Physiol Heart Circ Physiol*, vol. 303, pp. 1128–1134, 2012, doi: 10.1152/ajpheart.00482.2012.-Myocardial.

[248] A. J. Woodiwiss *et al.*, “Reduction in Myocardial Collagen Cross-Linking Parallels Left Ventricular Dilatation in Rat Models of Systolic Chamber Dysfunction,” 2001. [Online]. Available: http://www.circulationaha.org

[249] M. Nguyen-Truong *et al.*, “Establishment of adult right ventricle failure in ovine using a graded, animal-specific pulmonary artery constriction model,” *Animal Model Exp Med*, vol. 3, no. 2, pp. 182–192, Jun. 2020, doi: 10.1002/AME2.12124.

[250] D. W. Park, A. Sebastiani, C. H. Yap, M. A. Simon, and K. Kim, “Quantification of Coupled Stiffness and Fiber Orientation Remodeling in Hypertensive Rat Right-Ventricular Myocardium Using 3D Ultrasound Speckle Tracking with Biaxial Testing,” *PLoS One*, vol. 11, no. 10, Oct. 2016, doi: 10.1371/JOURNAL.PONE.0165320.

[251] F. Ahmad, S. Soe, J. Albon, R. Errington, and P. Theobald, “Quantifying the microstructural and biomechanical changes in the porcine ventricles during growth and remodelling,” *Acta Biomater*, vol. 171, pp. 166–192, Nov. 2023, doi: 10.1016/j.actbio.2023.09.044.

[252] M. Ren, C. W. Ong, M. L. Buist, and C. H. Yap, “Biventricular biaxial mechanical testing and constitutive modelling of fetal porcine myocardium passive stiffness,” *J Mech Behav Biomed Mater*, vol. 134, Oct. 2022, doi: 10.1016/j.jmbbm.2022.105383.

[253] F. H. Silver, I. Horvath, and D. J. Foran, “Mechanical implications of the domain structure of fiber-forming collagens: Comparison of the molecular and fibrillar flexibilities of the α1-chains found in types I-III collagen,” *J Theor Biol*, vol. 216, no. 2, pp. 243–254, 2002, doi: 10.1006/jtbi.2002.2542.

[254] C. Sanyal, N. Pietsch, S. Ramirez Rios, L. Peris, L. Carrier, and M. J. Moutin, “The detyrosination/re-tyrosination cycle of tubulin and its role and dysfunction in neurons and cardiomyocytes,” Mar. 15, 2023, *Elsevier Ltd*. doi: 10.1016/j.semcdb.2021.12.006.

[255] W. M. Torres *et al.*, “Regional and temporal changes in left ventricular strain and stiffness in a porcine model of myocardial infarction,” *Am J Physiol Heart Circ Physiol*, vol. 315, no. 4, pp. H958–H967, Oct. 2018, doi: 10.1152/ajpheart.00279.2018.

[256] I. J. Lundorff *et al.*, “Imaging-Tissue Doppler, Speckle Tracking and Strain Imaging Right ventricular speckle tracking in patients with heart failure-a comparison of right ventricular measures.” [Online]. Available: https://academic.oup.com/eurheartj/article/41/Supplement_2/ehaa946.0145/6003664

[257] N. Kawel-Boehm *et al.*, “Reference ranges (‘normal values’) for cardiovascular magnetic resonance (CMR) in adults and children: 2020 update,” Dec. 01, 2020, *BioMed Central Ltd*. doi: 10.1186/s12968-020-00683-3.

[258] A. I. Veress, J. A. Weiss, G. J. Klein’, and G. T. Gullberg’, “Quantification of 3D Left Ventricular Deformation using Hyperelastic Warping: Comparisons between MRI and PET Imaging.”

[259] H. Zou *et al.*, “Three-dimensional biventricular strains in pulmonary arterial hypertension patients using hyperelastic warping,” *Comput Methods Programs Biomed*, vol. 189, Jun. 2020, doi: 10.1016/j.cmpb.2020.105345.

[260] A. Youssef, E.-S. H. Ibrahim, G. Korosoglou, R. Abraham, R. G. Weiss, and N. F. Osman, “Strain-encoding cardiovascular magnetic resonance for assessment of right-ventricular regional function,” 2008, doi: 10.1186/1532-429X-10-33.

[261] G. Korosoglou *et al.*, “Real-time fast strain-encoded magnetic resonance imaging to evaluate regional myocardial function at 3.0 Tesla: Comparison to conventional tagging,” *Journal of Magnetic Resonance Imaging*, vol. 27, no. 5, pp. 1012–1018, May 2008, doi: 10.1002/jmri.21315.

[262] Z. A. Fayad *et al.*, “Right ventricular regional function using MR tagging: Normals versus chronic pulmonary hypertension,” *Magn Reson Med*, vol. 39, no. 1, pp. 116–123, 1998, doi: 10.1002/mrm.1910390118.

[263] G. Xiong *et al.*, “Comprehensive Modeling and Visualization of Cardiac Anatomy and Physiology from CT Imaging and Computer Simulations,” *IEEE Trans Vis Comput Graph*, vol. 23, no. 2, pp. 1014–1028, Feb. 2017, doi: 10.1109/TVCG.2016.2520946.

[264] S. M. Shavik *et al.*, “Computational Modeling Studies of the Roles of Left Ventricular Geometry, Afterload, and Muscle Contractility on Myocardial Strains in Heart Failure with Preserved Ejection Fraction,” *J Cardiovasc Transl Res*, vol. 14, pp. 1131–1145, Apr. 2021.

[265] R. Pourmodheji *et al.*, “Computational modelling of multi-temporal ventricular–vascular interactions during the progression of pulmonary arterial hypertension,” *Journal of Royal Society Interface*, vol. 19, Nov. 2022.

[266] M. Lei, M. Franz, J. A. Fraser, H. Zhang, and I. Adeniran, “Abnormal calcium homeostasis in heart failure with preserved ejection fraction is related to both reduced contractile function and incomplete relaxation: an electromechanically detailed biophysical modeling study,” *Frontiers in Physiology | www.frontiersin.org*, vol. 6, p. 78, 2015, doi: 10.3389/fphys.2015.00078.

[267] M. Pagani *et al.*, “Relationship of Transmural Variations in Myofiber Contractility to Left Ventricular Ejection Fraction: Implications for Modeling Heart Failure Phenotype With Preserved Ejection Fraction,” *Frontiers in Physiology | www.frontiersin.org*, vol. 1, p. 1003, 2018, doi: 10.3389/fphys.2018.01003.

[268] O. O. Odeigah, D. Valdez-Jasso, S. T. Wall, and J. Sundnes, “Computational models of ventricular mechanics and adaptation in response to right-ventricular pressure overload,” Aug. 24, 2022, *Frontiers Media S.A.* doi: 10.3389/fphys.2022.948936.

[269] K. L. Sack, N. H. Davies, J. M. Guccione, and T. Franz, “Personalised computational cardiology: Patient-specific modelling in cardiac mechanics and biomaterial injection therapies for myocardial infarction,” *Heart Fail Rev*, vol. 21, no. 6, pp. 815–826, Nov. 2016, doi: 10.1007/s10741-016-9528-9.

[270] T. Arts, T. Delhaas, P. Bovendeerd, X. Verbeek, and F. W. Prinzen, “Adaptation to mechanical load determines shape and properties of heart and circulation: the CircAdapt model,” *Am J Physiol Heart Circ Physiol*, vol. 288, pp. 1943–1954, 2005, doi: 10.1152/ajpheart.00444.

[271] S. M. Kim, E. B. Randall, F. Jezek, D. A. Beard, and N. C. Chesler, “Computational modeling of ventricular-ventricular interactions suggest a role in clinical conditions involving heart failure,” *Front Physiol*, vol. 14, 2023, doi: 10.3389/fphys.2023.1231688.

[272] M. J. Colebank and N. C. Chesler, “An in-silico analysis of experimental designs to study ventricular function: A focus on the right ventricle,” *PLoS Comput Biol*, vol. 18, no. 9, Sep. 2022, doi: 10.1371/journal.pcbi.1010017.

[273] C. Xi *et al.*, “Patient-Specific Computational Analysis of Ventricular Mechanics in Pulmonary Arterial Hypertension,” *J Biomech Eng*, vol. 138, no. 11, Nov. 2016, doi: 10.1115/1.4034559.

[274] A. D. Gomez, H. Zou, M. E. Bowen, X. Liu, E. W. Hsu, and S. H. McKellar, “Right ventricular fiber structure as a compensatory mechanism in pressure overload: A computational study,” *J Biomech Eng*, vol. 139, no. 8, Aug. 2017, doi: 10.1115/1.4036485.

[275] X. Henrik Finsberg *et al.*, “Computational quantification of patient-specific changes in ventricular dynamics associated with pulmonary hypertension,” *Am J Physiol Heart Circ Physiol*, vol. 317, pp. 1363–1375, 2019, doi: 10.1152/ajpheart.00094.

[276] R. Avazmohammadi *et al.*, “A Computational Cardiac Model for the Adaptation to Pulmonary Arterial Hypertension in the Rat,” *Ann Biomed Eng*, vol. 47, no. 1, pp. 138–153, Jan. 2019, doi: 10.1007/s10439-018-02130-y.

[277] R. Shimkunas *et al.*, “Left ventricular myocardial contractility is depressed in the borderzone after posterolateral myocardial infarction,” *Annals of Thoracic Surgery*, vol. 95, no. 5, pp. 1619–1625, May 2013, doi: 10.1016/j.athoracsur.2013.02.005.

[278] J. F. Wenk *et al.*, “A novel method for quantifying the in-vivo mechanical effect of material injected into a myocardial infarction,” *Annals of Thoracic Surgery*, vol. 92, no. 3, pp. 935–941, Sep. 2011, doi: 10.1016/j.athoracsur.2011.04.089.

[279] J. Walmsley *et al.*, “Fast Simulation of Mechanical Heterogeneity in the Electrically Asynchronous Heart Using the MultiPatch Module,” *PLoS Comput Biol*, vol. 11, no. 7, Jul. 2015, doi: 10.1371/journal.pcbi.1004284.

[280] S. M. Shavik, L. Zhong, X. Zhao, and L. C. Lee, “In-silico assessment of the effects of right ventricular assist device on pulmonary arterial hypertension using an image based biventricular modeling framework,” *Mech Res Commun*, vol. 97, pp. 101–111, Apr. 2019, doi: 10.1016/j.mechrescom.2019.04.008.

[281] A. T6zeren, “CONTINUUM RHEOLOGY OF MUSCLE CONTRACTION AND ITS APPLICATION TO CARDIAC CONTRACTILITY.”

[282] J. M. Guccione, L. K. Waltlman, and A. Mem, “Mechanics of Active Contraction in Cardiac Muscle: Part II-Cylindrical Models of the Systolic Left Ventricle,” 1991. [Online]. Available: http://asmedigitalcollection.asme.org/biomechanical/article-pdf/115/1/82/5766440/82_1.pdf

[283] C. Tossas-Betancourt *et al.*, “Data-driven computational models of ventricular-arterial hemodynamics in pediatric pulmonary arterial hypertension,” *Front Physiol*, vol. 13, Sep. 2022, doi: 10.3389/fphys.2022.958734.

[284] O. O. Odeigah, E. D. Kwan, K. M. Garcia, H. Finsberg, D. Valdez-Jasso, and J. Sundnes, “A computational study of right ventricular mechanics in a rat model of pulmonary arterial hypertension,” *Front Physiol*, vol. 15, 2024, doi: 10.3389/fphys.2024.1360389.

[285] S. G. Tewari, S. M. Bugenhagen, K. C. Vinnakota, J. J. Rice, P. M. L. Janssen, and D. A. Beard, “Influence of metabolic dysfunction on cardiac mechanics in decompensated hypertrophy and heart failure,” *J Mol Cell Cardiol*, vol. 94, pp. 162–175, May 2016, doi: 10.1016/j.yjmcc.2016.04.003.

[286] V. Vedula, J. Lee, H. Xu, C. C. J. Kuo, T. K. Hsiai, and A. L. Marsden, “A method to quantify mechanobiologic forces during zebrafish cardiac development using 4-D light sheet imaging and computational modeling,” *PLoS Comput Biol*, vol. 13, no. 10, Oct. 2017, doi: 10.1371/journal.pcbi.1005828.

[287] J. Lee *et al.*, “Moving Domain Computational Fluid Dynamics to Interface with an Embryonic Model of Cardiac Morphogenesis,” *PLoS One*, vol. 8, no. 8, Aug. 2013, doi: 10.1371/journal.pone.0072924.

[288] D. Vélez-Rendón and D. Valdez-Jasso, “Multiscale modeling of ventricular–vascular dysfunction in pulmonary arterial hypertension,” Sep. 01, 2019, *Elsevier B.V.* doi: 10.1016/j.cobme.2019.09.004.

[289] J. W. Gerringer, J. C. Wagner, D. Vélez-Rendón, and D. Valdez-Jasso, “Lumped-parameter models of the pulmonary vasculature during the progression of pulmonary arterial hypertension,” *Physiol Rep*, vol. 6, no. 3, Feb. 2018, doi: 10.14814/phy2.13586.

[290] C. Stevens, E. Remme, I. LeGrice, and P. Hunter, “Ventricular mechanics in diastole: Material parameter sensitivity,” *J Biomech*, vol. 36, no. 5, pp. 737–748, May 2003, doi: 10.1016/S0021-9290(02)00452-9.

[291] K. LeBar, K. Roth, E. Evans, A. Chicco, J. Pang, and Z. Wang, “Contribution of microtubule network to the passive anisotropic viscoelasticity of right ventricle free wall,” *https://doi.org/10.1152/physiol.2023.38.S1.5732821*, vol. 38, no. S1, May 2023, doi: 10.1152/PHYSIOL.2023.38.S1.5732821.

[292] W. M. Torres *et al.*, “Changes in Myocardial Microstructure and Mechanics With Progressive Left Ventricular Pressure Overload,” *Journal of the American College of Cardiology Basic Translational Sciences*, vol. 5, no. 5, pp. 463–480, Apr. 2020.

[293] H. Suga and K. Sagawa, “Instantaneous Pressure-Volume Relationships and Their Ratio in the Excised, Supported Canine Left Ventricle,” *Circ Res*, vol. 35, Jul. 1974.

[294] M. J. Faber *et al.*, “Right and left ventricular function after chronic pulmonary artery banding in rats assessed with biventricular pressure-volume loops,” *Am J Physiol Heart Circ Physiol*, vol. 291, no. 4, pp. 1580–1586, Oct. 2006.

[295] E. Naghavi *et al.*, “Rapid Estimation of Left Ventricular Contractility with a Physics-Informed Neural Network Inverse Modeling Approach,” Jan. 2024, [Online]. Available: http://arxiv.org/abs/2401.07331

Appendix

Biaxial/Uniaxial Mechanical Testing

DATE: _____ Experimentalist (initials): _____

Species: □ Rat □ Sheep Group/Treatment: _____

Sex: _____ Age: _____ Body weight: _____

TISSUE HARVEST: (rinse with saline and harvest the LV, RV, septum; slice the tissue(s) needed for mechanical tests and put the rest part of fresh tissue in -80C; then quickly transfer testing tissue to CPS or 1x PBS on ice, and then placed in BDM+CPS at 37C in tissue bath to get prepared for mechanical tests)

Tissue preparation: □ fresh tissue (___ hours post harvest) □ frozen tissue

Longitudinal (outflow tract) direction marked □ Yes □ No

LV weight (g): _____ RV weight (g): _____ Septum weight (g): _____

Original/Testing tissue thickness:

RV: ____, ____, ____, ____, ____ mm

Layers of myocardium for mechanical tests: □ epicardial □ middle □ endocardial

SETTING UP TESTER:

First, plug in the actuator, load cell, and camera wall plugs. Next, open Baumer's "IP config tool" computer app to set the camera to the correct IP address. Next, open the standard tester LabVIEW code "CVB Biaxial Tester Code (11-2-21)" which can be found in the C drive through the following:

Users - Public - Public Documents - CVB Biaxial Testing System - LabVIEW Codes - In use biaxial codes

When the LabVIEW is open, run the "Set Home" actuator function so that the actuators' internal programming is aware of their location. Let it run several times. The actuators will not obey any other movement commands if the Set Home function is not executed first. Make sure to do this before mounting the sample.

Once these steps are complete, the tester should be ready to run. When acquiring data, if the force acquisition lags (visually) redo the test. Also, if the image acquisition does not appear smooth (is choppy) redo the test.

TESTER SETTINGS:

LC Acquisition Rate (1000Hz rate & 50 = no. of samples is the standard): _____

LabVIEW code used if different than standard: _____

Number of buffers (5000 is standard) _____

□ Top and left camera borders are coincident or within mounting needles, and they are equidistant from the top left marker on the tissue sample

TISSUE MOUNTING:

□ Load cell force magnitudes are set to zero before mounting

□ Actuators are set home using "Set Home" function in LabVIEW before mounting

□ All the arms are parallel to the sample surface.

□ Each sample's four corners are at right angle (approximate)

□ Each sample is under the stretch stage and flat (approximate)

□ **Bath Check** pH: ____ Temperature: ____ □ **Marker**

PARAMETERS SETTING:

Strain range (max): _____ % (20% suggested for ventricles)

Strain rate at 0.1Hz: _____ mm/s; Strain rate at 1Hz: _____ mm/s

Strain rate at 2Hz: _____ mm/s; Strain rate at 5Hz: _____ mm/s

Strain rate at 8Hz: _____ mm/s

$Strain\ rate = \frac{displacement\ (mm)}{one\ cycle/2\ (s)}$, $displacement\ (mm) = Preload\ Length \times Strain\ Range$

Type of the cyclic load: ~~□ triangle~~ □ sinusoidal

Type of the test: □ Biaxial □ Constrained Biaxial □ Uniaxial □ Constrained Uniaxial

1. MECHANICAL TEST:

1. Equilibrium (30 min; in tissue bath with Kreb's solution + BDM; at 25-37°C)

2. Preconditioning at ___Hz (for 15 cycles),(same as the testing strain range)

3. Equibiaxial test **at each frequency**

    1) Cyclic tensile tests. Make sure to record at least 3 cycles of data (see the Table). (Force data: 1000Hz);
    2) Make sure that the DIC works at each frequency
    3) Drain the bath so that the solution level is even with the top of the tissue for 5 and 8Hz cyclic testing (Fixes DIC distortion problem)
    4) Stress relaxation (100 s. at each strain ratio; Ramp speed: the same as the corresponding cyclic test speed and detailed calculation see above "Strain rate") (force data: 1k Hz; image data: same frequency used for ramp.)

5) Run preload before colchicine testing in case of tissue not being “flat” in the mounting system.

□ 3% □6% □9% □ 12% □ 15%

5) Repeat for all frequencies and log the Table below:

Frequency (Hz)	FPS	Max Force (N)	Force vs Time Plot	Testing Cycle #	Rest Period (s)	Ramp speed (mm/s)
0.1	5			5	500	
1	50			15	150	
2	100			15	75	
5	200			15	37.5	
8	200			15	25.5	

4. Repeat the 1Hz test to ensure no plastic deformation (damage) in the tissue

5. Colchicine treatment (30 min; in tissue bath with 0.3 mM Col; at 25-37°C)

6. Stress relaxation testing:

a. 15% strain at 5Hz speed (at physiological frequency): Compare the results to the pre-colchicine treatment; If no change is seen, wait another 15 minutes before running further tests.

b. 15% strain at 8Hz speed (at exercise)

7. Cyclic equibiaxial testing: *make sure solution level is lower than markers

a. 5Hz for 15 cycles

b. 8hz for 15 cycles

Tissue storage:

□ Unused sample: store fresh tissue in centrifuge tube in **-80C (FIRSTLY before test)**

***Type of tissue varied depending on experiment. Suggestion: for rat, save left lung and non-fixed RV; for sheep, save un-tested RV.**

□ Tested sample: in 10% formalin (<= 1-2 weeks and embed in paraffin block)

Clean up: *ensure that all equipment and tissue bath container are "sterilized" following usage; wipe the mounting system with alcohol to remove blood stains and tissue residue.

Data Analysis

□ Analyze 3 cycles worth of images for biaxial testing

***The average cycle data is more trustworthy than only analyzing one cycle, especially for higher frequencies**

□ Once stress-strain curves are generated, shift stress values up 1 cell to account for image offset

Notes:

CVB Biaxial Tester User's Manual

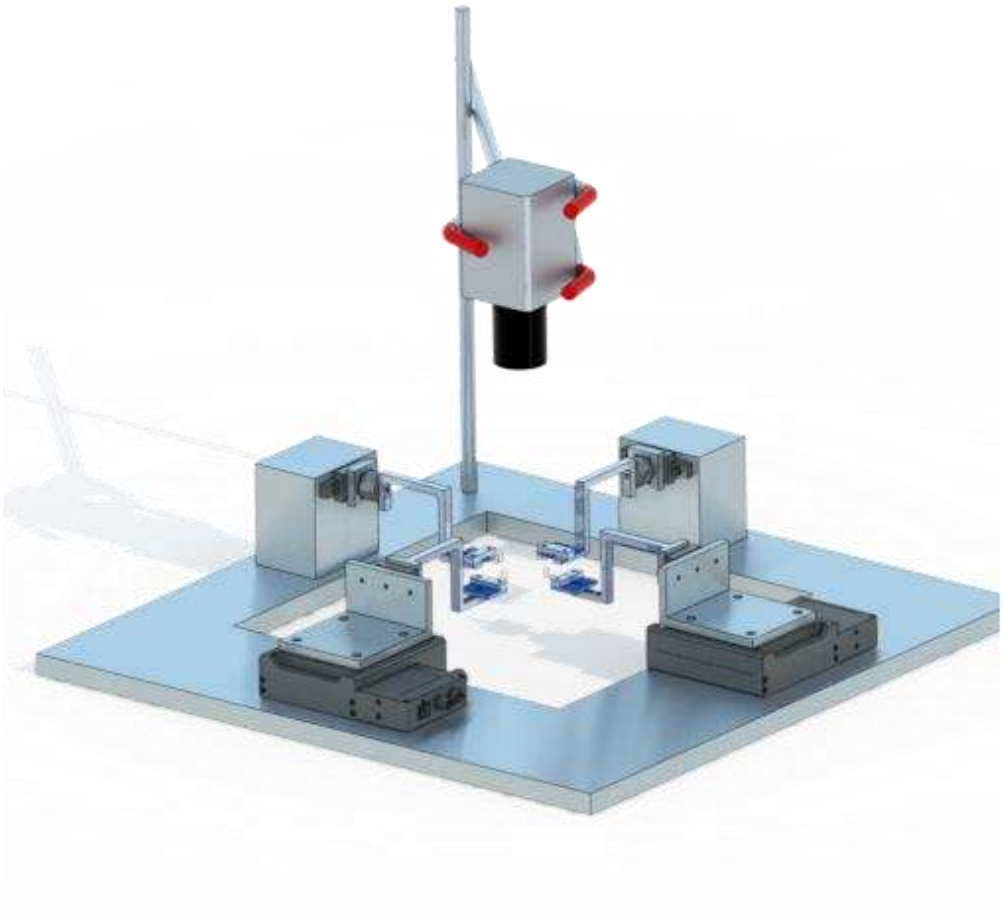

Version 1: Kellan Roth

Version 2: Brandyn Garcia, Olivia Pyke and Kristen LeBar

Setting up the biaxial tester

Do the following before mounting your testing sample

1. Plug in the camera, load cells, and actuators (each have a standard wall plug)

2. Open the “IP Config tool” program in the computer

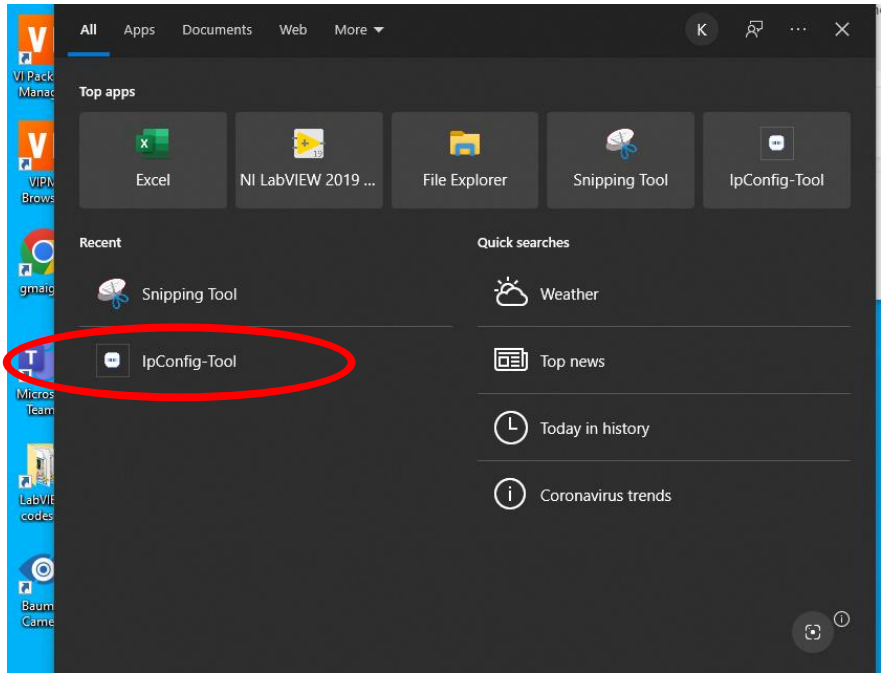

It may take a minute or two for the camera to show up. Once it does, the app shown below will appear. Select “Force-IP all” to allow the camera IP address to coordinate with the computer. Close the window when completed.

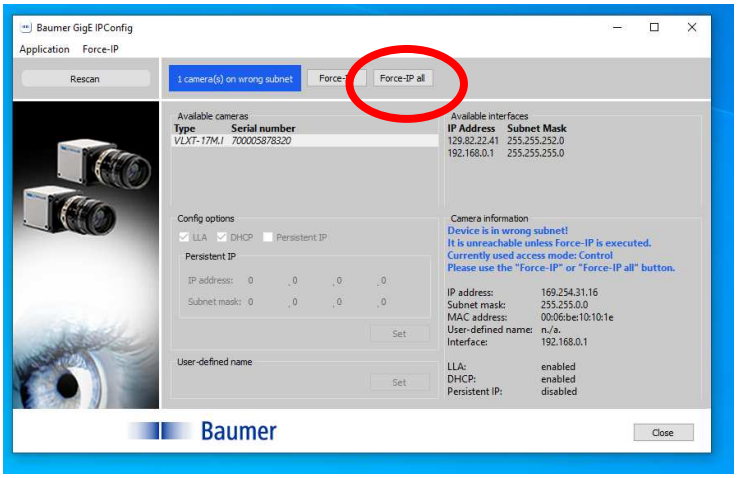

3. Open the biaxial testing LabVIEW code through the following folder chain:

Users > Public > Documents > CVB Biaxial Testing System >LabVIEW codes

> In Use Biaxial Test Codes

The image below shows the contents of this folder.

Select **CVB Biaxial Tester Code (11-2-21)** as the LabVIEW program to run for cyclic testing and for system setup. Past troubleshooting codes can be found under Kellan Roth in the folder shown below.

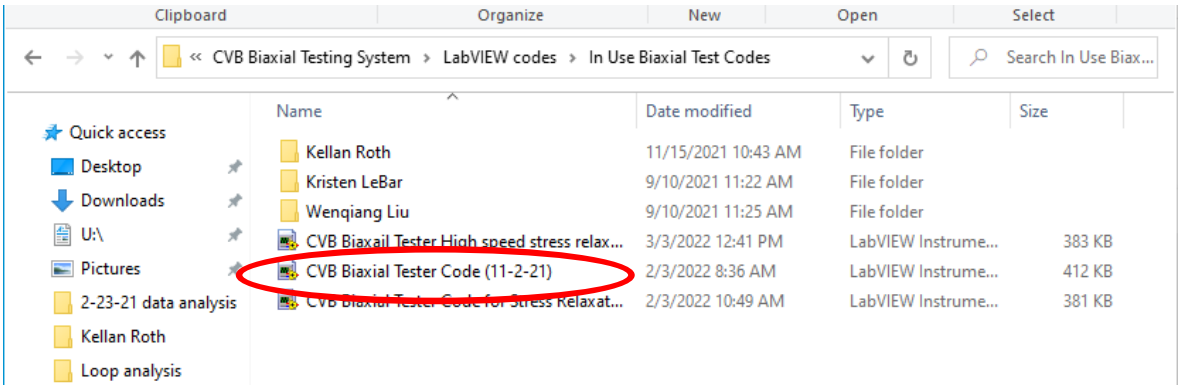

The front panel of this code is shown in the image below.

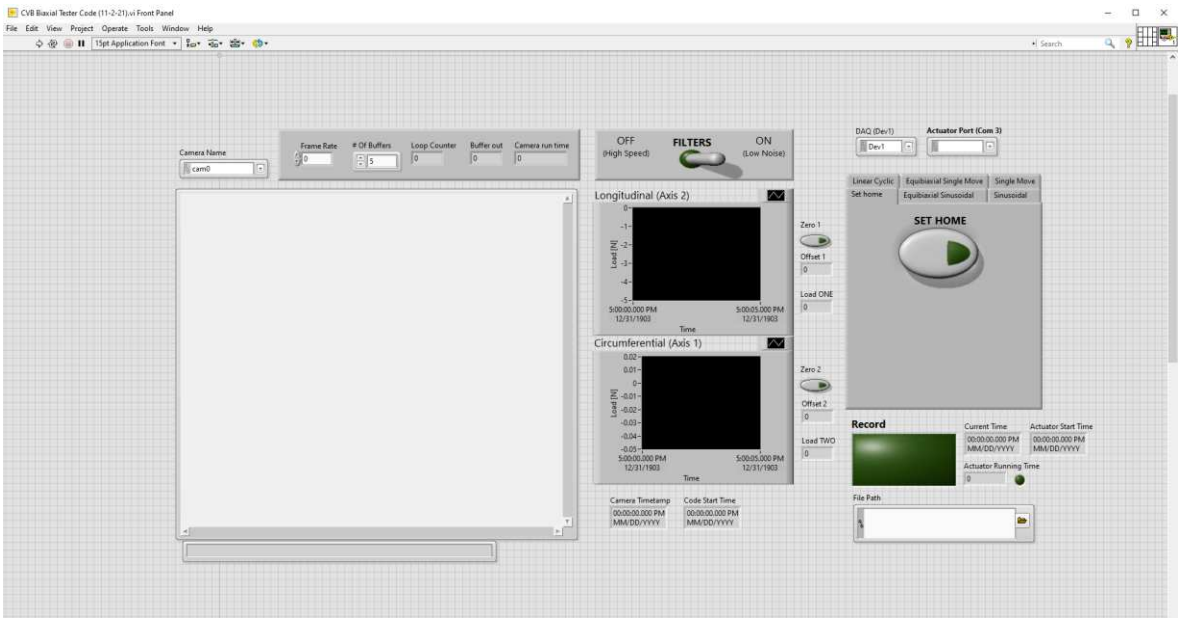

4. You can leave the camera frame rate at 0 for now. In the actuator control, set the port to COM3, as shown below.

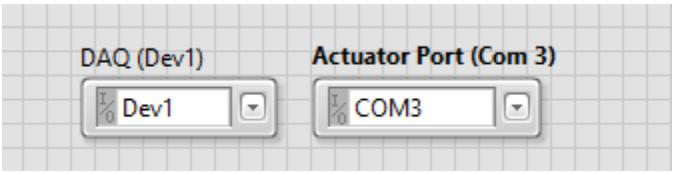

5. Run the software  and go to the set home function under the actuator control. Select the green arrow below SET HOME in the set home tab to allow the actuators to locate themselves to a neutral location. Allow them to move home several times, then stop the software. 

Different Testing Types

At this point, the tester is ready for a sample to be mounted

1. **Equibiaxial Testing:** Note, more detailed testing procedure for cyclic and stress relaxation tests can be found in the “Conducting testing and setting parameters” section

    - For Equibiaxial testing, mount your sample so that the mounting system rake tines are set equidistant from one another.
        i. It is possible to manually move the tines before mounting to adjust for different sample sizes

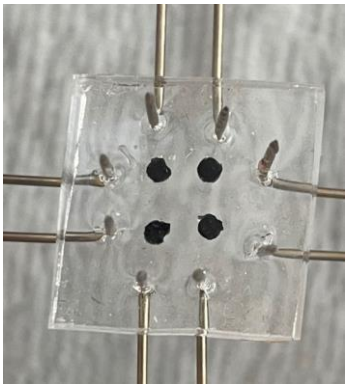

- Run the program and set the loadcell magnitudes to zero as shown in the image below using the Boolean switches.

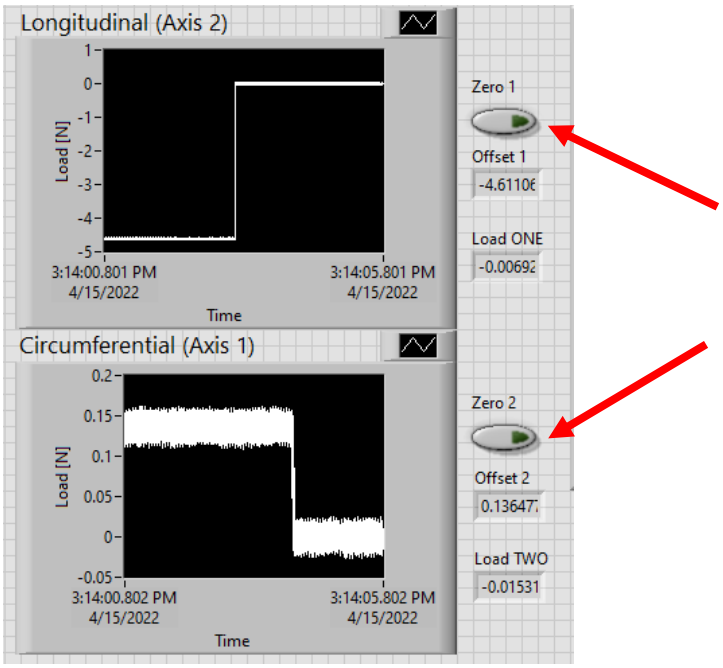

- Next, preload the sample (usually to 0.01N for small animal ventricles, 0.1N for large animal) using the single move actuator tab shown below. Be aware you will have to start and stop the LabVIEW code between different actions. Move the actuators individually by commanding different magnitudes and velocities in the respective actuator text boxes. Use small velocities and small initial displacements (e.g. 0.05mm/s, 0.1mm) for this process. It may take several attempts to reach your desired preload. Note: The testing system has tape labeling the two axes for reference.
- You also want the tissue to be flat (no curling on the edges) when it is on the mounting system, so you can adjust the tines until it is flat. Once it is at the desired position, measure the length and width of the tissue. This is for the area calculation in data post-processing protocol.

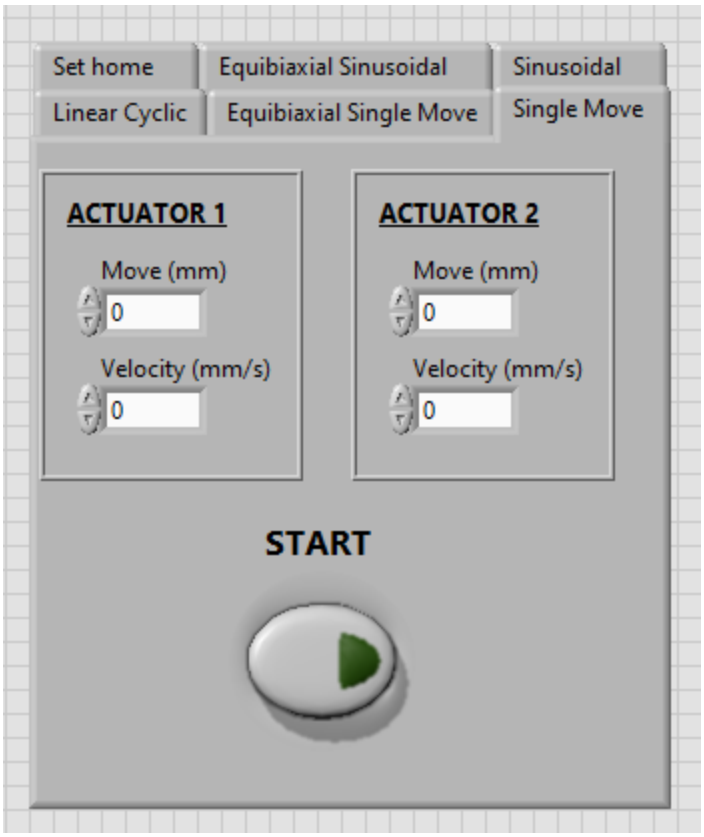

- At this point, once your sample is preloaded, you should use the equibiaxial sinusoidal actuator tab shown below for preconditioning and for equibiaxial cyclic testing. The number of cycles is generally **15** to precondition the sample during each test (location circled below).

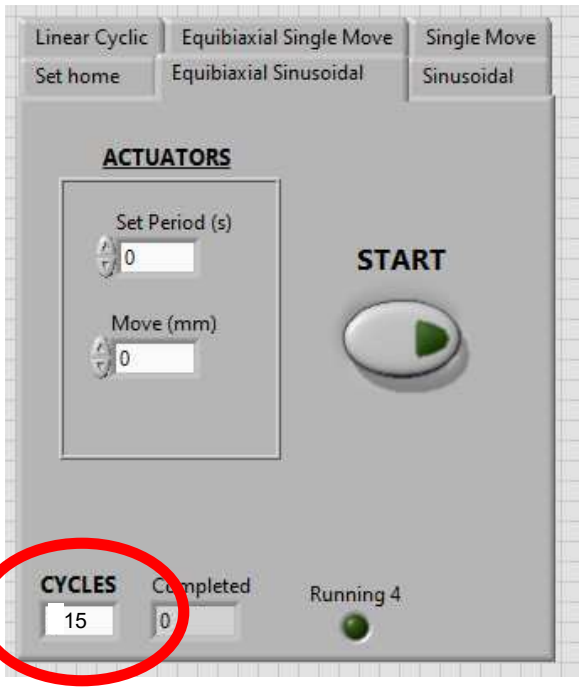

- For stress relaxation testing, use the Equibiaxial Single Move tab similarly as you used the sinusoidal tab.

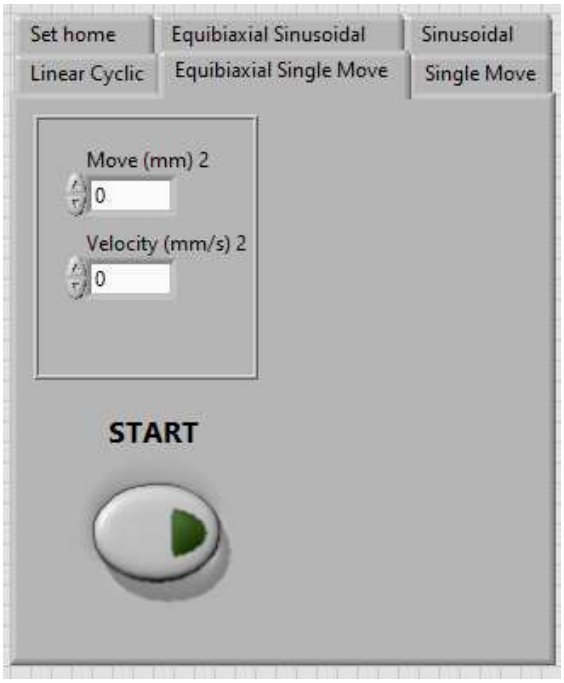

2. Non Equibiaxial Testing:

- Mount and preload the sample similarly as done with Equibiaxial testing.
- Use the Sinusoidal tab shown below to set different period and amplitudes for the different axes.

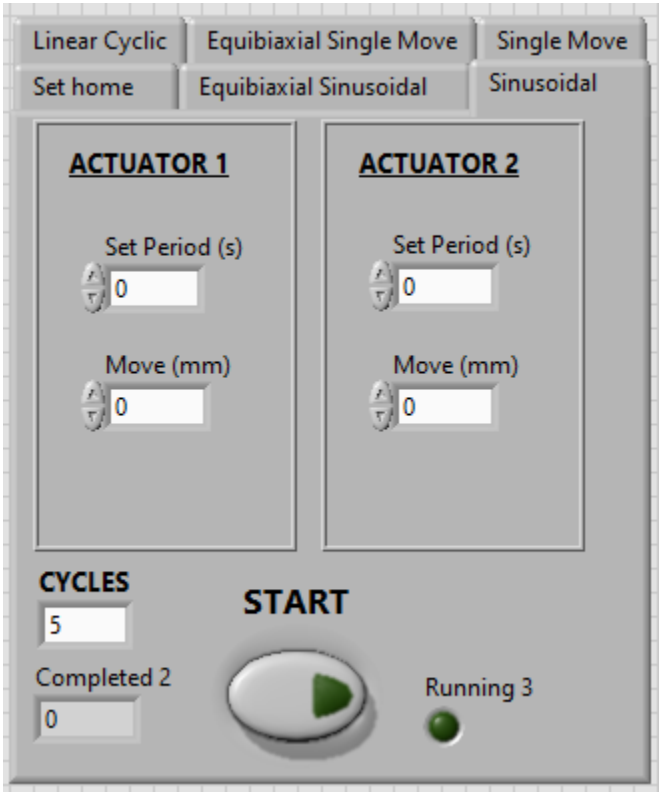

3. Constrained uniaxial testing
   - Mount and preload the sample similarly as done with Equibiaxial testing.
   - Use the sinusoidal tab shown under the Non Equibiaxial Testing section (section 2),but keep one axis at zero period and zero amplitude, and only change the axis which is being uniaxially deformed.
4. Unconstrained uniaxial testing
   - Mount the sample as shown in the image below where only two of the mounting systems are employed.

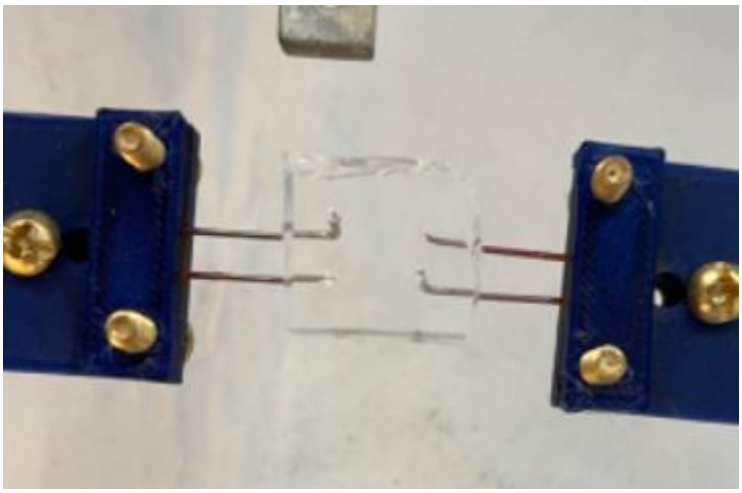

- Preload the sample using the single move function, and then conduct stress relaxation testing and cyclic testing using the single move tab and the sinusoidal tab as shown previously, but only commanding movement in one of the actuators.

Conducting testing & setting parameters

Cyclic testing:

1. Once the tissue is on the testing system, go into the LabVIEW interface and set the camera frame rate to the desired rate. Generally, set the number of buffers to 5000, as this should be sufficient for most applications (shown below).

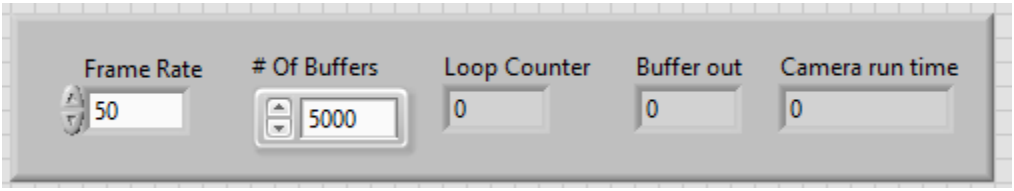

For determining the frame rate, always use a frame rate which will result in a constant achievable frame per cycle capability at the highest desired testing frequency. This will remove system induced variations in viscosity measurement. Current max frame rate capability (as of 4/21/22): 200FPS

Example: Rodent sample

Frequency	**Frames per testing cycle =FPS/max frequency or maximum of 50**	**Frame rate (FPS)**
0.1Hz	25	2.5
1Hz	25	25
2Hz	25	50
5Hz	25	125
8Hz	25	200

For this example, the max frames per cycle is 25 as 200FPS/8Hz is 25.

Example: Ovine sample

Frequency	**Frames per testing cycle =FPS/max frequency or maximum of 50**	**Frame rate (FPS)**
0.1Hz	50	5
1Hz	50	50
2Hz	50	100
3 Hz	50	150

For this example, the max frames per cycle is 50, as this is the desired standard frame per cycle, and 150FPS is achievable by the system.

2. For cyclic testing, always set the filters off as shown below.

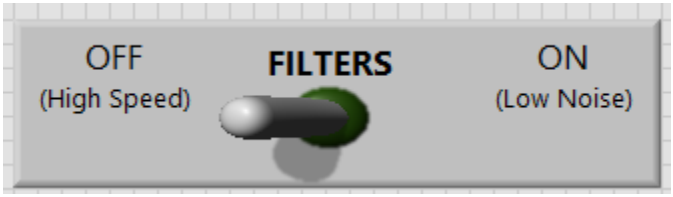

3. Set your file path to a desired location for storing your data. After testing, make sure to save a backup file in the CVB Testing System folder on the on-site computer.

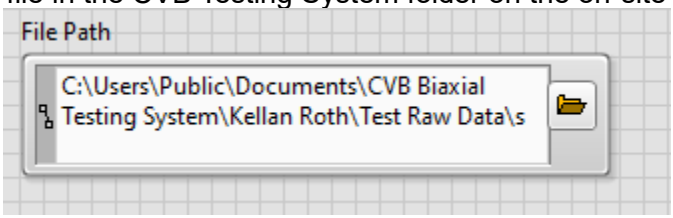

4. Using the sinusoidal tab that applies to your application (Equibiaxial or non-Equibiaxial), set your testing parameters for the testing period and amplitude.

    - The period is equal to 1/frequency

    - For amplitude, the magnitude is equal to the distance between jaws times the global strain. For example, if the sample is 10x10mm between the jaws, and the desired strain is 20%, the magnitude will be 2mm (10mm*0.2).

Frequency	Period (s)	Amplitude (mm)
0.1	10	2 (example)
1	1	2 (example)
2	0.5	2 (example)
5	0.2	2 (example)
8	0.125	2 (example)

5. Run 15 cycles of preconditioning at 1Hz and 20% strain under Equibiaxial sinusoidal deformation. Do not record this data.

6. Once your testing parameters (period, displacement) are put into the control tab, and your file path is set, run the program, and hit the record button when the camera starts capturing images (there is a delay before this starts to happen). Once recording, hit the

start button for the actuators to run for a set number of cycles (you must unselect the start button or the actuators will run continuously). When finished testing, stop recording and stop the LabVIEW interface. Check that your data was stored correctly.

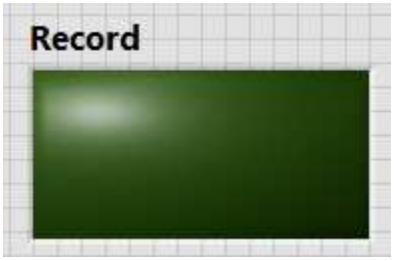

Note: In the block diagram, the number of samples and data rate should be set to 10 and 1000 respectively as shown in the image below. This will mitigate bottlenecking and lagging from the force data. An image is shown below on where to find this.

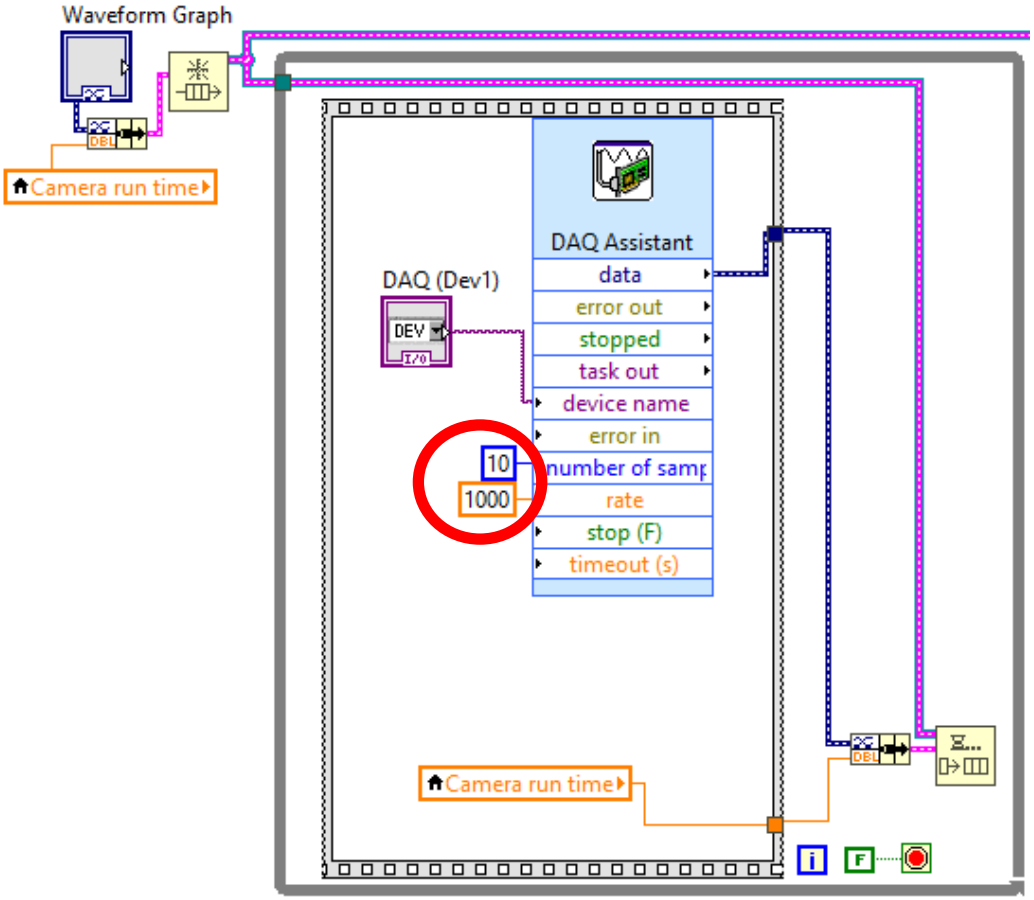

Stress Relaxation Testing

1. Stress relaxation can and is recommended to be done using a different LabVIEW interface than cyclic testing to avoid capturing images during the relaxation (unnecessary generally). The pathway on the lab computer to this code is as follows:

Users > Public > Documents > CVB Biaxial Testing System >LabVIEW codes

> In Use Biaxial Test Codes

The image below shows the contents of this folder.

Select: **CVB Biaxial Tester for Stress Relaxation** (circled) to conduct stress relaxation tests at low ramping speeds (corresponding to 1Hz and lower).

Select: **CVB Biaxial Tester high speed stress relaxation** (circled) to conduct stress relaxation tests at all ramping speeds.

This second code has a 3 second delay between commanding actuator movement and the actuators moving, which eliminates problems with stopping the actuator movement fast enough.

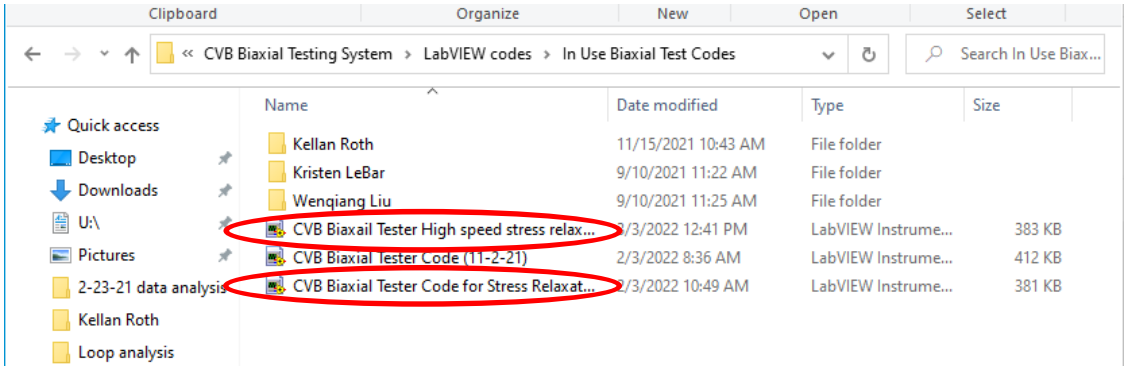

2. Using the Equibiaxial sinusoidal tab, precondition the sample with 15 cycles at 1Hz and 20% strain.

3. For setting stress relaxation parameters, use the following equation:

$$\text{Ramping Speed} = \frac{\Delta L}{\frac{1}{2}(T)}$$

where T=1/corresponding frequency (seconds), and $\Delta L = 0.2 \times$ unloaded length between tines (L_0).

For example: 10mm distance between jaws, 8Hz testing frequency

Ramping speed = 2mm/(1/2*0.125) = 32mm/s

4. Use the Equibiaxial single move tab, where the velocity is ramping speed, and the “Move” value is whatever strain you are measuring times the tines distance (usually 20% but can be anywhere from 3-25% depending on applications).

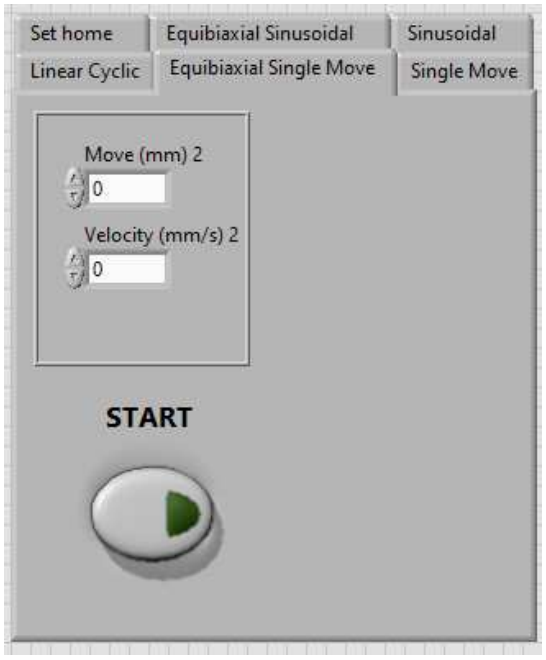

5. You can leave the filters on. Set the force values to zero (as described in setting up the biaxial tester section) before testing.

6. Once your testing parameters are put into the control tab, and your file path is set, run the program, and hit the record button. Once recording, hit the start button for the actuators to run. Wait for them to move, then **you must unselect**

the start button or the actuators will run continuously. When finished testing, stop recording and stop the LabVIEW interface. Check that your data was stored correctly.

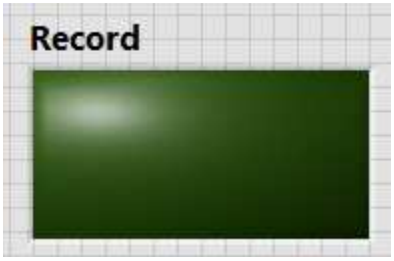

When Finished with Testing

1. Make sure all data is saved in the correct file location and in the backup files on the lab computer.
2. Close the tester code you were using (don’t need to save changes).
3. Turn off the light.
4. Unplug the actuators, camera, and light.
5. Log off of the computer.

Instructions for analyzing cyclic data

1. After testing, your saved data should include a force file, images, and an image timestamp file as shown below. Open the force and image timestamp files in excel. Save the Force_1 and Image_Timestamps files as excel documents. Save the Force_1 file as is to the “fwmatlabcodesfortheimagineanalysis” folder.

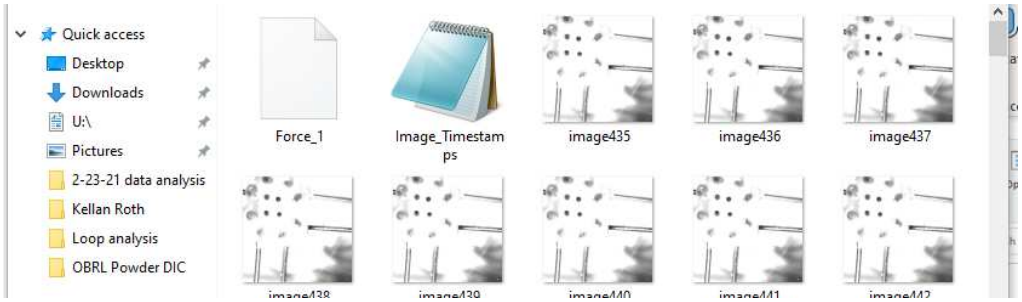

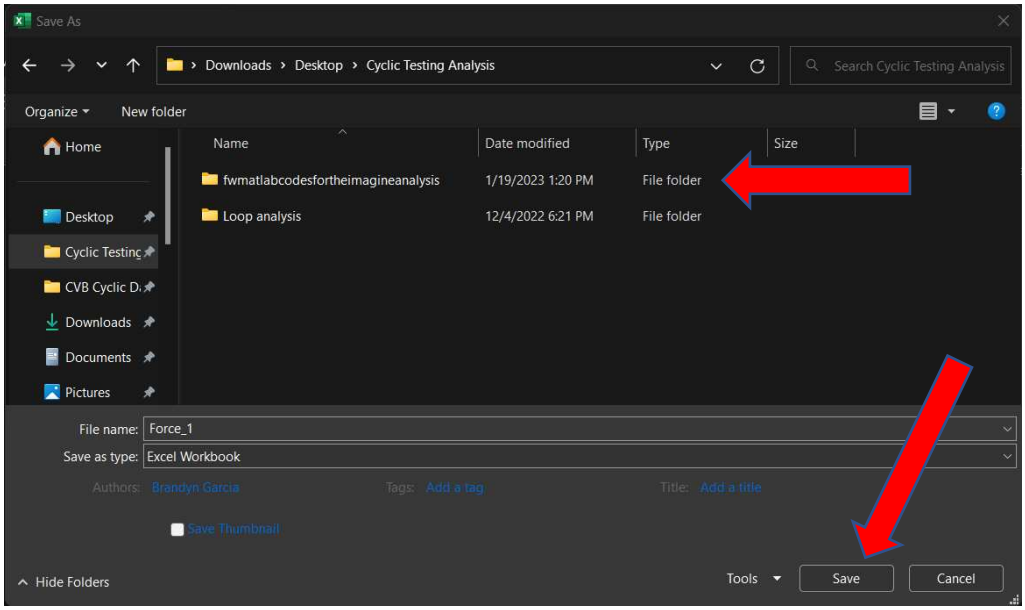

2. In your image timestamps file, there should be two columns. The second column (Column B in excel) holds the timestamps of interest. Add a third column in column C that starts with the number of the first image from the raw data images (image #435 in the first above figure) and iteratively adds one to that number until the bottom of the timestamp files, as shown in the figure below. This is to relate the image number with its corresponding time stamp.

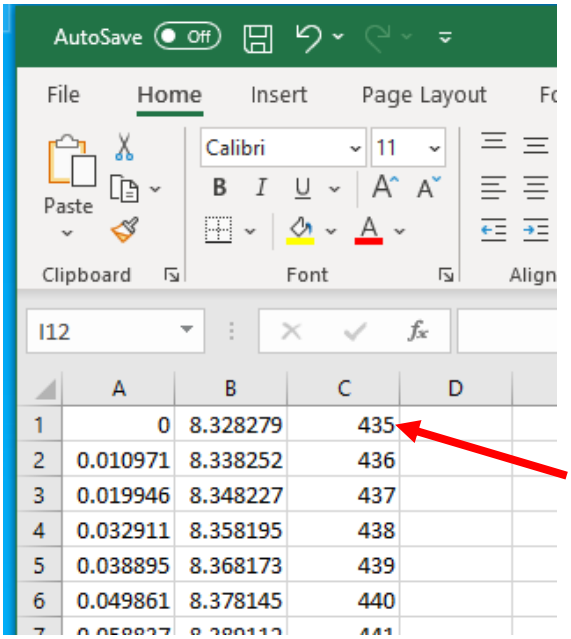

3. Next, go through your raw cyclic images to find the final 3 cycles of deformation captured. This will be at the end of the image files (or near the end). Keep in mind the testing frequency you are analyzing. Each testing frequency has a different number of frames per cycle (fps). The calculation can be done by using the following conversion: frames per cycle = fps/ testing frequency (Hz).
   The following frequencies have the corresponding fps:
   - 0.1 Hz→ 5 fps
   - 1 Hz→ 50 fps
   - 2 Hz→ 100 fps
   - 5 Hz→ 200 fps
   - 8 Hz→ 200 fps

   You then can run the simple conversion above of fps/ frequency to find the number of images per cycle. For example, if analyzing a 5 Hz sample, your frames per cycle will be 200/5 = 40 frames per cycle. Since we are analyzing the last 3 cycles; 3 x 40 = 120 images for three cycles imaged. This amount is the number of images you should have when selecting images comprising the last three cycles. Copy and paste the images of the final 3 testing cycles into the “Final 3” folder shown in the figure below. “Final 3” folder containing the images of the last three testing cycles should be in the Cycle Testing Analysis Folder.

   The file path for this step should look similar to the screenshot below.

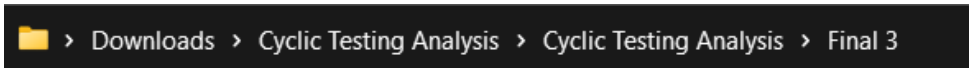

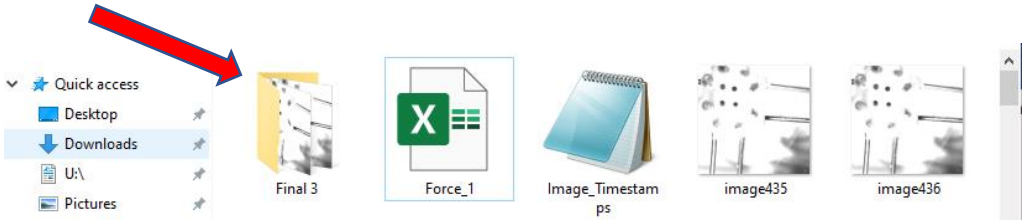

4. Next, in the image timestamp file, find the timestamps that correspond to the final three testing cycles. In the images shown below, the first image of the final three tests is 834, whose timestamp is highlighted.

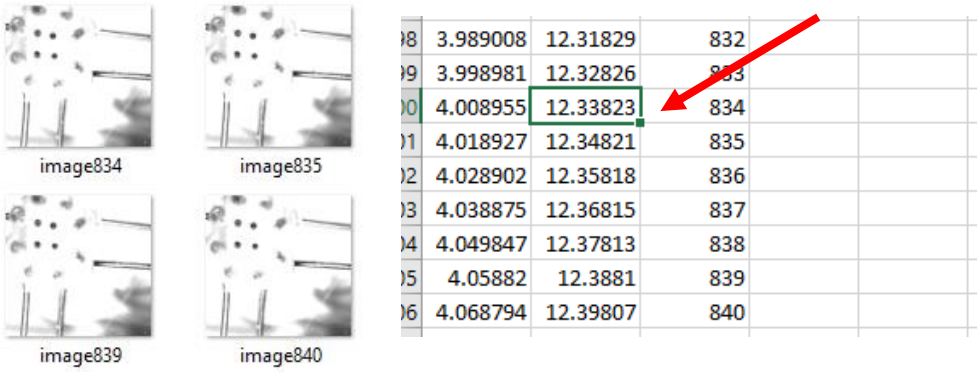

Note: If the final three cycles occur over a change from 900 to 1000 or 90 to 100, instead use the three cycles before the final three. The MATLAB code will rearrange the order of the images if they go from three digits to four digits.

For example: If I select images 950-1100, the code will reorder the images so that 1000-1100 are put before 950-999. This will completely change your results.

5. Copy and paste the timestamps that correspond with the final three testing cycles into column E of the Image timestamps file as shown below:

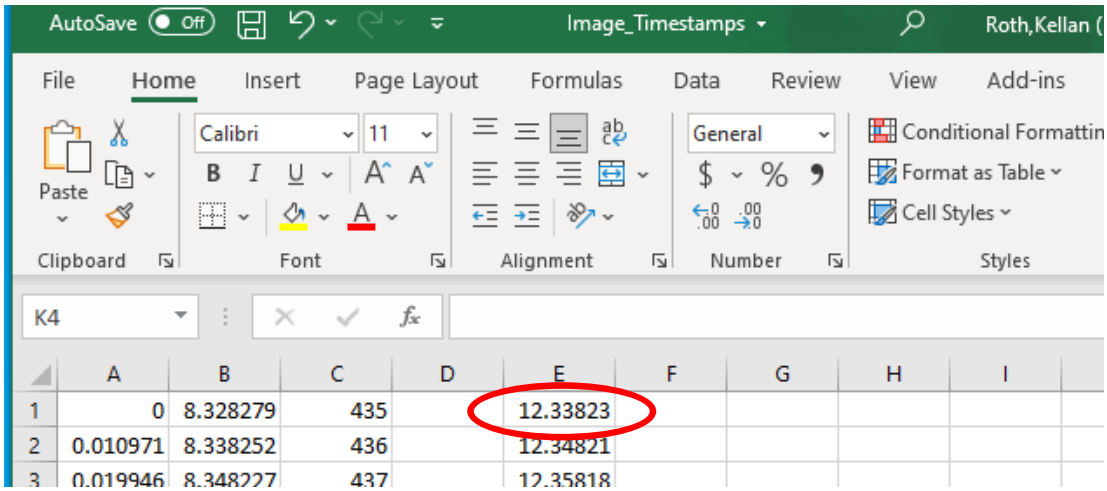

6. Now, save the image timestamps file as Image_Timestamps as an excel sheet (delete the .lvm that will likely automatically be in the name). This will result in the three data sets you need for MATLAB as shown below: The Final 3 images folder, the Force_1 excel file, and the updated Image_Timestamps file. Save the Image_Timestamps file in the "Cyclic Testing Analysis" folder. Double check to make sure that you have the "Final 3" folder is in here, too, and that the "Force_1" file is saved in the fwmatlabcodesfortheimagineanalysis folder before beginning any analysis.

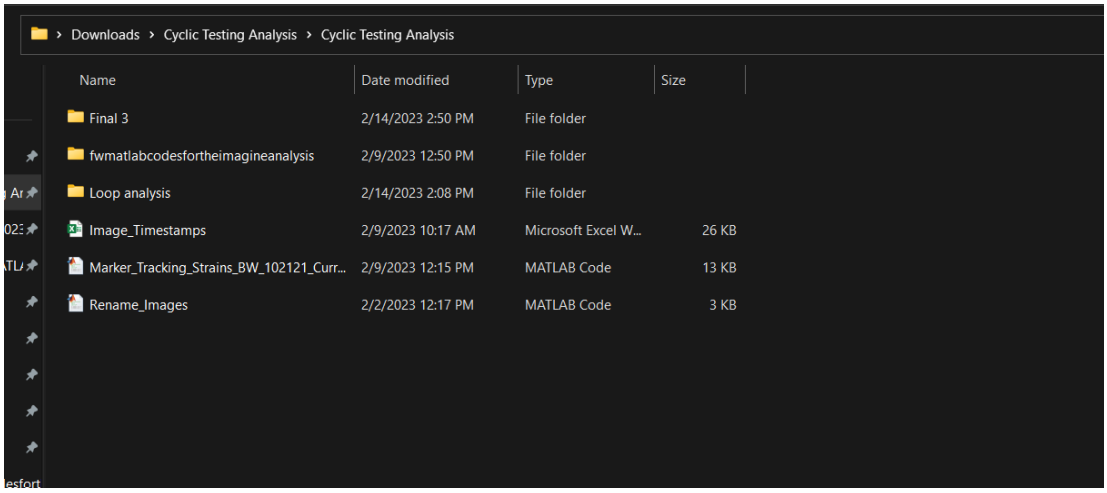

7. Open the following MATLAB codes (some of which are within the "fwmatlabcodesfortheimagineanalysis" folder shown above). These will be the only files you need for deriving stress strain curves from your raw data.

- Rename_Images.m
- Marker_Tracking_Strains_BW_102121_CurrentStandard.m
- DataFilter3.m
- Find_Force092021

- Biaxial_Sync_112221
- StressvsStrain.m

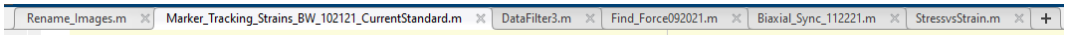

8. Run the “Rename_Images.m” MATLAB file, and in the popup window select the folder with your images from the final 3 cycles of testing (“Final 3” below). This will rename your images starting from image 0.

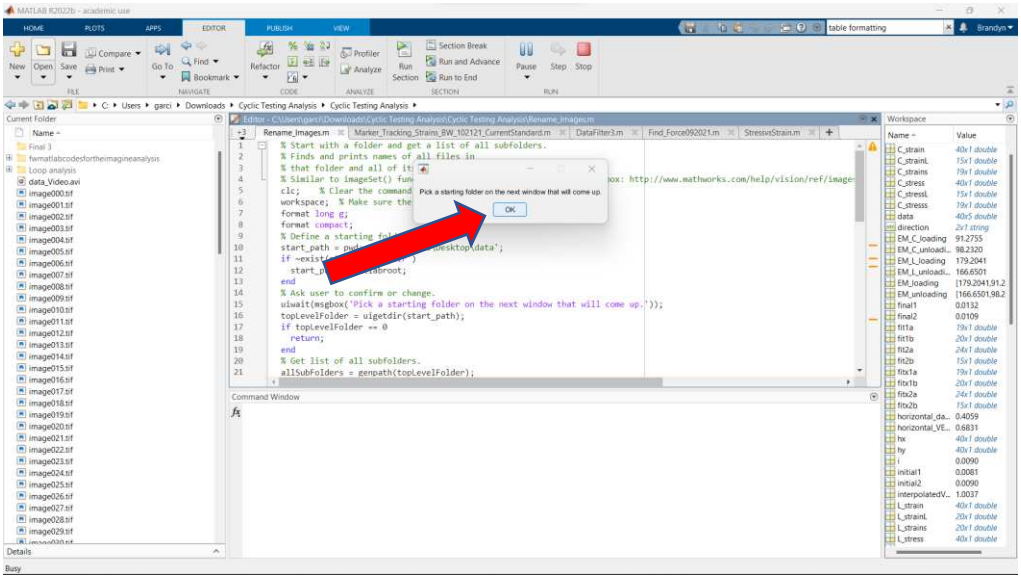

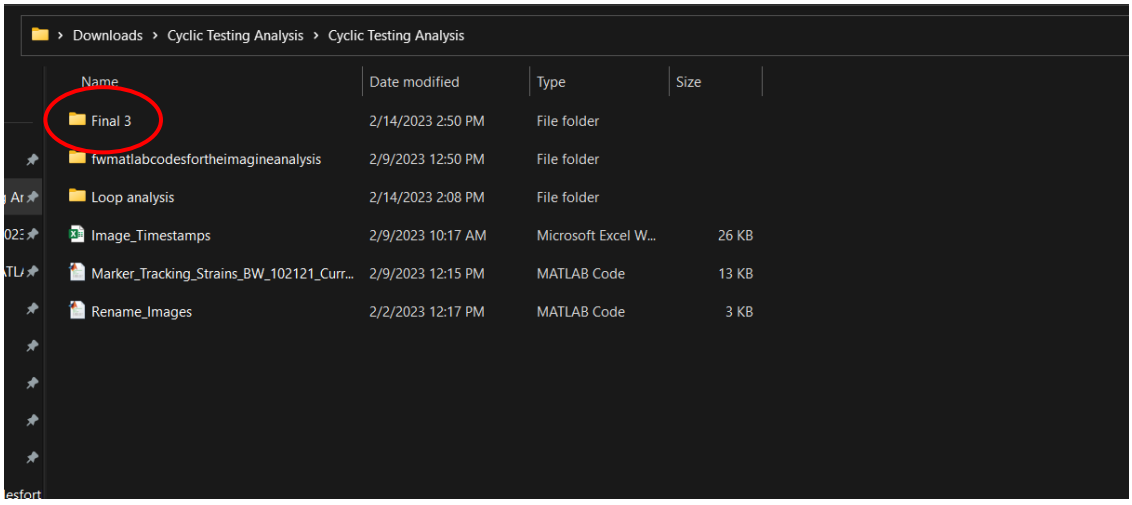

9. Once this has been done, the code will rename all existing images within the Final 3 folder. Once the rename images code has finished, double-check the “Final 3” images folder to verify that the image numbers have been renumbered starting with image #0. Cut the images from this folder and paste them into the Cycle Testing Analysis folder.

10. At this point, run the second MATLAB code “Marker_Tracking_Strains_BW_102121_CurrentStandard.m”. When prompted, input the total image count starting with 1 as shown in the image below. For this example, there were 150 total images (this was a 1Hz sample).

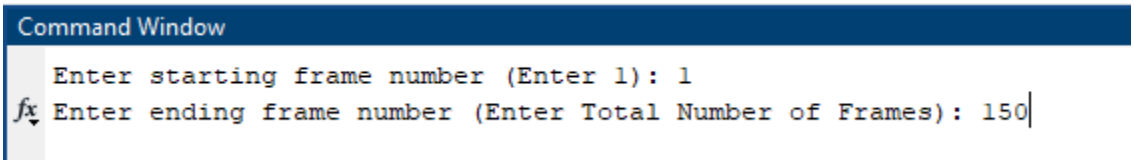

The code should run, and you will see a simulation video of the code locating the marker location of each image and tracking its displacement. If this video (shown below) does not appear, you will need to alter some values in the code which is explained below. A successful run of the marker tracking code occurs when the colored dots (shown below) stay on the markers for all three cycles (i.e., no jumping to the mounting tines or blemishes on the tissue).

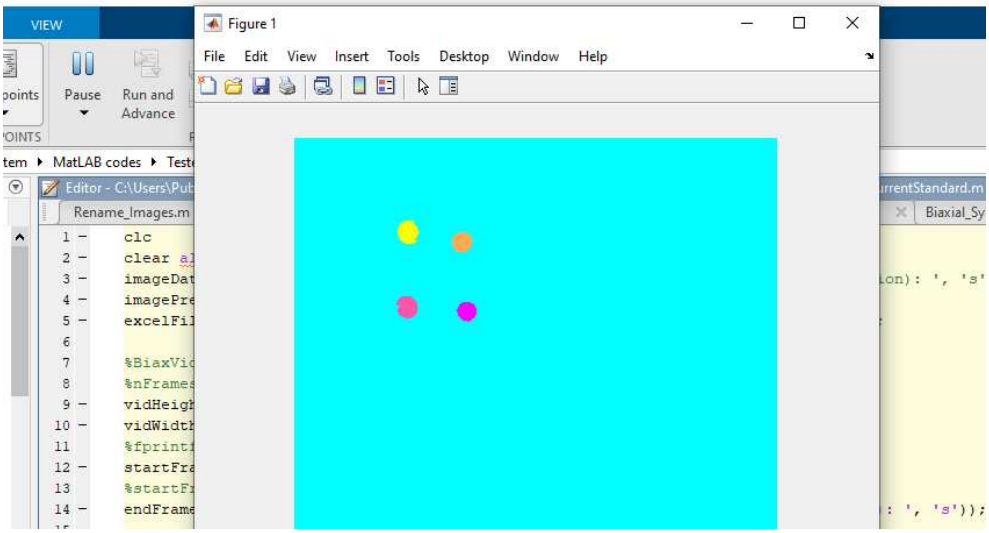

Changing the ratio constant (Line 16) value will refine the shape that the code tracks. Usually the best parameter is 100 (very circular). The area constant (line 18) will change the area threshold in which the code tracks markers. Values can range from 1-1000 If the markers are relatively small, it is best to keep this number low (around 100).

```
16 -    ratioConstant = 100; % shape contant (circularity vs oval)
17 -    isoperimetricRatio = ratioConstant;
18 -    areaConstant = 200; %Threshold for marker size
```

Changing the threshold value (line 88) is the most impactful change. Usually, the threshold will be within the 0.2-0.6 range, but you will likely need to alter it several times to get a good run. It is advised to start at 0.6 and drop by 0.05 until you have a successful run. If this does not work, try adjusting the area constant and restart the threshold to 0.6.

```
87 -    gray3 = gray2 - background;
88 -    threshold = 0.45;%graythresh(gray3); % Threshold for segmenting markers from background
89 -    BW = im2bw(gray3, threshold);
```

11. Once you successfully run the marker tracking strain code, copy the newly created Stretch file into the fwmatlabcode folder, as shown below.

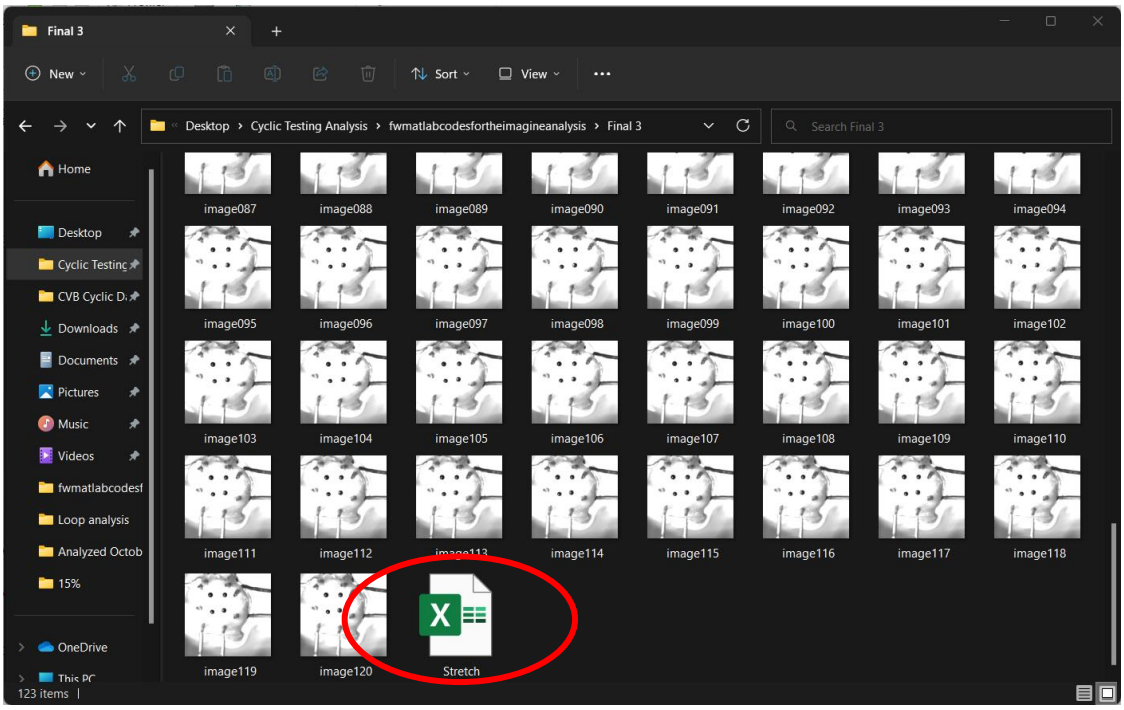

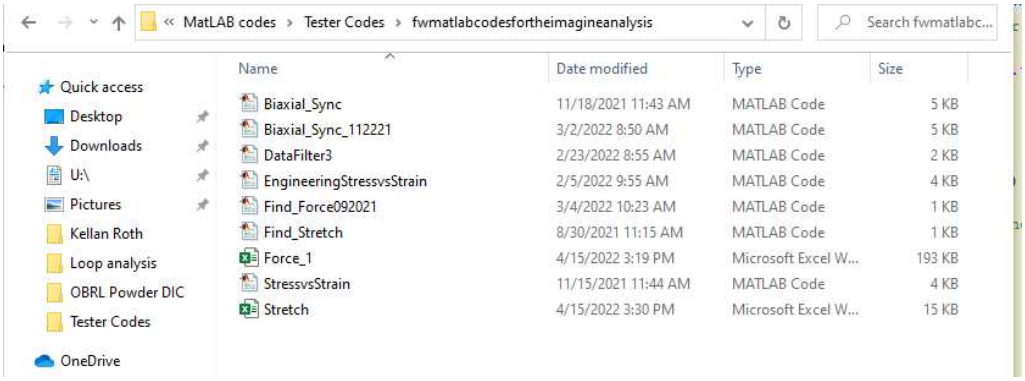

12. Run the DataFilter3 code. The data should be filtered similarly as shown below. When prompted, change the folder you are working under. Note: this image is for a 5Hz sample. For lower frequencies, the period is much larger, so the blue plot will be "thicker".

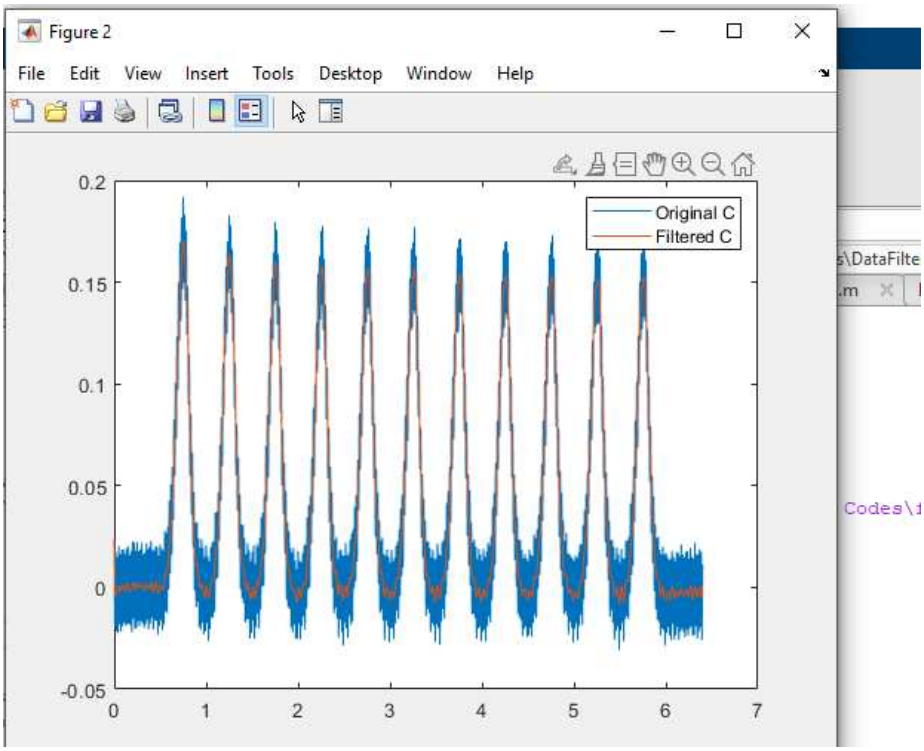

This code will create a Force_2 excel file with the filtered data. This file will appear in the fwmatlabcodesfortheimagineanalysis folder.

Name	Date modified	Type	Size
Biaxial_Sync	11/18/2021 11:43 AM	MATLAB Code	5 KB
Biaxial_Sync_112221	3/2/2022 8:50 AM	MATLAB Code	5 KB
DataFilter3	4/15/2022 3:32 PM	MATLAB Code	2 KB
EngineeringStressvsStrain	2/5/2022 9:55 AM	MATLAB Code	4 KB
Find_Force092021	3/4/2022 10:23 AM	MATLAB Code	1 KB
Find_Stretch	8/30/2021 11:15 AM	MATLAB Code	1 KB
Force_1	4/15/2022 3:19 PM	Microsoft Excel W...	193 KB
Force_2	4/15/2022 3:33 PM	Microsoft Excel W...	266 KB
StressvsStrain	11/15/2021 11:44 AM	MATLAB Code	4 KB
Stretch	4/15/2022 3:30 PM	Microsoft Excel W...	15 KB

13. Run the “Find_Force092021.m” script (straight forward). After you run this script, check in the folder that the Force.xlsx file was generated.

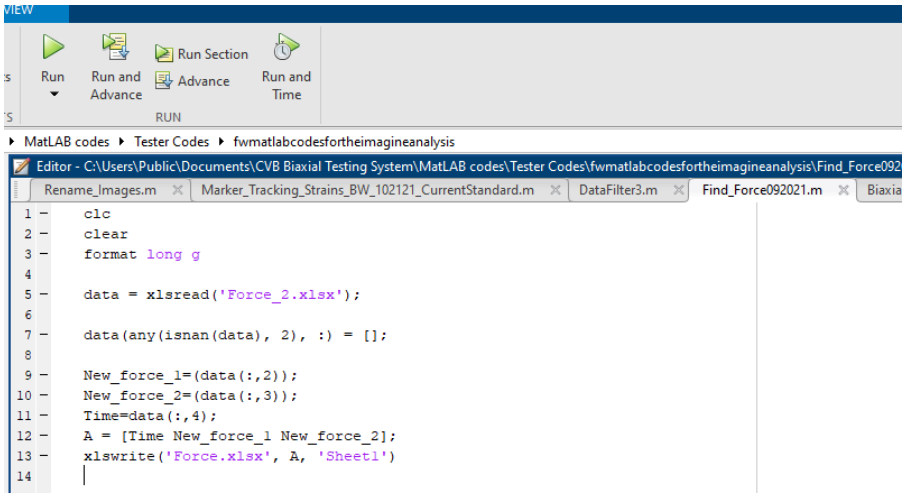

14. Run the “Biaxial_Sync_122221.m” code. When prompted, input the cross-sectional area (mm^2) of your testing sample in the longitudinal and circumferential directions.

15. Run the **<u>first section</u>** of the “StressvsStrain.m” code. To do this, click in the first section of the script. Then, in the editor tab of Matlab, click “Run Section”.

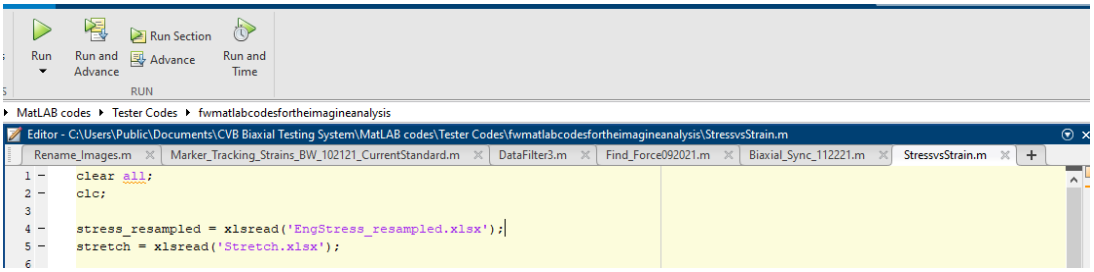

This will result in a Stress_StrainC2 file being saved into the fwmatlabcodesfortheimagineanalysis folder. Save this file, as well as all other excel files from this folder into the original data folder.

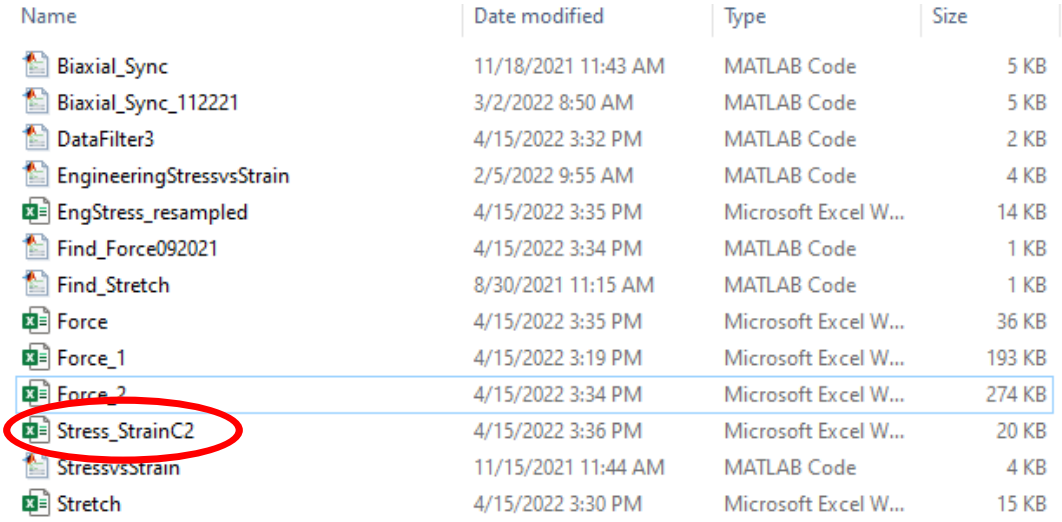

16. When opening your Stress_StrainC2 file, you should have 6 columns worth of data, with column B and C containing longitudinal strain and stress data, respectively. Columns G and H contain circumferential strain and stress data, respectively. Delete the first row of the stress data for each data set as shown in the image below, shifting the cells up. This will compensate for a built-in timestamp offset from the testing system.

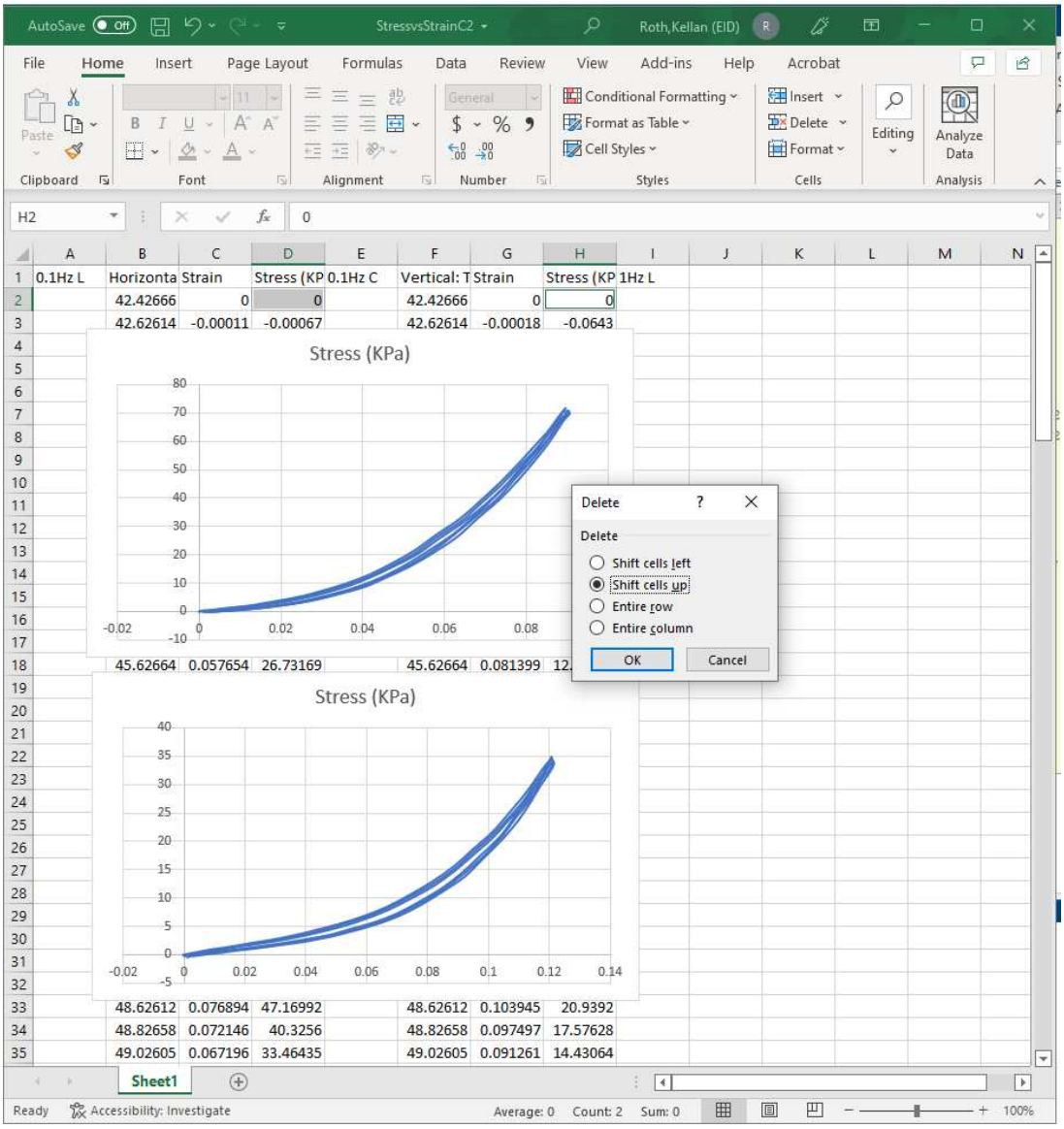

This will result in stress strain curves that should look like the ones in the image below.

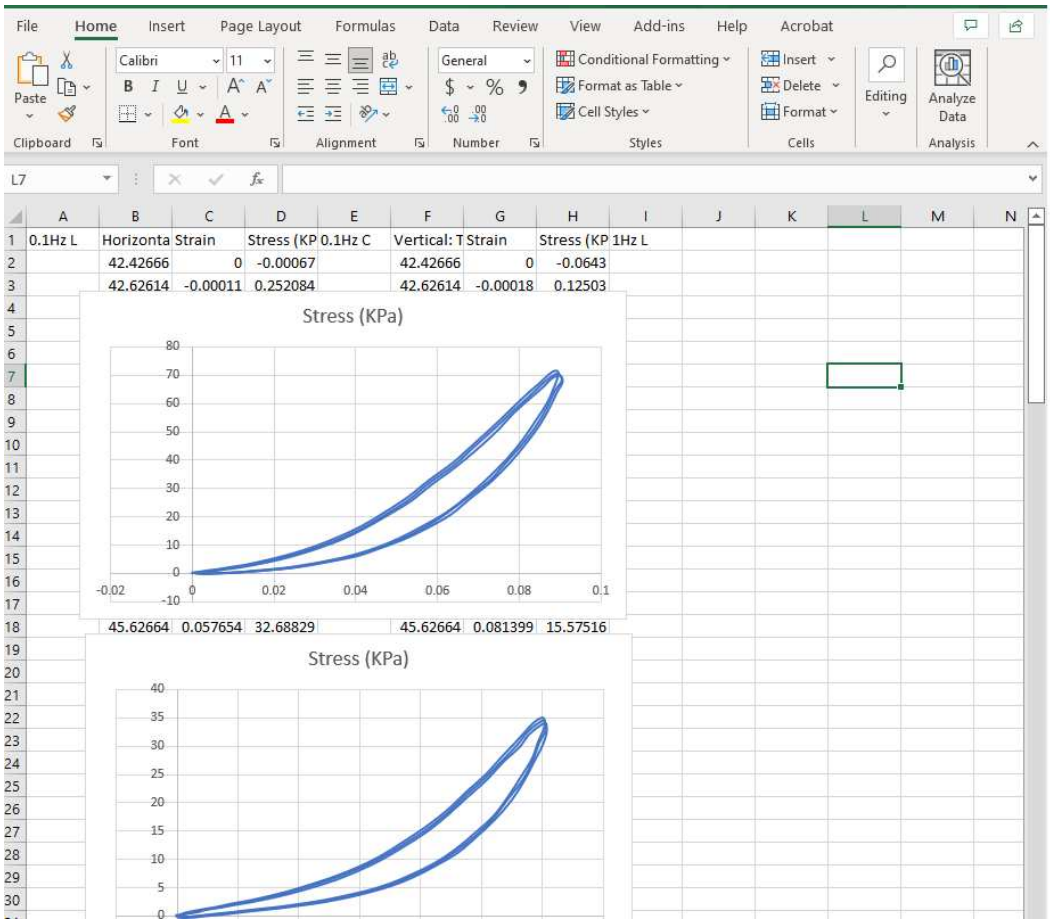

17. Once you have made this change, save the file using this naming convention:
    a. Sample Group_Sample Date_Frequency_Strain_Drug Treatment _Loops
    b. Ex: CTL 2.11.22 5Hz 20 Strain D2O Loops
18. At this point, you will need to average the loops for analysis. Open the loop analysis folder in the matlab tester codes as shown circled below.

Loop Analysis

Next, we need to analyze the biomechanical data of our averaged loops. These will include calculations such as Wd, Ws, Damping, loop width, the viscoelastic ratio (V/E ratio), and elastic modulus.

1. Take the stress-strain file that you saved with the loops from step 18 and copy and paste it in the “Loop Analysis” folder.

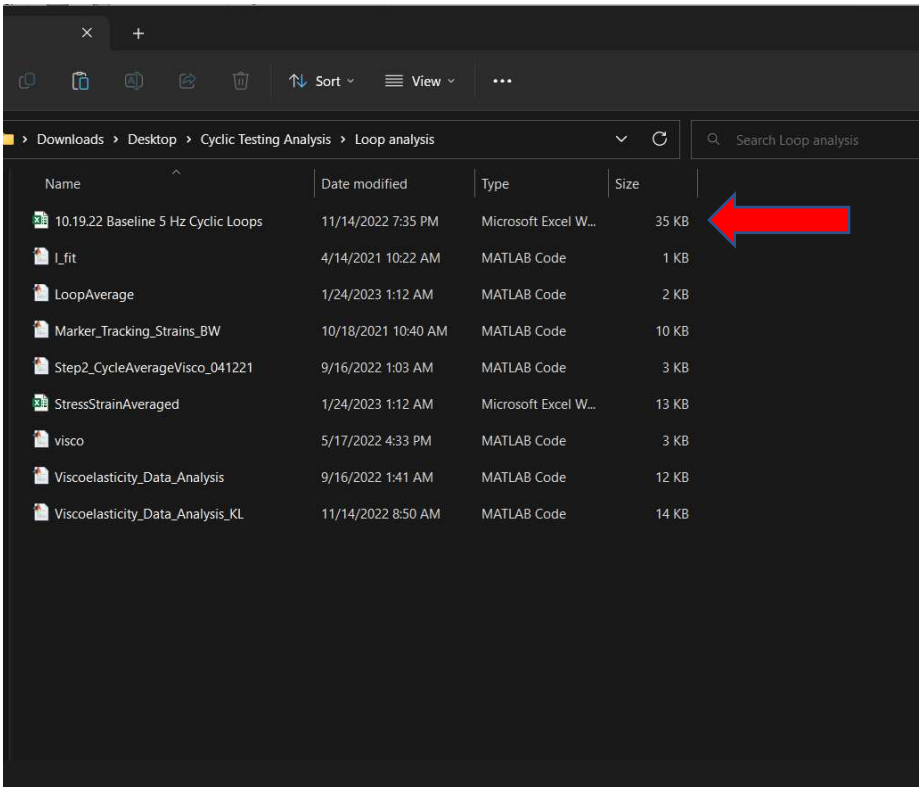

2. Run the “LoopAverage.m” code in the Loop Analysis folder. This will average the stress strain curves from the stress-strain file.

3. Before running the LoopAverage code, make sure that the correct file pathway is addressed in line #6 in the code’s script. This is so that MATLAB can address the file that is being analyzed and extract all necessary data for analyzing.

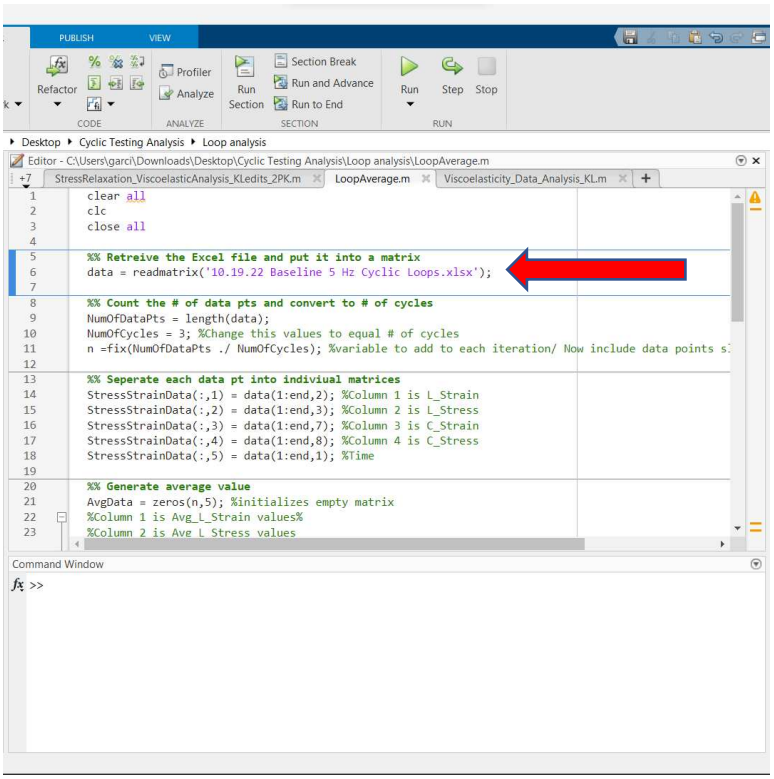

4. After running the LoopAverage code, you should end up with longitudinal and circumferential averaged loops (as seen in the image below). Note: the code is currently set to average 3 loops. If your sample only has 2 loops, change the variable NumofCycles to 2 (in line10). You will also need to change line 29 – remove the last term of the summation in this line (comment it out in line 30) and then run your sample.

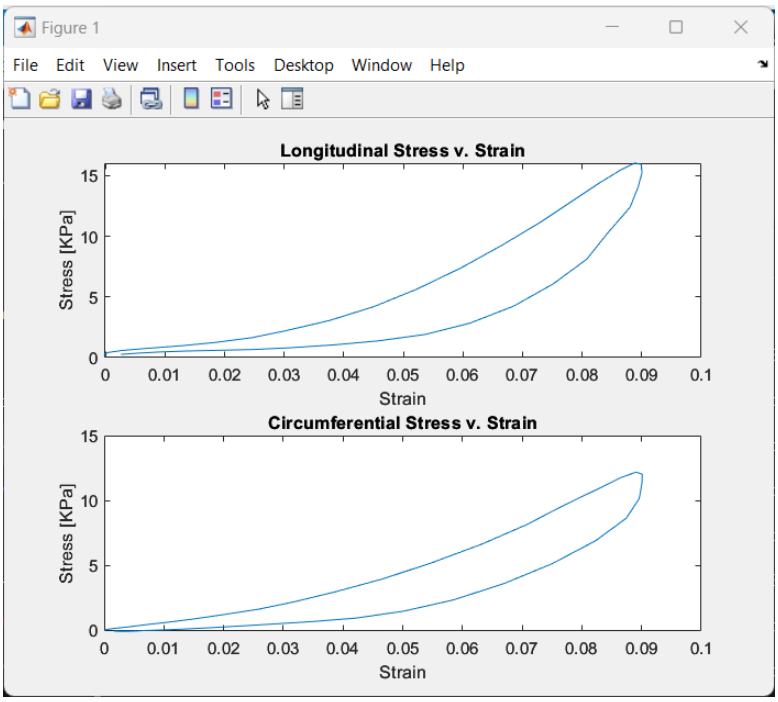

5. Once the code is done running, a new file named “StressStrainAveraged” will populate in the Loop analysis folder.
    a. Use the naming convention: StressStrainAveraged_Sample Group Sample Data Frequency Strain Level Drug Treatment
        i. Ex: StressStrainAveraged_CTL 2.11.22 5Hz 20 Strain Baseline

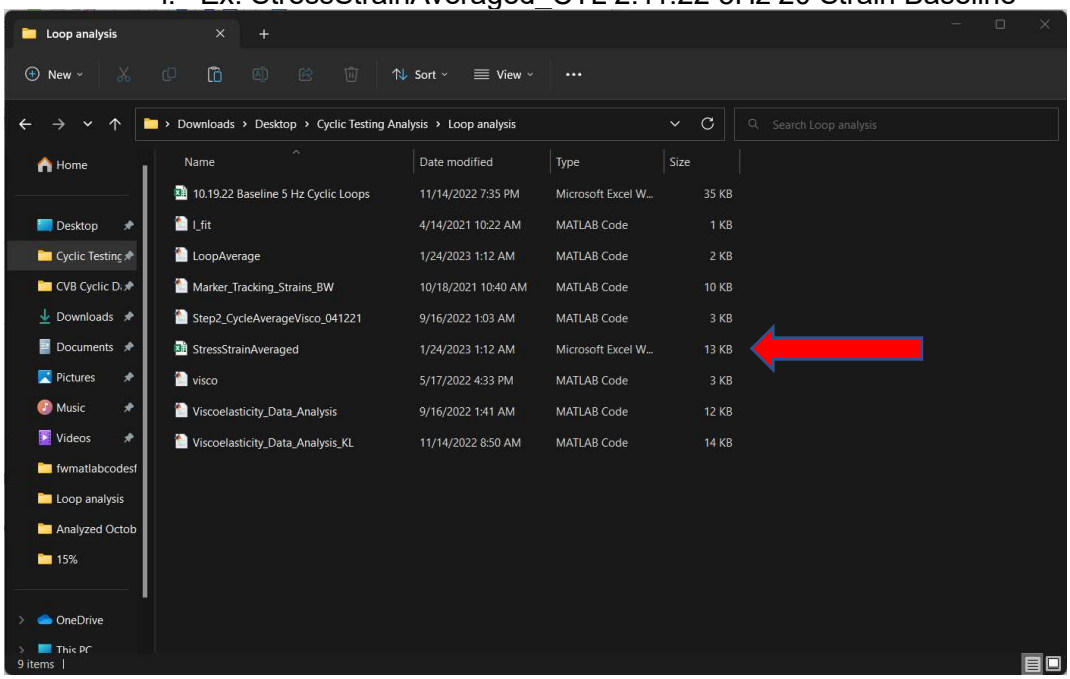

6. Next, go ahead and run the last code in the loop analysis: “Viscoelasticity_Data_Analysis_KL.m”.
7. Once Opened, verify the correct file path is inputted on line #28 of the code.

8. Run the script once the setup and configuration are complete. You should end up with biomechanical data as seen in the pictures below.

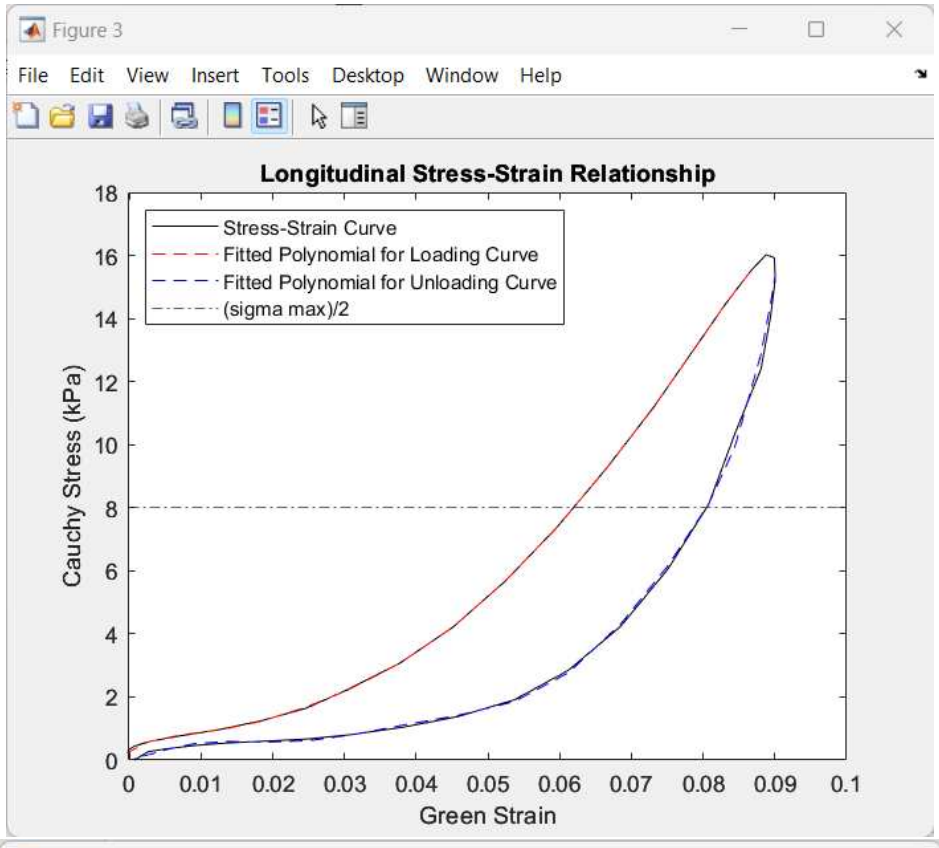
Figure 3
File Edit View Insert Tools Desktop Window Help
Longitudinal Stress-Strain Relationship
Stress-Strain Curve
Fitted Polynomial for Loading Curve
Fitted Polynomial for Unloading Curve
(sigma max)/2
Cauchy Stress (kPa)
Green Strain
0 2 4 6 8 10 12 14 16 18
0 0.01 0.02 0.03 0.04 0.05 0.06 0.07 0.08 0.09 0.1

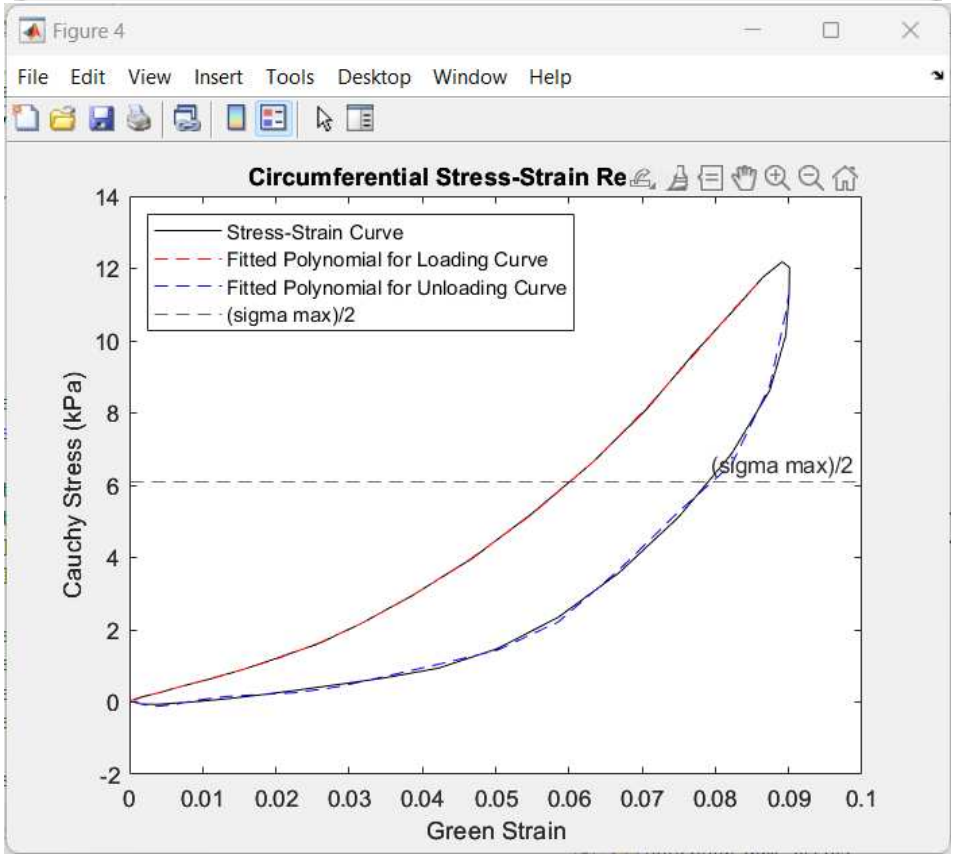
Figure 4
File Edit View Insert Tools Desktop Window Help
Circumferential Stress-Strain Re
Stress-Strain Curve
Fitted Polynomial for Loading Curve
Fitted Polynomial for Unloading Curve
(sigma max)/2
Cauchy Stress (kPa)
Green Strain
-2 0 2 4 6 8 10 12 14
0 0.01 0.02 0.03 0.04 0.05 0.06 0.07 0.08 0.09 0.1

	Wd	Ws	VE Ratio	Damping	EM Loading	EM Unloading
Longitudinal	0.0089280709079808	0.0130694995824779	0.683122628501443	0.405866225629476	179.204127126634	166.650107236748
Circumferential	0.0028559809085606	0.00252301737003169	1.13197037106595	0.530950329530134	91.2755487804798	98.2319834189373

9. Take the biomechanical data and input the values into an Excel spreadsheet and then format the data.

    - Congratulations! You have just finished a biaxial cyclic analysis of right ventricular tissue.

Tips and Tricks for Biaxial Cyclic Analysis

1. When running analysis, make sure to record the image numbers for which images you use for your final 3 cycles. This will make updating the Image_Timestamps file easier.

2. When running the' marker tracking' MATLAB code, Lines 88, 18, and 16 should be the only lines you alter if the displayed markers are not uniform during analysis. Start with line 88 and then alter line 18 in conjunction if need be. Line 16 should not need to be altered but can be useful in some cases.

3. Write down the marker tracking parameters for each analysis (record testing values specified for lines 16, 18, and 88). This helps expedite the process if the user needs to rerun the same sample at a later data after the initial analysis.

4. If the viscoelastic analysis loops (the last code ran in the analysis) have poorly conditioned polynomials fitted on the loops, lines 163 and 164 can be altered to whatever nth-degree polynomial the user wants to use. The higher the polynomial usually means a better fit (around 6^{th} or 7^{th} degree). This will cause the code to throw a warning error, however, this will not expect any experimental values produced.

Preparing data for StressRelaxation analysis:

1. Open Force_1.xlsx
2. Calculate the engineering stress (kPa) in the L and C directions:
    a. Insert column to the right of L force and C force
        i. L force is in column B
        ii. C force in column C
    b. Type out formula:
        i. Ex for L force:
            1. =1000*(B1/Area)
        ii. Double click on the bottom right corner of that cell to apply it to the rest of the column
3. Copy L stress and C stress to columns I and J
4. Insert column between them – they should now be in columns I and K
5. Zero the stresses by the first value
    a. Type out formula in I1 for L stress, and K1 for C stress
        i. Ex for L stress:
            1. =I1-I1
        ii. Double click on bottom right corner of that cell to apply it to the rest of the column
    b. This is now your final formulation of the stress data
6. Copy column A (time), column I (L stress) and column K (C stress) into a new excel file so that they are now in columns A,B,C in that file
7. Save this file as Stress_1.

Relaxation modulus and normalized stress calculation:

1. Open script RelaxModNormStressandEta.m
2. In line 13, copy and paste the file path for the data sheet you want to analyze
3. Follow the steps to convert the data in the sheet to engineering stress in the previous section.
   Stress relaxation analysis – Force_1.xlsx reformatting.
4. In line 17, update the stretch value so that it corresponds to the strain used in the data collection.
    a. If the strain level is 6%, the stretch is 1.06; 20% → 1.2
5. In line 33, update epsilon so that it corresponds to the strain used in the data collection.
    a. If the strain level is 6%, epsilon is 0.06; 20% → 0.2
6. Run code.
7. The two outputs you need are “rm” and “ns”
    a. Each table will display the parameter at the specified time points
    b. Column 1 is the longitudinal direction and column 2 is the circumferential direction

Dissipated and stored energy calculation:

1. Open script StressRelaxation_ViscoelasticityAnalysis_KLedits_2PK
2. In line 26, copy and paste the file path for the data sheet you want to analyze

3. In line 36, update the stretch value so that is corresponds to the strain used in the data collection:
    a. If the strain is 6%, the stretch is 1.06; 20% → 1.2
4. Run code
5. The outputs of interest are the “params” variables
    a. The time point of interest is included in each variable name
        i. params001 is the variable associated with 0.01s
        ii. params01 → 0.1s
        iii. params1 → 1s
        iv. params10 → 10s
        v. params100 → 100s
    b. the longitudinal direction is column 1, circumferential direction is column 2
    c. row 1: dissipated energy
    d. row 2: stored energy
    e. row 3: sum of dissipated and stored energy
    f. row 4: ratio of dissipated to stored energy
    g. row 5: damping

Miscellaneous

Biaxial tester commercial components

Part	Company/Link/Image	Quantity
Linear actuator	Zaber/ X-DMQ-DE 	2
Load Cell	Honeywell/ Model 31 	2
Amplifier	Honeywell/ Model UV 	2
DAQ	National Instruments/ NI USB-6002 	1
Power Source	Acopian/ Model 28EB30	1

		
Camera	Baumer/ BLXT-17M.I 	1
Camera Cable	Baumer/ Cable GigE M12X/RJ45 	1
PCI Card	Intel/ ZVA-Intel X550-T2 10GbE Serv Adapter (option) 	1
Lens	Ricoh/ ZVL-FL-BC3518-9M 	1 (2?)
Perpendicular movement rails	MiSUMi/ SSEB-MX10-55	4

		
Computer	HP/ Workstation Z4G4 Tower Core 	1
Camera holder	Fisher Scientific/31-501-955 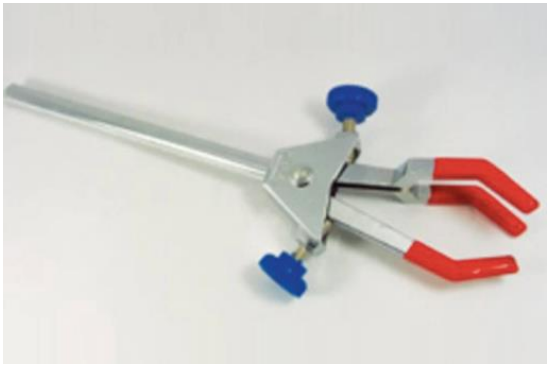	1

Stress relaxation, W_d, W_S, V/E ratio, and damping calculations

```
%% Stress Relaxation Energy Calculations
% Created by: Matt Ahern
% Created on: 2/15/22

% This code was created for the CSU CVB Lab to analyze stress relaxation
% data. The code determines the stored and dissipated engery of the curve.
% Code first removes delay at start of data and then shifts data down to
% start at zero. Calculates stored energy and dissipated energy at 0.01s and
% 100s after max force in L and C direction. Force does NOT get converted
%into stress. Code also calculates wd/ws, wd+ws, and wd/(wd+ws) from the
%values 100s after max.

% Modified by: Kristen LeBar
% Modified on: 7/22
% Main efforts in the revision: variable renaming; calculating damping and
% VE ratio at 0.01s; data filtering to improve calculations at 0.01s;
% calculate at multiple time points.

close all
clear
clc

%% SET UP

% Upload the data
data = xlsread(['D:\CSU\Collagenase Treatment_ex vivo 2023\MCT
6.24.24\Collagense\300g\SR\SR_filter on_20%\8Hz\Stress_1.xlsx']);

% Read the time, L force, C Force
timeL = data(:,1);
timeC = data(:,1);
Stress_L = data(:,2); %Longitudinal stress
Stress_C = data(:,3); %Circumferential stress

% Set time step
dt = timeL(2)-timeL(1); %time step in seconds

% Convert to 2nd PK
PKL = Stress_L/1.2;
PKC = Stress_C/1.2;

%Smooth data
% Force_L = smoothdata(Force1,'gaussian');
% Force_C = smoothdata(Force2, 'gaussian');
% [b,a] = butter(4,2/50,'low'); %research this function - we are taking the lower end
of the force values
% [d,c] = butter(4,1/40,'low');
% Force_L = filtfilt(b,a,Force1);
% PKC_f = filtfilt(d,c,PKC);

maxL = find(PKL==max(PKL));
maxC = find(PKC==max(PKC));

rampL = PKL(1:maxL);
```

```
rampC = PKC(1:maxC);

timeRL = timeL(1:maxL);
timeRC = timeC(1:maxC);

% Remove initial delay
delay = zeros(length(rampL),1);
delay2 = zeros(length(rampC),1);
n = 1;
m = 1;
for i = 2:length(rampL)
     a = rampL(i)-rampL(i-1);
    if a >= 0.0035              % Value may need to be modified to better fit ramping
        delay(n) = i;
        n = n+1;
    end
end

for i = 2:length(rampC)
     a = rampC(i)-rampC(i-1);
    if a >= 0.0035              % Value may need to be modified to better fit ramping
        delay2(m) = i;
        m = m+1;
    end
end

% Manually remove values if part of delay still present
PKL(1:delay(1)+0) = [];       % Can change '+/-' value to better include ramping'
PKC(1:delay2(1)+0) = [];
timeL(1:delay(1)+0) = [];
timeC(1:delay2(1)+0) = [];

% Start at time and force of zero
a = PKL(1);
b = PKC(1);
c = timeL(1);
d = timeC(1);
for j = 1:length(PKL)
    PKL(j) = PKL(j)-a;
    timeL(j) = timeL(j) - c;
end
for k = 1:length(PKC)
    PKC(k) = PKC(k)-b;
    timeC(k) = timeC(k) - d;
end

% Only include 100s after max
maxL2 = find(PKL==max(PKL));
maxC2 = find(PKC==max(PKC));
PKL(maxL2+(100/dt):end) = [];
PKC(maxC2+(100/dt):end) = [];
timeL(maxL2+(100/dt):end) = [];
timeC(maxC2+(100/dt):end) = [];

% Make sure Curve looks good
```

```
figure
plot(PKL)
% hold on
% plot(Force1)
figure
plot(PKC)
% hold on
% plot(PKC_f)

%% Energy Calculations
t = [0.01 0.1 1 10]; %vector of time points of interest (does not include 100s)

% 100s calculations
% Area Under Curve up to 100s after max (ws)
WsL100 = trapz(timeL,PKL);
WsC100 = trapz(timeC,PKC);
% Area Under Curve After Ramping
areaL100 = trapz(timeL(maxL2:end),PKL(maxL2:end));
areaC100 = trapz(timeC(maxC2:end),PKC(maxC2(1):end));
MaxForce = PKL(maxL2);
squareL100 = 100.*PKL(maxL2);
squareC100 = 100.*PKC(maxC2(1));
% Area above curve after ramping (wd)
WdL100 = squareL100 - areaL100;
WdC100 = squareC100 - areaC100;
% ws + wd
VEsumL100 = WsL100 + WdL100;
VEsumC100 = WsC100 + WdC100;
% wd/ws
VEratioL100 = WdL100/WsL100;
VEratioC100 = WdC100/WsC100;
% wd/(wd+ws)
dampL100 = WdL100./(WdL100+WsL100);
dampC100 = WdC100./(WdC100+WsC100);

% Calculations for all other time points
for i = 1:length(t)
    % Area under curve up to time t after max
    WsL(i) = trapz(timeL(maxL2:maxL2+(t(i)/dt)),PKL(maxL2:maxL2+(t(i)/dt)));
    WsC(i) = trapz(timeC(maxC2:maxC2+(t(i)/dt)),PKC(maxC2:maxC2+(t(i)/dt)));

    % Area under curve after ramping
    areaL(i) = trapz(timeL(maxL2:maxL2+(t(i)/dt)),PKL(maxL2:maxL2+(t(i)/dt)));
    areaC(i) = trapz(timeC(maxC2:maxC2+(t(i)/dt)),PKC(maxC2:maxC2+(t(i)/dt)));
    squareL(i) = t(i).*PKL(maxL2);
    squareC(i) = t(i).*PKC(maxC2(1));

    % Area above curve after ramping for 0.01s (wd)
    WdL(i) = squareL(i) - areaL(i);
    WdC(i) = squareC(i) - areaC(i);

    % ws + wd
    VEsumL(i) = WsL(i) + WdL(i);
    VEsumC(i) = WsC(i) + WdC(i);
```

```
    % wd/ws
    VEratioL(i) = WdL(i)/WsL(i);
    VEratioC(i) = WdC(i)/WsC(i);

    % Damping
    dampL(i) = WdL(i)/VEsumL(i);
    dampC(i) = WdC(i)/VEsumC(i);
end

% Organize Results
% [(Wd for 100s) (Wd for 0.01s) (Ws for 100s) (Ws for 0.01s) (Ws+Wd)
% (Wd/Ws) (Wd/Wd+Ws)] => 7 values for L-direction NaN 7 values for C-direction
% data = [WdL100 WdL01 WsL100 WsL001 VEsumL100 VEsumL01 VEratioL100 VEratioL01
dampL100 dampL01 NaN WdC100 WdC01 WsC100 WsC001 VEsumC100 VEsumC01 VEratioC100
VEratioC01 dampC100 dampC01];

params001 = [WdL(1) WdC(1); WsL(1) WsC(1); VEratioL(1) VEratioC(1); dampL(1)
dampC(1)];
params01 = [WdL(2) WdC(2); WsL(2) WsC(2); VEratioL(2) VEratioC(2); dampL(2)
dampC(2)];
params1 = [WdL(3) WdC(3); WsL(3) WsC(3); VEratioL(3) VEratioC(3); dampL(3) dampC(3)];
params10 = [WdL(4) WdC(4); WsL(4) WsC(4); VEratioL(4) VEratioC(4); dampL(4)
dampC(4)];
params100 = [WdL100 WdC100; WsL100 WsC100; VEratioL100 VEratioC100; dampL100
dampC100];
Wd = [WdL' WdC'];
Ws = [WsL' WsC'];
VER = [VEratioL' VEratioC'];
Damp = [dampL' dampC'];
```

Stress Relaxation – Relaxation Modulus, Normalized Stress, and Eta Calculations

```
%% Stress-Relaxation Data Analysis - Relaxation Modulus, Normalized Stress, Eta
%Created by Kristen LeBar
%Created on 5-17-22

%% Setup
clear all
close all
clc

%% Read in data
data=xlsread('D:\CSU\MCT Rat 2021 and 2022\Biaxial Testing\CTL 10.17.22\SR\SR_filter
on_15%\5Hz\Stress_1.xlsx');
time=data(:,1); %Time data
stretch = 1.15; % stretch value to calculate 2nd PK
stress_L=data(:,2)/stretch; %Stress data in Longitudinal Direction
stress_C=data(:,3)/stretch; %Stress data in Circumferential Direction

%Plot to Check
% figure (1)
% plot(time,force_L)
% hold on
% plot(time,force_C)
% xlabel('Time (s)')
% ylabel('Force (N)')
% legend('L Direction','C Direction')
% title('Force Over Testing Time')
% axis([0 100 0 0.15]) %Change axis limits

%% Variables
epsilon=0.15; %strain value
dt = time(2)-time(1); %time step (can check from raw time data - column A)
%% Find max force and the time at which it happens
[max_L,indexL]=max(stress_L); %max force in L direction; index_L is the row number at
which the peak occurs
time0_L=time(indexL); %time 0 for L direction
[max_C,indexC]=max(stress_C); %max force in C direction
time0_C=time(indexC); %time 0 for C direction
maxforce=table(max_L,max_C);

%% Find force at specified time points after the time at which max force occurs
%treat time at which max force occurs at t=0
t=[0 0.01 0.1 1 10]; %time points we are interested in AFTER the peak (including time
zero)

%Time row number
rL=zeros(1,length(t)); %initialize row number values vector
rC=zeros(1,length(t)); %initialize row number values vector
for i=1:length(t)
    rL(i)=indexL+(t(i)/dt); %row number for longitudinal data
    rC(i)=indexC+(t(i)/dt); %row number for circumferential data
end

%Find force
for i=1:length(rL)
```

```
    for j=1:length(rC)
        sL(i)=stress_L(rL(i)); %longitudinal force data for time t
        sC(j)=stress_C(rC(j)); %circumferential force data for time t
    end
end
sL(6) = stress_L(end);
sC(6) = stress_C(end);
peakstressL = sL(1);
peakstressC = sC(1);
peakstress = table(peakstressL, peakstressC);
%% Calculate stresses (*1000 converts to kPa)
% for i=1:length(fL)
%     for j=1:length(fC)
%         sL(i)=1000*fL(i)/A; %calculate stress in longitudinal
%         sC(j)=1000*fC(j)/A; %calculate stress in circumferential
%     end
% end
%% Relaxation Modulus
rm_L=sL./epsilon; %relaxation modulus (stiffness) in L direction (at time t)
rm_C=sC./epsilon; %relaxation modulus (stiffness) in C direction (at time t)
rm_L100 = sL(end)/epsilon;
rm_C100 = sC(end)/epsilon;
rm100 = [rm_L100 rm_C100];
rm_L(6) = rm_L100;
rm_C(6) = rm_C100;

times=["0s";"0.01s";"0.1s";"1s";"10s";"100s"];
rm=table(times,rm_L',rm_C'); %put relaxation modulus data into table

%% Normalized Stress
ns_L=sL./sL(1); %normalized stress in L direction at time t
ns_C=sC./sC(1); %normalized stress in C direction at time t
ns_L100 = sL(end)/sL(1);
ns_C100 = sC(end)/sC(1);
ns100 = [ns_L100 ns_C100];
ns_L(6) = ns_L100;
ns_C(6) = ns_C100;
ns=table(times,ns_L',ns_C'); %put normalized stress data into table

%% Eta calculations part 2: Kelvin Voigt; using:
https://zeus.plmsc.psu.edu/~manias/MatSE447/02_FluidModels.pdf
% eta = k*tau
% tau = -t/log(s_L/(k*epsilon))

t=[0.01 0.1 1 10 100];
tau = -t./log(sL(2:6)./rm_L100*epsilon);
eta = rm_L100*tau;
```

Hysteresis loop – 3 loop average calculation

```
%% Loop Average
clear all
clc
close all

%% Retreive the Excel file and put it into a matrix
data = readmatrix('C:\Users\keleb\OneDrive\Documents\CVB Research Lab\Cyclic Testing
Analysis\Loop analysis\CTL 10.17.22 20 Strain 5Hz loops.xlsx');

%% Count the # of data pts and convert to # of cycles
NumOfDataPts = length(data);
NumOfCycles = 3; %Change this values to equal # of cycles
n =fix(NumOfDataPts ./ NumOfCycles); %variable to add to each iteration

%% Seperate each data pt into indiviual matrices
StressStrainData(:,1) = data(1:end,2); %Column 1 is L_Strain
StressStrainData(:,2) = data(1:end,3); %Column 2 is L_Stress
StressStrainData(:,3) = data(1:end,7); %Column 3 is C_Strain
StressStrainData(:,4) = data(1:end,8); %Column 4 is C_Stress
StressStrainData(:,5) = data(1:end,1); %Time

%% Generate average value
AvgData = zeros(n,5); %initializes empty matrix
%Column 1 is Avg_L_Strain values
%Column 2 is Avg_L_Stress values
%Column 3 is Avg_C_Strain values
%Column 4 is Avg_C_Stress values

for i = 1:5
    for j = 1:n
        SumValue = StressStrainData(j,i) + StressStrainData(j+n,i) +
StressStrainData(j+2.*n,i);
%
        AvgValue = SumValue ./ NumOfCycles;AvgData(j,i) = AvgValue;
    end
end


%% Plot the stress strain
Avg_L_Strain = AvgData(:,1);
Avg_L_Stress = AvgData(:,2);
Avg_C_Strain = AvgData(:,3);
Avg_C_Stress = AvgData(:,4);
Avg_time = AvgData(:,5);

subplot(2,1,1)
plot(Avg_L_Strain,Avg_L_Stress)
title('Longitudinal Stress v. Strain')
ylabel('Stress [KPa]')
xlabel('Strain')

subplot(2,1,2)
plot(Avg_C_Strain,Avg_C_Stress)
title('Circumferential Stress v. Strain')
```

```
ylabel('Stress [KPa]')
xlabel('Strain')

% Calculate last stress value
Avg_L_Stress(end) = Avg_L_Stress(end-1) - (Avg_L_Stress(end-2)-Avg_L_Stress(end-1));
%L stress final value calculation
Avg_C_Stress(end) = Avg_C_Stress(end-1) - (Avg_C_Stress(end-2)-Avg_C_Stress(end-1));
%C stress final value calculation

% Assign strain and stress values to correct columns for data input in the
% VE analysis script
A=[Avg_L_Strain, Avg_L_Stress];
B=[Avg_C_Strain, Avg_C_Stress];
xlswrite('StressStrainAveraged.xlsx', A, 'A1:B50')
xlswrite('StressStrainAveraged.xlsx', B, 'D1:E50')

% Original file write:
% A=[Avg_time,Avg_L_Strain, Avg_L_Stress];
% B=[Avg_time,Avg_C_Strain, Avg_C_Stress];
% xlswrite('StressStrainAveraged.xlsx', A, 'A1:C50')
% xlswrite('StressStrainAveraged.xlsx', B, 'E1:G50')
```

Hysteresis (Cyclic) W_d, W_S, V/E Ratio, Damping, and Elastic Modulus Calculations

```
%% CVB Lab Viscoelasticity Property Analysis - Hysteresis

% Created by: Matt Ahern
% Date Created: 3/3/20
% Last Modified: 3/8/20
% Modified by: Wenqiang (3/17/20)
% Modified by: Kristen (7/2022) - efforts include annotations, linear fit
% of loading and unloading curve to calculate Young's modulus
% Modified By Brandyn (2/14/2023)- Formatted Biomechanical data into tables
% for easy data interpretation.
% Modified by: Olivia (4/2023) - annotated and calculated the stress that
% occured at max strain to calculate the loop height, which is another
% viscous parameter (similar to loop width formulation).


% This script was created for the intended use of the Cardiovascular
% Biomechanics Lab at Colorado State University. The code will take an
% input of longitudinal and circumferential Cauchy Stress and Green Strain values
% from mechanical vessel testing and calculate Wd, Ws, loop width and
% damping of the stress strain hysteresis loop for both the longitudinal
% and circumferential directions.


% Note: This section is modified from previously written code titled
%       Viscoelasticity_Area.m to calculate Wd. All other sections of the
%       script are the work of the above listed author.

close all;
clear;
clc;

%NOTE: This script and the file being analyzed must be saved in the same folder
data = xlsread('C:\Users\keleb\OneDrive\Documents\CVB Research Lab\Cyclic Testing
Analysis\Loop analysis\StressStrainAveraged_CTL 10.17.22 20 strain 5Hz.xlsx'); % Load
Desired Excel data set

L_strain = data(:,1);                              % Loads longitudinal strain values
L_stress = data(:,2);                              % Loads longitudinal stress values
C_strain = data(:,4);                              % Loads circumferential strain
values
C_stress = data(:,5);                              % Loads circumferential stress
values

L_strains = data(:,1);                              % Loads longitudinal strain values
(unloading)
L_stresss = data(:,2);                              % Loads longitudinal stress values
C_strains = data(:,4);                              % Loads circumferential strain
values
C_stresss = data(:,5);                              % Loads circumferential stress
values

L_strainL = data(:,1);                              % Loads longitudinal strain values
(loading)
L_stressL = data(:,2);                              % Loads longitudinal stress values
```

```
C_strainL = data(:,4);                              % Loads circumferential strain
values
C_stressL = data(:,5);                              % Loads circumferential stress
values

% Calculates Wd
Wd_horz = trapz(L_strain,L_stress);              % Longitudinal Wd - just area
between the two curves
Wd_vert = trapz(C_strain,C_stress);              % Circumferential Wd

maxeps_L = max(L_strain);
maxeps_C = max(C_strain);

%Normalize Wd by the maximum strain - to account for varying max strain and
%stress levels between samples
Wd_L_norm = Wd_horz/maxeps_L;
Wd_C_norm = Wd_vert/maxeps_C;


% NOTE: This script uses the built in matlab function trapz to calculate
% Wd. The function made in viscoarea.m can also be used to achieve a
% similar value. The silenced lines below can be used if the viscoarea
% function is preferred.
% Wd_horz = -viscoarea(L_strain,L_stress);
% Wd_vert = -viscoarea(C_strain,C_stress);


%% Calculating Ws

x = length(L_strain); % Finds length of matrices

% % find the max stress and use the unloading curve
sigma_max_h = max(L_stress);             % Finds maximum value of longitudinal stress
(sigma max)
sigma_max_v = max(C_stress);             % Finds maximum value if circumferential
stress (sigma max)

time1 = find(L_stress == sigma_max_h);   % Finds the time that sigma max occurs
(longitudinal)
time2 = find(C_stress == sigma_max_v);   % Finds the time that sigma max occurs
(circumferential)

L_stress(1:time1,:) = [];                % Deletes all values before sigma max
C_stress(1:time2,:) = [];                % Deletes all values before sigma max
L_strain(1:time1,:) = [];                % Deletes all values before sigma max
C_strain(1:time2,:) = [];                % Deletes all values before sigma max


Ws_horz = trapz(L_strain,L_stress).*(-1);                       % Finds the area
under the curve using trapezoidal summations.
Ws_vert = trapz(C_strain,C_stress).*(-1);                       % Finds the area
under the curve using trapezoidal summations.
Ws_horz2 = trapz(L_stress,L_strain).*(-1);
% NOTE: Since it is summing from right to left (in the negative x-direction),
multiply by -1 to get correct sign.
```

```
% find the max strain and use the unloading curve
sigmas_max_h = max(L_strains);             % Finds maximum value of longitudinal
stress (sigma max)
sigmas_max_v = max(C_strains);             % Finds maximum value if circumferential
stress (sigma max)

time1s = find(L_strains == sigmas_max_h);   % Finds the time that sigma max occurs
(longitudinal)
time2s = find(C_strains == sigmas_max_v);   % Finds the time that sigma max occurs
(circumferential)

L_stresss(1:time1s,:) = [];                % Deletes all values before sigmas max
C_stresss(1:time2s,:) = [];                % Deletes all values before sigmas max
L_strains(1:time1s,:) = [];                % Deletes all values before sigmas max
C_strains(1:time2s,:) = [];                % Deletes all values before sigmas max


Ws_horzs = trapz(L_strains,L_stresss).*(-1);                        % Finds the area
under the curve using trapezoidal summations.
Ws_verts = trapz(C_strains,C_stresss).*(-1);                        % Finds the area
under the curve using trapezoidal summations.

% find the max stress and use the loading curve
sigmaL_max_h = max(L_stressL);             % Finds maximum value of longitudinal
stress (sigma max)
sigmaL_max_v = max(C_stressL);             % Finds maximum value if circumferential
stress (sigma max)

time1L = find(L_stressL == sigmaL_max_h);   % Finds the time that sigma max occurs
(longitudinal)
time2L = find(C_stressL == sigmaL_max_v);   % Finds the time that sigma max occurs
(circumferential)

L_stressL(time1L:end,:) = [];                % Deletes all values before sigmas max
C_stressL(time2L:end,:) = [];                % Deletes all values before sigmas max
L_strainL(time1L:end,:) = [];                % Deletes all values before sigmas max
C_strainL(time2L:end,:) = [];                % Deletes all values before sigmas max


Ws_horzL = trapz(L_strainL,L_stressL);                      % Finds the area under
the curve using trapezoidal summations.
Ws_vertL = trapz(C_strainL,C_stressL);                      % Finds the area under
the curve using trapezoidal summations.

%% Linear Fit for Loading and Unloading Curve (Young's Modulus)
%Check to make sure the loading and unloading curve data is corrrect
figure(1)
plot(L_strainL,L_stressL) %longitudinal loading
hold on
plot(L_strains,L_stresss) %longitudinal unloading
title('Longitudinal')
legend('Loading','Unloading')
figure(2)
plot(C_strainL,C_stressL) %circumferential loading
```

```
hold on
plot(C_strains,C_stresss) %circumferential unloading
title('Circumferential')
legend('Loading','Unloading')

%Linear Fit
zLL=polyfit(L_strainL,L_stressL,1); %linear fit for loading Longitudinal
zLs=polyfit(L_strains,L_stresss,1); %linear fit for unloading Longitudinal
zCL=polyfit(C_strainL,C_stressL,1); %linear fit for loading Circumferential
zCs=polyfit(C_strains,C_stresss,1); %linear fit for unloading Circumferential

EM_L_loading=zLL(1);
EM_L_unloading=zLs(1);
EM_C_loading=zCL(1);
EM_C_unloading=zCs(1);
EM_loading=[EM_L_loading EM_C_loading];
EM_unloading=[EM_L_unloading EM_C_unloading];
direction=["Longitudinal"; "Circumferential"];
% rm=table(direction,EM_loading',EM_unloading') %put relaxation modulus data into
table
rm=table([zLL(1);zCL(1)],[zLs(1);zCs(1)],'VariableNames',{'EM Loading','EM
Unloading'},'RowName',{'Longitudinal','Circumferential'});

%% Calcualting Loop Widths

hx = data(:,1); % Reloads the longitudinal strain values
hy = data(:,2); % Reloads the longitudinal stress values
vx = data(:,4); % Reloads the circumferential strain values
vy = data(:,5); % Reloads the circumferential stress values

mp1 = sigma_max_h./2; % Midpoint is (sigma max)/2
mp2 = sigma_max_v./2; % Midpoint is (sigma max)/2


z1 = polyfit(L_strain,L_stress,6);                              % Fits a 5th degree
polynomial to the longitudinal loading curve, depends on the sample
z2 = polyfit(C_strain,C_stress,6);                              % Fits a 5th degree
polynomial to the circumferential loading curve, depends on the sample

% NOTE: The degree of polynomial used to fit the stress-strain curve can be
%       changed by replacing the 5s above with the desired nth degree polynomial.
%       The higher the order of the polynomial, generally the better the fit, but
%       orders around 6-7 and above tend to throw a warning that the polynomial
%       is badly conditioned. This is why a degree of 5 was chosen as the default.

fit1a = polyval(z1,L_strain); % Evaluates the generated polynomial for every
longitudinal strain value
fitx1a = L_strain;            % x-values for the fitted longitudinal polynomial
fit2a = polyval(z2,C_strain); % Evaluates the generated polynomial for every
circumferential strain value
fitx2a = C_strain;            % x-values for the fitted circumferential polynomial

for i = linspace(min(L_strain),max(L_strain),500)         % For 500 equally spaced
points between the minimum and maximum longitudinal strain
```

```
    interpolatedValues = polyval(z1,i);                                     %
Interpolates the fitted polynomial for every x value to get a y-value
    if interpolatedValues > (mp1-0.5) && interpolatedValues < (mp1+0.5)     % If the
interpolated value is equal to the midpoint +/- 0.5, x-value gets stored
        final1 = i;
    end
end

for i = linspace(min(C_strain),max(C_strain),500)             % For 500 equally
spaced points between the minimum and maximum circumfrential strain
    interpolatedValues = polyval(z2,i);                                     %
Interpolates the fitted polynomial for every x value to get a y-value
    if interpolatedValues > (mp2-0.5) && interpolatedValues < (mp2+0.5)     % If the
interpolated value is equal to the midpoint +/- 0.5, x-value gets stored
        final2 = i;
    end
end

% Lines 106 - 135 follow the same procedure as above but with the offload curve

L_strain = data(:,1);
L_stress = data(:,2);
C_strain = data(:,4);
C_stress = data(:,5);

L_stress(time1:x,:) = [];
C_stress(time2:x,:) = [];
L_strain(time1:x,:) = [];
C_strain(time2:x,:) = [];

z1 = polyfit(L_strain,L_stress,6);
z2 = polyfit(C_strain,C_stress,6);
fit1b = polyval(z1,L_strain);
fitx1b = L_strain;
fit2b = polyval(z2,C_strain);
fitx2b = C_strain;

for i = linspace(min(L_strain),max(L_strain),500)
    interpolatedValues = polyval(z1,i);
    if interpolatedValues > (mp1-0.5) && interpolatedValues < (mp1+0.5)
        initial1 = i;
    end
end

for i = linspace(min(C_strain),max(C_strain),500)
    interpolatedValues = polyval(z2,i);
    if interpolatedValues > (mp2-0.5) && interpolatedValues < (mp2+0.5)
        initial2 = i;
    end
end

loop_width_horz = final1 - initial1; % Loop width at the midpoint is the offloading
value - the loading value
loop_width_vert = final2 - initial2; % Loop width at the midpoint is the offloading
value - the loading value
```

```
%% Calculating Loop Height
Strain_L = max(L_strain) - min(L_strain); % Find the triangle width
Strain_C = max(C_strain) - min(C_strain);
Strain_midL = Strain_L/2;
Strain_midC = Strain_C/2;

    MidStress_LoadL = interp1(L_strainL, L_stressL, Strain_midL, 'cubic'); %loading
of longitudinal direction
    MidStress_UnloadL = interp1(L_strains, L_stresss, Strain_midL, 'cubic');
%unloading of longitudinal direction

    MidStress_LoadC = interp1(C_strainL, C_stressL, Strain_midC, 'cubic'); %loading
of circumferential direction
    MidStress_UnloadC = interp1(C_strains, C_stresss, Strain_midC, 'cubic');
%unloading of circumferential direction

Loop_Height_L = MidStress_LoadL - MidStress_UnloadL; %longitudinal
Loop_Height_C = MidStress_LoadC - MidStress_UnloadC; %circumferential
Loop_height = [Loop_Height_L Loop_Height_C];

%% Calculating VE ratio
%V/E = Wd/Ws;

horizontal_VEratio = Wd_horz./Ws_horz;
vertical_VEratio = Wd_vert./Ws_vert;
%% Calculating Damping

% Damping = Wd/(Wd + Ws)

horizontal_damping = Wd_horz./(Wd_horz+Ws_horz);
vertical_damping = Wd_vert./(Wd_vert+Ws_vert);

%% Plot Data with midpoint line

% Reloads all of the stress and strain values

L_strain = data(:,1);
L_stress = data(:,2);
C_strain = data(:,4);
C_stress = data(:,5);

figure;
plot(L_strain,L_stress,'k');            % Plots the longitudinal stress-strain
values in black
hold on
plot(fitx1b,fit1b,'r--'); % Plots the the fitted loading curve values in dashed blue
lines
plot(fitx1a,fit1a,'b--'); % Plots the the fitted unloading curve values in dashed
blue lines
hold off
title('Longitudinal Stress-Strain Relationship');
xlabel('Green Strain');
ylabel('Cauchy Stress (kPa)');
```

```
yline(mp1,'-.');                        % Puts a horizontal line in the plot at
(sigma max)/2
legend('Stress-Strain Curve','Fitted Polynomial for Loading Curve','Fitted Polynomial
for Unloading Curve','(sigma max)/2','Location','northwest');

figure;
plot(C_strain,C_stress,'k');                % Plots the circumferential stress-
strain values
hold on
plot(fitx2b,fit2b,'r--'); % Plots the the fitted loading curve values in dashed blue
lines
plot(fitx2a,fit2a,'b--'); % Plots the the fitted unloading curve values in dashed
blue lines
hold off
title('Circumferential Stress-Strain Relationship');
xlabel('Green Strain');
ylabel('Cauchy Stress (kPa)');
yline(mp2,'--','(sigma max)/2');            % Puts a horizontal line in the plot at
(sigma max)/2
legend('Stress-Strain Curve','Fitted Polynomial for Loading Curve','Fitted Polynomial
for Unloading Curve','(sigma max)/2','Location','northwest');

%% Format Biomechnaical Data into Table

params = [Loop_Height_L Loop_Height_C; Wd_horz Wd_vert; Ws_horz Ws_vert;
horizontal_VEratio vertical_VEratio; horizontal_damping vertical_damping;
EM_L_loading EM_C_loading; EM_L_unloading EM_C_unloading;];

%T = table ([Wd_horz;Wd_vert;
Ws_horz;Ws_vert]);[horizontal_VEratio;vertical_VEratio;horizontal_damping;vertical_da
mping];'VariableNames';{'Wd','Ws','VE
Ratio','Damping'};'RowName';{'Longitudinal','Circumferential'}; %#ok<VUNUS>
% T =
table([Ws_horz;Ws_vert],[Ws_horzs;Ws_verts],[Ws_horzL;Ws_vertL],[Wd_horz;Wd_vert],'Va
riableNames',{'Ws MaxStress Unloading','Ws MaxStrain Unloading','Ws MaxStress
Loading','Wd'},'RowName',{'Longitudinal','Circumferential'});
% T = table([Wd_horz Wd_vert] [Ws_horz Ws_vert] [horizontal_VEratio vertical_VEratio]
[horizontal_damping vertical_damping] [EM_L_loading  EM_C_loading] [EM_L_unloading
EM_C_unloading],'VariableNames',{'Wd','Ws','VE Ratio','Damping','EM Loading','EM
Unloading'},'RowName',{'Longitudinal','Circumferential'});
% disp(T);

% end script
```

PV Loop Modeling – Healthy RV Using Passive Elastic Stress

```
%For PV loop modeling using lumped model
%From Dr. Lik Chuan Lee
%Edited by Kristen LeBar
%Edited August-September, 2023
%Main efforts include updating geometry and circulation parameters to reflect
pulmonary circulation;
%adding a viscous term to the passive stress formulation.
%9.21.23, from Dr. Lee: added hemodynamic values for right atrium, updated
%volume values for PA, RV, veins and RA. Changed flow calculation for
%triscupid valve.
%9.2024, changed flow in tricuspid valve to reference venous pressure
%rather than atrial pressure - this is to remove "sawtooth" profile in
%volume and pressure
% function out = main()
clear; clear all; clc; close all;

% Initial volumes
VPA = 54.6;
Vcv = 1520;
Vrv = 57.5;
prev_Vrv = Vrv;
Vra = 165;

Vw = 40; % RV wall volume (ml)
Vu = 100; % unloaded cavity volume (ml) - volume at zero pressure % 120mL gives
representative loops

% Resistance of circulation
Rpa = 1000*0.2; %  pulmonary arteries resistance
Rcv = 1000*0.004; % distal pulmonary veins resistance
Rpv = 1000*0.002; % pulmonary valve resistance
Rtv = 1000*0.002; % triscupid valve - assumed from PV resistance

% Compliance of circulation
CPA = 4.4; % pulmonary arterial compliance
Ccv = 280; % distal pulmonary vein compliance - assume CPA vs Ccv is 1/20
Cra = 50; % right atrium compliance

% Resting volumes - corresponds to volume at min pressure
VPA0 = 1; % proximal pulmonary arteries
Vcv0 = 10; % distal pulmonary veins
Vra0 = 70; % right atrium (LCL)

HR =  60;

BCL = 60/HR*1000;
ncyc = 10; %number of cycles
dt = 1; %delta time %LCL (Units in ms)
nsteps = ncyc*BCL/dt; %number of steps %LCL
nstepscyc = nsteps/ncyc; % number of steps per cycle


Tmax = 1045; %isometric tension achieved at the longest sarcomere length (MPa) LCL -
why increase from 145 to 1045?
```

```
t = linspace(0,ncyc*BCL,nsteps);

Vol = zeros(length(t)-1,4); %initialize volume
Prs = zeros(length(t)-1,4); %initialize pressure
thickness = zeros(length(t)-1,3);
stress = zeros(length(t)-1,3);
stretch = zeros(length(t)-1,3);
strain = zeros(length(t)-1,3);

cyc_cnt = 1; %cycle count


figure(1)
P1 = subplot(2,2,[1,3]);
P1_ = plot(Vol(:,1), Prs(:,1));
set( get(P1,'XLabel'), 'String', 'Volume' );
set( get(P1,'YLabel'), 'String', 'Pressure' );
set( get(P1,'Title'), 'String', 'PV loop' );


P2 = subplot(2,2,2);
P2_ = plot(t(2:end), Prs(:,1));
set( get(P2,'XLabel'), 'String', 'Time' );
set( get(P2,'YLabel'), 'String', 'Pressure' );
set( get(P2,'Title'), 'String', 'Pressure' );
set(P2, 'XLim', [0,t(end)]);

P3 = subplot(2,2,4);
P3_ = plot(t(2:end), Vol(:,1));
set( get(P3,'XLabel'), 'String', 'Time' );
set( get(P3,'YLabel'), 'String', 'Volume' );
set( get(P3,'Title'), 'String', 'Volume' );
set(P3, 'XLim', [0,t(end)]);


% Iterating with time
for i = 1:size(t,2)-1

    dt =  (t(i+1) - t(i)); % time step

    PPA = (1/CPA)*(VPA - VPA0); % PA pressure
    Pcv = (1/Ccv)*(Vcv - Vcv0); % distal pulmonary veins pressure
    Pra = (1/Cra)*(Vra - Vra0); % RA

    % Apply Laplace Law
    out = laplace(Vrv, prev_Vrv, t(i+1), HR, Tmax, Vw, Vu, BCL, dt); %LCL
    PRV = out(1)*7.5;
    sigma = out(2);
    th = out(3);
    lbda = out(4);
    active = out(6);
    passive = out(5);
```

```
alpha = 1;
if(alpha*(PRV - PPA) <= 20)
    QPA = 1/(Rpv*alpha)*log(1 + exp(alpha*(PRV - PPA)));
else
    QPA = 1/Rpv*(PRV - PPA);
end

if(PRV >= Pcv)
    Qtv = 0;
else
   Qtv = 1/Rcv*(Pcv - PRV); %tricuspid valve
end

Qcv = 1/Rcv*(Pcv - Pra);
Qppa = 1/Rpa*(PPA - Pcv);

Vrv = Vrv + dt*(Qtv - QPA);
prev_Vrv = Vrv - dt*(Qtv-QPA);
VPA = VPA + dt*(QPA - Qppa);
Vcv = Vcv + dt*(Qppa - Qcv);
Vra = Vra + dt*(Qcv - Qtv);

prev_Vol(i,1) = prev_Vrv;
Vol(i,1) = Vrv;
Vol(i,2) = VPA;
Vol(i,3) = Vcv;
size(Vol);

Prs(i,1) = PRV;
Prs(i,2) = PPA;
Prs(i,3) = Pcv;
Prs(i,4) = Pra;
size(Prs);

thickness(i) = th;
stress(i) = sigma;
act_stress(i,1) = active;
pas_stress(i,1) = passive;
stretch(i) = lbda;
strain(i) = 0.5*(lbda^2 - 1); % stays same for formulation of RV

cyc_cnt = cyc_cnt + 1;


if(mod(i, 100) == 0)

    figure(1)
    P1_.XData = Vol(2:i,1);
    P1_.YData = Prs(2:i,1);

    P2_.XData = t(2:i);
    P2_.YData = Prs(2:i,1);

    P3_.XData = t(2:i);
    P3_.YData = Vol(2:i,1);
```

```
    end

end
disp([Vrv, VPA, Vcv, Vra])

figure (2)
plotted_Vol = Vol(end-(nstepscyc-2):end,1);
plotted_Prs = Prs(end-(nstepscyc-2):end,1);
plot(plotted_Vol, plotted_Prs);
xlabel('Volume (mL)')
fontsize(gcf,12, "points")
ylabel('Pressure (mmHg)')
fontsize(gcf,12, "points")
title('Healthy RV Pressure Volume Relation')
% title('Diseased RV Pressure Volume Relation')
fontsize(gcf,16, "points")

plotted_prev_Vol = prev_Vol(end-(nstepscyc-2):end,1);

figure(3)
plot(t(1:999),stress(end-(nstepscyc-2):end,1))

figure(4)
plot(t(1:999),plotted_Prs)
ylabel('Pressure (mmHg)')
xlabel('Time (ms)')

figure(5)
plot(t(1:999), plotted_Vol)
ylabel('Volume (mL)')
xlabel('Time (ms)')

figure(6)
plot(t(1:999),Prs(1:999,4))
hold on
plot(t(1:999),Prs(1:999,3))
legend('Right atrium','Veins')

figure(7)
plot(t(1:999), pas_stress(end-(nstepscyc-2):end,1))
ylabel('Elastic Stress')
fontsize(gcf,12, "points")
xlabel('Time(ms)')
fontsize(gcf,12, "points")

% Hemodynamic output
[ESV,index_ESV] = min(plotted_Vol); % end-systolic volume
[EDV,index_EDV] = max(plotted_Vol); % end-diastolic volume
[ESP,index_ESP] = max(plotted_Prs); % end-systolic pressure
EDP = plotted_Prs(index_EDV); % end-diastolic pressure
[min_pres, index_min_pres] = min(plotted_Prs);
SV = EDV-ESV; % stroke volume
SW = SV*ESP; % stroke work
EF = SV/EDV; % ejection fraction
```

```
CO = SV*HR; % cardiac output
for i=1:length(plotted_Prs)-1
    dPdt(i) = (plotted_Prs(i+1)-plotted_Prs(i))/dt;
end
dPdt_max = max(dPdt);
dPdt_min = min(dPdt);

% Diastolic phase - derive EDPVR
v_range = linspace(plotted_Vol(index_min_pres),EDV,10000);
p_range = linspace(min_pres,plotted_Prs(index_EDV),10000);
linear = polyfit(v_range,p_range,1);
EDPVR = linear(1);

% Systolic phase - derive ESPVR
ESPVR = ESP/plotted_Vol(index_ESP);

variables = ["ESV"; "EDV"; "ESP"; "EDP"; "SV"; "SW"; "EF"; "CO"; "dP/dt max"; "dP/dt
min";"EDPVR"; "ESPVR"];
values = [ESV; EDV; ESP; EDP; SV; SW; EF; CO; dPdt_max; dPdt_min; EDPVR; ESPVR];
hemo = table(variables, values);

function out = laplace(RVV, prev_RVV, t, HR, Tmax, Vw, Vu, BCL, dt)

    ri0 = (3*Vu/(2*pi))^(1/3); % Unloaded cavity radius
    ri = (3*RVV/(2*pi))^(1/3); % Loaded cavity radius
    lbda = ri/ri0; % stretch

    th = fzero(@(x) Vw - 2/3*pi*((ri + x)^3 - ri^3), 1.0); % solving for thickness
(close to 1)
    vw = (1/3)*pi*(((ri+th)*(ri+th)^2)-ri^3); %loaded cavity volume

    tmod = t - floor(t/(HR/60*BCL))*BCL ; %LCL

    out = modifiedguccionemyostress(lbda, tmod, Tmax, RVV, prev_RVV, Vu, dt);
    sigma = out(1); %total stress
    sigma_pas = out(2);
    sigma_act = out(3);

    PRV = (1/3)*sigma*log(1+(vw/Vu)); % pressure in the RV formulation
    out = [PRV, sigma, th, lbda, sigma_pas, sigma_act];

end

% Active and passive constitutive law
function out = modifiedguccionemyostress(lbda, t, Tmax, RVV, prev_RVV, Vu, dt)

    % Passive stress
    Cparam = 0.18; %parameter associated with the strain energy function
    bff = 34; % longitudinal bff, from Eric's 2021
    Eff = 0.5*(lbda.^2 - 1); %fiber strain
    pas_stress = 2*Cparam*bff*Eff*lbda*lbda*exp(bff*Eff^2); %passive stress
formulation

    % Active stress
    Ca0 = 4.35; %peak intracellular calcium concentration
```

```
    Ca0max = 4.35; %maximum peak intracellular calcium concentration
    B = 4.75*0.1; %some constant - why is this scaled by 0.1?
    lr = 1.85; %stress-free sarcomere length
    l0 = 1.58; %sarcomere length at which no active tension develops
    t0 = 250; %time taken to reach peak tension
    tau = 25; %relaxation constant
    trans = 300; %time where the relaxation starts?

    if(lbda*lr >= l0)
        ECa0 = Ca0max/sqrt(exp(B*(lbda*lr - l0)) - 1); %ECa0=length-dependent calcium
sensitivity
    else
        ECa0 = 1e2;
    end

    if(t <= trans)
        Ct = 0.5*(1 - cos(pi*t/t0));
    else
        Ct = 0.5*(1 - cos(pi*trans/t0))*exp(-(t - trans)/tau);
    end


    act_stress = Tmax*Ca0.^2/(Ca0.^2 + ECa0.^2)*Ct; %active stress formulation

    out = [(pas_stress + act_stress), pas_stress, act_stress];

end
```

PV Loop Modeling – Diseased RV Using Passive Elastic Stress

```
%For PV loop modeling using lumped model
%From Dr. Lik Chuan Lee
%Edited by Kristen LeBar
%Edited August-September, 2023
%Main efforts include updating geometry and circulation parameters to reflect
pulmonary circulation;
%adding a viscous term to the passive stress formulation.
%9.21.23, from Dr. Lee: added hemodynamic values for right atrium, updated
%volume values for PA, RV, veins and RA. Changed flow calculation for
%triscupid valve.
% function out = main()
clear; clear all; clc;

% Initial volumes
VPA = 54.6;
Vcv = 1520;
Vrv = 57.5;
Vra = 165;

Vw = 40; % RV wall volume (ml)
Vu = 120; % unloaded diseased cavity volume (ml) - volume at zero pressure % 120mL
gives representative loops

% Resistance of circulation
Rpa = 1000*0.5; %  pulmonary arteries resistance
Rcv = 1000*0.004; % distal pulmonary veins resistance
Rpv = 1000*0.002; % pulmonary valve resistance
Rtv = 1000*0.002; % triscupid valve - assumed from PV resistance

% Compliance of circulation
CPA = 3; % pulmonary arterial compliance
Ccv = 200; % distal pulmonary vein compliance - assume CPA vs Ccv is 1/20
Cra = 10; % right atrium compliance

% Resting volumes - corresponds to volume at min pressure
VPA0 = 1; % proximal pulmonary arteries
Vcv0 = 10; % distal pulmonary veins
Vra0 = 70; % right atrium (LCL)

HR =  60;

BCL = 60/HR*1000;
ncyc = 10; %number of cycles
dt = 1; %delta time %LCL (Units in ms)
nsteps = ncyc*BCL/dt; %number of steps %LCL
nstepscyc = nsteps/ncyc; % number of steps per cycle


Tmax = 1045; %isometric tension achieved at the longest sarcomere length (MPa) LCL -
why increase from 145 to 1045?

t = linspace(0,ncyc*BCL,nsteps);

Vol = zeros(length(t)-1,4); %initialize volume
```

```
Prs = zeros(length(t)-1,4); %initialize pressure
thickness = zeros(length(t)-1,3);
stress = zeros(length(t)-1,3);
stretch = zeros(length(t)-1,3);
strain = zeros(length(t)-1,3);

cyc_cnt = 1; %cycle count


figure(1)

P1 = subplot(2,2,[1,3]);
P1_ = plot(Vol(:,1), Prs(:,1));
set( get(P1,'XLabel'), 'String', 'Volume' );
set( get(P1,'YLabel'), 'String', 'Pressure' );
set( get(P1,'Title'), 'String', 'PV loop' );


P2 = subplot(2,2,2);
P2_ = plot(t(2:end), Prs(:,1));
set( get(P2,'XLabel'), 'String', 'Time' );
set( get(P2,'YLabel'), 'String', 'Pressure' );
set( get(P2,'Title'), 'String', 'Pressure' );
set(P2, 'XLim', [0,t(end)]);

P3 = subplot(2,2,4);
P3_ = plot(t(2:end), Vol(:,1));
set( get(P3,'XLabel'), 'String', 'Time' );
set( get(P3,'YLabel'), 'String', 'Volume' );
set( get(P3,'Title'), 'String', 'Volume' );
set(P3, 'XLim', [0,t(end)]);


% Iterating with time
for i = 1:size(t,2)-1

    dt =  (t(i+1) - t(i)); % time step

    PPA = (1/CPA)*(VPA - VPA0); % PA pressure
    Pcv = (1/Ccv)*(Vcv - Vcv0); % distal pulmonary veins pressure
    Pra = (1/Cra)*(Vra - Vra0); % RA LCL

    % Apply Laplace Law
    out = laplace(Vrv, t(i+1), HR, Tmax, Vw, Vu, BCL); %LCL
    PRV = out(1)*7.5;
    sigma = out(2);
    th = out(3);
    lbda = out(4);

 alpha = 1;
    if(alpha*(PRV - PPA) <= 20)
        QPA = 1/(Rpv*alpha)*log(1 + exp(alpha*(PRV - PPA)));
    else
        QPA = 1/Rpv*(PRV - PPA);
    end
```

```
    if(PRV >= Pcv)
       Qtv = 0;%1/Rtv*(Pcv - PRV); %tricuspid valve
    else
       Qtv = 1/Rtv*(Pcv - PRV); %tricuspid valve
    end


    Qcv = 1/Rcv*(Pcv - Pra);
    Qppa = 1/Rpa*(PPA - Pcv);

    Vrv = Vrv + dt*(Qtv - QPA);
    VPA = VPA + dt*(QPA - Qppa);
    Vcv = Vcv + dt*(Qppa - Qcv);
    Vra = Vra + dt*(Qcv - Qtv);

    Vol(i,1) = Vrv;
    Vol(i,2) = VPA;
    Vol(i,3) = Vcv;
    size(Vol);

    Prs(i,1) = PRV;
    Prs(i,2) = PPA;
    Prs(i,3) = Pcv;
    size(Prs);

    thickness(i) = th;
    stress(i) = sigma;
    stretch(i) = lbda;
    strain(i) = 0.5*(lbda^2 - 1); % stays same for formulation of RV

    cyc_cnt = cyc_cnt + 1;


    if(mod(i, 100) == 0)

        figure(1)
        P1_.XData = Vol(2:i,1);
        P1_.YData = Prs(2:i,1);

        P2_.XData = t(2:i);
        P2_.YData = Prs(2:i,1);

        P3_.XData = t(2:i);
        P3_.YData = Vol(2:i,1);

    end

end
disp([Vrv, VPA, Vcv, Vra])

figure (2)
disease_Vol = Vol(9000:9999,1);
disease_Prs = Prs(9000:9999,1);
plot(Vol(8000:9999,1),Prs(8000:9999,1));
```

```
xlabel('Volume (mL)')
fontsize(gcf,12, "points")
ylabel('Pressure (mmHg)')
fontsize(gcf,12, "points")
title('Pressure-overloaded RV Pressure Volume Relation')
fontsize(gcf,16, "points")
xlim([90,165])

% Hemodynamic output
[ESV,index_ESV] = min(disease_Vol); % end-systolic volume
[EDV,index_EDV] = max(disease_Vol); % end-diastolic volume
[ESP,index_ESP] = max(disease_Prs); % end-systolic pressure
EDP = disease_Prs(index_EDV); % end-diastolic pressure
[min_pres, index_min_pres] = min(disease_Prs);
SV = EDV-ESV; % stroke volume
SW = SV*ESP;
EF = SV/EDV; % ejection fraction
CO = SV*HR; % cardiac output
for i=1:length(disease_Prs)-1
    dPdt(i) = (disease_Prs(i+1)-disease_Prs(i))/dt;
end
dPdt_max = max(dPdt);
dPdt_min = min(dPdt);

% Diastolic phase - derive EDPVR
v_range = linspace(disease_Vol(index_min_pres),EDV,10000);
p_range = linspace(min_pres,disease_Prs(index_EDV),10000);
linear = polyfit(v_range,p_range,1);
EDPVR = linear(1);

variables = ["ESV"; "EDV"; "ESP"; "EDP"; "SV"; "SW"; "EF"; "CO"; "dP/dt max"; "dP/dt
min";"EDPVR"];
values = [ESV; EDV; ESP; EDP; SV; SW; EF; CO; dPdt_max; dPdt_min; EDPVR];
hemo = table(variables, values);

function out = laplace(RVV, t, HR, Tmax, Vw, Vu, BCL)

    ri0 = (3*Vu/(2*pi))^(1/3); % Unloaded cavity radius
    ri = (3*RVV/(2*pi))^(1/3); % Loaded cavity radius
    lbda = ri/ri0; % stretch

    th = fzero(@(x) Vw - 2/3*pi*((ri + x)^3 - ri^3), 1.0); % solving for thickness
(close to 1)
    vw = (1/3)*pi*(((ri+th)*(ri+th)^2)-ri^3); %loaded cavity volume

    tmod = t - floor(t/(HR/60*BCL))*BCL ; %LCL

    out = modifiedguccionemyostress(lbda, tmod, Tmax);
    sigma = out(1); %total stress
    sigma_pas = out(2);
    sigma_act = out(3);

    PRV = (1/3)*sigma*log(1+(vw/Vu)); % pressure in the RV formulation
    out = [PRV, sigma, th, lbda, sigma_pas, sigma_act];
```

```
end

% Active and passive constitutive law
function out = modifiedguccionemyostress(lbda, t, Tmax)

    % Passive stress
    Cparam = 0.88;
    bff = 34; %parameter associated with the strain energy function
    Eff = 0.5*(lbda.^2 - 1); %fiber strain
    pas_stress = 2*Cparam*bff*Eff*lbda*lbda*exp(bff*Eff^2); %passive stress
formulation

    % Active stress
    Ca0 = 4.35; %peak intracellular calcium concentration
    Ca0max = 4.35; %maximum peak intracellular calcium concentration
    B = 4.75*0.1; %some constant - why is this scaled by 0.1?
    lr = 1.85; %stress-free sarcomere length
    l0 = 1.58; %sarcomere length at which no active tension develops
    t0 = 250; %time taken to reach peak tension
    tau = 25; %relaxation constant
    trans = 300; %time where the relaxation starts?

    if(lbda*lr >= l0)
        ECa0 = Ca0max/sqrt(exp(B*(lbda*lr - l0)) - 1); %ECa0=length-dependent calcium
sensitivity
    else
        ECa0 = 1e2;
    end

    if(t <= trans)
        Ct = 0.5*(1 - cos(pi*t/t0));
    else
        Ct = 0.5*(1 - cos(pi*trans/t0))*exp(-(t - trans)/tau);
    end


    act_stress = Tmax*Ca0.^2/(Ca0.^2 + ECa0.^2)*Ct; %active stress formulation

    out = [(pas_stress + act_stress), pas_stress, act_stress];

end
```

PV Loop Modeling – Healthy & Diseased RV Using Passive Viscoelastic Stress

```
%For PV loop modeling using lumped model
%From Dr. Lik Chuan Lee
%Edited by Kristen LeBar
%Edited August-September, 2023
%Main efforts include updating geometry and circulation parameters to reflect
pulmonary circulation
%9.21.23, from Dr. Lee: added hemodynamic values for right atrium, updated
%volume values for PA, RV, veins and RA. Changed flow calculation for
%triscupid valve.
%October 12, 2023: changed code to output only the final loop
%October 24, 2023: changing total passive stress formulation to include
%viscous component.
%January 2024: changed stress, strain, and stretch matrix sizes to only
%assign values to the first column.
%Sept. 2024: Update active stress formulation as in caporizzo 2018 (use
%strain rate)
%Sept. 17 2024: changed flow in tricuspid valve to reference venous pressure
%rather than atrial pressure - this is to remove "sawtooth" profile in
%volume and pressure
%Sept. 18 2024: add distal pulmonary artery to circulatory system (not just
%proximal).
%Sept. 23 2024: Use soft plus function to derive flow in pulmonary artery
% function out = main()
clear; clear all; clc; close all;


% Initial volumes
VPA = 54.6;
Vcv = 1520;
Vrv = 57.5;
prev_Vrv = Vrv;
Vra = 165;
Vcp = 2.0;

Vw = 40; % RV wall volume (ml)
Vu = 100; % unloaded cavity volume (ml) - volume at zero pressure % 120mL gives
representative loops
% Vu = 120; % diseased

% Resistance of circulation
Rpa = 1000*0.2; % proximal pulmonary arteries resistance - this value is different
from 2022 paper (LCL)
% Rpa = 1000*0.5; % diseased
Rcv = 1000*0.004; % distal pulmonary veins resistance
Rpv = 1000*0.002; % pulmonary valve resistance - in the 2022 paper, Rpv=Rpa
Rtv = 1000*0.2; % triscupid valve - assumed from PV resistance
Rcp = 1000*0.05; % distal pulmonary artery resistance - this value is 25x the Rpa
(consistent relation as in 2022 paper)

% Compliance of circulation (mL/kPa)
CPA = 4.4; % proximal pulmonary arterial compliance - value determined by CVB
% CPA = 3; % diseased
Ccp = 6.5; % distal pulmonary arterial compliance - from 2022 paper
Ccv = 280; % distal pulmonary vein compliance - assume CPA vs Ccv is 1/20
```

```
% Ccv = 200; % diseased
Cra = 50; % right atrium compliance - LCL
% Cra = 10; % diseased

% Resting volumes - corresponds to volume at min pressure
VPA0 = 1; % proximal pulmonary arteries
Vcp0 = 2; % distal pulmonary arteries - from 2022 paper
Vcv0 = 10; % distal pulmonary veins
Vra0 = 70; % right atrium (LCL)

HR =  60;

BCL = 60/HR*1000; % what is this parameter? units: ms/beat
ncyc = 10; %number of cycles
dt = 1; %delta time %LCL (Units in ms)
nsteps = ncyc*BCL/dt; %number of steps %LCL
nstepscyc = nsteps/ncyc; % number of steps per cycle


Tmax = 1045; %isometric tension achieved at the longest sarcomere length (MPa) LCL -
why increase from 145 to 1045?

t = linspace(0,ncyc*BCL,nsteps);


Vol = zeros(length(t)-1,4); %initialize volume
Prs = zeros(length(t)-1,4); %initialize pressure
thickness = zeros(length(t)-1,3);
stress = zeros(length(t)-1,3);
stretch = zeros(length(t)-1,3);
strain = zeros(length(t)-1,3);
prev_strain = zeros(length(t)-1,3);
next_strain = zeros(length(t)-1,3);
strain_rate = zeros(length(t)-1,3);

cyc_cnt = 1; %cycle count


figure(1)

P1 = subplot(2,2,[1,3]);
P1_ = plot(Vol(:,1), Prs(:,1));
set( get(P1,'XLabel'), 'String', 'Volume' );
set( get(P1,'YLabel'), 'String', 'Pressure' );
set( get(P1,'Title'), 'String', 'PV loop' );

P2 = subplot(2,2,2);
P2_ = plot(t(2:end), Prs(:,1));
set( get(P2,'XLabel'), 'String', 'Time' );
set( get(P2,'YLabel'), 'String', 'Pressure' );
set( get(P2,'Title'), 'String', 'Pressure' );
set(P2, 'XLim', [0,t(end)]);

P3 = subplot(2,2,4);
P3_ = plot(t(2:end), Vol(:,1));
```

```
set( get(P3,'XLabel'), 'String', 'Time' );
set( get(P3,'YLabel'), 'String', 'Volume' );
set( get(P3,'Title'), 'String', 'Volume' );
set(P3, 'XLim', [0,t(end)]);

% Iterating with time
for i = 1:size(t,2)-1

    dt =  (t(i+1) - t(i)); % time step

    PPA = (1/CPA)*(VPA - VPA0); % proximal PA pressure
    Pcv = (1/Ccv)*(Vcv - Vcv0); % distal pulmonary veins pressure
    Pra = (1/Cra)*(Vra - Vra0); % RA LCL
    Pcp = (1/Ccp)*(Vcp - Vcp0); % distal PA pressure

    % Apply Laplace Law
    out = laplace(prev_Vrv, Vrv, t(i+1), HR, Tmax, Vw, Vu, BCL, dt); %LCL
    PRV = out(1)*7.5;
    sigma = out(2);
    th = out(3);
    lbda = out(4);
    prev_lbda = out(5);
    sigma_pas = out(6);
    sigma_act = out(7);
    sigma_elastic = out(8);
    sigma_viscous = out(9);
    strainrate = out(10);
    epsilon = out(11);

    alpha = 0.65;
    if(alpha*(PRV - PPA) <= 20)
        QPA = 1/(Rpv*alpha)*log(1 + exp(alpha*(PRV - PPA)));
    else
        QPA = 1/Rpv*(PRV - PPA);
    end

    if(PRV >= Pcv)
       Qtv = 0; %1/Rtv*(Pcv - PRV); %tricuspid valve
    else
       Qtv = 1/Rcv*(Pcv - PRV); %tricuspid valve
    end

    Qcv = 1/Rcv*(Pcv - Pra);
    Qppa = 1/Rpa*(PPA - Pcp); %proximal to distal PA
    Qcp = 1/Rcp*(Pcp-Pcv); % distal PA to vein

    Vrv = Vrv + dt*(Qtv - QPA);
    prev_Vrv = Vrv - dt*(Qtv-QPA);
    VPA = VPA + dt*(QPA - Qppa);
    Vcp = Vcp + dt*(Qppa - Qcp); % distal PA flow
    Vcv = Vcv + dt*(Qcp - Qcv); % distal PA to vein flow
    Vra = Vra + dt*(Qcv - Qtv);

    prev_Vol(i,1) = prev_Vrv;
    Vol(i,1) = Vrv;
```

```
    Vol(i,2) = VPA;
    Vol(i,3) = Vcv;
    size(Vol);

    Prs(i,1) = PRV;
    Prs(i,2) = PPA;
    Prs(i,3) = Pcv;
    size(Prs);

    thickness(i,1) = th;
    stress(i,1) = sigma;
    stretch(i,1) = lbda;
    prev_stretch(i,1) = prev_lbda;
    elastic(i,1) = sigma_elastic;
    viscous(i,1) = sigma_viscous;
    active(i,1) = sigma_act;
    passive(i,1) = sigma_pas;

    strain(i,1) = 0.5*(lbda^2 - 1); % stays same for formulation of RV
    prev_strain(i,1) = 0.5*(prev_lbda^2 - 1); % calculate the previous strain point
    strain_rate(i,1) = 1000*(strain(i,1)-prev_strain(i,1))./dt;
    strain_rate_check(i,1) = strainrate;
    epsilon(i,1) = epsilon;


    cyc_cnt = cyc_cnt + 1;


    if(mod(i, 100) == 0)

        figure(1)
        P1_.XData = Vol(2:i,1);
        P1_.YData = Prs(2:i,1);

        P2_.XData = t(2:i);
        P2_.YData = Prs(2:i,1);

        P3_.XData = t(2:i);
        P3_.YData = Vol(2:i,1);

    end

end
disp([Vrv, VPA, Vcv, Vra])

figure (2)
plotted_Vol = Vol(end-(nstepscyc-2):end,1);
plotted_Prs = Prs(end-(nstepscyc-2):end,1);
PVloop = [plotted_Vol plotted_Prs];
plot(plotted_Vol(:,1),plotted_Prs(:,1));
xlabel('Volume (mL)')
fontsize(gcf,12, "points")
ylabel('Pressure (mmHg)')
fontsize(gcf,12, "points")
title('Healthy RV Pressure Volume Relation')
```

```
% title('Diseased RV Pressure Volume Relation')
fontsize(gcf,16, "points")

% Output stress and strain
plotted_stress = stress(end-(nstepscyc-2):end,1);
plotted_strain = strain(end-(nstepscyc-2):end,1);
plotted_prev_strain = prev_strain(end-(nstepscyc-2):end,1);

figure(3)
plot(t(end-(nstepscyc-2):end)',Vol(end-(nstepscyc-2):end,1))
fontsize(gcf,20, "points")
xlabel('Time (ms)')
fontsize(gcf,16, "points")
ylabel('Volume (mL)')
fontsize(gcf,16, "points")

figure(4)
plotted_viscous = viscous(end-(nstepscyc-2):end);
plotted_elastic = elastic(end-(nstepscyc-2):end);
VE_stress = [plotted_elastic plotted_viscous];
VE = plotted_viscous./plotted_elastic;
plot(t(1:999)',elastic(end-(nstepscyc-2):end)')
hold on
plot(t(1:999)',viscous(end-(nstepscyc-2):end)')
xlabel('Time(ms)')
fontsize(gcf,12, "points")
ylabel('Stress (kPa)')
fontsize(gcf,12, "points")
legend('Elastic stress','Viscous stress')
fontsize(gcf,12, "points")

figure(5)
plot(t(end-(nstepscyc-2):end)',plotted_Prs(:,1))
xlabel('Time(ms)')
ylabel('Pressure (mmHg)')

figure(6)
plot(t(end-(nstepscyc-2):end)',strain_rate(end-(nstepscyc-2):end,1))
xlabel('Time(ms)')
ylabel('Strain rate (1/s)')

figure(7)
plot(t(end-(nstepscyc-2):end)',active(end-(nstepscyc-2):end,1))
xlabel('Time(ms)')
ylabel('Active stress (kPa)')

figure(8)
plot(stretch(1:999,1))

figure(9)
plotted_passive = passive(end-(nstepscyc-2):end,1);
plot(t(1:999),passive(end-(nstepscyc-2):end,1))
xlabel('Time (ms)')
fontsize(gcf,12, "points")
ylabel('Total passive stress (kPa)')
```

```
fontsize(gcf,12, "points")

figure(10)
plot(t(1:999),VE)
xlabel('Time (ms)')
ylabel('V/E Ratio')

% Hemodynamic output
[ESV,index_ESV] = min(plotted_Vol); % end-systolic volume
[EDV,index_EDV] = max(plotted_Vol); % end-diastolic volume
[ESP,index_ESP] = max(plotted_Prs); % end-systolic pressure
EDP = plotted_Prs(index_EDV); % end-diastolic pressure
[min_pres, index_min_pres] = min(plotted_Prs);
SV = EDV-ESV; % stroke volume
EF = SV/EDV; % ejection fraction
CO = SV*HR; % cardiac output
SW = SV*ESP;
for i=1:length(plotted_Prs)-1
    dPdt(i) = (plotted_Prs(i+1)-plotted_Prs(i))/dt;
end
dPdt_max = max(dPdt);
dPdt_min = min(dPdt);

% Diastolic phase - derive EDPVR
v_range = linspace(plotted_Vol(index_min_pres),EDV,10000);
p_range = linspace(min_pres,plotted_Prs(index_EDV),10000);
linear = polyfit(v_range,p_range,1);
EDPVR = linear(1);

% Systolic phase - derive ESPVR
ESPVR = ESP/plotted_Vol(index_ESP);

variables = ["ESV"; "EDV"; "ESP"; "EDP"; "SV"; "SW"; "EF"; "CO"; "dP/dt max"; "dP/dt
min";"EDPVR";"ESPVR"];
values = [ESV; EDV; ESP; EDP; SV; SW; EF; CO; dPdt_max; dPdt_min; EDPVR; ESPVR];
hemo = table(variables, values);

function out = laplace(prev_RVV, RVV, t, HR, Tmax, Vw, Vu, BCL, dt)

    ri0 = (3*Vu/(2*pi))^(1/3); % Unloaded cavity radius
    ri = (3*RVV/(2*pi))^(1/3); % Loaded cavity radius
    ri_prev = (3*prev_RVV/(2*pi))^(1/3); % Loaded cavity radius in the previous
moment
    lbda = ri/ri0; % stretch
    prev_lbda = ri_prev/ri0; % stretch in the previous moment

    th = fzero(@(x) Vw - 2/3*pi*((ri + x)^3 - ri^3), 1.0); % solving for thickness
(close to 1)
    vw = (1/3)*pi*(((ri+th)*(ri+th)^2)-ri^3); %loaded cavity volume

    tmod = t - floor(t/(HR/60*BCL))*BCL ; %LCL

    out = modifiedguccionemyostress(prev_lbda, lbda, tmod, Tmax, RVV, prev_RVV, dt,
Vu);
    sigma = out(1); %total stress
```

```
    sigma_pas = out(2);
    sigma_act = out(3);
    sigma_elastic = out(4);
    sigma_viscous = out(5);


    PRV =(1/3)*sigma*log(1+(vw/Vu)); % pressure in the RV formulation
    out = [PRV, sigma, th, lbda, prev_lbda, sigma_pas, sigma_act, sigma_elastic,
sigma_viscous];

end


% Active and passive constitutive law
function out = modifiedguccionemyostress(prev_lbda, lbda, t, Tmax, RVV, prev_RVV, dt,
Vu)

% Updated passive stress - Kelvin-Voigt Model, spring-dashpot in parallel
% Governing equation: stress = (modulus*strain) + (eta*strain rate)
% Elastic calculation - using Fung's model fitting for elastic stress
Cparam = 0.18; %healthy
% Cparam = 0.88; %diseased
bff = 34; % from Eric's Frontiers paper
Eff = 0.5*(lbda^2 - 1); %fiber strain
elastic = 2*Cparam*bff*Eff*lbda*lbda*exp(bff*Eff^2); %passive

 % Viscous stress
%      eta = 1.8; % diseased
    eta = 0.8; % healthy
    prev_Eff = 0.5*(prev_lbda.^2 - 1);
    Vdot = (RVV-prev_RVV)/dt;
    viscous = -1.0*sign(Vdot)*1000*eta*(1/3)*((1/Vu)^(2/3))*(RVV^(-1/3))*abs(Vdot);
%LC Lee 2.7.24
    pas_stress = elastic+viscous;

% Active stress
    Ca0 = 4.35; %peak intracellular calcium concentration
    Ca0max = 4.35; %maximum peak intracellular calcium concentration
    B = 4.75*0.1; %some constant - why is this scaled by 0.1?
    lr = 1.85; %stress-free sarcomere length
    l0 = 1.58; %sarcomere length at which no active tension develops
    t0 = 250; %time taken to reach peak tension
    tau = 25; %relaxation constant
    trans = 300; %time where the relaxation starts?

    if(lbda*lr >= l0)
        ECa0 = Ca0max/sqrt(exp(B*(lbda*lr - l0)) - 1); %ECa0=length-dependent calcium
sensitivity
    else
        ECa0 = 1e2;
    end

    if(t <= trans)
        Ct = 0.5*(1 - cos(pi*t/t0));
    else
```

```
        Ct = 0.5*(1 - cos(pi*trans/t0))*exp(-(t - trans)/tau);
    end


    act_stress = Tmax*Ca0.^2/(Ca0.^2 + ECa0.^2)*Ct; %active stress formulation


    out = [(pas_stress + act_stress), pas_stress, act_stress, elastic, viscous];
end
```